Title
Structure-Function Studies of Anthrax Protective Antigen Octamer

Author
Kintzer, Alexander F.

Publication Date
2012

Peer reviewed|Thesis/dissertation

Structure-Function Studies of Anthrax Protective Antigen Octamer

by

Alexander Frederick Kintzer

A dissertation submitted in partial satisfaction of the

requirements for the degree of

Doctor of Philosophy

in

Chemistry

in the

Graduate Division of the University of California, Berkeley

Committee in charge:

Professor Bryan Krantz, Chair

Professor Jan Liphardt

Professor Jay T. Groves

Spring 2012

Structure-Function Studies of Anthrax Protective Antigen Octamer

Abstract

Structure-Function Studies of Anthrax Protective Antigen Octamer

by

Alexander Frederick Kintzer

Doctor of Philosophy in Chemistry

University of California, Berkeley

Professor Bryan Krantz, Chair

The assembly of bacterial toxins and virulence factors is critical to their function, but the regulation of holotoxin assembly during infection has not been studied. The protective antigen (PA) component of the toxin assembles into ring-shaped homooligomers that bind the two other enzyme components of the toxin, lethal factor (LF) and edema factor (EF), to form toxic complexes. To disrupt the host, these toxic complexes are endocytosed, such that the PA oligomer forms a membrane-spanning channel that LF and EF translocate through to enter the cytosol.

We found using single-channel electrophysiology that PA channels contain two populations of conductance states, which correspond with two different PA pre-channel oligomers observed by electron microscopy—the well-described heptamer and a novel octamer. Octameric complexes are likely integral to the PA assembly mechanism, as dimeric and tetrameric intermediates are the intial populated species during assembly. While complexes are functional translocases, a 3.2Å crystal structure suggests that the PA octamer prechannel may be more thermodynamically stable than the heptamer. Indeed, the octamer comprises 20-30% of the oligomers on cells, but predominates (70-80%) during assembly in physiological plasma.

To probe the mechanism of octamer stability, we measured the pH-dependence of channel formation using circular dichroism, mass spectrometry, and electron microscopy. We found that octamers form channels at lower pH than heptamers. This results in heptamer inactivation under physiological conditions, while LT complexes containing octameric PA maintain maximal cytotoxic activity. Thus the PA octamer is a physiological, stable, and active assembly state capable of forming lethal toxins that may withstand the hostile conditions encountered in the bloodstream. This assembly mechanism demonstrates a novel means to control cytotoxicity during anthrax infection.

Finally, we studied the mechanism of channel formation. We found from structural, thermodynamic, and kinetic studies that two barriers define the prechannel to channel transition—a pH-dependent and independent process. Further analysis revealed that the protonation of the membrane insertion loop, dissociation of domains 2 and 4, and interactions with phenylalanine-clamp comprise the rate-limiting, pH-dependent barrier.

Dedicated to Eva Greenstein and my family, Maria, Frederick, Eric, and Katherine.

Table of Contents

List of Figures

List of Tables

List of Abbreviations

γ-DPGA, poly-γ-D- glutamic acid
Δψ, membrane potential
$\Delta G^{\ddagger}$, activation free energies
ΔpH, proton gradient
ϕ-clamp, phenylalanine clamp
Atx, anthrax toxin
ANTXR, anthrax toxin receptor
B factor, atomic displacement parameter
CD, circular dichroism
D2, domain 2
D2-D4, interface of domains 2 and 4
D4, domain 4
dsANTXR, dimeric soluble Atx receptor
EC_{50}, effective concentration for 50% cytolysis
EF, edema factor
EM, electron microscopy
L-capsule, lower molecular mass capsule
LF, lethal factor
LF_N, lethal factor amino-terminal protective antigen-binding domain
LT, lethal toxin
MIL, membrane insertion loop
MS, mass spectrometry
msATR, monomeric soluble ATR
nanoESI, nanoelectrospray ionization
nPA, nicked protective antigen
PA, protective antigen
$PA_{\Delta D4}$, PA lacking D4
PA_7, heptameric PA oligomer
PA_8, octameric PA oligomer
PLB, planar lipid bilayer
sANTXR2, soluble extracellular domain of anthrax toxin receptor 2
SRCD, synchrotron radiation circular dichroism
$t_{1/2}$, time for half of substrate to translocate
TCEP, tris(2-carboxyethyl) phosphine HCl
UBB, universal bilayer buffer
WT, wild type

Acknowledgements

I would like to recognize all the hard work on the part of my fellow lab members and collaborators. In particular, I thank all the members of the Krantz laboratory, Harry Sterling from the Williams group, and Jakob von Moltke from the Vance laboratory. We thank R. Zalpuri at the Robert D. Ogg Electron Microscope Laboratory for assistance with EM. This work was supported by University of California start-up funds, NIH research grants R01-AI077703 (Bryan A. Krantz) and R01-GM064712 (Evan R. Williams), and a project grant from the U.K. BBSRC to Bonnie A. Wallace, and NIH training grants T32GM066698 and T32GM008295 to Alexander F. Kintzer.

In addition, I would like to thank my girlfriend, Eva Greenstein, for sticking with me all these years and for continuing to support my scientific endeavors. My family has also been an important part of my experience. Through college, graduate school, and soon to be postdoctoral training, they supply me with nourishment, financial support, and priceless inspiration during the torrential periods of academic research. I am grateful for all the support and hope these experiences will be of mutual benefit in the years to come.

Chapter 1

Introduction to Protein Translocation and Bacterial Toxins.

1.1 Transmembrane transport. Signaling and transport across membranes are ubiquitous processes and required for all living cells to respond to changes in the environment. Transmembrane signaling confers sensitivity to nutrients (Locher, Lee, & Rees, 2002; Oldham, Khare, Quiocho, Davidson, & Chen, 2007), proteins (Krantz et al., 2005), or even toxic chemicals (Murakami, Nakashima, Yamashita, & Yamaguchi, 2002). Integral membrane proteins can facilitate the transmission of chemical signals across membrane. One method for signal transduction is simply allowing molecules or proteins to pass through channels that are embedded in the lipid bilayer. A broad class of integral membrane proteins, called transporters, form aqueous channels, through which molecules are driven. Transporters must expend energy to efficiently move molecules or proteins across the membrane. The free energy gain from movement of molecules down their respective gradients can be coupled to up-hill transport. Alternatively, chemical reactions, such as ATP hydrolysis, performed by the channel itself may drive transport (Locher et al., 2002; Oldham et al., 2007). The principles of transport underlie many important processes in the cell that dysfunction in human diseases, such as cancer (Souba, 1993), neurodegenerative disorders (Skaper, 2011), cystic fibrosis (Gadsby, Vergani, & Csanady, 2006), and even bacterial infections (Baucheron et al., 2004). Therefore, it is of great importance to understand the general principles of cellular transport by integral membrane proteins.

The transport of hydrophilic proteins across membranes presents a formidable challenge to the cell, yet nearly all proteins must move across a membrane at some point in their lifetime (Leppla, 1982; Schatz & Dobberstein, 1996). This is accomplished by protein transporters, or translocases, which provide a hydrophilic, aqueous channel through the membrane for proteins to pass. However, translocase pores are often much too narrow to transport fully folded proteins (Krantz et al., 2005; Van den Berg et al., 2004). Since, proteins are stably folded into complex three-dimensional structures, protein translocases must unfold their substrates as part of the transport mechanism (Thoren, Worden, Yassif, & Krantz, 2009). This requires intrinsically maintained cellular driving forces to be coupled by the channel to protein substrate unfolding (Figure 1.1). Often, proton-gradients that are maintained across cellular membranes are sufficient to drive transport, but also ATP-hydrolysis may be used (Van den Berg et al., 2004). This can be accomplished by the channel itself or by accessory proteins that deliver unfolded substrates to the pore lumen (Mitra et al., 2005; Van den Berg et al., 2004). The principles of transport underlie many important processes in the cell that dysfunction in human diseases such as cancer (Souba, 1993), neurodegenerative disorders (Skaper, 2011), cystic fibrosis (Gadsby et al., 2006), and even bacterial infections (Baucheron et al., 2004). Therefore, it is of great importance to understand the general principles of cellular transport by integral membrane proteins.

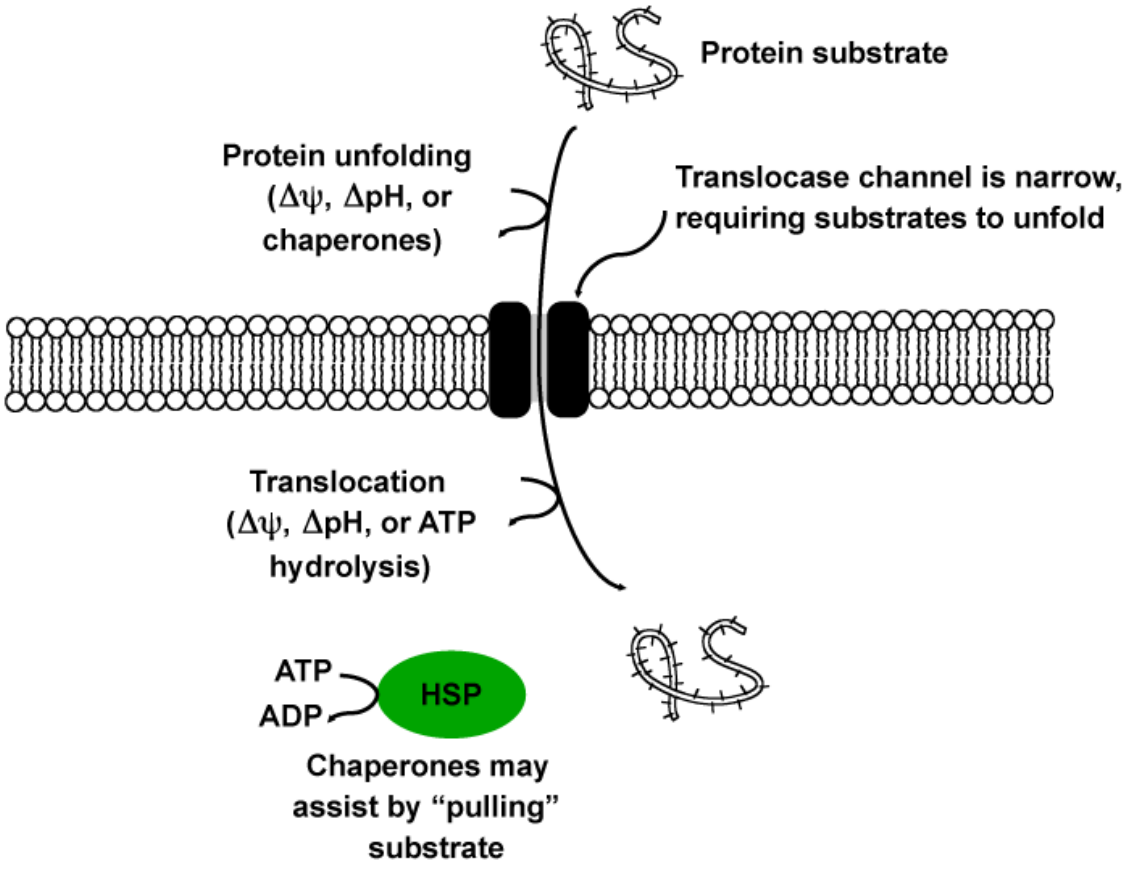

Figure. 1.1. General mechanism of protein transport. A hypothetical protein transport channel is shown in black. Driving forces, such as transmembrane potential (Δψ) or pH-gradient (ΔpH) can be directly coupled to substrate unfolding by the channel. Alternatively, ATP-dependent chaperones (e.g., heatshock proteins (HSP)), shown in green, can deliver unfolded substrates to the transport channel or aide in refolding after transport. For a review see (Schatz & Dobberstein, 1996).

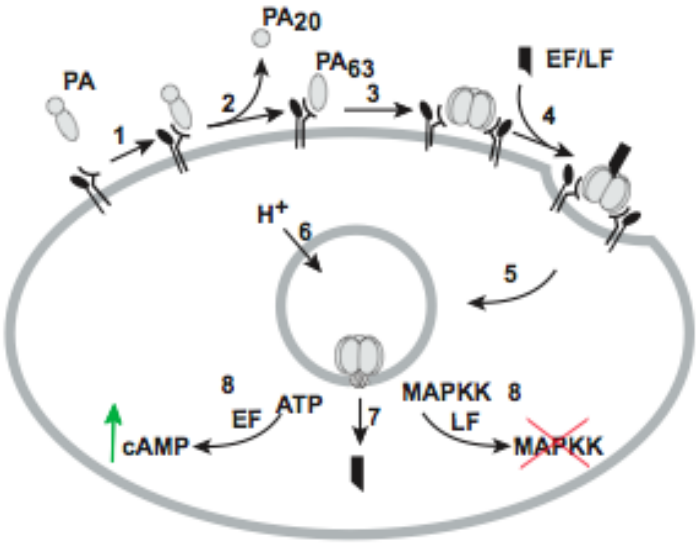

Figure. 1.2. Historic Model of Atx assembly and translocation. 1, PA binds an anthrax toxin receptor complex, which includes an ANTXR (Bradley, Mogridge, Mourez, Collier, & Young, 2001; Scobie, Rainey, Bradley, & Young, 2003) and a putative co-receptor (J. J. Young et al., 2007); 2, proteolytic activation of PA by furin-type protease and dissociation of a small 20-kDa fragment (PA_{20}); 3, PA_{63} monomers self associate into a homooligomeric pre-channel state (Lacy, Wigelsworth, Melnyk et al., 2004); 4, EF and LF bind to the pre-channel; 5, endocytosis occurs; 6, acid-induced conversion of the pre-channel to the transmembrane channel state through which LF/EF passage (Krantz et al., 2005; Miller et al., 1999), and the amino-terminal domains of LF and EF (LF_N and EF_N) are destabilized and convert to a molten globule form (Krantz, Trivedi, Cunningham, Christensen, & Collier, 2004); 7, either a membrane potential ($\Delta\psi$) or a proton gradient (ΔpH) can drive the translocation of acid-destabilized LF and EF (Krantz, Finkelstein, & Collier, 2006); 8, LF and EF can then disrupt the normal physiology of the cell by modifying cytosolic substrates. LF, a 90-kDa, Zn-protease cleaves a variety of mitogen-activated protein kinase kinases (MAPKK) (Duesbery et al., 1998; Pannifer et al., 2001); and LF plus PA is capable of leading to animal death (H Smith & Keppie, 1954). EF, a 89-kDa, Ca^{2+}/calmodulin-activated adenylyl cyclase (Drum et al., 2002), increases the cellular pool of 3'-5'-cyclic adenosine monophosphate (cAMP) up to ~200-fold by hydrolyzing adenosine-5'-triphosphate (ATP), leading to swelling of tissues and death (Beall, Taylor, & Thorne, 1962). For a review, see (Mitra et al., 2005; J. A. Young & Collier, 2007).

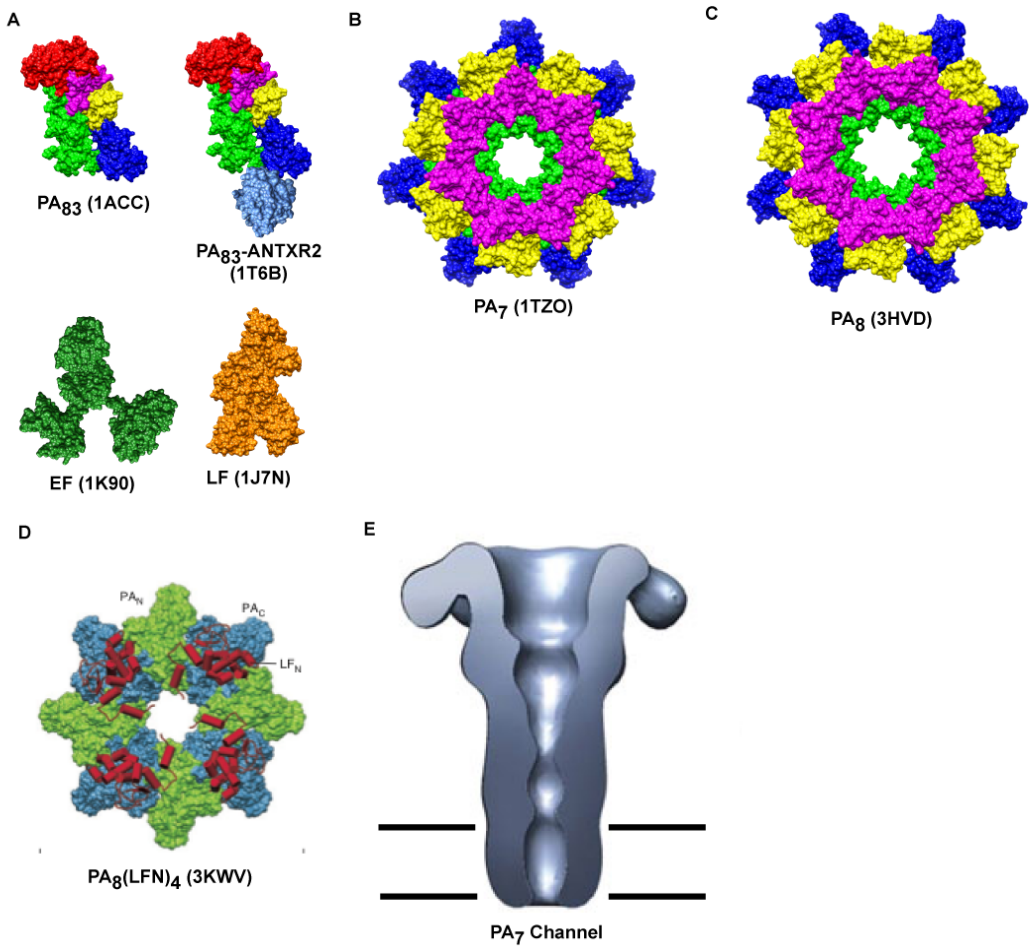

Figure. 1.3. An overview of Atx structure. (A) Crystal structures of the monomeric toxin components PA_{83} (Petosa, Collier, Klimpel, Leppla, & Liddington, 1997), PA_{83}-ANTXR2 complex (Santelli, Bankston, Leppla, & Liddington, 2004), EF (Drum et al., 2002), and LF (Pannifer et al., 2001). Crystal structures of the (B) PA_7 (Lacy, Wigelsworth, Melnyk et al., 2004), (C) PA_8 (Kintzer et al., 2009), and (D) $PA_8(LFN)_4$ prechannel oligomers (Feld et al., 2010). (E) An EM structure of the PA_7 channel (Katayama et al., 2008).

1.2 Introduction to bacterial toxin trafficking and assembly. Bacterial pathogens utilize highly evolved systems to translocate protein effectors into host cells. However, the transporters must be precisely targetted within the host-cell (Watson & Spooner, 2006). For instance, most toxins bind specific mammalian receptors, triggering internalization (Abrami, Kunz, & van der Goot, 2010; Weis et al., 1988) and trafficking to specific cellular compartments (Abrami, Liu, Cosson, Leppla, & van der Goot, 2003; Guichard et al., 2010; Weis et al., 1988). This specificity allows toxins to be used to target toxin-protein fusions to specific cell types and with specific intracellular localization (Zhao et al., 2012), which is the concept behind many biological therapeutics (Pastan & FitzGerald, 1991). Therefore, the structure and mechanism of transport by bacterial toxins may have implications for the development of human therapies.

Pathogenic bacteria secrete channel- and pore-forming toxins, often as monomeric protein subunits, that assemble at the host cell surface into non-membrane inserted pre-pores or pre-channel oligomeric structures (Bann, 2012; Choe et al., 1992; E. Gouaux, 1997; Rossjohn, Feil, McKinstry, Tweten, & Parker, 1997; Wiener, Freymann, Ghosh, & Stroud, 1997). Alternatively, toxins may assemble in solution with particular ligands, before reaching the cell (J. E. Gouaux et al., 1994). However, once bound to cells, a series of conformational changes triggered by changes in local environment on or within the host cell then allow these pre-channel oligomers to then obtain their final membrane-inserted channel state (Rossjohn et al., 1997; Song et al., 1996a). Crystallographic and electrophysiological studies have suggested substructures within the individual monomer subunits unfold, for example, in response to ligand binding or changes in pH (Schuerch, Wilson-Kubalek, & Tweten, 2005), and then refold to form the transmembrane domain (De & Olson; M. Mueller, Grauschopf, Maier, Glockshuber, & Ban, 2009; Song et al., 1996b; Yamashita et al.). In some cases these conformational changes involve half of the total residues (M. Mueller et al., 2009), resulting in large structural changes in the oligomeric architecture (Katayama et al., 2008; M. Mueller et al., 2009). Local environmental sensing of pH conditions within the cell can provide critical signals to a toxin or virus complex that are often required for virulence (Choe et al., 1992; Rossjohn et al., 1997; Wiener et al., 1997). Nevertheless, the molecular basis of toxin assembly and the conformational changes required to convert to the prechannel oligomer a transmembrane channel are not well understood.

1.3 Questions. Understanding the structure, function, and transport mechanisms of bacterial toxins are critical to achieving a molecular view of protein transport and trafficking. These systems use highly evolved and robust bacterial proteins, making membrane biophysical studies more feasible than with other more complicated mammalian systems. Using toxins as model systems, we are poised to answer important fundamental questions. For instance, we would like to know how oligomeric transporters assemble into fully functional transport channels. Many of the molecular determinants are missing. Since toxins often decouple these steps, forming prechannel oligomers that then convert to a channel, we may be able to use a large number of biophysical techniques to define the structure and mechanism of transporter assembly and channel formation. Understanding the structural, kinetic, and thermodynamic principles of assembly and channel formation could have important implications for the transport mechanism.

Since toxins are secreted by opportunistic pathogens that infect mammalian cells, the environment in which they function is extremely complex and heterogeneous. We hypothesize that toxin assembly may be regulated by other secreted virulence factors or host proteins. We would like a structural view of the relevant physiological structures of fully functional toxin species. Bacterial pathogenesis essentially involves a war between the pathogen and the host

immune system. We surmise that the pathogen possesses mechanisms to regulate toxin activity during infection, to maximize its fitness. What are the molecular mechanisms for the regulation of toxin activity? Are these principles encoded by the toxin structure? Is the toxin structure then regulated by ligands or other factors encountered during infection? These questions remain unanswered for many toxins, in part due to the lack of structural and mechanistic studies in physiological contexts. Here we propose to study the structure and function of bacterial toxins, using anthrax toxin as a model system.

1.4 Anthrax toxin as a model system. Anthrax toxin (J. A. Young & Collier, 2007) (Atx) is a binary, A_2B toxin, comprised of three nontoxic proteins, secreted by *Bacillus anthracis*, which combine on eukaryotic host cell surfaces to make non-covalent, toxic complexes (Figure 1.2). Protective antigen (PA) is the 83-kDa, cell-binding, *B* component, which ultimately forms a translocase channel for the two ~90-kDa, enzymatically-active, *A* components—lethal factor (LF) and edema factor (EF). LF is a 90-kDa, Zn^{2+}-dependent protease (Duesbery & Vande Woude, 1999b; Duesbery et al., 1998; Pannifer et al., 2001), which cleaves host mitogen-activated protein kinase kinases (Duesbery & Vande Woude, 1999b; Duesbery et al., 1998). While PA and LF are individually nontoxic, the combination of LF and PA creates lethal toxin (LT), which can cause death (Pezard, Berche, & Mock, 1991). EF is a 89-kDa, Ca^{2+}/calmodulin-activated adenylyl cyclase (Drum et al., 2002; Leppla, 1982, 1984), which increases the cellular pool of 3'-5'-cyclic adenosine monophosphate (cAMP) in the host up to ~200-fold (Leppla, 1982). In an analogous manner, PA and EF combine to form edema toxin, which can cause tissue swelling (Fish & Lincoln, 1968a; Pezard et al., 1991) and lead to death in a manner distinct from LT (Firoved et al., 2005). Following secretion, PA binds to the host cell via one of two known Atx receptors, ANTXR1 (Bradley et al., 2001) and ANTXR2 (Scobie et al., 2003), and is then cleaved by a furin-type protease to make the proteolytically-activated form, called $_n$PA. The 63-kDa, receptor-bound portion of $_n$PA then self-assembles into a ring-shaped homooligomer, or pre-channel, which has been shown to be heptameric (Katayama et al., 2008; Lacy, Wigelsworth, Melnyk et al., 2004; Milne, Furlong, Hanna, Wall, & Collier, 1994; Mogridge, Cunningham, & Collier, 2002; Petosa et al., 1997). The pre-channel can bind LF or EF to make lethal or edema toxins, respectively. These toxin complexes are endocytosed and brought to an acidic compartment (Friedlander, 1986). Under acidic conditions, the PA pre-channel inserts into the membrane (Blaustein, Koehler, Collier, & Finkelstein, 1989) to form a translocase channel. LF and EF translocate through the channel (Krantz et al., 2006) to enter the cytosol, where they catalyze reactions that disrupt the host cell (Figure 1.2). However, the molecular mechanisms of channel formation and protein substrate transport are not fully understood.

A second key virulence factor of *B. anthracis* is the poly-γ-D-glutamic acid (γ-DPGA) capsule (Ivanovics & Erdos, 1937; Zwartouw & Smith, 1956b) surrounding the bacillus. Strains deficient in the pXO2 plasmid (Green, Battisti, Koehler, Thorne, & Ivins, 1985b), which encodes the machinery (Candela & Fouet, 2005; Makino, Uchida, Terakado, Sasakawa, & Yoshikawa, 1989; Makino, Watarai, Cheun, Shirahata, & Uchida, 2002a; Scorpio, Chabot, Day, O'Brien D et al., 2007; Uchida et al., 1993a) that produces and exports γ-DPGA, have significantly reduced virulence (S. L. Welkos, 1991b). The poly-γ-D-glutamic acid (γ-DPGA) capsule consists of long, linear polypeptides (50 to 200 kDa) that are polymerized via the γ-carboxylate side chain and the α-amino group of adjacent D-Glu monomers (Hanby & Rydon, 1946). For *B. anthracis*, the genes responsible for producing the γ-DPGA polymer (Makino et al., 1989), anchoring it to the peptidoglycan cell wall (Candela & Fouet, 2005), and cleaving it into smaller dissociable

fragments (Candela & Fouet, 2005; Makino et al., 2002a; Scorpio, Chabot, Day, O'Brien D et al., 2007; Uchida et al., 1993a), may augment its virulence by allowing the bacillus to evade the host innate immune system (Makino et al., 2002a; Maurer, 1965b; Scorpio, Chabot, Day, O'Brien D et al., 2007). The γ-DPGA purified from *B. anthracis* is exclusively composed of D-Glu (Hanby & Rydon, 1946). Two racemases maintain the chiral homogeneity of γ-DPGA in *B. anthracis*; and notably, these racemases are not conserved in other species (Dodd et al., 2007). However, other bacilli may regulate capsule chirality by other mechanisms (Zwartouw & Smith, 1956a). In *Bacillus licheniformis*, extracellular metal ions regulate racemization of the capsule; the capsule is composed of ~90% D-Glu in the presence of high concentrations of Mn(II) but 25-50% D-Glu in the absence of Mn(II), where the balance is the L-Glu isomer (Ashiuchi et al., 2004; Cromwick & Gross, 1995). The significance of these changes in chirality is not well understood. *B. anthracis* produces both Atx and the capsule production via the AtxA promoter (Bourgogne, Drysdale, Hilsenbeck, Peterson, & Koehler, 2003), suggesting that their concentrations may be co-regulated. Interestingly, during infection lower-molecular-weight capsular fragments (L-capsule) are released from the bacillus by the hydrolytic enzyme dep, or capD (Candela & Fouet, 2005; Makino et al., 2002a; Scorpio, Chabot, Day, O'Brien D et al., 2007; Uchida et al., 1993a). These L-capsule γ-DPGA fragments can bind to PA, and they co-purify with PA isolated from anthrax-infected blood (Ezzell et al., 2009). Nonetheless, it is unknown whether γ-DPGA interacts with assembled LT complexes and whether this interaction may affect LT assembly, stability, or activity.

1.5 Atx strucure and assembly. Assembly is paramount to Atx function (Cunningham, Lacy, Mogridge, & Collier, 2002; Mogridge, Mourez, & Collier, 2001) and its cellular internalization (Abrami et al., 2003). ANTXRs are slowly internalized by the host cell, but PA-bound ANTXR can internalize rapidly once it dimerizes (Abrami et al., 2003), making proper oligomerization a critical step in the internalization pathway. ANTXR can also dimerize (Go, Chow, & Mogridge, 2009; Go et al., 2006), further complicating the assembly mechanism, since PA oligomers are believed to be odd-numbered and heptameric (Lacy, Wigelsworth, Melnyk et al., 2004; Milne et al., 1994). Furthermore, the binding site of LF on PA has been shown to straddle the interface of two PA molecules, forming a stable dimer complex (Cunningham et al., 2002; Feld et al., 2010; Lacy et al., 2005; Lacy, Mourez, Fouassier, & Collier, 2002). Therefore, the assembly of an asymmetric heptamer from purely dimeric species seems unlikely. Nevertheless, the mechanism of toxin assembly remains unknown. Other toxins have been previously shown to form mutiple oligomeric states (Czajkowsky, Sheng, & Shao, 1998), though no mechanism for their functionality in pathogenesis has been demonstrated. In Chapter 2, we describe the discovery of an octameric form of Atx, which was found by examining the toxin structure under physiological conditions.

1.6 Regulation of Atx thermostability. Formation of the PA_7-ANTXR complex has been shown to stabilize the complexes tremendously. This, of course, requires PA to reach the cell surface. However, a potential extracellular assembly mechanism has become apparent in the investigation of animals infected with *B. anthracis* (H. Smith, Keppie, & Stanley, 1954), where LF is found alongside proteolytically-activated $_nPA$, (Ezzell et al., 2009; Mabry et al., 2006), implying that the PA is potentiated for assembly. Toxin concentrations in the blood of infected animals at the later stages of anthrax can be as high as 80-100 μg/ml PA (Mabry et al., 2006), 10-20 μg/ml LF (Ezzell & Abshire, 1992b; Kintzer et al., 2009; Moayeri, Wiggins, & Leppla, 2007). The

concentrations of these toxin components vary, however, depending upon the host species (Mabry et al., 2006), and the stage of the disease (Boyer et al., 2009). Also increased levels of bacteremia tend to correlate with increased levels of these Atx components and L-capsular γ-DPGA (Boyer et al., 2009). With these high levels of Atx components and proteolytic activity capable of activating PA, a receptor-free Atx assembly pathway in the blood seems unavoidable, which may be parallel in certain respects to the cell-surface pathway. Animal infection models show that PA is rapidly cleared in the bloodstream, implying that the toxin has a finite lifetime there and competes with various host clearance mechanisms (Moayeri et al., 2007) and aggregation (Fish & Lincoln, 1968b; Fish, Mahlandt, Dobbs, & Lincoln, 1968). The existence of stabilization mechanisms would allow the toxin to persist and remain efficacious in the plasma and other extracellular environments. PA_7 complexes, nevertheless, are unstable at physiological temperatures and pH, where they readily convert to an inactive, aggregated state (Katayama et al., 2008). Developing an understanding of the physiological stabilities and molecular configurations of anthrax lethal and edema toxins is, therefore, of paramount importance to understanding their function throughout the stages of anthrax infection. In Chapters 2, 3, and 4 we describe the role of the octameric form of PA as a thermostable toxin and the molecular mechanism of octamer stability.

1.7 Role of the γ-DPGA capsule. Relative to Atx produced in vitro, the toxin produced in vivo (i.e., isolated from the blood of animals suffering from anthrax) forms unique assemblies as evidenced by their unique resistance to antibody binding, and the in vivo derived toxin is more lethal (Fish & Lincoln, 1968b). The former observation is reminiscent of the efforts to produce an anthrax vaccine, where the γ-DPGA capsule was immunologically neutral in vivo (Chabot et al., 2004). The Atx produced in vivo was shown to have high glutamic acid contamination (Fish & Lincoln, 1968b), suggesting that Atx may associate with γ-DPGA. This was confirmed by recent in vivo studies, suggesting that γ-DPGA may alter the activity of Atx and co-purify with PA during infection (Ezzell et al., 2009; Jang et al., 2011). However, the γ-DPGA used in these studies was exclusively L-capsule. The relative effects of high and low molecular weight capsule have not been tested. Since the cell wall is shrouded in a thick layer of high molecular weight γ-DPGA, we hypothesize that PA may interact with this species as well. However, the molecular basis of PA's putative interactions with γ-DPGA is still not known. We hypothesize that binding of γ-DPGA to Atx could regulate its activity. In Chapter 5, we demonstrate the role of γ-DPGA in regulating the pH-dependence of PA channel formation.

1.8 Mechanism of PA channel formation. The PA channel architecture is not yet known in atomic detail. The current model of the structure, based on electrophysiology (Benson, Huynh, Finkelstein, & Collier, 1998; Nassi et al., 2002b) and electron microscopy studies (Katayama et al., 2008), suggests that PA channels have a mushroom-shaped architecture with an ~100-Å-long, hollow, β-barrel stem that penetrates the membrane to form a narrow, ~15-Å-diameter channel (Figure 1.3). To transform into this channel state, the β-hairpin formed by 2β1-2β3 in D2 is thought to unfold and then subsequently refold to form the final β barrel structure (Benson et al., 1998; Nassi et al., 2002b; Petosa et al., 1997).

Ultimately, the hydrophobic tips of these β strands can penetrate the lipid bilayer, thereby forming an aqueous passageway for LF/EF to translocate through into the host cell (Krantz et al., 2004; Wesche, Elliott, Falnes, Olsnes, & Collier, 1998; Zhang, Udho, Wu, Collier, & Finkelstein, 2004). Acidic endosomal conditions likely serve two purposes: (1) to drive

conformational changes in PA that lead to formation of the transmembrane channel and insertion into the lipid bilayer and (2) to destabilize LF and EF by acid denaturation (Krantz et al., 2004), allowing proton gradient-driven translocation through PA (Krantz et al., 2006). PA also contains a required ring of phenylalanine side chains, or ϕ clamp, which catalyzes translocation (Krantz et al., 2005), and likely plays a role in the channel formation mechanism (Sun, Lang, Aktories, & Collier, 2008). However, the molecular mechanism of pH-sensing and its role in the conformational changes required for channel formation are not known. In Chapter 5, we describe the structural and molecular basis for the rate-limiting barriers to PA channel formation.

Chapter 2

The Protective Antigen Component of Anthrax Toxin Forms Functional Octameric Complexes

2.1 Abstract

The assembly of bacterial toxins and virulence factors is critical to their function, but the regulation of assembly during infection has not been studied. We begin to address this question using anthrax toxin as a model. The protective antigen (PA) component of the toxin assembles into ring-shaped homooligomers that bind the two other enzyme components of the toxin, lethal factor (LF) and edema factor (EF), to form toxic complexes. To disrupt the host, these toxic complexes are endocytosed, such that the PA oligomer forms a membrane-spanning channel that LF and EF translocate through to enter the cytosol. We show using single-channel electrophysiology that PA channels contain two populations of conductance states, which correspond with two different PA pre-channel oligomers observed by electron microscopy—the well-described heptamer and a novel octamer. Mass spectrometry demonstrates that the PA octamer binds four LFs, and assembly routes leading to the octamer are populated with even-numbered, dimeric and tetrameric, PA intermediates. Both heptameric and octameric PA complexes can translocate LF and EF with similar rates and efficiencies. Here we also report a 3.2-Å crystal structure of the PA octamer. The octamer comprises ~20-30% of the oligomers on cells, but outside of the cell, the octamer is more stable than the heptamer under physiological pH. Thus the PA octamer is a physiological, stable, and active assembly state capable of forming lethal toxins that may withstand the hostile conditions encountered in the bloodstream. This assembly mechanism may provide a novel means to control cytotoxicity during anthrax infection.

2.2 Introduction

Anthrax toxin (J. A. Young & Collier, 2007) (Atx) is a binary, A_2B toxin, comprised of three nontoxic proteins, secreted by *Bacillus anthracis*, which combine on eukaryotic host cell surfaces to make noncovalent, toxic complexes. Protective antigen (PA) is the 83-kDa, cell-binding, *B* component, which ultimately forms a translocase channel for the two ~90-kDa, enzymatically-active, *A* components—lethal factor (LF) and edema factor (EF). Following secretion, PA binds to the host cell via one of two known Atx receptors, ANTXR1 (Bradley et al., 2001) and ANTXR2 (Scobie et al., 2003), and is then cleaved by a furin-type protease to make the proteolytically-activated form, called $_n$PA. The 63-kDa, receptor-bound portion of $_n$PA then self-assembles into a ring-shaped homooligomer, or pre-channel, which has been shown to be heptameric (Katayama et al., 2008; Lacy, Wigelsworth, Melnyk et al., 2004; Milne et al., 1994; Mogridge et al., 2002; Petosa et al., 1997). The pre-channel can bind LF or EF to make lethal or edema toxins, respectively. These toxin complexes are endocytosed and brought to an acidic compartment (Friedlander, 1986). Under acidic conditions, the PA pre-channel inserts into the membrane (Blaustein et al., 1989) to form a translocase channel. LF and EF translocate through the channel(Krantz et al., 2006) to enter the cytosol, where they catalyze reactions that disrupt the host cell.

PA channels have a mushroom-shaped architecture (Katayama et al., 2008) with an ~100-Å-long, hollow, β-barrel stem that penetrates the membrane to form a narrow, ~15-Å-diameter channel, requiring LF and EF to unfold prior to translocation (Krantz et al., 2004; Wesche et al., 1998; Zhang et al., 2004). Acidic endosomal conditions serve two purposes: first, they destabilize LF and EF by acid denaturation (Krantz et al., 2004); and second, they drive translocation via a proton gradient (ΔpH) (Krantz et al., 2006). PA also contains a required ring of phenylalanine side chains, or ϕ clamp, which catalyzes translocation (Krantz et al., 2005), exemplifying how the channel's structure is crucial to its translocase function. Assembly is paramount to Atx function (Cunningham et al., 2002; Mogridge et al., 2001) and its cellular internalization (Abrami et al., 2003). ANTXR receptors are slowly internalized by the host cell, but PA-bound ANTXR can internalize rapidly once it dimerizes (Abrami et al., 2003), making proper oligomerization a critical step in the internalization pathway. ANTXR is dimeric (Go et al., 2009; Go et al., 2006), further complicating the assembly mechanism, since PA oligomers are believed to be odd-numbered and heptameric. Toxins have been previously shown to form mutiple oligomeric states, though no mechanism for their functionality in pathogenesis has been demonstrated. A potential extracellular assembly mechanism has become apparent in the investigation of animals infected with *B. anthracis*, where it has been shown that anthrax toxin accumulates in the blood of animals (H. Smith et al., 1954). Specifically, LF is found alongside proteolytically-activated $_{n}$PA (Ezzell et al., 2009; Mabry et al., 2006), implying that the PA is potentiated for assembly. Relative to toxin produced in vitro, the toxin produced in vivo (i.e., isolated from the blood of animals suffering from anthrax) forms unique assemblies as evidenced by their unique resistance to antibody binding, and the in vivo derived toxin is more lethal (Fish & Lincoln, 1968b). We probe assembly in various cellular and extracellular contexts, using electrophysiology, electron microscopy, mass spectrometry, and crystallography, and we conclude that the activity of the toxin may be regulated through assembly, potentially affecting the degree of cytotoxicity throughout the stages of anthrax.

2.3 Results

PA can form two different channel sizes. PA channels were inserted into planar lipid bilayers following one of two different assembly methods outlined in Figure 2.1A. An oligomer sample, called $_{Q}$PA (trypsin-nicked PA assembled on Q-sepharose anion-exchange resin (Blaustein et al., 1989)) was applied to the bilayer, and discrete single-channel steps were observed (Figure 2.1B). $_{Q}$PA channels had a mean conductance of 95.5 pS (n = 360). Single-channel conductance values (γ) for wild type (WT) PA channels were reported to range from 85 to 110 pS (Blaustein, Lea, & Finkelstein, 1990). We also observed that the $_{Q}$PA sample contained two discrete channel sizes: a prevalent, smaller one and a rarer, larger one. The overall γ-value distribution recorded from many individual membranes was broad (Figure 2.1C).

To determine if the method of PA assembly affected the γ-value distribution, we studied trypsin-nicked PA ($_{n}$PA) samples assembled in the presence of LF's amino-terminal domain (LF_N), called $_{n}PA+LF_N$. Again, larger-conductance channels appeared among smaller-conductance channels in two discrete sizes, but the frequency of observing larger channels increased. The mean γ value for $_{n}PA+LF_N$ [98 pS (n = 107)] increased relative to that observed for $_{Q}$PA. Moreover, a lower-tailed Whitney-Mann test (WMT) shows that $_{Q}$PA and $_{n}PA+LF_N$ distributions are unique from one another (p > 0.95). Finally, three separate $_{Q}$PA samples contained a consistently lower mean conductance of ~95 pS relative to two other $_{n}PA+LF_N$

samples, which had a mean conductance of ~98 pS. Thus the method of assembly shifts the single-channel-conductance distribution (Figure 2.1C).

Inherent variability in bilayer thickness, combined with the presence of another more-conducting conformation, likely contributes to the broad aggregate distributions (Figure 2.1C). To mitigate this, we examined the discrete differences in channel conductance within each membrane by tabulating the set of all the pairwise differences (δ) in γ values per membrane, $[\gamma_i - \gamma_j]$, where $i \neq j$. A histogram of δ values recorded for the $_n$PA+LF$_N$ sample shows that two sizes of channel conductance are present, as the distribution fits best to a two-Gaussian distribution (Figure 2.1D). Based upon our fit, these two populations of γ values differ from one another by 8 (±2) pS, or about ±10%, where the larger-sized conductance state represents 25 (±6)% of the population. This result led us to conclude that PA forms two discrete conductance states that may be differentially populated, depending upon the method of assembly.

We tested whether larger-conductance channels were a substate of less-conducting channels due to a conformational rearrangement. To test this possibility, we measured ~6-minute-long recordings of single channels (Figure 2.1E). While fluctuations to a more conducting substate are observed, these fluctuations are relatively small; and large-conductance channels (>102 pS) did not interconvert to smaller ones (<95 pS) during these and all other recordings. Therefore, either two unique channel sizes exist in PA samples or the timescale of the conformational rearrangements between the large- and small-conductance states is slow.

Electron microscopy reveals two PA oligomers. Under the assumption that the ~10% difference in conductance states may correspond to slow-timescale structural changes in the channel diameter (Hille, 1968; Krantz et al., 2005), we examined the $_Q$PA oligomers for structural heterogeneity by electron microscopy (EM). Reference-free analysis of ~10^4 negatively-stained particles identified two classes of ring-shaped oligomers—the heptamer and a novel octamer (Figure 2.2A).

Mass spectrometry reveals Atx heterogeneity. To further establish the observed heterogeneity, we used nanoelectrospray ionization mass spectrometry (nanoESI-MS). We assembled WT $_n$PA with WT LF$_N$ and then analyzed the mixtures by nanoESI-MS (Figure 2.3A). We identified two large molecular mass species, 537,082 (±186) and 631,167 (±217) Da, corresponding to the oligomers, PA$_7$(LF$_N$)$_3$ and PA$_8$(LF$_N$)$_4$, respectively, as well as two minor (and likely intermediate) complexes of 158,193 (±38) and 315,395 (±27) Da, corresponding to PA$_2$LF$_N$ and PA$_4$(LF$_N$)$_2$, respectively (Table 2.1). The PA$_7$(LF$_N$)$_3$ species was observed previously (Mogridge et al., 2002). However, the PA$_8$(LF$_N$)$_4$ complex is novel and not only corroborates the presence of the octameric PA species, but also suggests that an octamer can carry a payload of four LFs or EFs—one more than its heptameric counterpart. Finally, the previously undetected forms, PA$_2$LF$_N$ and PA$_4$(LF$_N$)$_2$, suggest a pathway of assembly for the octamer via even-numbered intermediates.

We then probed the kinetics of PA assembly with nanoESI-MS (Figure 2.3B). Here oligomerization was initiated by mixing $_n$PA and LF$_N$ in a 1:1 ratio, using the assembly method described in the single-channel studies. The ion abundances in the ESI mass spectra were recorded for ~1 hour at several time points. The abundances of both PA$_7$(LF$_N$)$_3$ and PA$_8$(LF$_N$)$_4$ increase with approximately the same rate constant (when fit to a single-exponential expression). Also the appearance of either oligomer correlates to a decrease in the relative ion abundances for free PA monomer and PA$_4$(LF$_N$)$_2$ species. We observed an initial burst in abundance of the PA$_4$(LF$_N$)$_2$ species followed by a subsequent decrease with time; the decrease was concomitant with the increase in the formation of PA$_7$(LF$_N$)$_3$ and PA$_8$(LF$_N$)$_4$. The trend in PA$_4$(LF$_N$)$_2$

abundance suggests that it is a stable intermediate in the formation of the higher-order complexes. $PA_8(LF_N)_4$, however, is not an intermediate species in the heptamerization pathway, since its relative abundance did not decrease during the experiment.

Stabilizing dimeric PA intermediates promotes octamer formation. To further investigate how even-numbered intermediates influence assembly, we conducted EM studies using PA oligomers prepared in the presence of a dimeric soluble Atx receptor domain (dsANTXR), LF_N, or EF_N (EF's PA-binding, amino-terminal domain). A dimeric ANTXR construct was also chosen based upon evidence that the receptor may exist in a dimeric state on cell surfaces (Go et al., 2006). PA pre-complexed to dsANTXR (Figure 2.2B), but not to monomeric ANTXR (msANTXR) (Figure 2.2C), showed increased proportions of octamers upon assembly. Further studies demonstrated that when dsANTXR was loaded under less saturating conditions, the octamer levels decreased (Figure 2.7B). Thus the more saturating conditions allow the dsANTXR sites to fully populate with PA prior to assembly, which increases the probability of forming the even-numbered, octameric form.

LF or EF can form a ternary complex with PA dimers (Cunningham et al., 2002). We have also observed this species in our mass spectrometry experiments (Figure 2.3A; Table 2.1). When LF_N or EF_N is used to assemble $_n$PA into oligomers (Figure 2.2D, E), ~25% of the population became octameric. This increase is five- to ten-fold more than that observed for PA oligomerized in the absence of LF_N or EF_N. Also a PA mutant, S170C, which can form a disulfide-bonded homodimer, increases the proportion of octamers relative to unlinked WT PA (Figure 2.2F). Finally, our reference-free EM analysis was supported, when possible, with reference-based analysis, mass spectrometry, and electrophysiology (Table 2.2). Therefore, we conclude that by increasing the population of even-numbered PA_2-precursor complexes, we observe an increase in the proportion of octamers.

PA forms octamers on cells. These in vitro results led us to probe the oligomerization pathway on cell surfaces. We used a Chinese hamster ovary (CHO) cell line, expressing ANTXR2, called C-CHO (J. J. Young et al., 2007). PA with a carboxy-terminal six histidine tag (His6), called His6-PA, was added to the extracelluar medium of cultured C-CHO cells and incubated to assemble. Endosomal acidification was blocked with ammonium chloride to prevent the conversion of the pre-channel oligomers to the channel state. The cells were harvested, lysed in detergent and purified on His6-

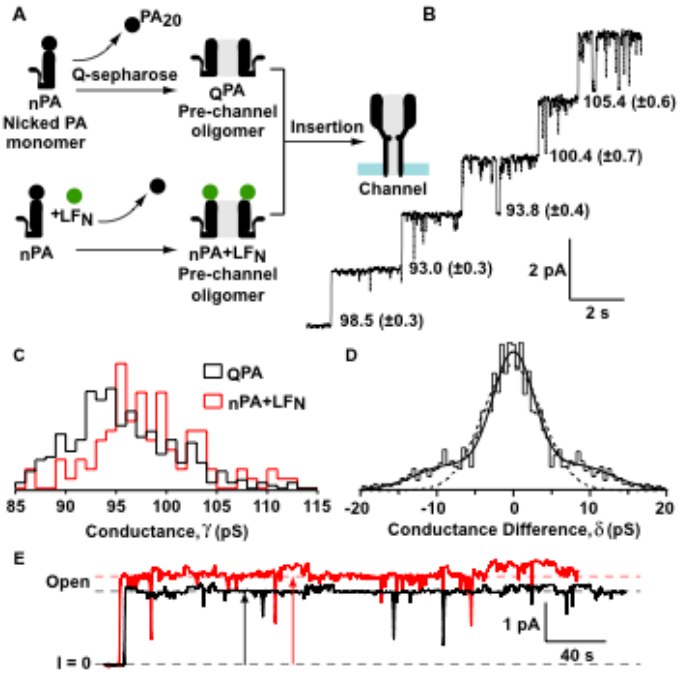

Figure 2.1. Heterogeneous PA channel conductance distributions. (A) Two PA samples were analyzed: (i) PA is nicked by trypsin to make $_{n}$PA; a 20-kDa piece (PA_{20}) dissociates, allowing PA to oligomerize into the pre-channel on a Q-sepharose column, making $_{Q}$PA; and (ii) $_{n}$PA is mixed with LF_N to drive oligomerization, making $_{n}$PA+LF_N. Either pre-channel oligomer forms a channel upon inserting into the membrane. **(B)** Example of 200-Hz-filtered, single-channel data collected at a $\Delta\psi$ of 20 mV, 100 mM KCl, pH 6.60; γ values computed by $\gamma = i/\Delta\psi$ are listed next to each channel insertion. **(C)** Normalized histograms of the estimated single-channel γ values for the $_{Q}$PA and $_{n}$PA+LF_N samples. Data bins are one-pS wide, and the number of channels, n, in each sample are normalized for comparison. The samples, $_{Q}$PA (n = 360; black bars) and $_{n}$PA+LF_N (n = 107; red bars), are statistically distinct by a non-parametric, lower-tailed, Whitney-Mann test ($p > 0.95$). **(D)** Histogram of all the pairwise differences, δ, between measured γ values identified within the same membrane for the $_{n}$PA+LF_N sample. The δ histogram was fit to one- (dotted line) and two-Gaussian (solid line) functions, using $A(\delta) = A_1/\sigma_1\sqrt{(\pi/2)}\exp(-2\delta^2/\sigma_1^2) + A_2/\sigma_2\sqrt{(\pi/2)}\,[\exp(-2((\delta-\mu_2)/\sigma_1)^2) + \exp(-2((\delta+\mu_2)/\sigma_1)^2)]$, with R values of 0.89 and 0.96, respectively, yielding best-fit parameters: peak area A_1 = 470 (±80), A_2 = 140 (±40); mean, μ_2 = 8 (±2) pS; and standard deviation, σ_1 = 5.5 (±0.5) pS, σ_2 = 9 (±2) pS. (See also Table 2.2.) **(E)** Single-channel current records for smaller- (black) and larger-sized (red) PA channels in 100 mM KCl, pH 6.6. Arrows indicate the two respective channel sizes. Data were acquired at 400 Hz and filtered further with a 100-point-per-σ Gaussian filter to better reveal conductance sub-states.

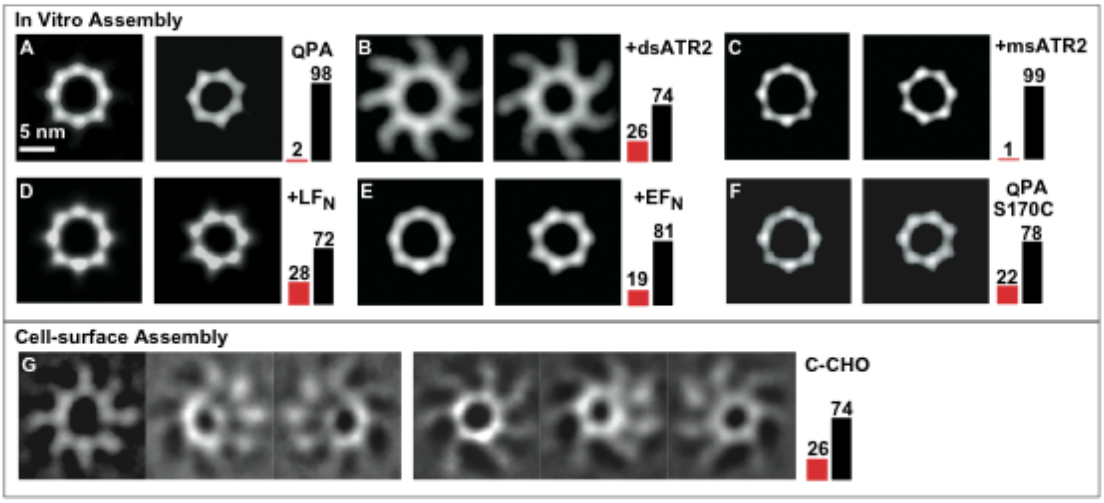

Figure 2.2. EM studies of heptameric and octameric PA. EM images of negative-stained samples of WT PA oligomers assembled either in vitro (upper panels A-F) or in vivo on cell surfaces (lower panel). Representative class averages of octamers (left) and heptamers (right) are shown. The total number of particles assessed, *n*, and relative percentages of heptamers and octamers are given. The proportions of heptamers and octamers are indicated by bars colored black and red, respectively. In vitro samples include: **(A)** $_{n}$PA assembled on an anion-exchange column ($_{Q}$PA; *n* = 12589; 98% heptamer; 2% octamer); **(B)** $_{n}$PA assembled in the presence of soluble dimeric ANTXR2 at a 4:1 stoichiometry (+dsANTXR; *n* = 837; 74% heptamer; 26% octamer); **(C)** $_{n}$PA assembled in the presence of soluble monomeric ANTXR2 (+msANTXR; *n* = 9401; 99% heptamer; 1% octamer); **(D)** $_{n}$PA assembled in the presence of LF_N; (+LF_N; *n* = 8409; 72% heptamer; 28% octamer); **(E)** $_{n}$PA assembled in the presence of EF_N; (+EF_N; *n* = 5363; 81% heptamer; 19% octamer); and **(F)** disulfide-bonded PA S170C assembled on an anion-exchange column ($_{Q}$PA S170C; *n* = 2933; 78% heptamer; 22% octamer). Oligomers extracted from cells: **(G)** His6-PA assembled on cells expressing ANTXR2 (C-CHO; *n* = 4729; 74% heptamer; 26% octamer), where three classes of octamers and heptamers are shown, resulting from reference-based analysis. The 5-nm scale bar shown in panel A is consistent for all images. Percentages of oligomers are means of reference-free and crystal-structure-referenced alignments unless noted otherwise. (Specific percentages are listed in Table 2.2.)

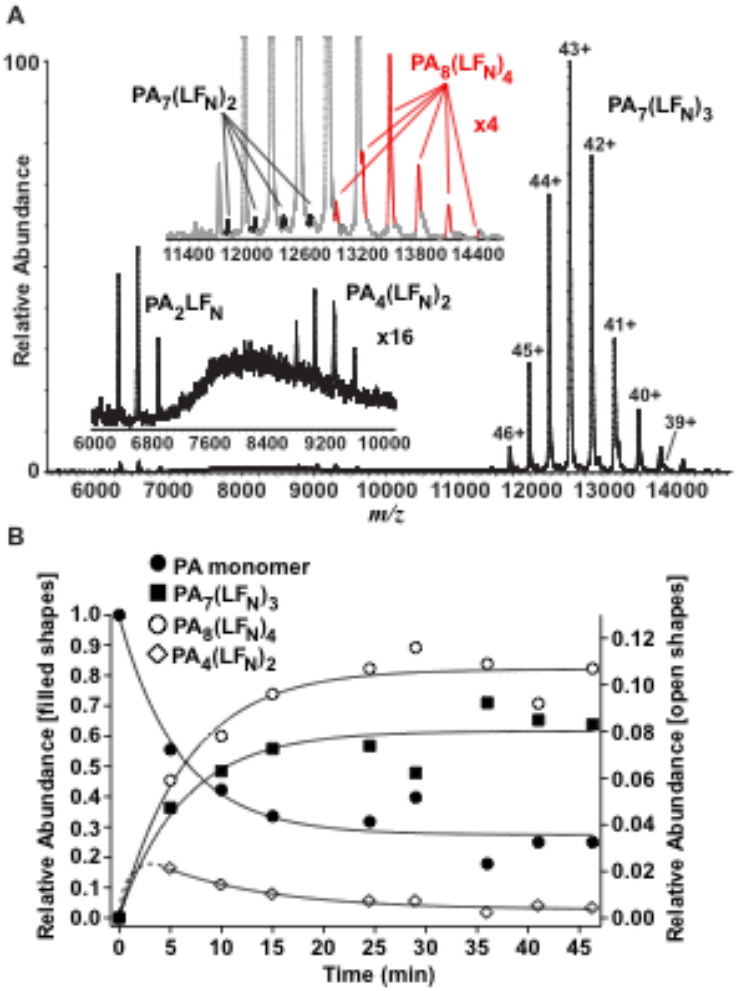

Figure 2.3. Mass spectrometry studies of Atx assembly. (A) NanoESI mass spectrum of $_n$PA co-assembled with LF_N. Multiple charge-state distributions are observed that correspond to five different PA-LF_N complexes. Charge states and molecular weights were calculated according to a prior method (McKay, Ruotolo, Ilag, & Robinson, 2006). The $PA_7(LF_N)_3$ distribution clearly has the highest relative abundance and is shown above labeled with charge states. Insets show distributions of less intense oligomers $PA_7(LF_N)_2$ and $PA_8(LF_N)_4$, and low abundances of PA_2LF_N and $PA_4(LF_N)_2$ that may be stable intermediates in the formation of the higher order complexes. The molecular weight was assigned from the charge-state distribution that resulted in the smallest standard deviation in calculated molecular weight. (Table 2.1 summarizes the observed masses and describes the solvent correction.) **(B)** Assembly kinetics for the 63-kDa PA monomer, $PA_7(LF_N)_3$, $PA_8(LF_N)_4$, and $PA_4(LF_N)_2$ from a solution of $_n$PA mixed with excess LF_N. Data for all but $PA_4(LF_N)_2$ were fit with single exponentials. The oligomers, $PA_7(LF_N)_3$ and $PA_8(LF_N)_4$, have similar rate constants for assembly and PA monomer a comparable rate constant for decay. Data at early times indicate a rapid increase in the abundance of $PA_4(LF_N)_2$ followed by slow decay for $t \geq 5$ min that was fit to a single exponential, suggesting it is an intermediate in the formation of the higher order complexes. All four analytes reach steady-state levels in ~30 minutes.

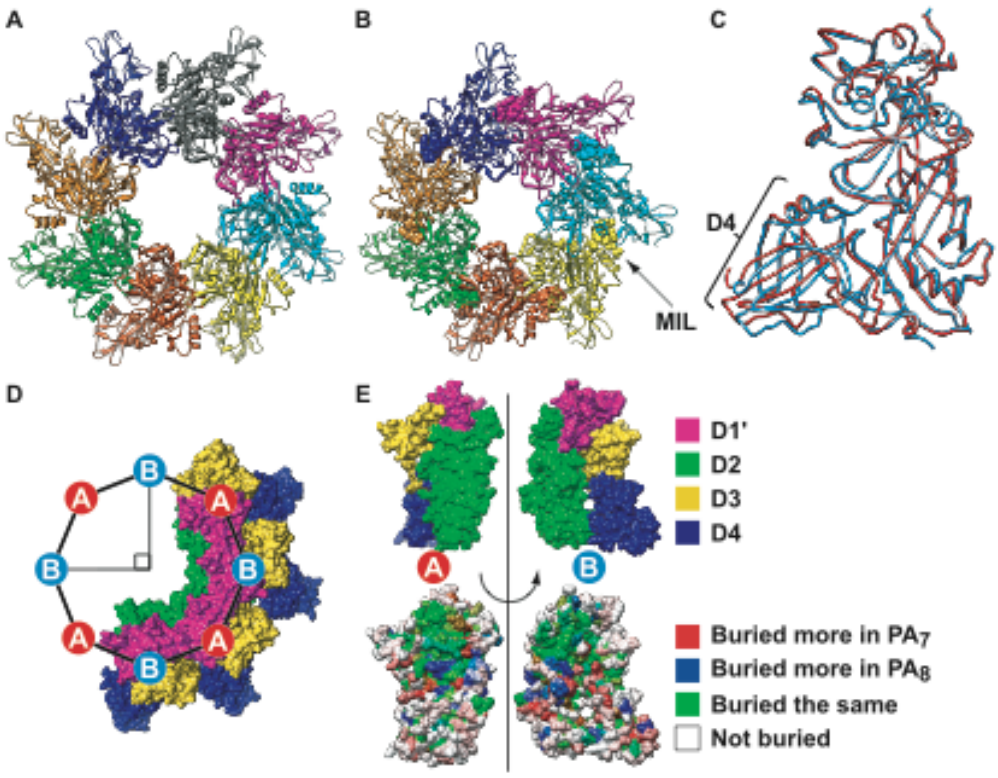

Figure 2.4. X-ray crystal structure of PA in the octameric oligomerization state. Axial views of **(A)** the $PA^{\Delta MIL}$ octamer (PDB 3HVD) side-by-side with **(B)** the WT PA heptamer (PDB 1TZO) (Lacy, Wigelsworth, Melnyk, Harrison, & Collier, 2004). Monomer subunit chains are colored uniquely. The MIL is depicted with spheres in the latter structure of WT heptamer. **(C)** A backbone alignment of two adjacent PA monomers, chains A and B, called conformation A (red) and B (blue), showing the displacement of D4. **(D)** Superimposed on a surface rendering of half an octamer is the square planar arrangement of symmetrically related A and B conformers calculated from the positions of each chain's center of mass. Chains A, C, E, G are conformation A; and chains B, D, F and H are conformation B. Adjacent A-B pair center of masses are 64.3 (± 0.1) Å apart at angles of 90 (±0.1)º. Domains are colored as: D1' (magenta), D2 (green), D3 (gold), and D4 (blue). **(E)** An A-B oligomerization interface split apart to compare relative differences in surface area burial at the oligomerization interface of the heptamer and octamer structure among the four domains. The domains (upper panel) are colored as in panel D. The relative degrees of surface area buried (lower panel) are colored as follows: surface buried equally (i.e., to within 10%) in either structure (green); surface buried 10% more buried in the heptamer (red); surface buried 10% more in the octamer (blue); and surface buried <75% in both structures (white). All molecular graphics were rendered using CHIMERA (Pettersen et al., 2004b).

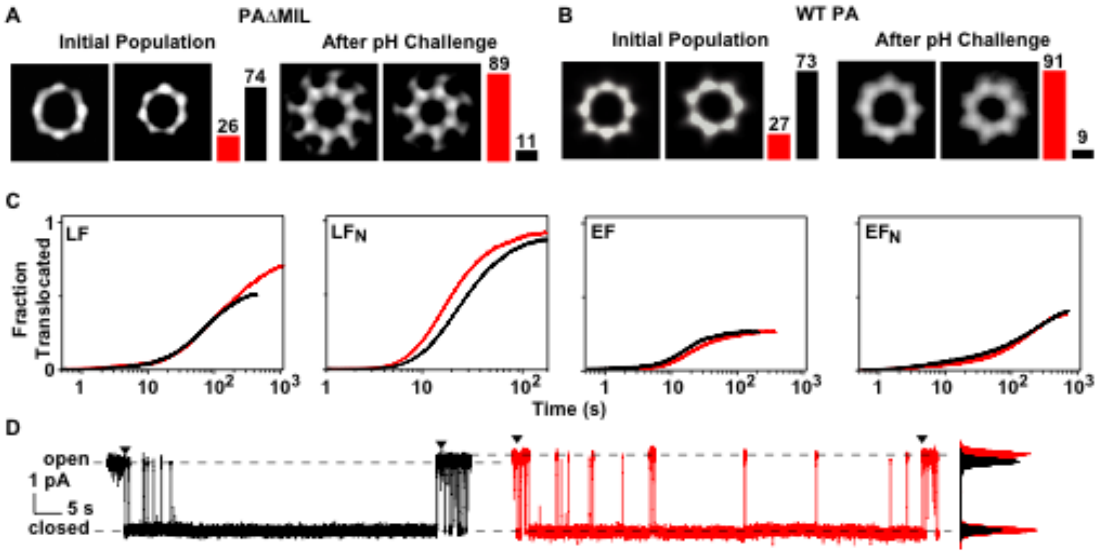

Figure 2.5. Octameric and heptameric PA stability and activity. Negative-stained EM class-average images of PA heptamers and octamers. **(A)** Heptameric and octameric $PA^{\Delta MIL}$ before (left) and after (right) exposure to pH 5.7 (4 ºC). Before exposure, 25% octamer, 75% heptamer, n = 10409. After exposure, 89% octamer, 11% heptamer, n = 14516. **(B)** Heptameric and octameric WT PA oligomer complexes with LF_N before (left) and after (right) exposure to pH 7 (37 ºC). Before exposure, 28% octamer, 73% heptamer, n = 8409. After exposure, 91% octamer, 9% heptamer, n = 1084. Relative percentages are given by the bars on the right for heptamers (black) and octamers (red). **(C)** Ensemble protein translocation records measured using planar lipid bilayer electrophysiology. Panels compare the relative translocase activities two types of samples: ${}_{Q}PA+LF_N$, which is >95% heptameric (black); and ${}_{n}PA+ LF_N$, which had been purified and shown to contain ~90% octamer (red). Four substrates (LF, LF_N, EF, or EF_N) were used, and each was translocated at the indicated $\Delta\psi$ and ΔpH conditions. Records shown are the average of a set of three repetitions. The y-axes are normalized to the fraction of substrate-blocked channels that become unblocked due to translocation. Rates are given as $t_{½}$ (time for half of the substrate to translocate). LF translocated at $\Delta\psi$ = 30 mV, ΔpH = 1 using heptameric ($t_{½}$ = 57 s) and octameric PA ($t_{½}$ = 96 s). LF_N translocated at $\Delta\psi$ = 50 mV using heptameric ($t_{½}$ = 16 s) and octameric PA ($t_{½}$ = 12 s). EF translocated at $\Delta\psi$ = 50 mV, ΔpH = 1 using heptameric ($t_{½}$ = 50 s) and octameric PA ($t_{½}$ = 66 s). EF_N translocated at $\Delta\psi$ = 60 mV using heptameric ($t_{½}$ = 137 s) and octameric PA ($t_{½}$ = 135 s). **(D)** (Right) Single-channel translocations of LF_N at 50 mV through either a large- (red) or small-sized (black) channel. Black arrowheads on either end of the translocation indicate the beginning and end of each translocation. (Left) Histogram profiles of portions of the conductance levels of the large- and small-sized channels for comparison of the open-channel conductance levels.

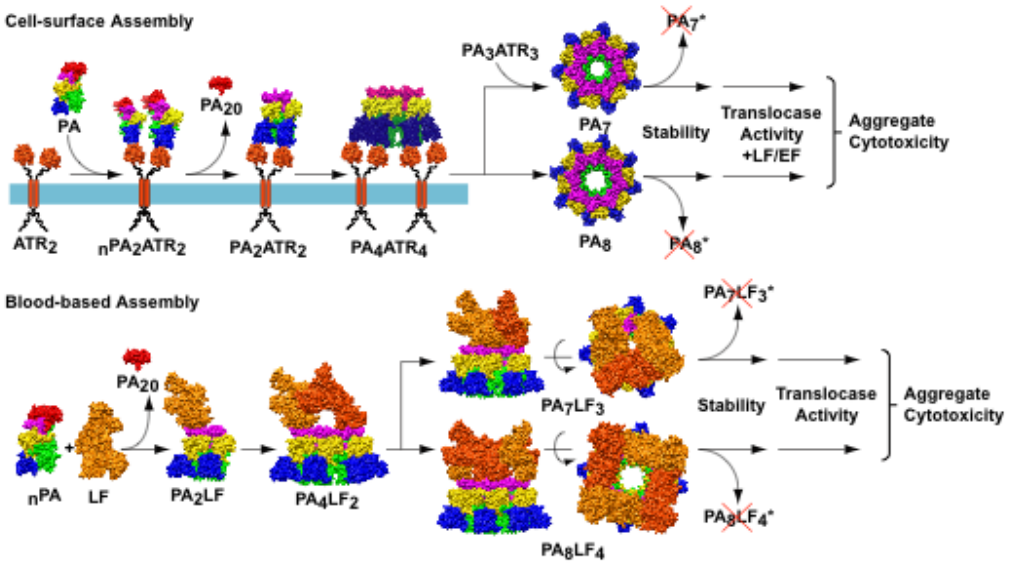

Figure 2.6. Heterogeneous assembly mechanism may regulate toxin activity. (A) On cells, PA may encounter dimeric ANTXR sites and assemble into PA_2 and PA_4 intermediates. Intermediates can combine to form either PA_8 or PA_7, which can load with EF and/or LF. (In principle, LF and EF may be involved in the mechanism as well to produce similar outcomes.) Extracellularly, PA may encounter LF or EF, making the intermediates, PA_2LF_N and $PA_4(LF_N)_2$, which then form either $PA_8(LF_N)_4$ or $PA_7(LF_N)_3$. Models of LF-PA complexes are derived from a theoretical model (Lacy et al., 2005). Toxin activity is a combination of the oligomer's stability and translocase activity; instability may lead to the formation of inactive oligomeric complexes (*).

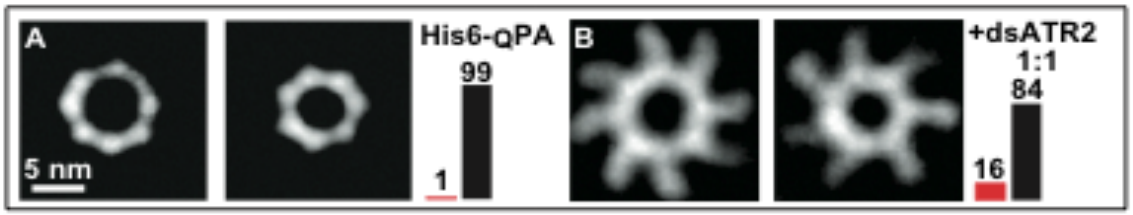

Figure 2.7. EM analysis of additional PA oligomer samples. Class-averaged EM images of PA oligomers are shown. The single-particle sample sizes, n, as well as the relative percentages of heptamers and octamers are given. The proportions of each are given to the right as bars colored black and red bars for heptamers and octamers, respectively. Pairs of images are octameric (left) and heptameric (right) oligomers obtained by class-average analysis. Both reference-free and reference-based analyses were performed to determine the percentages of each oligomer (Table 2.2). (A) His6-PA assembled on a Q-sepharose column at pH 8 (His6-QPA; n = 6115; 98% heptamer; 2% octamer). (B) nPA assembled in a 1:1 stoichiometric ratio with (+dsANTXR2 1:1; n =312; 84% heptamer; 16% octamer). The 5-nm scale bar in panel A is for all images shown.

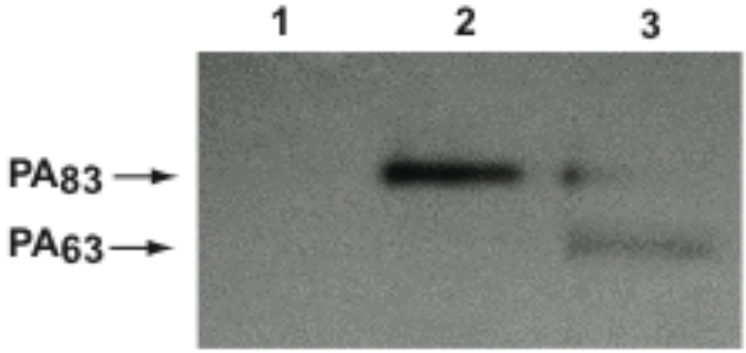

Figure 2.8. Western blot of PA oligomers extracted from CHO cells. Carboxy-terminal His6-tagged PA (His6-PA) was applied to C-CHO cells,6 incubated, washed, and extracted from cell surfaces in detergent. The extract was separated by 15% SDS-PAGE and then monitored by an anti-His6-HRP western blot. The anti-His6-HRP probed western blot is shown. (Lane 1) 10 ng WT PA83 (in the full-length 83-kDa form lacking a His6 tag). (Lane 2) 10 ng of WT His6-PA83. (Lane 3) Protein detected by HRP from the C-CHO cell extract is consistent with WT His6-PA63 (i.e., in the proteolytically-activated 63-kDa form typically observed on cell surfaces).

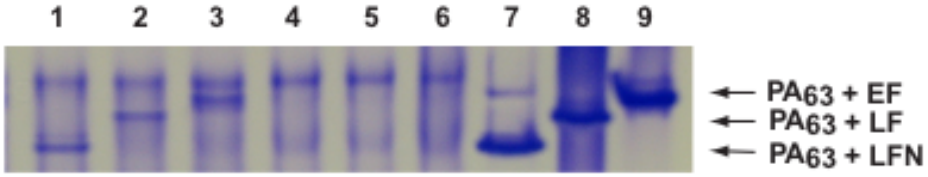

Figure 2.9. Native gel of PA toxin complexes assembled in bovine blood. Native gel of His6-PA oligomers in complex with LF_N, LF, or EF, assembled in heparinized bovine serum, defibrinated bovine plasma, or preassembled in buffer. When PA was assembled in the blood plasma, it was activated to the $_n$PA state by native protease activity in the plasma, as reported previously (Ezzell & Abshire, 1992a). (See also Materials and Methods). (Lanes 1-3) The PA oligomers in complex with LF_N, LF, and EF, respectively, assembled in heparinized bovine plasma. High molecular weight bands corresponding to assembled PA complexes are indicated. (Lanes 4-6) LF_N, LF, and EF, respectively, incubated in bovine plasma in the absence of PA. Lanes 7-9) Preassembled complexes of His6-PA with LF_N, LF, and EF, respectively, mixed with bovine plasma as a control. We demonstrate that preassembled complexes of His6-PA with LF_N, LF, and EF run identically to complexes that assemble in heparinized bovine plasma. Arrows mark the mobility of assembled His6-PA complexes

Analyte	Measured MW (Da)	FWHM (*m/z*)	Corrected MW (Da)	Theoretical MW (Da)	Deviation (%)
PA_2LF_N	158,193 (±38)	N.A.[b]	N.A.[b]	157,968	N.A.[b]
$PA_4(LF_N)_2$	316,417 (±27)	20	315,395 (?27)	315,936	-0.171
$PA_7(LF_N)_2$	507,542 (±162)	N.A.[c]	N.A.[c]	506,520	N.A.[c]
$PA_7(LF_N)_3$	538,704 (±186)	26	537,082 (±186)	537,431	-0.065
$PA_8(LF_N)_4$	633,528 (±218)	34	631,167 (±217)	631,871	-0.111
				Average Deviation	-0.116

Table 2.1. Molecular weights[a] of PA-LF_N complexes from nanoESI-MS.
[a]Experimental measured molecular weights (MW) compared to theoretical molecular weights, determined by their known amino acids sequences. Corrected molecular weights of the complexes were calculated using the method of Robinson and coworkers(McKay et al., 2006) in which the full width half maximum (FWHM) of the most intense peaks in a given charge state distribution were averaged and used to estimate the extent of solvent adduction: Adduction % = 160 Å~ FWHM/(m/z) - 0.03. m is the mass, and z is the charge. [b]N.A. (not available). The PA_2LFN analyte is outside the dynamic range of the correction method. cThis complex did not have high enough signal-to-noise to reliably estimate the peak widths.

Sample	Electron Microscopy			Electrophysiology		nanoESI-MS
	n[b]	Ref.-free, % PA_8	Ref.-based[c], % PA_8	n[d]	Pairwise analysis[e] of δ, % large γ	Approximate %[f] $PA_8(LF_N)_4$
$_Q$PA	12589	3	1.8	1616	10 (±10)	~8
$_n$PA+dsATR2 (saturated [$_n$PA] at a 4:1 ratio)	837	27	25	N/A[g]	N/A	N/A
$_n$PA+msATR2	9401	0	1.8	N/A	N/A	N/A
$_n$PA+LF_N	8409	28.5	27	1508	25 (±6)	~17
$_n$PA+LF_N (after treatment 37 °C pH 7)[h]	1084	~100	91	N/A	N/A	~100
$_n$PA+EF_N	5363	15	22	N/A	N/A	N/A
C-CHO extracted PA oligomers	4729	N/A	26	N/A	N/A	N/A
$_Q$PA S170C	2933	29	14	N/A	N/A	N/A
$_Q$PA$^{\Delta MIL}$ (initial population, pH 8)	10409	25	26	N/A	N/A	~20
$_Q$PA$^{\Delta MIL}$ (after pH 5.7 treatment)[i]	10000 3799 717	85 >99 N/A [89][i]	N/A 86 >99 [88][i]	N/A	N/A	~86
$_Q$PA His6	6115	0	1.3	N/A	N/A	N/A
$_n$PA+dsATR2 (with less saturating [$_n$PA] at a 1:1 ratio)	312	16	15	N/A	N/A	N/A

Table 2.2. Octamer percentages[a] from EM, electrophysiology, and nanoESI-MS. [a]All reported percentages are of PA_8, where the balance is PA_7, totaling 100%. [b]Number of single particles, n, used in either reference-free (Ref.-free) or reference-based (Ref.-based) class average analysis. [c]Ref.-based analysis of single particles using projections of the known crystal structures of heptameric[2] and octameric PA. [d]Number, n, of pairwise differences in single-channel conductance, analyzed according to Figure 2.1D. [e]Calculated from the relative peak areas of two-Gaussian fits shown in Figure 2.1D, using to $\sqrt{(\frac{1}{2}\rho 1 - \frac{1}{2}\sqrt{(\rho 12 - \rho 22)}}$ to get the percentage of PA_8 from the normalized amplitudes, ρ, of the Gaussian fits, where $\rho 1 = A1/(A1 + 2A2)$ and $\rho 2 = 2A2/(A1 + 2A2)$. [f]Approximation of relative abundances of octameric species from mass spectra. LFN was added to samples in the case of Q-sepharose-purified oligomers (QPA and QPAΔMIL) in order to obtain the spectra. [g]Not applicable. [h]See Materials and Methods for the isolation of WT octamer-LFN complexes. [i]See Materials and Methods for the octamer crystal structure sample preparation. Multiple datasets obtained on different sample preparations. The weighted mean value is listed in brackets below.

Resolution range (Å)	47.3-3.21 (3.31-3.21)
$\langle I/\sigma(I)\rangle$	28 (2.1)
R_{sym}	0.044 (0.595)
Unique reflections	94,967
Completeness (%)	99.7 (97.3)
Redundancy	3.9 (3.7)
Space group	P1
a, *b*, *c* (Å)	125.60, 125.67, 125.82
α, β, γ (°)	106.64, 110.82, 110.98
Monomers per asymmetric unit	8
R_{free} (%)	23.05
R_{work} (%)	19.72
Solvent content (%)	60.7
Matthews Coefficient (Å^3/Da)	3.1
Wilson *B* (Å^2)	66.0
Water molecules	8
Bond lengths rmsd (Å)	0.003
Bond angles rmsd (°)	0.669
Ramachandran plot (%)	
Most favorable	80.3
Allowed	19.7
Not allowed	0.0

Table 2.3. Crystallography data and refinement statistics. Last resolution shell statistics are shown in parentheses. $R_{sym} = \sum|I - \langle I\rangle| / \sum I$, where I is intensity. $R_{work} = \sum||F_o| - |F_c|| / \sum|F_o|$. R_{free}, the free R-value.

affinity resin. SDS-PAGE gels of His6-pure extracts were western blotted, confirming that the purified fraction contained His6-PA in the 63-kDa form (Figure 2.8).

EM studies of these extracts identified oligomeric rings consistent with the size and shape of PA oligomers; however, these complexes were less well oriented than the other in vitro samples, perhaps due to the presence of cellular components, like full-length ANTXR, which may form the observed extensions from the oligomeric structure. Several tilted class averages were obtained to capture this heterogeneity. From these, we determined that ~20-30% of the oligomers were octameric (Figure 2.2G). Control experiments show that His6-PA on its own forms ~1% octamer (Figure 2.7A), confirming that the His6 tag is not responsible for the high levels of octamer observed on cells. We also examined extracts from T-CHO cells (expressing ANTXR1) and from C-CHO cells that were co-treated with both PA and LF_N; and we found that octamer levels were ~20-30% under all cell-surface conditions tested (data not shown). Thus PA forms a mixture of octamers and heptamers on cell surfaces.

Crystal structure of the octamer. Mutations were then introduced into PA to probe the molecular mechanism of assembly. The most interesting mutations identified disrupted the interface between two PA subunits at the interface of domain 4 (D4) and the neighboring membrane insertion loop (MIL) in the adjacent PA subunit. One mutant replaced the MIL (i.e., residues 305-324) with a type II turn, deleting all possible hydrophobic interactions between L668 of D4 and F313 and F314 in the MIL. This type of PA oligomer ($PA^{\Delta MIL}$) was reported to form heptameric rings (Miller et al., 1999); but our version made an enriched source of octameric rings as observed by EM (Figure 2.5A; Table 2.2).

We used $PA^{\Delta MIL}$ oligomers as a concentrated source of octameric PA and solved its crystal structure to 3.2-Å resolution (Figure 2.4A; Table 2.3). Molecular replacement identified eight PA monomers arranged as a ring in the asymmetric unit. We find that the octamer is best described as having fourfold noncrystallographic symmetry (NCS), because there are two types of PA monomer conformations [called A and B (Figure 2.4C)] that occupy alternating positions around the ring (Figure 2.4D). From structural alignments, these two conformers differ in the orientation of D4 (Figure 2.4C). This conformational heterogeneity is notable, since D4 interacts with the MIL and may be a structural feature in the assembly mechanism. D4's flexibility is also consistent with the higher than average B factors observed there and also in the MIL of the heptamer structure.(Lacy, Wigelsworth, Melnyk et al., 2004) Thus plasticity in these two regions may provide a mechanism for octamer formation, where modulation of the structure in these regions may occur either (i) via ANTXR binding, which reorients D4 relative to D2 (Lacy, Wigelsworth, Melnyk et al., 2004; Santelli et al., 2004); or (ii) via exposure to a more acidic pH, which may alter the conformation of the MIL.

Consistent with our single-channel data, the mean pore diameter of the octamer pre-channel is ~10% larger than the heptamer [46 (±4) and 40 (±4) Å, respectively] (Figure 2.4A,B). The residues lining the pre-channel of the octamer are similar to those in the heptamer; all types of chemistries are represented, though the charge composition is more anionic overall. The octamer buries ~3300 $Å^2$ of solvent accessible surface area (ΔASA) per monomer, which is ~800 $Å^2$ less than the heptamer; the MIL and its interactions with its neighboring docking groove in D4 largely account for this difference. The octamer forms additional contacts (not found in the heptamer) at sites more proximal to the central pore, accounting for ~350 $Å^2$ of additional buried surface (Figure 2.4E). For WT octameric PA, the MIL should form analogous interactions with this D4-docking groove; and therefore, the octamer may bury at least 350 $Å^2$ more surface area per monomer than the heptamer when the MIL is present. Thus WT octamer will bury ~6100 $Å^2$

of additional surface relative to the heptamer, when including the eighth subunit and additional increases in burial per monomer.

The angles, θ, between *n* adjacent monomers arranged symmetrically about a ring are ideally equal to 180 - 360/*n*, and these angles widen ~6º for the octamer (Figure 2.4A) with respect to the heptamer (Figure 2.4B). We found this is accomplished by a subtle shift in the inter-monomer packing interfaces (Figure 2.4E), where the octamer buries more surface area in regions proximal to the central channel. During assembly, the steric mass of the MIL may act as a non-specific wedge that effectively nudges the adjacent monomer toward a more acute θ in the heptamer. Thus $PA^{\Delta MIL}$, in the absence of this constraint, is able to relax θ to achieve the octameric configuration. The MIL has two functions: (i) to form the channel in the membrane; and (ii) to control the oligomerization number of pre-channel assemblies.

The relative stability of the PA heptamer and octamer. To test whether, octameric and heptameric complexes differed in their stabilities, we incubated mixtures of heptameric and octameric PA at different temperatures and pHs. Under mildly acidic conditions (pH 5.7), we found that the heptameric form precipitated almost quantitatively as judged by both EM and nanoESI-MS (Figure 2.5A; Table 2.2); however, the octameric form maintained its solubility and persisted. This difference provided us with the means to isolate the octameric form for crystallization. Since these experiments used the $PA^{\Delta MIL}$ construct, we tested the relative stability of WT PA oligomers formed in the presence of LF_N at physiological pH. After the assembly under physiological conditions, we found that the sample could be purified by S400 gel filtration, generating ~90%-pure octamer, as judged by EM and nanoESI-MS (Figure 2.5B; Table 2.2). Therefore, we conclude that the heptameric form assembled and was subsequently inactivated by aggregation under physiological conditions; however, the octameric form persisted as a soluble complex.

Translocase activity of octameric channels. The pre-channel PA oligomer forms the translocase channel state under acidic pH conditions;(Blaustein et al., 1989; Miller et al., 1999) the β-barrel, which penetrates the membrane, is comprised of the MIL and adjacent β-strands in D2. Our structure reveals that the contacts made in D1' (ΔASA of ~1100 $Å^2$) and those immediately adjacent to it in D2 (~1400 $Å^2$) are largely identical and sufficient to form and maintain stable oligomeric complexes even when the MIL is not present. Therefore, the octamer may form channels, and the two Gaussian populations of conductance levels observed in planar bilayers (Figure 2.1B, C) may reflect octamers and heptamers, which have stably inserted into membranes.

We then tested this further and asked whether octamers and heptamers possessed similar translocase activity. Here we compared $_QPA$, which is ~98% heptameric, to a sample, $_nPA+LF_N$, ~90% enriched in octamer. In an ensemble translocation experiment, channels are first inserted into a membrane at 20 mV; the channels are loaded with LF_N, which blocks the conductance; excess LF_N is removed by perfusion; and then the LF_N is translocated at a higher voltage, or Δψ. We observe that LF, EF, LF_N, and EF_N translocate through the two different PA oligomers with similar efficiencies and rates (Figure 2.5C). (Efficiency is the measured amplitude translocated divided by the maximum theoretical amplitude; the rate is estimated by the time it takes for half of the protein to translocate).

To further verify that larger-sized and smaller-sized channels are capable of translocating protein, we performed single-channel translocation experiments (Figure 2.5D). Here we formed single PA channels at 20 mV and then added LF_N. Once the channel closed due to LF_N binding, the voltage was raised to 50 mV. Translocation events (n ~ 10) were recorded until the channel

became inactive. This procedure was repeated on a second channel obtained in the same membrane, which had a ~10% larger conductance. Therefore, we conclude that large and small PA channels are functional translocases, and both the octameric and heptameric forms of the PA channel are functional.

2.4 Discussion

We suggest that the octameric form of PA has not been previously observed (Katayama et al., 2008; Lacy, Wigelsworth, Melnyk et al., 2004; Milne et al., 1994; Mogridge et al., 2002; Petosa et al., 1997), because the standard method of PA assembly, which uses an anion-exchange column (Blaustein et al., 1989), yields oligomers virtually devoid of octamers (Figure 2A). Assembly in the presence of the ligands LF_N, EF_N, or dimeric ANTXR produces a 25-30% population of octameric oligomers in vitro (Figure 2.1, 2.2B-D). This heterogeneous assembly mechanism is physiological, because a similar proportion of octameric oligomers is observed on the surface of cells (Figure 2G). Our crystal structure of the octamer is not a regular octagon, but rather is composed of four PA dimer pairs arranged in a square planar symmetry. This symmetry suggests that dimeric PA intermediates populate the assembly pathway, and indeed mass spectrometry reveals that dimeric PA species are general assembly intermediates (Figure 2.3B). While heptameric and octameric channels have similar translocase activity, octameric oligomers are more stable under physiological pH and temperature (Figure 2.5). We propose that these two different oligomerization states are functionally relevant to anthrax pathogenesis, namely in the two different environments in which the toxin assembles (Figure 2.6): (i) on cell surfaces, assembly bottlenecks may be mitigated allowing for proper endocytosis of functional complexes by having the two assembly routes; and (ii) in blood plasma, PA may assemble prior to reaching the cell surface and require a more stable oligomeric configuration, since the heptamer is weakly stable under physiological conditions, especially in the absence of its cellular receptor.

Cell-surface assembly and endocytosis. The current model for anthrax toxin assembly proposes that PA assembles into a heptamer on cell surfaces expressing ANTXRs (Figure 2.7). Initially, PA binds a cell-surface receptor, ANTXR1 or ANTXR2, is cleaved by a furin-type protease, and then begins to assemble into the ring-shaped oligomer. While the current model predicts that these oligomers will be heptameric(J. A. Young & Collier, 2007), the oligomeric states populated on cell surfaces have not been reported. We specifically addressed this question by extracting oligomers from cell surfaces and analyzing the distribution of oligomeric states by electron microscopy. We find that PA forms both a heptamer and the novel octamer in about a 2:1 ratio, using cell lines expressing either ANTXR1 or ANTXR2. What selection pressures on the toxin might maintain this dual-oligomerization-state mechanism? Currently, it is known that cell-surface assembly and endocytosis may be coupled processes. For example, the rate of cellular internalization through endocytosis for either free ANTXR or PA bound ANTXR is slow; and this basal rate is only accelerated if the PA is pre-assembled into PA heptamers or PA-bound ANTXR subunits are aggregated by antibody cross-linking (Abrami et al., 2003). Therefore, PA assembly and the corresponding aggregation of ANTXRs triggers endocytosis.

If we extend our current understanding of assembly, we now can improve upon the initial model. First, we can assume that ANTXR1 and ANTXR2 are effectively dimeric on cell surfaces, because ANTXR-mediated assembly in solution only promotes octameric assembly when the receptor is dimeric (Figure 2.2B, C). A dimeric receptor model agrees with previous studies, which examined the aggregation state of ANTXR1's transmembrane helix (Go et al., 2006). Therefore, we propose that the antibody cross-linking experiment reported by Abrami et

al (Abrami et al., 2003), more likely involves a higher order aggregation of PA subunits beyond the formation of PA dimers. We anticipate this, because it is known that LF and EF promote the dimerization of PA (Figure 2.3) (Cunningham et al., 2002)); and an unintended consequence of this dimerization may be that PA_2LF or PA_2EF ternary complex intermediates would be improperly endocytosed prior to assembly into functional ring-shaped oligomeric complexes. Thus an efficient coupling of cell-surface assembly and endocytosis would limit premature endocytosis of non-functional dimers and tetramers.

The best explanation for the presence of the octameric and heptameric oligomers may ultimately be to allow for assembly under a range of PA monomer concentrations. If we consider the two extreme cases of either low or high PA monomer concentrations, assembly would be hindered if only one oligomeric state were possible. On one hand, supposing only the octameric assembly pathway were possible and the PA monomer concentration was low, then the dimeric ANTXR sites may not be saturated, and assembly would be inhibited at the critical oligomerization step, allowing unassembled complexes to be endocytosed. On the other hand, supposing only the heptameric form were possible and the PA monomer concentration was high, the dimeric ANTXR sites would be fully saturated with PA, and assembly would be inhibited until one PA could dissociate from its ANTXR binding site, allowing for an odd number of subunits to assemble immediately before endocytosis. This latter scenario is especially prohibited knowing that the dissociation lifetime for the PA-ANTXR2 interaction is on the order of days (Wigelsworth et al., 2004). In sum, the mixed-oligomerization mechanism mitigates these potential assembly bottlenecks, allowing the toxin components to fully assemble and remain efficacious under the wide dynamic range of PA concentrations.

Extracellular assembly in blood plasma. Anthrax toxin complexes were first identified in the blood of *B. anthracis*-infected guinea pigs; and this blood (after sterilization with antibiotic treatment) could then be subsequently administered to a second uninfected animal to impart its lethal affect (H. Smith et al., 1954). Throughout the later stages of infection, both the proteolytically-activated form of PA ($_nPA$) and LF are found in the sera of infected animal models (Mabry et al., 2006). This form of PA, of course, may co-assemble with LF; however, the prior study did not test this possibility. We demonstrate here, using native gel electrophoresis, that PA can be proteolytically activated in bovine blood plasma, and toxin complexes can form stably (Figure 2.9). Under aqueous conditions, we have shown that octamers will form in the presence of LF_N or EF_N (Figure 2.2D, E). Thus octamer formation is not limited to a receptor-dependent mechanism, and octamers may occur extracellularly in blood plasma in an LF- or EF-dependent manner (Figure 2.6).

Toxin stability. Recent work in vitro revealed that heptameric pre-channel complexes are unstable under physiological conditions, readily converting to the channel state.(Katayama et al., 2008) Here we demonstrate that physiological temperatures and pH lead to irreversible aggregation of the heptameric form, such that the octameric form is left behind in stable, isolable complexes (Figure 2.5A, B). We think this effect may be linked to pH-dependent differences in the octameric pre-channel to channel transition or inherent differences in the stability of octameric toxin complexes. ANTXRs have been shown previously to stabilize the pre-channel conformation under physiological conditions (Lacy, Wigelsworth, Melnyk et al., 2004; Leppla, 1991; Miller et al., 1999; Novak, Stein, Little, Leppla, & Friedlander, 1992). Toxin complexes assembled in the bloodstream, however, do not benefit from ANTXR stabilization. Thus octameric complexes may represent a more stable toxin configuration that may persist in the

blood of infected animals, serving a primary role to maintain cytotoxicity under physiological conditions.

Octamer structure. Our crystal structure shows that the octamer is a ring of eight PA monomers, consisting of a square-planar arrangement of four PA dimers (Figure 2.4C, D). This structure is in contrast to the near-perfect, regular heptagon model of the heptamer (Lacy, Wigelsworth, Melnyk et al., 2004). Our EM and crystallographic studies of toxin complexes suggest that the octamer is composed of four pairs of PA subunits that are conformational heterodimers; and the heptamer may actually consist of three PA heterodimers and one asymmetric monomer (Figure 2.2). Our analysis of the precise symmetry of the heptamer by EM should be tempered by the resolution of the technique, however; and further crystallographic studies are required. Nonetheless, the octamer and its tetrameric arrangement of PA pairs suggests that dimeric PA intermediates produced by interactions with LF, EF or a dimeric ANTXR subsequently assemble in a pairwise fashion to form the octamer (Figure 2.2, 6).
From the crystal structure, we conclude that the WT octamers should bury 6100 $Å^2$ of additional surface per oligomer relative to the heptamer, indicating that octamers may possess greater inherent stability, preventing disassembly and/or premature conversion to the channel state. Each PA heterodimer, of course, is poised to bind an LF/EF molecule (or a pair of ANTXRs), affording the octamer four binding sites and the heptamer three (Figure 2.3, 2.6). The improved stability of octameric toxin complexes may result from full occupancy of four heterodimeric, hydrophobic, LF binding sites; whereas for the heptamer, only three of such sites can be occupied, leaving one PA subunit exposed. Moreover, additional interfaces between adjacent LF subunits in the octameric complex may create a novel ring of interfaces between adjacent LF subunits, adding stability that cannot be attained in the heptameric complex (Figure 2.6). Future structural studies will elucidate how these two lethal toxin configurations may differ. We conclude that the added surface burial and structural symmetry of the even-numbered octameric configuration of toxin complexes may explain the improved stability over the heptameric configuration.

Toxin activity. We propose that the general paradigm for the aggregate physiological anthrax toxin activity is a product of the catalytic rate of translocation and the inherent stability of the two possible oligomeric configurations: the heptamer and the octamer (Figure 2.6). A secondary effect relates to the fact that the octameric configuration provides an additional LF- and EF-binding site per complex (Figs. 2.3A, 2.6), increasing the potential toxicity of saturated octameric toxin complexes. We find in our planar lipid bilayer translocation assays that the two oligomers translocate LF and EF at similar rates (Figure 2.5C). Therefore, we propose differences in toxin activity will likely result from intrinsic differences in oligomer stability. Without ANTXR stabilization, heptameric toxin complexes will be quickly inactivated under physiological conditions (Figure 2.5A,B), whereas octameric toxin complexes will remain soluble and fully functional. We hypothesize that these physiological conditions are present when the toxin assembles in the blood or plasma during infection, and the octameric form should be favored in that environment.

Staphylococcal α-hemolysin. The pathogenic factor produced by Staphylococcus aureus, called α-hemolysin, is comprised of multiple copies of a 293 residue polypeptide (Bhakdi et al., 1996). The assembled toxin ultimately forms a circular, β-barrel-type, ion- conducting pore with a mushroom-like architecture (Song et al., 1996a). Interestingly, this pore-forming toxin is believed to have multiple oligomeric states. EM (Arbuthnott, Freer, & Bernheimer, 1967; Olofsson, Kaveus, Thelestam, & Hebert, 1988; Ward & Leonard, 1992), atomic force

microscopy (Czajkowsky et al., 1998) studies, and electrophysiology studies (Furini, Domene, Rossi, Tartagni, & Cavalcanti, 2008) determined that the α-hemolysin can be hexameric. However, chemical cross-linking studies (J. E. Gouaux et al., 1994), crystallographic studies (J. E. Gouaux et al., 1994; Song et al., 1996a), single-molecule, photo-bleaching fluorescence methods (Das, Darshi, Cheley, Wallace, & Bayley, 2007), and electrophysiology studies (Furini et al., 2008) suggest the toxin forms a heptamer. However, the relative populations of the two oligomeric states and the conditions affecting these relative distributions have not been reported.

Pathogenesis. Why may PA assemble into a mixture of oligomers? For *B. anthracis* to optimize its lifecycle and proliferate in its host, it secretes a toxin, which at the initial stages of pathogenesis, may selectively suppress the immune system, while avoiding premature death of its host. It is known that upon infection, *B. anthracis* secretes low, undetectable concentrations of the toxin components; and at the latest stages of infection, 100 μg/mL levels of PA are detectable in the blood of infected animals (Mabry et al., 2006). This large increase in PA concentration immediately precedes death in animal models (Ezzell et al., 2009). Such a wide dynamic range in toxin levels suggests a relationship between toxin assembly and cytotoxicity. We propose that, on the cell surface, assembly of octameric oligomers alleviates a potential assembly bottleneck imposed by ANTXR dimerization, while in the bloodstream the octameric toxin complexes may function as a more stable species that serves to regulate toxin levels. Thus heterogeneous assembly may function in two key contexts: the known cell surface assembly pathway (Figure 2.6) and a putative toxin assembly pathway in the blood (Figure 2.6, 2.9).

PA assembly pathways are further complicated by dimerization of ANTXRs (Go et al., 2009; Go et al., 2006) and induced dimerization of PA subunits by LFN and EFN. The heptameric assembly route may be efficient at low concentrations, where PA likely assembles predominantly from monomers. On the other hand, PA assembly would be attenuated at high concentrations, where PA assembles via dimeric intermediates, in the absence of the octameric assembly route. Endocytosis coincides with PA assembly (Abrami et al., 2003), and a loss in toxin activity could occur if partially-assembled complexes were endocytosed. Therefore, we reason that the observed heterogeneity (Figure 2.2G) may serve to alleviate these potential assembly bottlenecks, incurred during oligomerization.

At later stages in anthrax infection, when PA and LF concentrations are high, a significant proportion of toxin complexes may assemble prior to encountering cell surface ANTXRs. In fact, the blood of infected animals contains PA that is almost exclusively proteolytically activated (Mabry et al., 2006). Here we demonstrated that PA, LF, and EF assemble into lethal and edema toxin complexes in bovine blood (Figure 2.9). Assembly in the bloodstream should produce a similar proportion of octameric toxin complexes as we observe in vitro (Figure 2.2). However, we expect that octameric complexes should persist in the bloodstream, while heptameric complexes should form inactive aggregates. Therefore, octamer formation could provide a mechanism of overcoming the inherently harsh and attenuating conditions encountered in the bloodstream. The proposed differential oligomer stability model implies that the anthrax toxin can regulate its aggregate activity through assembly, allowing the toxin dose to be controlled after secretion from the bacillus. Further structure/function studies of heptameric and octameric oligomers will clarify this molecular mechanism.

2.5 Materials and Methods

Proteins

PA. Recombinant WT PA, carboxy-terminally His6-tagged PA (Sun, Vernier, Wigelsworth, & Collier, 2007), and all other PA mutants described herein were overexpressed in the periplasm of *E. coli* BL21(DE3), and they were purified as 83-kDa monomers as described (Wigelsworth et al., 2004) A modified QuikChange procedure (Zheng, Baumann, & Reymond, 2004) using pFu Turbo polymerase (Agilent Technologies, Santa Clara, CA) was implemented to make a deletion construct ($PA^{\Delta MIL}$) from the PA expression vector, PA_{83} pET22b+ (EMD Chemicals, Gibbstown, NJ) (Benson et al., 1998). In $PA^{\Delta MIL}$, residues 305-324 were deleted and two point mutations (V303P and H304G) were introduced simultaneously, leaving a Type II turn in place of the MIL [residue numbering as in 1ACC (Petosa et al., 1997)].

Dimeric PA. The QuikChange procedure was also used to engineer in a S170C point mutation into WT PA. PA S170C, purified under oxidizing conditions, was judged to be dimeric by SDS-PAGE.

Soluble dimeric ANTXR2. Recombinant soluble anthrax toxin receptor domain (sANTXR2), residues 40–217 (Wigelsworth et al., 2004), was expressed from a pGEX vector (GE Healthcare) as a glutathione-S-transferase (GST) fusion protein, affinity purified on glutathione sepharose as described (Wigelsworth et al., 2004). The GST-sANTXR was shown to be fully dimeric by nanoESI-MS and is called dsANTXR2.

Soluble monomeric ANTXR2. A monomeric version of sANTXR2 (msANTXR) was made by subcloning residues 40-217 of ANTXR2 into pET15b (EMD Chemicals) via the Nde I and BamH I restriction sites, using a pGEX expression clone (Wigelsworth et al., 2004). This construct has an amino-terminal His6 tag as described previously (Santelli et al., 2004). The protein was similarly purified on a His6 column and judged to be pure by SDS-PAGE, and it was confirmed to be monomeric by nanoESI-MS.

LF_N and EF_N. Recombinant LF_N (LF residues 1-263) and EF_N (residues 1-254 of EF) were overexpressed from pET15b constructs (Lacy et al., 2002) and then purified from the cytosol using His6 affinity chromatography. LF_N was further processed by incubating with bovine α-thrombin to remove the amino-terminal His6 tag and purified over Q-sepharose anion exchange as described previously (Krantz et al., 2005). EF_N was used with its His6 tag and not processed any further. Each protein sample was verified by MALDI mass spectrometry.

PA oligomerization on a Q-sepharose. PA monomers were first treated with trypsin at a 1:1000 mass ratio for 15 minutes at room temperature, making $_nPA$. The trypsin was blocked by the addition of a 1:100 mass ratio of soybean trypsin inhibitor and 1 mM phenylmethylsulphonyl fluoride (PMSF). Then the small, 20-kDa fragment, released by trypsinization, was separated by anion exchange chromatography, using Q-Sepharose High Performance resin (GE Healthcare), such that the remaining ~60 kDa portion oligomerized as previously described.(Blaustein et al., 1989; Wigelsworth et al., 2004) This crude, oligomeric PA mixture ($_QPA$) was used throughout and contains mixtures of both heptameric and octameric complexes as judged by EM and nanoESI-MS.

$_nPA$ oligomerization in the presence of LF_N/EF_N or ms/dsANTXR2. $_nPA$ was prepared as describe above and then diluted to into an appropriate buffer containing stoichiometric amounts of LF_N/EF_N or ms/dsANTXR2. LF_N/EF_N assembly experiments were carried out by diluting $_nPA$ to ~1 mg/mL in 20 mM phosphate, 150 mM sodium chloride, pH 7.5, containing excess LF_N/EF_N. The assembly reaction was allowed to equilibrate for two hours at room temperature to afford complete oligomerization, as assessed by native gel. The dsANTXR2- and msANTXR2-assembly experiments were carried out by diluting $_nPA$ to ~2 mg/mL in 20 mM cacodylate buffer, 150 mM sodium chloride, 1 mM calcium chloride, pH 7.5, containing the

determined stoichiometric amounts of msANTXR2 or dsANTXR2. The assembly reaction was allowed to equilibrate for ten minutes at room temperature to afford complete oligomerization (as assessed by native gel electrophoresis). Assembly reactions were purified on an S200 gel filtration column equilibrated in assembly buffer to remove unassembled components. msANTXR2 does not promote oligomerization of $_{n}$PA, so it was assembled in the manner that $_{Q}$PA is assembled as described above.

Isolation of wild type octameric PA. $_{n}$PA+LF_N complexes were prepared as described above, dialyzed against 10 mM Tris, pH 8, and diluted to 2 mg/mL in 0.1 M cacodylate buffer, pH 7. The sample was incubated for 5 minutes at 37 ºC, concentrated, and purified on an S400 gel filtration column. The purity and oligomeric homogeneity of the resulting complexes were assessed by electron microscopy and mass spectrometry.

Electrophysiology. An Axopatch 200B amplifier (Molecular Devices Corp., Sunnyvale, CA) was used in the voltage-clamp, capacitor-feedback mode. The amplifier was interfaced to a CyberAmp 320 signal conditioner (Molecular Devices), which typically filtered the data at 200 Hz via a low-pass, 4-pole, Bessel section. The filtered, analog signal was typically recorded by computer at 400 Hz using a Digidata 1440A analog-to-digital converter (Molecular Devices) and AXOCLAMP software (Molecular Devices). Most data analysis, post-acquisition filtering, and curve fitting used a combination of CLAMPFIT (Molecular Devices), ORIGIN6.1 (OriginLab Corp., Northampton, MA), and custom Perl scripts.

Relative macroscopic membrane insertion activities for WT PA and mutant forms were assayed as follows. Planar lipid bilayers (PLB) were painted(P. Mueller, Rudin, Tien, & Westcott, 1963) using a 3% solution of the lipid, 1,2-diphytanoyl-*sn*-glycerol-3-phosphocholine (DPhPC; Avanti Polar Lipids, Alabaster, AL), in *n*-decane solvent. The bilayer was painted inside either a 100 or 200 μM aperture of a 1-mL, white delrin cup while bathed in aqueous Buffer S: 100 mM KCl, 1 mM EDTA and 10 mM succinic acid, pH 6.6. Cis (side to which the PA oligomer is added) and trans compartments were bathed in symmetric Buffer S. For macroscopic current measurements, PA oligomer (25 pM) was added to the cis compartment, which was held at a $\Delta\psi$ of +20 mV. ($\Delta\psi$, the membrane potential, is defined as $\Delta\psi = \Delta\psi_{cis} - \psi_{trans}$, where $\psi_{trans} \equiv 0$ mV.) Channel insertion increased over a period of minutes and stabilized after 20 to 30 minutes. Macroscopic currents were then measured at this point or the channel-inserted membrane was used in translocation experiments as described below.

Single-channel measurements were obtained using DPhPC/decane films formed on a 100 μM aperture in a white delrin cup. Single-channel conductance measurements were carried out at a $\Delta\psi$ of +20 mV in symmetric Buffer S. Single-channel channel current recordings were determined by adding a dilute solution (~10^{-14} M) of PA oligomer to the cis chamber, stirring briefly, and then waiting 5 to 30 minutes until discrete steps in current were observed. The clamping voltage and current responses were acquired at 400 Hz under low-pass filtering at 200 Hz. To observe subtle, slow-timescale fluctuations in the single-channel current records, we implemented a Gaussian-filter algorithm; this filter does not cause 'overshoot' during channel opening and closing transitions. The filter's Gaussian kernel was defined with a σ having a width of 100 data points. A Perl script was written to apply the Gaussian filter to our datasets.

To calculate the mean unitary conductance levels, time courses not treated with the Gaussian filter were analyzed by fitting Gaussians to 0.003 to 0.03 pA binned histograms of the current responses, using either ORIGIN6.1 or CLAMPFIT. Some records contained multiple, but readily separable, current steps up to as many as ten single channels. Means, μ, from Gaussian curve fits were then subtracted from similar fits to the noise observed at 'zero' current to obtain each

single-channel current, *i*. The single-channel conductance, γ, is calculated from the single-channel current, *i*, and voltage, *V*, by $\gamma = i / V$. Errors from μ's were propagated to establish errors in γ's for each measurement, which were ~ 0.5 pS.

Single-channel recordings of the $_{n}$PA+LF$_N$ sample. We also analyzed the $_{n}$PA+LF$_N$ sample, which was formed by taking 0.1 mg/ml of nPA and adding a stoichiometric equivalent of LF$_N$. The mixture was incubated at room temperature for 1 hour. The assembled complex (as judged by native gel electrophoresis, gel filtration, and EM) was applied to PLB membranes at ~10^{-14} M. We initially observe channel insertion at a Δψ of -20 mV to preclude the LF$_N$ moiety from binding within the channel and blocking the conductance. Note that because the PA sample was diluted 10^9-fold, newly inserted channels could be shifted back to a Δψ of +20 mV to record their currents once the LF$_N$ dissociated from the channel.

Electrophysiology-based translocation assay. For translocation experiments, a universal bilayer buffer (UBB) was used (10 mM oxalic acid, 10 mM MES, 10 mM phosphoric acid, 1 mM EDTA, 100 mM KCl). The pH of the UBB is either 5.6 or 6.6 depending on whether a ΔpH will be formed during the translocation assay. Once a membrane was formed, $_{Q}$PA+LF$_N$ or $_{n}$PA+LF$_N$ was added to the cis compartment (at pH 5.6); the cis compartment was held at a Δψ of ±20 mV with respect to the trans compartment. (I.e., in the case of $_{n}$PA+LF$_N$, the Δψ was held at -20 mV to allow for channel insertion to be observed, because at +20 mV, LF$_N$ would block the channel). When $_{n}$PA+LF$_N$ was used, the excess LF$_N$ was perfused away, and residual bound LF$_N$ was then translocated at 80 mV to clear the channels prior to initiating further translocation experiments. After the ensemble channel population was established, LF, LF$_N$, EF, or EF$_N$ were added to the cis compartment. The progress of substrate binding to PA$_{63}$ channels was monitored by the continuous fall in conductance. After the conductance block of PA channels was complete, excess substrate was removed from the cis compartment with perfusion with UBB, using push-pull, hand-crank-driven, 10-mL syringe pump. The cis compartment was perfused with 10 ml of UBB at a flow rate of 2 ml/min and Dy held at +20 mV. Translocation of LF, LF$_N$, EF, and EF$_N$ were initiated by jumping the Dy to a higher positive voltage and/or jumping the ΔpH to a higher positive value (where $\Delta pH \equiv pH_{trans} - pH_{cis}$.) The ΔpH is induced by adding predetermined amounts of 0.4 M phosphoric acid to the cis chamber. The final pH is determined using a pH meter following the completion of the translocation recording.

Electron microscopy. All the samples were prepared for EM in a similar manner. PA oligomer at 20-30 nM (in monomer concentration) was incubated in Buffer E (20 mM Tris, 100-250 mM NaCl, pH 8) for 5 minutes. 400 mesh copper grids were successively covered by a holey carbon film and a continuous carbon film. 4 μl of sample was applied to a freshly glow-discharged support grid for 30 s and then stained in 5 successive drops (75μl) of either 1% uranyl formate (Structure Probe, Inc., West Chester, PA) or 2% uranyl acetate (Sigma-Aldrich, St. Louis, MO).

Negative-stain EM images were recorded with a Tecnai 12 (FEI Company, Hillsboro, OR) operated at 100 or 120 kV at a magnification of either 49,000× or 50,000×. In some cases, data were collected on Kodak SO163 films (Eastman Kodak, Rochester, NY) at 600 to 800 nm underfocus. Film images were digitized with a Nikon Super Coolscan 8000 (Nikon U.S.A., Melville, NY) at a 12.7 μm pixel size, resulting in a 2.54 Å/pixel at the specimen scale. In other cases, data was collected directly on a CCD camera, resulting in a 2.13 Å/pixel at the specimen scale. Particle images were selected for each data set using automatic or manual particle picking using boxer in EMAN (Ludtke, Baldwin, & Chiu, 1999).

Reference-free processing was done using the software package, IMAGIC (Image Science Software, Berlin, Germany) or SPIDER (Frank et al., 1996). Images were subjected to three successive cycles of multi-reference alignment, multivariate statistical analysis, and classification (Stark et al., 1995; van Heel, Harauz, Orlova, Schmidt, & Schatz, 1996). The last classification was done using only the lowest order eigenvectors as described elsewhere (White, Saibil, Ignatiou, & Orlova, 2004) to separate the data by size and the heptameric and octameric oligomerization states.

A second method of image processing was used whereby reference images were made from 2D-projections of low resolution density maps generated from the crystal structures of the PA heptameric (Lacy, Wigelsworth, Melnyk et al., 2004) and octameric pre-channels, using SPIDER (Frank et al., 1996). Boxed images were then subjected to reference-based alignment and classification using the lowest order eigenvectors as stated above. Final class-average images were manually inspected for their oligomer number, designated as either heptamer or octamer, and tabulated to produce the final percentages of heptamers and octamers. Each method of classification, reference-free or crystal-structure-referenced, produced similar results (Table 2.2).

Extraction of PA oligomers from CHO cells. C-CHO and T-CHO cells were a kind gift from Arthur Frankel. The cell line was created from a spontaneous ANTXR-deficient CHO cell mutant line (PR230-CHO). The C-CHO and T-CHO lines were derived from stable transfections with the human ANTXR2 and ANTXR1 expression clones, respectively.(Liu & Leppla, 2003) The cell lines were grown to confluence in Ham's F12 medium (Invitrogen), 10% fetal bovine serum (Invitrogen), 100 units/mL penicillin, 100 μg/mL streptomycin (Sigma-Aldrich) in humid 5% CO_2 atmosphere at 37 ºC, as described (J. J. Young et al., 2007). Confluent cells were treated for one hour with 50 mM ammonium chloride, 50 mM 4(2-hydroxyethyl)-1-piperazineethanesulfonic acid (HEPES), pH 7.3 in Ham's Media to inhibit endosomal acidification, preventing conversion of PA to the channel state.(Rainey et al., 2005) His6-PA monomers (WT PA with a carboxy-terminal His6 tag) were applied to cells in the same medium at 100 μg/mL. Cells were incubated with His6-PA for one hour at 4 ºC, washed with five volumes ice-cold phosphate buffered saline (PBS) to remove unbound PA, and lysed in Buffer L: 20 mM Tris, 0.35 M NaCl, 10 mM imidazole, 1% Nonidet P-40 (or IPEGAL), 0.25% deoxycholic acid, 1 mM PMSF, pH 8, as described previously (Liu & Leppla, 2003). Cells debris was removed by centrifugation and the supernatant incubated with 0.5 mL His6-affinity resin (Ni-NTA Superflow, Qiagen, Valencia, CA) overnight at 4 ºC with stirring. The resin was washed with five volumes of Buffer L and eluted in Buffer L supplemented with 300 mM imidazole. The elution was applied to electron microscopy grids for analysis.

Mass spectrometry. Mass spectra of the protein complexes were acquired using a quadrupole time-of-flight (Q-Tof) mass spectrometer equipped with a Z-spray ion source (Q-Tof Premier, Waters, Milford, MA). Ions were formed using a nanoelectrospray (nanoESI) emitters prepared by pulling borosilicate capillaries (1.0 mm O.D./0.78 mm I.D., Sutter Instruments, Novato CA) to a tip I.D. of ~1 mm with a Flaming/Brown micropipette puller (Model P-87, Sutter). The instrument was calibrated with CsI clusters formed by nanoESI using a 24 mg/mL solution of CsI in 70:30 Milli-Q water:2-propanol prior to mass measurement. The protein solution for the stoichiometry determinations was prepared as described above and then concentrated to 10 mM followed by dialysis into 10 mM ammonium bicarbonate, pH 7.8. Immediately prior to mass analysis, the solution was diluted 1:1 with 200 mM ammonium acetate, pH 7.8. A platinum wire (0.127 mm diameter, Sigma, St. Louis, MO) was inserted through the capillary into the solution and electrospray was initiated and maintained by applying

1-1.3 kV to the wire (relative to instrument ground). Raw data was smoothed three times using the Waters MassLynx software mean smoothing algorithm with a window of 50 *m*/*z* (mass-charge ratio).

The reactions for assembly kinetics were initiated by mixing 10 mM ammonium bicarbonate solutions of purified $_{n}$PA and LF_N monomer in a 1:1 ratio to initiate oligomerization, and mass spectra were acquired continuously for 50 minutes. Variation in the voltage applied to the nanospray capillary and new capillaries at ~19 minutes and ~30 minutes were required to maintain ion current. Mass spectra were averaged for five-minute intervals and smoothed three times using the Waters MassLynx software mean smoothing algorithm with a window of 50 *m*/*z*. Each peak in a given charge-state distribution was integrated and the peak areas summed to give an absolute abundance for the corresponding analyte. Relative abundances were calculated as a fraction of the total abundances of the four analytes of interest monitored during the experiment.

Protein crystallization. Purified $_{Q}PA^{\Delta MIL}$ oligomer (judged to be rich in octameric complexes by EM) was prepared in Buffer X, which contained 74 mM sodium acetate, 7 mM Tris, 0.62 M NaCl, 37 mM tetrabutylammonium bromide, 7% ethanol, 0.07% *n*-dodecyl-β-D-maltopyranoside, pH 5.7, centrifuged to remove precipitated protein, and concentrated to 13 mg/mL. Initial crystallization conditions were established by sparse-mANTXRix crystallization screens (Jancarik & Kim, 1991), except our screens contained ~1000 unique conditions. A Mosquito nanoliter, liquid-handling robot (TTP Labtech, Cambridge, MA) was used to form 200 nL drops in 96-well format at 18 ºC, using the hanging-drop, vapor-diffusion method.(McPherson, 1976) Diffraction-quality crystals were formed with 1 µL hanging drops using the Mosquito (at 18 ºC), containing a one-to-one mixture of 13 mg/ml $_{Q}PA^{\Delta MIL}$ oligomer in Buffer X with the reservoir solutions (ranging from 18 to 30 % *t*-butanol, 0.1 M Tris, pH 7.5 to 8.5). Often irregular, rectangular-prism-shaped crystals formed overnight; these grew as large as ~200 × 200 × 75 µm. Crystals were harvested in a 30% v/v polyethylene glycol (PEG) 400 cryoprotectant, where the PEG only replaced the water in the mother liquor, and immediately flash-frozen in liquid nitrogen.

X-ray diffraction data collection, solution and refinement. X-ray diffraction data were collected at the Advanced Light Source in Lawrence Berkeley National Lab, Beamline 8.3.1,(MacDowell et al., 2004) using a Quantum 315r CCD area detector (ADSC, Poway, California). The crystals diffracted to 3.2 Å in the triclinic space group, *P*1, with unit cell dimensions of 125.60, 125.67, and 125.82 Å for *a*, *b*, and *c*, respectively, and 106.64, 110.82, and 110.98º for α, β, and γ (Table 2.3). The diffraction data were indexed and scaled in HKL2000 (Otwinowski & Minor, 1997). The scaled dataset was 98.7% complete to 3.2 Å. The self-rotation function in the CCP4 suite(Collaborative Computational Project, 1994) revealed strong peaks at a χ angles of 45º, 90º and 180º. Molecular replacement (MR) was performed using PHASER(Storoni, McCoy, & Read, 2004a) in CCP4, where the search model was a loop-stripped chain A from 1TZO (Lacy, Wigelsworth, Melnyk et al., 2004). This MR solution placed eight PA monomer chains in the asymmetric unit. The MR solution was refined with rigid-body constraints defined by the known domain boundaries in PA, using PHENIX (Adams et al., 2004a). NCS was established by first making structural alignments of individual monomers in CHIMERA(Pettersen et al., 2004b) and then calculating the center of mass of each chain to compute the geometric arrangement of the chains about the oligomeric ring. We found the oligomer was an irregular octagon, and pairs of monomers of two different conformations, 'A' and 'B', formed the sides of a regular, square, planar tetramer. Subsequent rounds of model building in COOT (Emsley & Cowtan, 2004a) were followed by coordinate and B-factor

refinement, with fourfold NCS restraints, using PHENIX. $2F_o–F_c$ and $F_o–F_c$ omit electron density maps were recalculated after iterations of model building and refinement, where F_o and F_c are the observed and calculated structure factors, respectively. MOLPROBITY (Davis et al., 2007) and PROCHECK (Laskowski, MacArthur, Moss, & Thornton, 1993) were used to validate the structure's geometry and stereochemistry during model building. Surface burial calculations were made using GETAREA1.1 (Fraczkiewicz & Braun, 1998). Molecular graphics renderings were computed using CHIMERA (Pettersen et al., 2004b).

Western blot analysis of PA oligomer extracts. The cell-surface-assembled protective antigen (PA) extract was separated by 10% SDS-PAGE, blotted on nitrocellulose at 10 V, 4 ºC overnight in blotting buffer (25 mM Tris, 0.192 M glycine, 20% methanol, pH 8.3), blocked with 1% non-fat milk powder in PBS. The blot was probed with an anti-His6-horse radish peroxidase (HRP) primary antibody (EMD Chemicals), following the manufacturer's recommendation, except that we visualized bound HRP with the following stain: 0.3% 4-chloro-1-naphthol (Sigma-Aldrich) and 0.3% hydrogen peroxide in phosphate buffered saline.

PA oligomerization in bovine blood serum and plasma. His6-PA monomer and LFN, LF, or EF were mixed in a one to one molar ratio and incubated in heparinized bovine serum (Rockland Immunochemicals, Inc.) or defibrinated bovine plasma (made from whole defibrinated bovine blood also purchased from Rockland) at a final PA concentration of 100 µg/mL for one to six hours at 37 ºC (six hours was sufficient to afford complete proteolytic activation and toxin assembly). After six hours, the plasma or serum was incubated with 50 µL His6-affinity resin for one hour at room temperature, with stirring. The resin was washed with five volumes of Buffer M: 20 mM Tris, 0.15 M NaCl, 10 mM imidazole and eluted in Buffer M supplemented with 300 mM imidazole. Preassembled complexes were prepared by mixing QPA with LFN, LF, or EF in a 1:1 molar ratio, followed by incubation at room temperature for ten minutes. Approximately 10 µg of protein was separated on 4-20% native PAGE (Invitrogen) at 150 V for two hours, on ice. Complexes were observed directly by Coomassie Brilliant Blue G-250 stain. The mobility of complexes assembled in bovine serum or plasma was compared with complexes preassembled in buffer.

Accession numbers. Coordinates and structure factors for the PA octamer have been deposited in the Protein Data Bank (PDB) with accession number 3HVD.

Chapter 3

Role of the protective antigen octamer in the molecular mechanism of anthrax lethal toxin stabilization in plasma

3.1 Abstract

Anthrax is caused by strains of *Bacillus anthracis* that produce two key virulence factors, anthrax toxin (Atx) and a poly-γ-D-glutamic acid capsule. Atx is comprised of three-proteins: protective antigen (PA) and two enzymes, lethal factor (LF) and edema factor (EF). To disrupt cell function, these components must assemble into holotoxin complexes, which contain either a ring-shaped homooctameric or homoheptameric PA oligomer bound to multiple copies of either LF and/or EF, producing lethal toxin (LT), edema toxin, or mixtures thereof. Once a host cell endocytoses these complexes, PA converts into a membrane-inserted channel that translocates LF and EF into the cytosol. LT may assemble on host cell surfaces or extracellularly in plasma. We show that under physiological conditions in bovine plasma that LT complexes containing heptameric PA aggregate and inactivate more readily than LT complexes containing octameric PA. LT complexes containing octameric PA possess enhanced stability, channel forming activity, and macrophage cytotoxicity relative to those containing heptameric PA. Under physiological conditions, multiple biophysical probes reveal that heptameric PA can prematurely adopt the channel conformation, but octameric PA complexes remain in their soluble prechannel configuration allowing them to resist aggregation and inactivation. We conclude that PA may form an octameric oligomeric state as a means to produce a more stable and active LT complex that may circulate freely in the blood.

3.2 Introduction

Bacterial pathogens utilize highly evolved systems to translocate protein effectors into host cells. Anthrax toxin (J. A. Young & Collier, 2007) (Atx) is an elegant example of such a translocation system, and it is a key virulence factor produced by pathogenic strains of *B. anthracis*. Atx consists of three nontoxic proteins (Beall et al., 1962; H Smith & Keppie, 1954; Stanley & Smith, 1961) genetically encoded on a virulence island of the plasmid, pXO1 (Okinaka et al., 1999). These proteins are secreted by vegetative *B. anthracis* in response to mammalian-host cues, such as bicarbonate and physiological body temperature (Sirard, Mock, & Fouet, 1994). Atx is responsible for imparting host cell damage (Fish & Lincoln, 1968a; Pezard et al., 1991), disabling immune system function (Pezard et al., 1991), facilitating bacteremia (S. Welkos, Little, Friedlander, Fritz, & Fellows, 2001), and eventually causing host death, even after an infection is cleared with antibiotics (Firoved et al., 2005; Pezard et al., 1991).

Protective antigen (PA_{83}) is an 83-kDa, cell-binding component of Atx that ultimately forms a translocase channel capable of delivering the other two enzyme components, lethal factor (LF) and edema factor (EF), into the cytosol of a host cell. LF is a 90-kDa, Zn^{2+}-dependent protease (Duesbery & Vande Woude, 1999b; Duesbery et al., 1998; Pannifer et al., 2001), which cleaves host mitogen-activated protein kinase kinases (Duesbery & Vande Woude, 1999b;

Duesbery et al., 1998). While PA and LF are individually nontoxic, the combination of LF and PA creates lethal toxin (LT), which can cause death (Pezard et al., 1991). EF is a 89-kDa, Ca^{2+}/calmodulin-activated adenylyl cyclase (Drum et al., 2002; Leppla, 1982, 1984), which increases the cellular pool of 3'-5'-cyclic adenosine monophosphate (cAMP) in the host up to ~200-fold (Leppla, 1982). In an analogous manner, PA and EF combine to form edema toxin, which can cause tissue swelling (Fish & Lincoln, 1968a; Pezard et al., 1991) and lead to death in a manner distinct from LT (Firoved et al., 2005). To achieve cytotoxicity, PA, LF, and EF must first self-assemble into holotoxin complexes. In one possible assembly mechanism, PA forms complexes on the surface of host cells in a receptor-dependent manner. PA first binds to one of two known Atx receptors (ANTXR) (Bradley et al., 2001; Scobie et al., 2003). PA is then cleaved by a furin-type protease to make the proteolytically-activated form, called $_{n}$PA. After a 20-kDa portion of $_{n}$PA (PA_{20}) dissociates, the remaining 63-kDa (PA_{63}), receptor-bound portion assembles into a mixture of ring-shaped heptameric (PA_7) (Katayama et al., 2008; Lacy, Wigelsworth, Melnyk et al., 2004; Milne et al., 1994; Mogridge et al., 2002; Petosa et al., 1997) and octameric (PA_8) (Kintzer et al., 2009) oligomers. These prechannel oligomers can bind up to three and four LF and/or EF molecules, respectively (Kintzer et al., 2009; Mogridge et al., 2002). The complexes are endocytosed (Abrami et al., 2003) and brought to an acidic compartment (Friedlander, 1986). The PA oligomer then transforms into a translocase channel, (Miller et al., 1999) allowing the transmembrane proton gradient to drive LF and EF translocation (Katayama et al., 2008; Krantz et al., 2006) into the cytosol, where LF and EF can catalyze reactions(Drum et al., 2002; Pannifer et al., 2001) that disrupt the host cell.

A second key virulence factor of *B. anthracis* is the poly-γ-D-glutamic acid (γ-DPGA) capsule surrounding the bacillus (Ivanovics & Erdos, 1937; Zwartouw & Smith, 1956b). Strains deficient in the pXO2 plasmid (Green et al., 1985b), which encodes the machinery (Candela & Fouet, 2005; Makino et al., 1989; Makino et al., 2002a; Scorpio, Chabot, Day, O'Brien D et al., 2007; Uchida et al., 1993a) that produces and exports γ-DPGA, have significantly reduced virulence (S. L. Welkos, 1991b). Long, linear γ-DPGA chains (~50 kDa) can be isolated from vegetative *B. anthracis* grown in vivo (Hanby & Rydon, 1946). For *B. anthracis*, the genes responsible for producing the γ-DPGA polymer (Makino et al., 1989), anchoring it to the peptidoglycan cell wall (Candela & Fouet, 2005), and cleaving it into smaller dissociable fragments (Candela & Fouet, 2005; Makino et al., 2002a; Scorpio, Chabot, Day, O'Brien D et al., 2007; Uchida et al., 1993a), augment its virulence perhaps through a variety of mechanisms, namely allowing the bacillus to resist complement (Makino et al., 2002a; Maurer, 1965b) and phagocytosis (Scorpio, Chabot, Day, O'Brien D et al., 2007). Interestingly, during infection lower-molecular-weight capsular fragments (L-capsule) are released from the bacillus by the hydrolytic enzyme dep, or capD (Candela & Fouet, 2005; Makino et al., 2002a; Scorpio, Chabot, Day, O'Brien D et al., 2007; Uchida et al., 1993a). These L-capsule γ-DPGA fragments can bind to PA, and they co-purify with PA isolated from anthrax-infected blood (Ezzell et al., 2009). Nonetheless, it is unknown whether γ-DPGA interacts with assembled LT complexes and whether this interaction may affect LT assembly, stability, or activity.

In the blood of infected animals at the later stages of anthrax, there is sufficient PA (80-100 μg/ml), LF (10-20 μg/ml), and PA-activating proteolytic activity (Ezzell & Abshire, 1992b; Kintzer et al., 2009; Mabry et al., 2006; Moayeri et al., 2007) to allow for LT assembly. The concentrations of these toxin components vary, however, depending upon the host species (Mabry et al., 2006), and the stage of the disease (Boyer et al., 2009). Also increased levels of bacteremia tend to correlate with increased levels of these Atx components and L-capsular γ-

DPGA (Boyer et al., 2009). With these high levels of Atx components and the presence of proteolytic activity capable of activating PA, we have proposed that there is a receptor-free Atx assembly pathway in the blood, which is parallel in certain respects to the cell-surface pathway (Kintzer et al., 2009). Animal infection models show that PA is rapidly cleared in the bloodstream, implying that the toxin has a finite lifetime there and competes with various host clearance mechanisms (Moayeri et al., 2007). Thus toxin stabilization mechanisms would allow the toxin to persist and remain efficacious in the plasma and other extracellular environments.

PA_7 complexes, nevertheless, are unstable at physiological temperatures and pH (Kintzer et al., 2009), where they readily convert to an inactive, aggregated state (Kintzer et al., 2009; Vernier et al., 2009). How do LT complexes endure the conditions encountered in blood at physiological pH and temperature? PA_8 complexes have more favorable characteristics than their PA_7 counterparts, as they can remain soluble at physiological pH and temperature (Kintzer et al., 2009), albeit it is unknown whether PA_8 complexes can form in plasma. Plasma is a complex, crowded environment, and it is unclear what the relative half lives of PA_7- and PA_8-containing LT complexes will be there. Developing an understanding of the physiological stabilities and molecular configurations of anthrax lethal and edema toxins is, therefore, of paramount importance to understanding their function throughout the stages of anthrax infection.

3.3 Results

PA_7 and PA_8 complexes assemble in bovine plasma. Previous studies have shown that PA complexes can assemble in plasma (Kintzer et al., 2009), because sufficient proteolytic activity is present in bovine plasma to form proteolytically-nicked PA ($_n$PA). Using a His_6-tagged PA construct, we assembled PA in defibrinated bovine plasma at 37 ºC, purified the resulting complexes, and characterized their oligomeric composition using electron microscopy (EM) (Figure 3.1a). The resulting micrographs were analyzed by crystal-structure-referenced alignment and classification. Prior experiments revealed that reference-free image analysis and this crystal-structure-referenced image analysis yield similar percentages of the two oligomers (Kintzer et al., 2009). Based upon this analysis, we find that plasma-assembled PA contains both the PA_7 and PA_8 oligomers (Figure 3.1b). We found that assembly reactions conducted at pH 8 resulted in a predominately heptameric oligomer population; however, at pH 7.3, a predominately octameric oligomer population was observed (Figure 3.1b). Also we found that EM images taken of the pH-7.3 assembly reactions contained large aggregates and particles that were more consistent with the elongated shape and size of the PA channel (Katayama et al., 2008) (Figure 3.10). Thus we conclude that there is a pH-dependent shift in the oligomer population, which favors the octameric form at pH 7.3.

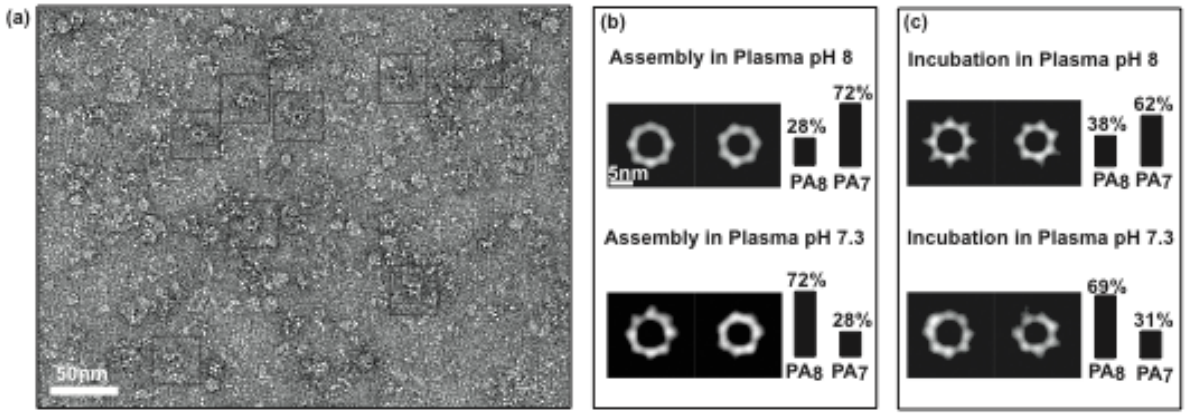

Figure 3.1. PA_8 is the predominate oligomer that forms in bovine plasma. Negative-stain EM analysis of His_6-PA-LF_N complexes either assembled in or incubated in defibrinated bovine plasma at 37 ˚C. Class-averaged images containing 10-100 particles of the resulting PA_7 and PA_8 oligomers; the total particle count, *n*; and percentages of each oligomer are indicated (black bars next to the representative images). **(a)** An electron micrograph at a magnification of 49,000× shows affinity-purified His_6-PA-LF_N oligomers, resulting from assembly in bovine plasma at pH 8.0. Representative soluble complexes are outlined by black boxes. **(b)** Class-average images of affinity-purified complexes assembled in bovine plasma at pH 8.0 (top, n = 1132; 28% PA_8; 72% PA_7) and at pH 7.3 (bottom, n = 434; 72% PA_8; 28% PA_7). **(c)** Class-average images of the soluble complexes remaining after incubating pre-assembled PA complexes in bovine plasma for 5 minutes at 37 ºC. The starting mixture of His_6-PA-LF_N oligomers contained 74% PA_7 and 26% PA_8 by EM (n = 2572). Final class-averaged images are shown for the pH-8 incubation (top, n = 861; 38% octamer; 62% heptamer) and the pH-7.3 incubation (bottom, n = 300; 69% octamer; 31% heptamer).

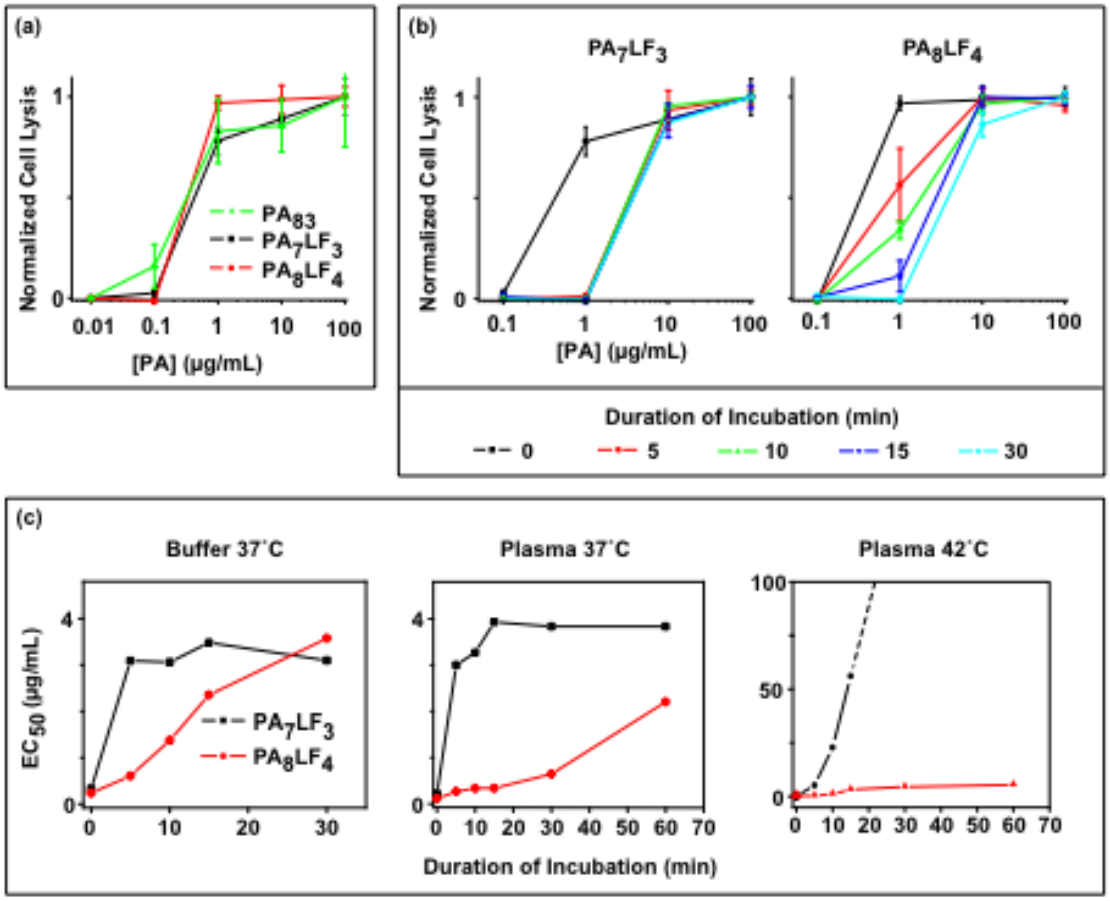

Figure 3.2. The stability of LT's macrophage cytotoxicity activity. (a) Macrophage cytotoxicity assays were performed on PA_{83}, PA_7LF_3, and PA_8LF_4 in the presence of constant LF (1 μg/ml), using immortalized bone-marrow macrophages derived from 129 mice. PA concentrations reported on the *x*-axes are standardized in concentration to μg/ml of total PA. **(b)** Purified PA_7LF_3 and PA_8LF_4 complexes were challenged by incubation in pH-7.3 buffer or pH-7.3 buffered bovine plasma at 37 ˚C for the indicated durations. Macrophage cytotoxicity profiles of (left) PA_7LF_3 and (right) PA_8LF_4 complexes following their incubation in buffer (37 ˚C, pH 7.3) for the indicated durations. **(c)** Plots of the EC_{50} values for PA_7LF_3 and PA_8LF_4 complexes as a function of the incubation duration: (left) buffer at 37 ˚C, pH 7.3; (middle) bovine plasma at 37 ˚C, pH 7.3; and (right) bovine plasma at 42 ˚C, pH 7.3. Dashed lines in the last panel estimate the EC_{50} values, which are beyond the assayable range (i.e., > 300 μg/mL).

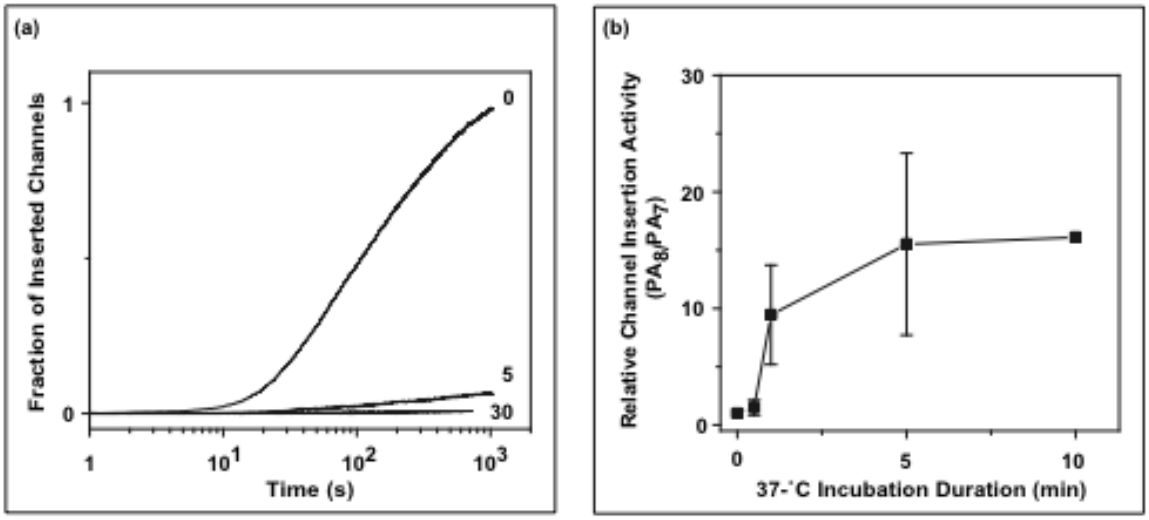

Figure 3.3. The stability of PA's channel-forming activity. Studies of PA channel formation in planar lipid bilayers compare the physiological stabilities of the $PA_7(LF_N)_3$ and $PA_8(LF_N)_4$ complexes at 37 ˚C, pH 7.4. **(a)** Time courses of the fraction of inserted channels for purified $PA_7(LF_N)_3$ complexes. The normalized fraction of inserted channels is calculated as the instantaneous current observed per mole of 37-˚C pre-incubated PA oligomer sample divided by the final current per mole of PA oligomer for the 0-minute sample (which is the sample has not been subjected to a 37-˚C incubation.) The 37-˚C incubation durations (either 0, 5 or 30 minutes) are indicated on each time course. **(b)** A plot of the relative insertion efficiencies of PA complexes versus the duration of incubation at 37 ˚C, pH 7.4. The relative insertion efficiencies for each incubation duration is determined as the normalized fraction of inserted PA_8 channels divided by the normalized fraction of inserted PA_7 channels. Error bars represent a propagation of errors from standard deviations obtained for the averages of at least three PA_7 and three PA_8 samples.

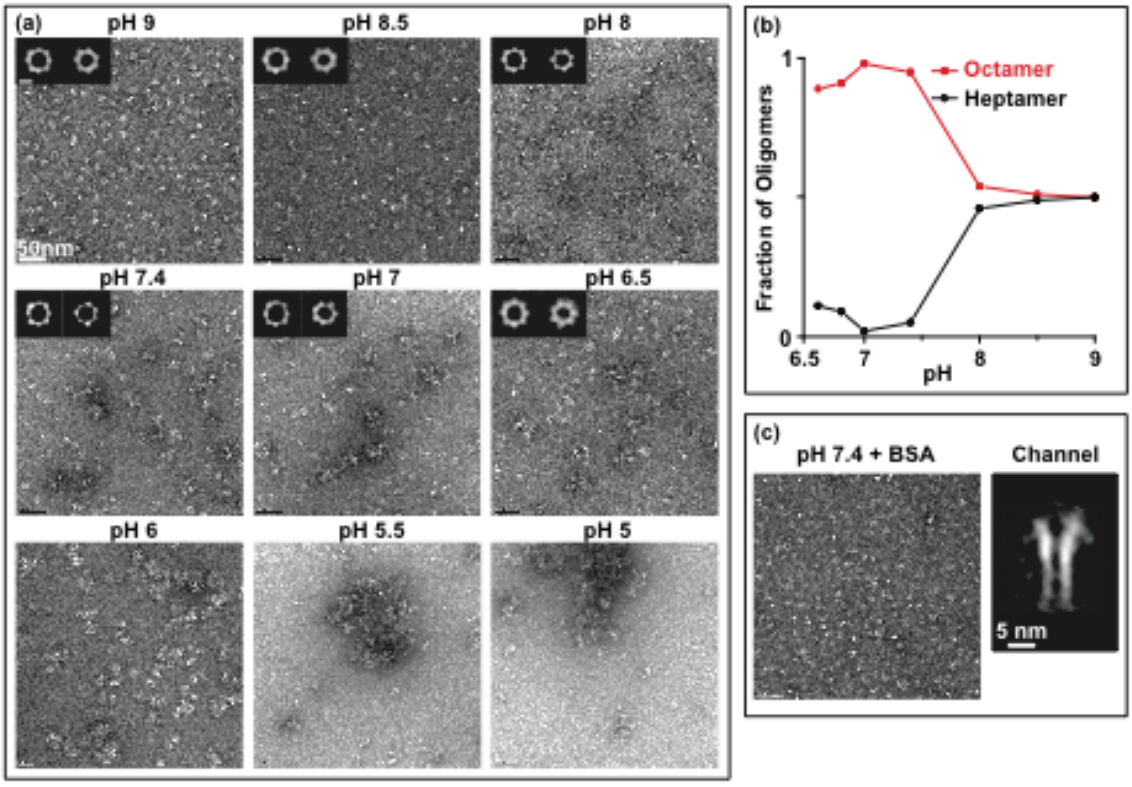

Figure 3.4. pH-dependent PA oligomer aggregation coincides with a decrease in the proportion of soluble PA_7 complexes. (a) Electron micrographs of negatively-stained heptameric and octameric $_nPA\text{-}LF_N$ complexes following a five-minute, 37-˚C incubation at the specified pHs. Class-average images containing 50-150 particles of PA_7 and PA_8 complexes are shown in the top left corner of each micrograph. The white scale bar in the inset is 5 nm. The final percentages and specific particle counts are reported in Table 3.1. Class-average images were not obtained at pH 6, 5.5 and 5 due to extreme aggregation. **(b)** A plot of the fraction of soluble PA_7 (black) and PA_8 (red) complexes versus pH resulting from the analysis shown in panel (a). **(c)** $PA\text{-}LF_N$ complexes were incubated for 5 minutes at pH 7.4, as above, except 10% BSA was also included in the incubation. (left) Distinct, isolated particles with elongated structures were obtained alongside particles consistent with axial views of the PA_7 and PA_8 prechannel. The scale in this micrograph is the same as in panel (a). (right) A class-average image representing 49 elongated particles (dimensions of 15 × 5 nm) in the micrograph. This image is consistent with a sagittal section of the PA channel conformation.(Katayama et al., 2008)

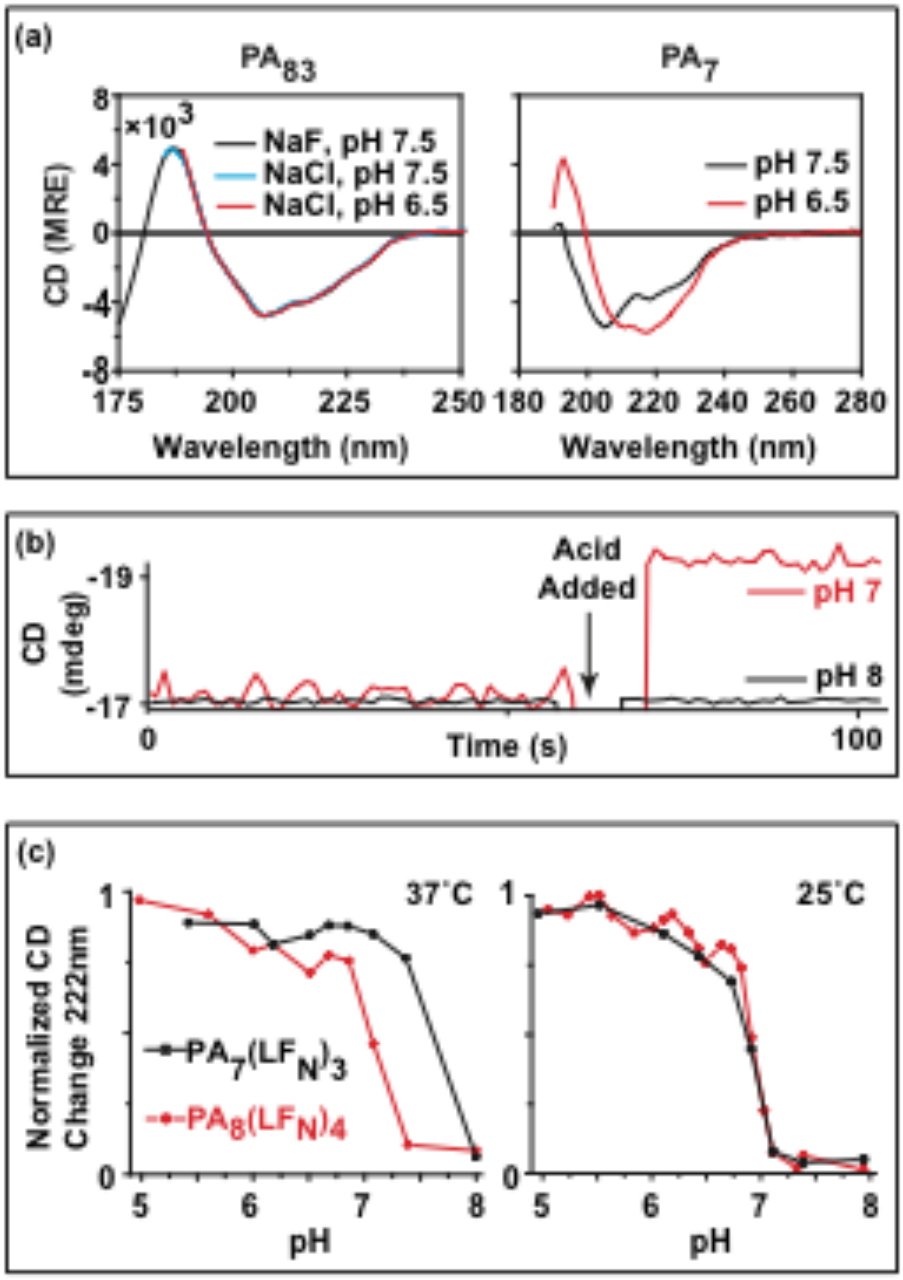

Figure 3.5. pH-dependent changes in the circular dichroism spectra of PA oligomers. (a) SRCD spectra of (left) the PA_{83} monomer and (right) the PA heptamer at pH 7.5 (black) and pH 6.5 (red). **(b)** Time-course records of CD signal at 222 nm (CD_{222}) after an acid pulse to pH 7 (red trace) and control (no pH pulse, pH 8.0 final, black trace) are shown. **(c)** The pH-dependence of the CD_{222}-signal change for $PA_7(LF_N)_3$ and $PA_8(LF_N)_4$ complexes at (left) 37 ˚C and (right) 25 ˚C. Traces were normalized to the initial and final CD_{222} signals obtained.

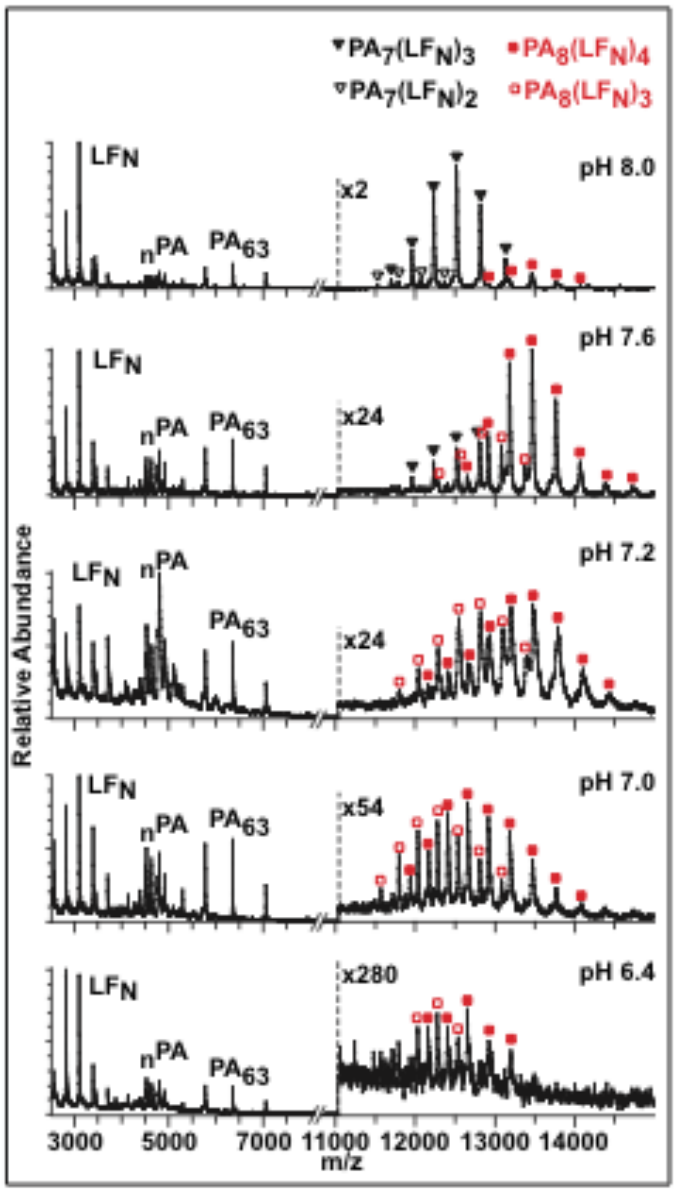

Figure 3.6. Mass spectrometry analysis of pH-dependent changes in the populations and conformations of PA oligomers. $_{n}$PA-LF$_{N}$ complexes were diluted into ammonium acetate buffered solutions (pH 8-6). Mass spectra of the PA-LF$_{N}$ complexes were taken as the sample was sprayed from an electrospray microcapillary that was heated to 37 ˚C. The PA$_{63}$ monomer charge state distribution in the mass spectra is the product of gas-phase dissociation of $_{n}$PA into its two constituent noncovalently bound subunits in regions of the instrument preceding the time-of-flight analyzer. Fully and partially saturated PA$_{7}$(LF$_{N}$)$_{3}$, PA$_{7}$(LF$_{N}$)$_{2}$, and PA$_{8}$(LF$_{N}$)$_{4}$ complexes are observed at pH 8. Heptamer signal rapidly degrades below pH 8.0, leaving predominately signal for PA$_{8}$(LF$_{N}$)$_{4}$ and PA$_{8}$(LF$_{N}$)$_{3}$ complexes from pH 7.6-6.4. PA$_{8}$(LF$_{N}$)$_{4}$ and PA$_{8}$(LF$_{N}$)$_{3}$ complexes transition to a distinct, higher charge-state distribution at pH 7.0, likely indicative of a structural transition to the channel state. See Table 3.2 for the specific charge-state values obtained for each species at each pH.

PA_7 complexes aggregate more readily than PA_8 complexes in bovine plasma. The prior experiment suggests that heptamers may aggregate at pH 7.3, causing the measured shift in the composition of the oligomers. To further test this notion, we challenged pre-assembled PA complexes in plasma at pH 7.3 and 8.0. Our pre-assembled complexes (called His_{6}-$_{n}$PA-LF_N) were 78% PA_7 and 22% PA_8 (Table 3.1). We then incubated this His_{6}-$_{n}$PA+LF_N mixture for 5 minutes at 37 ˚C in defibrinated bovine plasma, adjusted to either pH 7.3 or pH 8.0. At pH 8.0, we found that PA_7 complexes were the predominant form (Figure 3.1c), consistent with the previous assembly experiment (Figure 3.1b). However, at pH 7.3, PA_8 was the predominant species among the soluble complexes (Figure 3.1c). Large aggregates were also observed more frequently under the lower pH condition. We conclude that PA_8 is better able to resist aggregation than PA_7 in bovine plasma under physiological pH and temperature conditions (pH 7.3, 37 ˚C).

The stability of LT's cytotoxicity activity depends upon PA's oligomerization state. We next examined the stability of LT's macrophage cytotoxicity activity, using purified heptameric (PA_7LF_3) and octameric (PA_8LF_4) LT. Our enriched PA_7LF_3 sample contained 98% PA_7 and 2% PA_8, and our enriched PA_8LF_4 sample contained 69% PA_8 and 31% PA_7 (Table 3.1). Immortalized bone-marrow macrophages were then incubated with increasing amounts of PA (0.01-100 μg/mL) and constant LF (1 μg/mL) and assayed for lytic activity. $PA_7(LF)_3$, $PA_8(LF)_4$, and mixtures of the unassembled monomers (LF plus PA_{83}) all possess similar macrophage cytotoxicity activity (Figure 3.2a).

However, when these LT complexes were challenged at 37 ˚C in either pH-7.3 buffer or pH-7.3 defibrinated bovine plasma, their cytotoxicity changed markedly. For $PA_7(LF)_3$ complexes, the challenge incubation caused an ~10-fold loss of cytotoxicity with a half-life of ~2 minutes (Figure 3.2b, c). However, $PA_8(LF)_4$ complexes exhibited a significantly longer half-life, losing ~10-fold of their activity with ~12- and ~45-minute half-lives for buffer alone and buffered bovine plasma, respectively (Figure 3.2b, c). We also found that PA_7LF_3 complexes were as susceptible to inactivation when incubated in either 10% BSA, bovine plasma or buffer alone (Figure 3.11). The activities of monomeric PA and LF were not affected by incubation under these conditions. Interestingly, when PA_7LF_3 was incubated in bovine plasma at 42 ºC, it lost 1000-fold of its activity with a 10-minute half-life (Figure 3.2c); but under identical conditions, $PA_8(LF)_4$ only lost 10-fold of its activity with a 10-minute half-life (Figure 3.2c). We conclude that $PA_8(LF)_4$ complexes have a more thermostable and robust macrophage cytolysis activity than $PA_7(LF)_3$ complexes.

The stability of PA's channel-forming activity depends on its oligomerization state. We then asked how well $PA_7(LF_N)_3$ and $PA_8(LF_N)_4$ complexes insert into planar lipid bilayers (PLB) following a challenge at 37 ˚C, pH 7.4. Steady-state current levels were recorded for $PA_7(LF_N)_3$ or $PA_8(LF_N)_4$ complexes before and after a timed incubation at 37 ˚C, pH 7.4. The normalized fraction of inserted channels, *f*, was determined for each type of oligomer by measuring the ratio of steady-steady currents obtained from incubated and non-incubated samples (Figure 3.3a). The ratio of octamer to heptamer insertion efficiency (f_{PA8}/f_{PA7}) is plotted in Figure 3.3b. Within the first few minutes of incubation, the PA_7 complexes lost their ability to insert, but the PA_8 complexes remained active (Figure 3.3b). Overall PA_8 complexes exhibited ~15-fold greater insertion efficiency than their PA_7 counterparts (Figure 3.3b). We assume that this experiment underestimates the difference in the stability of the channel-forming activity, since the PA_7 and PA_8 samples are not 100% pure. We conclude that the PA_7 complexes are rapidly inactivated

under physiological conditions, while PA_8 complexes maintain a consistent level of channel-insertion activity even following an extended incubation at 37 °C, pH 7.4.

BSA and LF_N augment PA channel-forming activity. We then asked whether the observed losses in PA insertion activity could be preserved by the including 10% BSA in the incubation reaction (Figure 3.12a). When 10% BSA was included in the incubation, the insertion rate actually slowed by a factor of two (Figure 3.12a). The specific insertion activity, however, increased by a factor of two. We also found that PA insertion activity was augmented ~2-fold for $PA_7(LF_N)_3$ co-complexes relative to unliganded PA_7 complexes (Figure 3.12b). Therefore, PA channel insertion activity is stabilized when liganded with either specific or non-specific binding partners.

EM analysis of PA_7 and PA_8 complexes as a function of pH. Previously, we found that as soluble PA_7 complexes were depleted from mixtures of PA oligomers, large aggregates appeared. Here we examined, in finer detail, the pH dependence of the correlated disappearance of the two different PA oligomers and appearance of the aggregates. Purified $_nPA\text{-}LF_N$ complexes (containing a roughly 2:1 mixture of PA_7 and PA_8 complexes) were incubated at 37 ˚C for 5 minutes across a range of pHs, and then the complexes were imaged by negative-stain EM (Figure 3.4a). Aggregates first appeared at pH 7.4; and these aggregates increased in size until large precipitates were observed below pH 6.5. Free, resolvable PA prechannel complexes were selected at each pH (down to pH 6.5, which was the lowest pH individual complexes could be indentified). We generated class-average images of the PA_7 and PA_8 complexes at each pH (Figure 3.4a). A plot of the relative fraction of PA_7 and PA_8 complexes versus pH reveals a steep, sigmoidal relationship with a pH midpoint of 7.7 (Figure 3.4b). By pH 7.4, only trace levels of PA_7 complexes were observed, and >90% of the remaining particles were PA_8 complexes (Table 3.1). We also measured the average number of soluble PA_8 and PA_7 complexes per micrograph (Figure 3.13). The average number of PA_8 and PA_7 complexes was consistent from pH 9.0 to pH 8.0; however, a steep transition occurred below pH 8.0, corresponding to an abrupt decrease in the number of PA_7 complexes per micrograph (Figure 3.13). The number of complexes was relatively constant from pH 7.4 to 6.5, as was their composition, which was >90% PA_8 (Figure 3.4b). Starting at pH 6.5, we found, however, that the number of soluble PA_8 complexes began to decrease, reaching undetectable levels, when the pH was less than 6.0 (Figure 3.4b, 3.13).

Does the observed pH-dependent aggregation of $PA\text{-}LF_N$ complexes result from PA prematurely adopting the channel state? PA channels are discernable by EM,(Katayama et al., 2008) and we found that even at pH 9, similar elongated structures, corresponding to the PA channel state appeared in our EM micrographs, albeit they were observed infrequently (Figure 3.4a). To better image PA channels, we found that the addition of 10% BSA minimized their aggregation (Figure 3.4c) and improved our identification of mono-dispersed channel-shaped particles. These solution conditions revealed similar proportions of soluble octameric and heptameric prechannels when compared with samples prepared in the absence of BSA (Table 3.1; Figure 3.4c). Interestingly, we found that our 2D-class-average images (Figure 3.4c) were consistent with previous images of heptameric channels (Katayama et al., 2008).

We then estimated the percentages of the oligomers that adopt the channel state under these conditions (pH 7.4, 37 °C, 10% BSA). First, we employed reference-free alignment, classification, and averaging to generate class-averages of the observed elongated channel particles and the axially-oriented rings. We identified four classes, consistent with PA_7 and PA_8 prechannels, elongated channel structures, and contracted PA_7 rings, comprising 11.3, 35.1, 6.1,

and 47.4% of the population, respectively. While it is assumed the elongated structure represents a sagittal section of the PA channel, we could not determine the precise subunit stoichiometries of these images. Using SPIDER (Frank et al., 1996), we instead analyzed the axial classes, which comprised 93.1% of the population, and we determined the centers of each subunit in the respective axial views of each oligomer class. From these values, we calculated the center of mass of the complex and the mean radius from each subunit to the center of the complex. For PA_7 and PA_8 prechannel complexes, we find that these mean radii are 33.7 (±0.8) Å and 39 (±1) Å, respectively. However, when the complexes were incubated at 37 °C, pH 7.4, 10% BSA, the mean radii of the three different axially-oriented oligomer classes, (i) contracted PA_7, (ii) uncontracted PA_7, and (iii) PA_8, were 27 (±2) Å, 33 (±2) Å, and 39 (±2) Å, respectively. The mean-radius metric for the heptameric class, but not the octameric class, contracts significantly by 7 (±2) Å. The contraction of the PA_7 rings to 27 Å is consistent with the contraction observed for the heptameric channel state.(Katayama et al., 2008) Since the PA_8 rings do not contract, we do not assume that they form the channel state under these conditions. Of the total population of prechannel and channel states, PA_7 channels are observed 53.5% of the time; however, the channel classes we observe are predominantly heptameric. The 10% BSA additive modestly stabilizes the heptameric prechannel, since it represents approximately 10% of the sample, following the 5-minute, 37-°C incubation. Thus we conclude that PA_7 readily converts to the channel state at pH 7.4, 37 ˚C; and, while BSA minimizes aggregation, it does not prevent PA heptamers from converting to the channel state.

Probing PA channel conversion with circular dichroism (CD) spectroscopy. We then used CD spectroscopy to probe PA's structural transition to channel state. Upon lowering the pH from 7.5 to 6.5, the CD signal at 222 nm (CD_{222}) for PA_7 and PA_8 prechannels increased ~10-20% (Figure 3.5a, b, 3.14). The time dependence of this increase is rapid with respect to the drop in pH (occurring on a timescale of ~1 s). Control experiments on monomeric PA_{83} (Figure 3.5a) confirmed that the CD_{222} signal change is oligomer-specific, and we hypothesize that the CD_{222} signal change corresponds to the pH-dependent prechannel-to-channel transition.

To analyze the nature of the pH-dependent CD signal change, we obtained synchrotron radiation circular dichroism (SRCD) spectra at various pHs. SRCD, as opposed to conventional CD spectroscopy, enables for higher quality far UV CD measurements in the high salt conditions required, thereby facilitating the determination of more accurate secondary structure values. We found that NaF (the preferred salt in CD measurements) could be used during PA_{83} monomer measurements, but the F^- ion caused the PA_7 oligomer to precipitate, and consequently, we used NaCl in all PA oligomer measurements. SRCD spectra of PA_{83} and PA_7 were obtained at pH 7.5 and pH 6.5 (Figure 3.5a). The helix and sheet content deduced from the spectrum of PA_{83} was 9% and 37%, respectively, in close agreement with its crystal structure (Petosa et al., 1997). The spectrum also did not change as a function pH (7.5 or 6.5) or salt (NaF or NaCl). Analyses of the SRCD spectra of PA_7 samples at pH 7.5 and pH 6.5 indicated an increase in ordered secondary structure content, i.e., one with more helix and sheet. From the analysis, PA_7 at pH 7.5 is 17% helix, 25% sheet, and 33% loop or coil; and PA_7 at pH 6.5 is 22% helix, 27% sheet and 30% loop/coil. We conclude that coil/loop structures in the prechannel convert to sheet and helix structures in the channel.

To verify that the CD-detected increases in helix and sheet structure corresponded to the conversion of the prechannel to the channel state, we measured the pH dependence of the SRCD spectra of PA_7 in the presence of the extracellular, soluble domain from human anthrax receptor domain, sANTXR2 (Figure 3.15). The SRCD spectral change is only evident when the pH is

lowered to 5.5, consistent with previous studies.(Lacy, Wigelsworth, Melnyk et al., 2004) The pH-6.5 spectrum for sANTXR2-liganded heptamer is similar to that observed at pH 7.5, and thus the binding of sANTXR2 to PA shifted the pH dependence of the SRCD spectrum shift by approximately one unit (Figure 3.15). We conclude that the pH-dependent CD-signal change corresponds to the prechannel-to-channel transition.

We then compared the pH-dependent CD_{222} signal change for $PA_7(LF_N)_3$ and $PA_8(LF_N)_4$ complexes at 25 ˚C and 37 ˚C. The change in the CD_{222} signal occurred at distinct pH thresholds for $PA_7(LF_N)_3$ and $PA_8(LF_N)_4$ complexes (Figure 3.5c, 3.14). At 25 ˚C, both oligomers show a similar increase in CD_{222} signal at pH 7.0. However, at 37 ˚C, $PA_7(LF_N)_3$ complexes exhibit an increase in CD_{222} at pH 7.4, whereas $PA_8(LF_N)_4$ complexes show a similar increase in CD_{222} signal at pH 7.0 (Figure 3.5c). We conclude that $PA_8(LF_N)_4$ complexes are more pH-resistant to conversion to the channel state at 37 ˚C.

Mass spectrometry studies of pH-dependent changes in PA-LF_N complexes. We then used nanoelectrospray ionization mass spectrometry (nanoESI-MS) to monitor how pH affected the conformation, stability and solubility of PA_7 and PA_8 complexes. A 2:1 mixture of $PA_7(LF_N)_3$ and $PA_8(LF_N)_4$ complexes was diluted into buffers, ranging from pH 8.0 to 6.2. The mass spectrum acquired at pH 8.0 exhibits charge state distributions for LF_N, $_nPA$, and the complexes, $PA_7(LF_N)_2$, $PA_7(LF_N)_3$, and $PA_8(LF_N)_4$ (Figure 3.6). We also observed a 63-kDa species consistent with the mass expected for $_nPA$ monomer that has dissociated into free PA_{63} and free PA_{20} species. This 63-kDa species was determined to be produced by gas-phase dissociation of $_nPA$, consistent with a weak noncovalent interaction between PA_{63} and PA_{20}. The relatively low average charge for this ion (10.2+), compared to that for the $_nPA$ ion (17.8+), is the result of asymmetric charge partitioning (Jurchen, Garcia, & Williams, 2004; Jurchen & Williams, 2003). The spectrum is, however, dominated by signal for $PA_7(LF_N)_3$, where the remaining ~20% relative abundance corresponds to the $PA_8(LF_N)_4$ complex, which is partially obscured by overlap with peaks from the heptameric distribution. A partial complex, $PA_4(LF_N)_2$, was observed in all of the spectra at low abundances.

The spectrum acquired at pH 7.6 (Figure 3.6) exhibits the same monomer distributions with no significant change in the average charge states (Table 3.2). In contrast, there is a dramatic decrease in the relative abundance of $PA_7(LF_N)_3$ concomitant with a slight increase in the average charge (43.1+ to 43.4+); and the $PA_7(LF_N)_2$ complex is fully depleted. The relative abundance of $PA_8(LF_N)_4$ increases dramatically, but neither its absolute abundance nor its average charge changes significantly (46.6+ to 47.1+). A distribution of ions for $PA_8(LF_N)_3$ is observed, which may be due to loss of a single LF_N from $PA_8(LF_N)_4$ in solution or may be visible at this pH due to the loss of signal for the adjacent $PA_7(LF_N)_3$ distribution. The loss of signal for $PA_7(LF_N)_3$ at this pH and temperature (37 ºC) is consistent with results obtained by EM (Figure 3.4a,b, 3.13) and CD (Figure 3.5), likely corresponding to the prechannel-to-channel transition.

At pH 7.2, the observed average-charge states for the protein monomer's mass spectra do not change significantly (Figure 3.6, Table 3.2). The population of $PA_7(LF_N)_3$ is fully depleted while higher charge ions for $PA_8(LF_N)_3$ and $PA_8(LF_N)_4$ are observed, causing an increase in the average charge of the distributions to 47.9+ for both complexes (Table 3.2). The small decrease in the relative abundance of $PA_8(LF_N)_4$ may be due to the lower overall signal-to-noise ratio observed for all of the charge state distributions in this spectrum. Significantly, the charge state distributions for $PA_8(LF_N)_3$ and $PA_8(LF_N)_4$ increase from 47.9+ to 49.0+ and 50.1+, respectively, in the spectrum acquired from a pH-7.0 solution (Figure 3.6). This change is not observed for the monomer charge state distributions in this spectrum, where the average charge for LF_N is

unchanged (10.4+), $_n$PA increases from 17.6+ to 17.9+ (note that at pH 8.0, $_n$PA has an average charge of 17.8+), and PA_{63} increases from 10.3+ to 10.4+ (Table 3.2). In the spectra acquired with solutions at pH 6.8, 6.6, and 6.4, no significant changes were observed in the average charges of the monomer proteins or complexes (Table 3.2), while we observed a continual decrease in the signal-to-noise ratio of the complexes, but not the monomers. No signal was observed for the complexes in the pH-6.2 solution, while the monomers appeared unchanged (Table 3.2). Thus we conclude that the increase in average charge observed for octamer complexes represents either a soluble form of the PA_8 channel or a soluble intermediate formed as PA_8 prechannel converts to the channel state.

The heptamer, but not the octamer, produces detergent-resistant aggregates. We used the sodium-dodecylsulfate-(SDS)-resistance assay—an established method to detect PA channel formation (Miller et al., 1999)—to corroborate the pH/temperature dependencies of prechannel-to-channel conversion for the two different oligomers. In the SDS-resistance assay, $PA_7(LF_N)_3$ and $PA_8(LF_N)_4$ prechannel complexes were incubated for 1 hour at either room temperature or 37 ˚C in solutions buffered from pH 8 to 5. The SDS-treated samples were then separated by SDS-polyacrylamide gel electrophoresis (PAGE). The resulting gels showed two major bands: (i) the lower, higher-mobility band corresponds to the dissociated monomer, PA_{63}; and (ii) the upper, low-mobility band, is the SDS-resistant PA channel (Miller et al., 1999) (Figure 3.7). We reproduced the previous results, finding that incubating heptameric prechannel preparations at 25 ˚C causes an SDS-resistant PA channel band to appear when the pH $\leq$ 7 (Miller et al., 1999). However, when we repeated the experiment on the heptameric form at 37 ˚C, we found that the SDS-resistant band began to appear at higher pHs (pH $\leq$ 7.4; Figure 3.7a). We then tested the PA octamer, and found that it did not fully convert into an SDS-resistant species at 25 or 37 ˚C (Figure 3.7b). The residual, SDS-resistant band in $PA_8(LF_N)_4$ lanes likely corresponds to the 5-10% $PA_7(LF_N)_3$ contamination. We conclude that at 37 ºC, PA_7 converts to the SDS-resistant state at pH 7.4, while PA_8 does not.

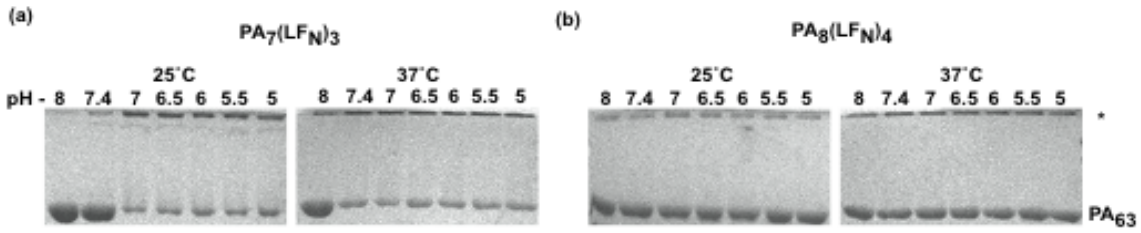

Figure 3.7. The pH dependence of the SDS-resistance of PA depends on its oligomeric state and the temperature. SDS-resistance assays(Miller et al., 1999) were performed on (a) $PA_7(LF_N)_3$ and (b) $PA_8(LF_N)_4$ complexes incubated in the indicated pH at either 25 ˚C or 37 ˚C. The two species of interest on the SDS-PAGE gels are indicated as either the high-molecular-weight, SDS-resistant PA oligomer band (*) or low-molecular-weight SDS-soluble, PA_{63} monomer band (PA_{63}).

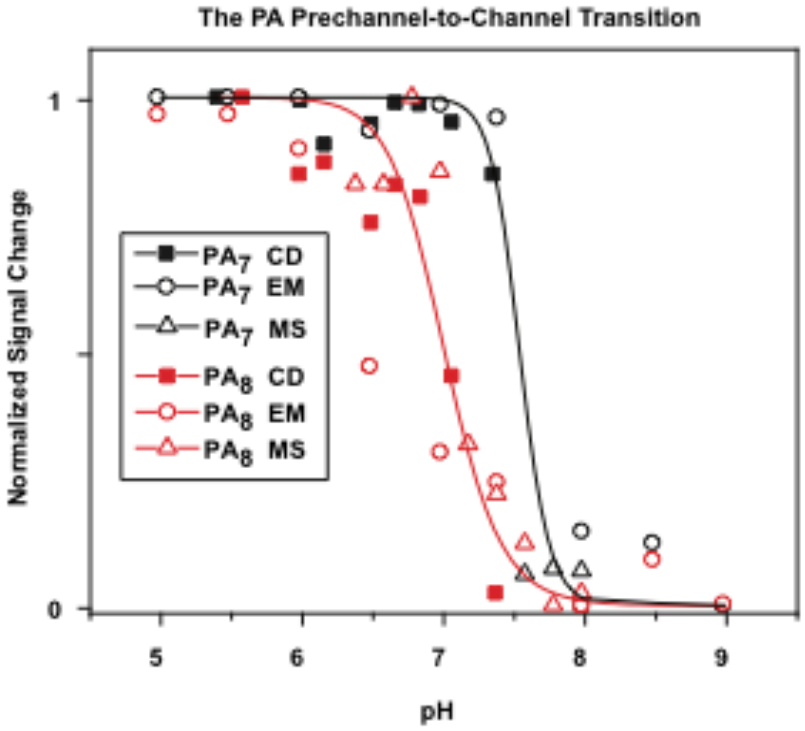

Figure 3.8. The pH dependence of PA channel formation depends on its oligomeric state. Multiple biophysical probes report on conformational changes observed in PA oligomers: $PA_7(LF_N)_3$ (black symbols) and $PA_8(LF_N)_4$ (red symbols). The circular dichroism (CD) probe (□) is the observed pH-dependent increase in the CD_{222} signal. The electron microscopy (EM) probe (○) is the pH-dependent change in average number of respective PA oligomers per micrograph (which is due to the loss of PA complexes upon channel formation and aggregation). The mass spectrometry (MS) probe (Δ) is the observed pH-dependent average charge-state increase for PA_8 complexes. Each dataset was normalized to the minimum and maximum values obtained for each signal. The solid-line sigmoid curves are meant to guide the eye; the estimated pH midpoints for the PA_7 and PA_8 curves are 7.5 and 7.0, respectively.

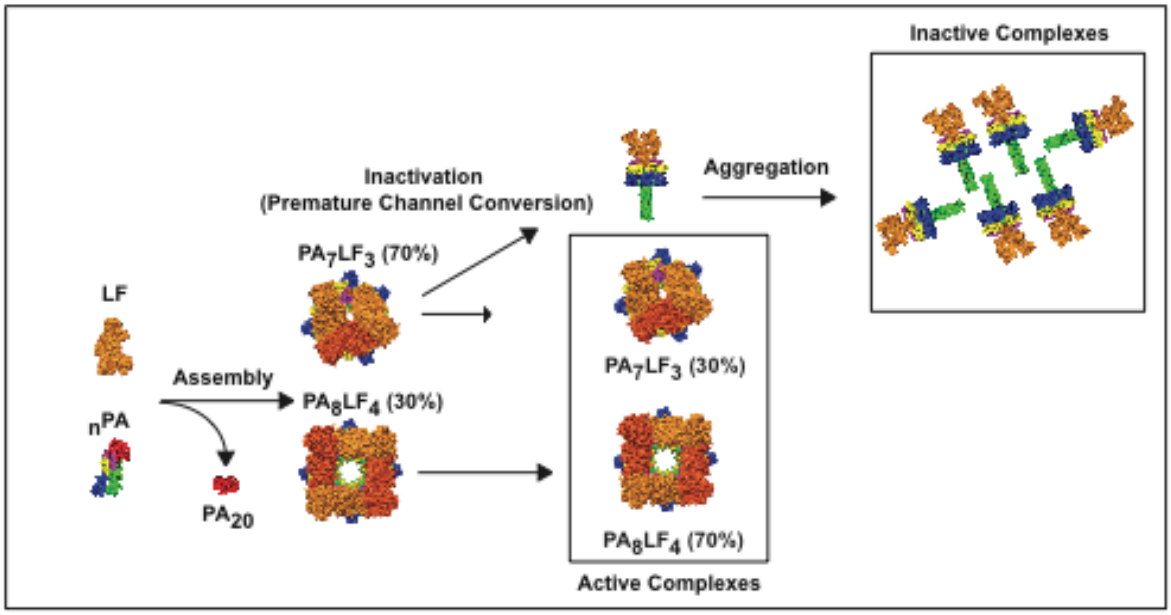

Figure 3.9. A model for anthrax toxin assembly. PA_{83} monomers are proteolytically activated in the bloodstream by a serum protease. The resulting $_nPA$ can assemble in the presence of LF to form heptameric and octameric LT complexes. Heptameric LT complexes are unstable, however, readily converting to the channel state under physiological temperature and pH. Inactivated heptameric channels subsequently form aggregates. Octameric LT complexes have a lower pH threshold for forming the channel state, and thus they are the predominant LT species in plasma. Models were made in CHIMERA (Pettersen et al., 2004c) using the PDB coordinates of LF (1J7N) (Pannifer et al., 2001), PA_{83} (1ACC) (Petosa et al., 1997), PA_7 (1TZO) (Lacy, Wigelsworth, Melnyk et al., 2004), and PA_8 (3HVD) (Kintzer et al., 2009), and unpublished coordinates of the $PA_8(LF_N)_4$ complex.

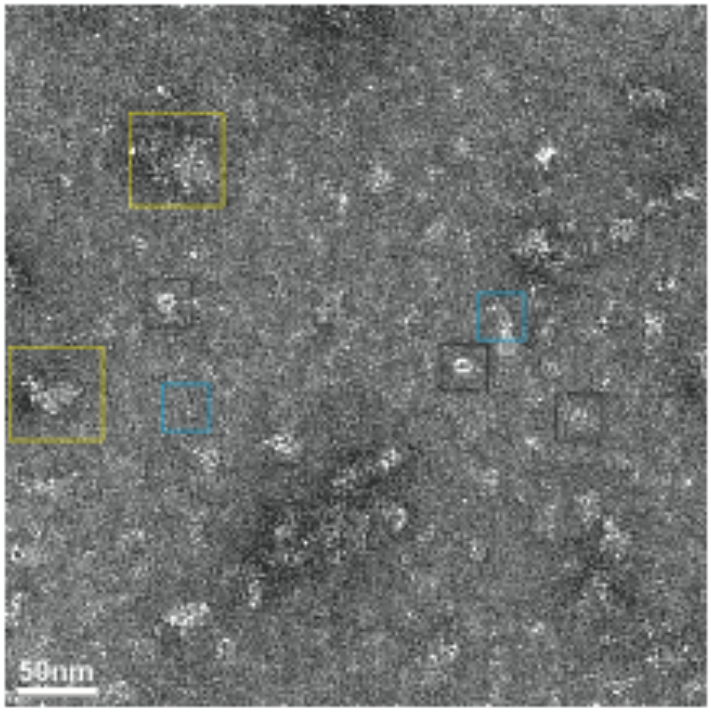

Figure 3.10. PA aggregates form in bovine plasma at pH 7.3. Electron micrograph of affinity-purified His_6-PA-LF_N complexes resulting from assembly in bovine plasma at pH 7.3, 37 ˚C. Soluble His_6-PA-LF_N prechannel complexes (black); aggregates of His_6-PA-LF_N complexes (yellow); and elongated, channel-shaped complexes (cyan) are outlined by boxes.

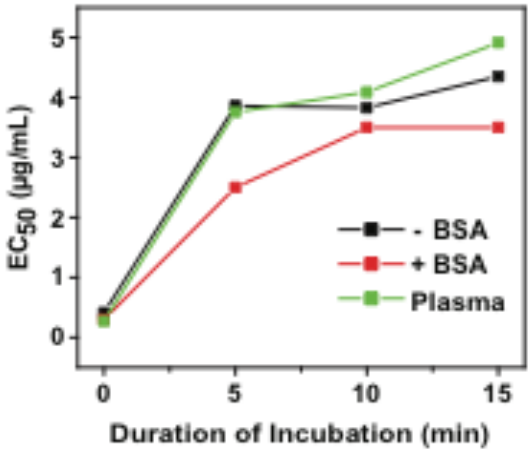

Figure 3.11. BSA does not stabilize PA_7LF_3 LT activity. Macrophage LT cytotoxicity assays were performed on PA_7LF_3 complexes, which were incubated in pH-7.3 buffer (black), pH-7.3 buffer containing 10% BSA (red), or pH-7.3 defibrinated bovine plasma (green) for the specified durations at 37 ˚C. Plots of the EC_{50} values versus the duration of the incubation at 37 ˚C are given.

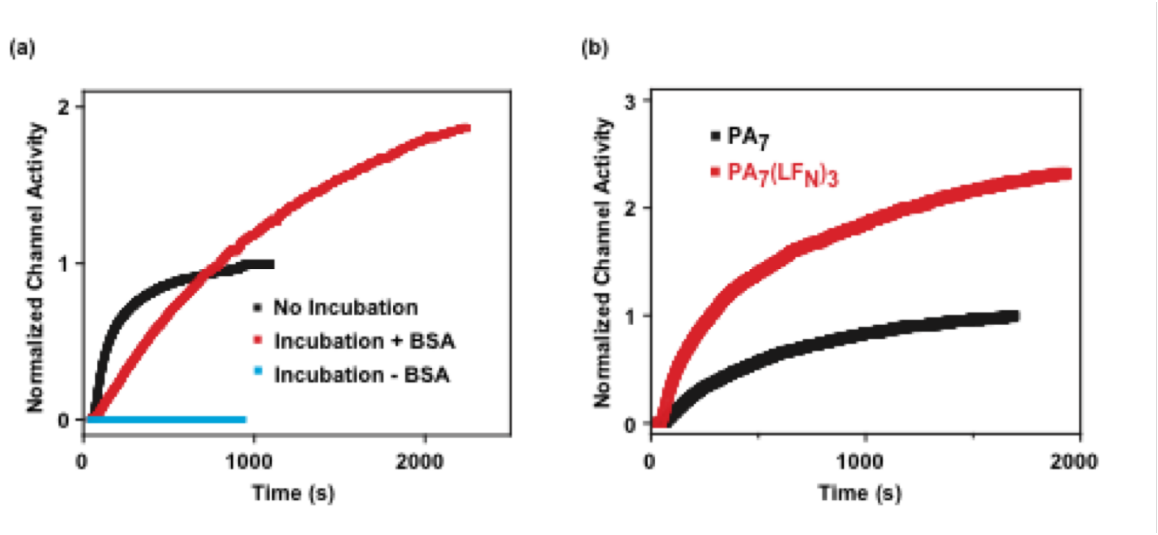

Figure 3.12. BSA and LF_N enhance PA_7 channel insertion activity. Electrophysiology studies of the PLB-insertion activity of PA_7 in the presence of LF_N and/or BSA. **(a)** Insertion of $PA_7(LF_N)_3$ complexes into PLBs was measured for samples that were incubated for 5 minutes in pH-7.4 buffer, at 37 ˚C, in the presence (red) and absence (cyan) of 10% BSA. A control record for a $PA_7(LF_N)_3$, which was not incubated at 37 ˚C is also shown (black). The current traces are the average of three records, which were normalized to the untreated PA complex (black trace). **(b)** The PLB-insertion activity of PA_7 and $PA_7(LF_N)_3$ complexes at pH 5.5. The current traces shown are the average result of three trials. The two records are normalized to the steady-state current for PA_7 complexes.

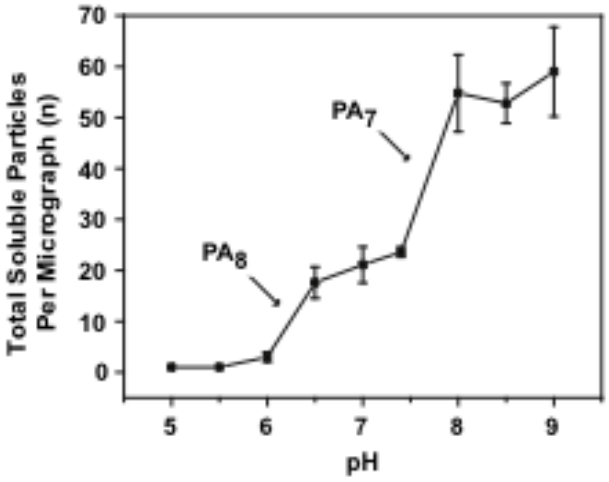

Figure 3.13. The number of soluble PA oligomers is pH-dependent. The average number of soluble $_nPA\text{-}LF_N$ prechannel complexes per EM micrograph was determined for samples after they were incubated for 5 minutes at 37 ˚C in the specified pH conditions. The average number, *n*, was computed from 10 micrographs per condition. Error bars are standard deviations from the average value. Arrows indicate where the prechannel-to-channel transitions occur for the PA_7 and PA_8 oligomer populations.

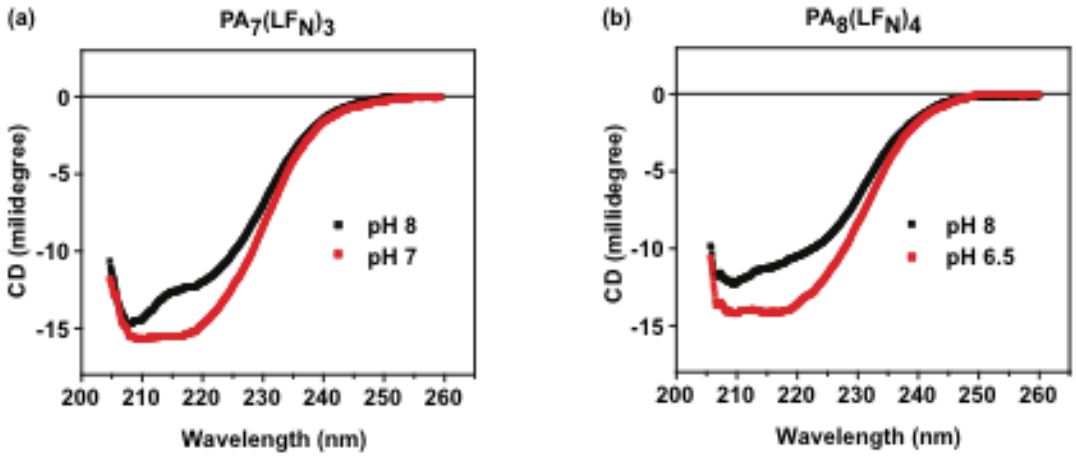

Figure 3.14. CD spectra of $PA_7(LF_N)_3$ and $PA_8(LF_N)_4$. CD spectra of $PA_7(LF_N)_3$ and $PA_8(LF_N)_4$ complexes at 25 ˚C. **(a)** CD spectra of $PA_7(LF_N)_3$ at pH 8 (black) and pH 7.0 (red). **(b)** CD spectra of $PA_8(LF_N)_4$ complexes at pH 8.0 (black) and pH 6.5 (red).

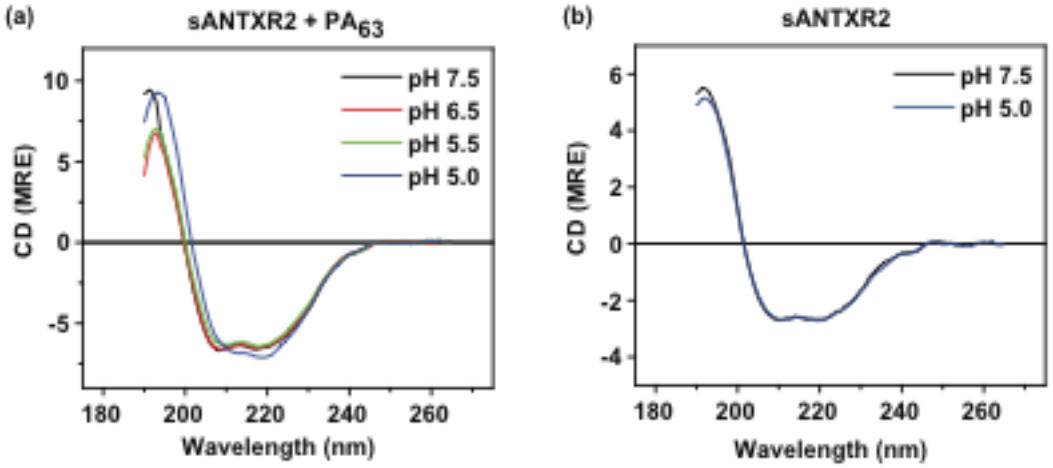

Figure 3.15. When PA_7 is bound to sANTXR2 the pH threshold for channel conversion shifts to lower pH. SRCD Spectra of PA_7-sANTXR2 and sANTXR2 at various pHs. **(a)** SRCD spectra of PA_7-sANTXR2 complexes at pH 7.5 (black), pH 6.5 (red), pH 5.5 (green), and pH 5.0 (blue). **(b)** CD spectra of sANTXR2 at pH 7.5 (black) and pH 5.0 (blue).

PA[3]	Ligand[4]	Sample preparation method[5]	Buffer[6]	pH	Total particles[7] (*n*)	PA_8 (%)	PA_7 Prechannel (%)	PA_7 Channel[8] (%)
His_6-PA	LF_N	assembly	plasma	8.0	1132	28	72	-
His_6-PA	LF_N	assembly	plasma	7.3	434	72	28	-
His_6-$_n$PA	LF_N	assembly	buffer	8.0	2572	26	74	-
His_6-$_n$PA	LF_N	incubation	plasma	8.0	861	38	62	-
His_6-$_n$PA	LF_N	incubation	plasma	7.3	300	69	31	-
$_n$PA	LF	incubation	buffer	7.0	922	69	31	-
$_n$PA	LF_N	incubation	buffer	9.0	476	50	50	-
$_n$PA	LF_N	incubation	buffer	8.5	564	51	49	-
$_n$PA	LF_N	incubation	buffer	8.0	1821	54	46	-
$_n$PA	LF_N	incubation	buffer	7.4	1428	98	2	-
$_n$PA	LF_N	incubation	buffer	7.0	1332	98	2	-
$_n$PA	LF_N	incubation	buffer	6.6	1248	89	11	-
$_n$PA	LF_N	incubation	buffer + 10% BSA	7.4	487	35	11	48 (6)

Table 3.1. Oligomeric composition[1] of various PA samples determined by negative-stain[2] EM. [1]Oligomeric composition (%) was determined using crystal-structure-referenced alignment and classification analysis. [2]Uranyl acetate stain, 2%. [3]The PA construct used to produce the sample. Nicked PA constructs ($_n$PA) were produced by a limited proteolysis with trypsin. His_6 constructs contain a carboxy-terminal His_6 tag to allow for affinity purification to isolate the PA complexes from the complex mixture of components found in plasma. [4]The ligand [either LF_N (LF residues 1-263) or full-length LF] used to assemble the PA complexes. [5]In an "incubation" experiment, a pre-assembled population of PA complexes (78% PA_7 and 22% PA_8) was incubated in the specified buffer and pH condition. In an "assembly" experiment, the PA construct and LF_N ligand were added to plasma, which contains sufficient proteolytic activity to activate PA and allow for assembly. All "incubation" and "assembly" samples were prepared at 37 ˚C. [6]The buffer condition: either "buffer," simple buffer; "plasma," defibrinated bovine plasma; or "buffer + 10% BSA," buffer supplemented with 10% BSA. [7]Total particles is the number of particles, *n*, used in the classification analyses to determine the percentages of each oligomer. [8]Percentages are reported for axial and sagittal views of the PA_7 channel in parentheses. Dashes indicate where analysis of channel particles was not performed. [9]Refers to the figure in the main text in which the sample is used.

	Average Charge (+)									
	pH 8.0	pH 7.8	pH 7.6	pH 7.4	pH 7.2	pH 7.0	pH 6.8	pH 6.6	pH 6.4	pH 6.2
LF_N	10.3	10.3	10.3	10.3	10.4	10.4	10.5	10.4	10.5	10.4
$_0PA$	17.8	17.4	17.6	17.6	17.6	17.9	18.0	17.8	17.9	17.9
PA_{63}	10.2	10.1	10.3	10.2	10.3	10.4	10.5	10.3	10.3	10.3
$PA_7(LF_N)_2$	42.1	42.2	--	--	--	--	--	--	--	--
$PA_7(LF_N)_3$	43.1	42.9	43.4	--	--	--	--	--	--	--
$PA_8(LF_N)_3$	--	--	46.8	47.3	47.9	49.0	49.6	48.7	49.5	--
$PA_8(LF_N)_4$	46.7	46.6	47.1	47.5	47.9	50.1	50.7	50.0	50.0	--

Table 3.2. Average charge[1] of PA-LF_N complexes and components as a function of pH.
[1]Average charge is measured using nanoESI-MS, and it is calculated as the weighted average of the background-subtracted intensity of each peak in a given charge-state distribution.

3.4 Discussion

Reports (Ross, 1957) on inhalational anthrax infections reveal that *B. anthracis* spores are first taken up by alveolar macrophage cells in the lungs; the spores are then transported by macrophage cells to lymph nodes in the mediastinum, where they germinate, allowing vegetative *B. anthracis* to ultimately disseminate into the blood. Blood is a complex mixture of plasma, immune cells, red blood cells, and platelets. The plasma fraction of blood is the liquid component, which constitutes more than half of the blood's total volume and consists mainly of water, electrolytes, and high concentrations of proteins, including albumins, immunoglobulins, proteases, and factors required for clotting. Here in this complex, crowded environment, *B. anthracis* secretes the three protein components that ultimately constitute anthrax lethal and edema toxins.

Analyses of blood taken from anthrax-afflicted animals in the latest stages of anthrax infection reveal a relatively high concentration of LT components and lower molecular weight γ-DPGA fragments (Mabry et al., 2006). The PA and LF components are at 80-100 μg/ml and 10-20 μg/ml concentrations, respectively (Mabry et al., 2006). Due to the presence of a serum protease, most of the PA is proteolytically-activated and potentiated for co-assembly with LF (Ezzell & Abshire, 1992b; Moayeri et al., 2007). These conditions suggest that LT complexes can assemble in lymph and plasma prior to reaching the cell surface, as we have demonstrated *in vitro* in bovine plasma (Kintzer et al., 2009). Studies of PA proteolysis and clearance in blood show that PA is rapidly cleared (Moayeri et al., 2007), implying that they have a finite lifetime and must endure the conditions encountered in the bloodstream long enough to reach cell surfaces. Of course, once PA complexes bind to their cell-surface receptors, they are stabilized and premature channel conversion is attenuated (Lacy, Wigelsworth, Melnyk et al., 2004). However, it is unknown how soluble forms of assembled LT, which are found in the blood, are stabilized. Here we report the thermostabilities and half-lives of LT complexes, which contain either the PA_7 or PA_8 oligomer. We propose that a critical mechanism for LT stabilization involves the ability of PA to assemble into the more stable octameric complex.

PA_8 is the preferred oligomerization state in bovine plasma. We have shown that PA_7 and PA_8 complexes form on cell surfaces in roughly a 2:1 ratio (Kintzer et al., 2009), however, the ratio of these two different PA oligomers in plasma is unknown. In bovine plasma at pH 7.3, we find that the PA_7:PA_8 ratio favors PA_8 30:70; but at pH 8, PA_7 is favored 70:30 (Figure 3.1b). The pH-dependent shift in favor of PA_8 may result from several possible mechanisms: (1) The assembly rate of octamers is faster at physiological temperature and pH; or (2) the two oligomers interconvert; or (3) the heptameric complexes are inactivated through a pH-dependent process. The first possibility is unlikely as mass spectrometry studies have shown that heptamers and octamers form at similar rates (Kintzer et al., 2009). The second possibility is also implausible as it has been found that oligomers do not readily exchange monomers (Christensen, Krantz, & Collier, 2006). The third possibility involving a pH-dependent inactivation of PA_7 complexes is more likely based upon our prior assembly results in buffer (Kintzer et al., 2009) and in plasma (Figure 3.1). This pH-dependent process manifests in the formation of large aggregates, containing inactivated PA complexes (Figure 3.10). Thus in plasma under physiological conditions (pH 7.3, 37 ºC), the octameric oligomerization state is the predominant form, because it is able to resist aggregation, unlike its heptameric counterpart (Figure 3.1, 3.10).

The stability of LT activity in bovine plasma. Previous reports suggest that LT complexes can form in the blood of infected animals (Ezzell et al., 2009; Fish & Lincoln, 1968a), and this in vivo form of the toxin is more potent than that isolated in vitro from *B. anthracis*

cultures (Fish & Lincoln, 1968a). Knowing that the toxin can form in two unique configurations, we tested their individual stabilities in macrophage cytotoxicity assays. In agreement with our EM analysis, we found that the macrophage cytotoxicity activity of PA_7LF_3 LT was rapidly inactivated following a brief, 5-minute incubation in plasma at 37 ˚C (Figure 3.2c). Conversely, PA_8LF_4 complexes have a longer lifetime in either pH-7.3 buffer or bovine plasma (Figure 3.2b, c). In buffer, PA_8LF_4 loses ~10-fold of its activity with a half-life of ~12 minutes [albeit this half-life was extended ~6 times longer than PA_7LF_3 under these conditions (Figure 3.2b, c)]. Interestingly, in bovine plasma, the lifetime of PA_8LF_4 complexes is significantly prolonged. Only ~10-fold of its activity is lost with a half-life of ~45 minutes (Figure 3.2c). Additionally, PA_8LF_4 LT complexes are even more resilient than PA_7LF_3 LT complexes at elevated, fever-like temperatures (42 °C). Since our most enriched samples of PA_8LF_4 contain ~30% PA_7LF_3 by EM (Table 3.1) and both PA_7LF_3 and PA_8LF_4 complexes have comparable LT activity prior to the challenge incubation (Figure 3.2a), the observed loss of PA_8LF_4 LT activity may be attributed to PA_7LF_3 contamination. Therefore, our results underestimate the relative thermostability of PA_8LF_4 complexes. Consistently, the incubation of $PA_7(LF_N)_3$ in pH-7.4 buffer causes a rapid decrease in its PLB-insertion activity (Figure 3.3a), but $PA_8(LF_N)_4$ complexes retain ~15-fold more PLB-insertion activity under identical conditions (Figure 3.3b). Therefore, PA_8 complexes maintain a more robust macrophage-lysis, channel-forming, and translocase activity than PA_7 complexes. We conclude that PA's octameric oligomerization state is a means to stabilize receptor-free LT complexes, allowing active LT complexes to circulate freely in the blood.

Premature channel formation is the molecular basis for heptameric LT inactivation. At physiological pH and temperature, PA complex aggregation (Figure 3.10) correlates with a rapid, irreversible loss of macrophage-cytotoxicity (Figure 3.2c) and PLB-insertion (Figure 3.3) activities. PA_8 complexes, however, are less susceptible than PA_7 complexes to inactivation under these conditions. What molecular mechanism best explains these differences? We found that elongated, channel-shaped structures were observed alongside aggregates in plasma samples (Figure 3.10), suggested that conversion to the channel state may facilitate aggregation and inactivation of PA_7 complexes (Figure 3.2c, 3). To corroborate this molecular mechanism, we measured the pH dependence of the prechannel-to-channel transition by several methods: EM (Figure 3.4b), CD and SRCD (Figure 3.5), SDS-resistance PAGE (Figure 3.7a), and mass spectrometry. The pH-dependency results of these various studies for the two different purified PA oligomers (Figure 3.6) suggest the following hypothesis: PA_7 converts to the channel state at pH 7.4, while PA_8 may only convert to the channel state at pHs ≤ 7 (Figure 3.8). We conclude that PA_8's decreased pH-sensitivity to channel formation may allow it to persist stably in plasma (Figure 3.9).

Insights into the mechanism of channel formation. PA channel formation is a pH-dependent process, likely involving the protonation of groups that drive the partial unfolding of certain regions of domain 2 in PA (Lacy, Wigelsworth, Melnyk et al., 2004; Miller et al., 1999; Nassi et al., 2002b). In this model, a large-scale rearrangement occurs, requiring the unfolding of the β1 and β4 strands and dissociation of the loops that interact with residues in domain 4 of the neighboring subunit (Lacy, Wigelsworth, Melnyk et al., 2004); β_2, β_3, and the membrane insertion loop then form the final β-barrel channel structure. By EM and crystallographic studies, the PA prechannel forms relatively compact heptameric and octameric rings with dimensions of 170 × 170 × 80 Å and 180 × 180 × 80 Å, respectively (Kintzer et al., 2009; Lacy, Wigelsworth, Melnyk et al., 2004). A recent EM structure of the heptameric channel suggested that the large

conformational change associated with the prechannel-to-channel transition produces an elongated structure with approximate dimensions of 50 × 50 × 170 Å (Katayama et al., 2008).

Here we further analyzed structural changes in PA-LF_N complexes using nanoESI-MS. Owing to the gentle nature with which biomolecules are transferred to the gas phase, nanoESI-MS permits structural analysis of intact proteins (Chowdhury, Katta, & Chait, 1990) and protein complexes (Dobo & Kaltashov, 2001; Konermann & Douglas, 1998; Siuzdak et al., 1996). By nanoESI-MS, the observed pH-dependent shift in average charge in the mass spectra of $PA_8(LF_N)_4$ complexes at pH 7 is consistent with the putative structural rearrangement proposed for the prechannel-to-channel transition (Figure 3.6, Table 3.2), which we have monitored using EM (Figure 3.4b) and CD (Figure 3.5c). Finally, we found that $PA_8(LF_N)_4$ may form a more soluble channel state, as its abundance did not decrease, as we observed with the $PA_7(LF_N)_3$ complex (Figure 3.6). Despite the change in average charge observed in MS experiments, the $PA_8(LF_N)_4$ complexes showed minimal loss of their LF_N ligands, demonstrating that these complexes remain intact when PA forms the channel state. The mechanism of channel formation has remained elusive, due to PA's propensity to form aggregates (Katayama et al., 2008; Vernier et al., 2009); however, PA_8 oligomers form more soluble channel complexes that may be amenable to future mechanistic and structural studies.

The large-scale rearrangement of secondary structure upon channel conversion likely corresponds to a net-increase in β-sheet content. SRCD measurements can calculate the change in secondary structure content of the prechannel and channel states by providing spectral information in the far UV wavelengths due to the increased brightness of the synchrotron light source. Detection of CD signal at these lower wavelengths is critical to assigning secondary structure content (Compton & Johnson, 1986; Provencher & Glockner, 1981; van Stokkum, Spoelder, Bloemendal, van Grondelle, & Groen, 1990). PA_7 complexes exhibited a pH-dependent increase in CD signal within the range 200-230 nm, which corresponded to increases in β (and surprising α) structure (Figure 3.5a). However, this signal change only occurs in the oligomer, as pH-dependent increases in CD signal were not observed for monomeric PA_{83}. The pH dependence of the CD signal change also shifted one pH unit in the presence of sANTXR2 (Figure 3.15), consistent with the known stabilization imparted by ANTXR binding (Lacy, Wigelsworth, Melnyk et al., 2004). Previous studies concluded that these CD signal changes indicated that the channel state has more α-helical content than the prechannel state (Vernier et al., 2009). We also observed a large change in CD signal at wavelengths below 200 nm, which also corresponded to a loss of disordered coil structure, upon acidification of the PA oligomer (Figure 3.5a). We conclude that the transition observed in the CD spectrum likely corresponds to omega loop/coil structures and disordered regions in the prechannel state (Kintzer et al., 2009; Lacy, Wigelsworth, Melnyk et al., 2004; Petosa et al., 1997), that refold into β barrel structures in the channel state (Katayama et al., 2008; Nassi et al., 2002b).

Specific and non-specific LT stabilization mechanisms. Atx components are secreted into a complex milieu of plasma components, including high concentrations of protein (~100 mg/ml), the most common of which are serum albumins. LT complexes have been shown to assemble in plasma (Kintzer et al., 2009), but the effect of plasma components on their stability has not been studied. It is known that crowed environments, containing high concentrations of a protein, such as BSA, can stabilize folded proteins and protein complexes, preventing the aggregation of their unfolded states by reducing the diffusional mobility of partially unfolded forms (Minton, 2000). Aggregation of the PA_7 channel was inhibited in the presence of BSA, resulting in discreet channel-shaped particles by EM (Figure 3.4c). Interestingly, BSA also

prevented losses in the PLB-insertion activity of pre-incubated PA-LF_N complexes (Figure 3.12a). The channel-insertion rate decreased by a factor of two, suggesting that reduced diffusional mobility may play a role in the stabilization mechanism. The formation of LT complexes may also prevent aggregation, as $PA_7(LF_N)_3$ complexes insert more efficiently into PLBs than non-liganded PA_7 (Figure 3.12b). This result indicates that fully assembled LT is more stable than partially assembled forms with substoichiometric loadings of LF. Perhaps BSA may stabilize partially unfolded PA intermediates that populate as PA converts to the channel state. The unfolding of PA's β-strands may expose surfaces, which BSA may bind, thereby impeding channel formation; however, it may also minimize PA inactivation and aggregation. The bacterial chaperone, GroEL, has been reported to bind PA channels in the D1' domain responsible for binding LF (Katayama et al., 2008). GroEL binding limited PA channel aggregation (Katayama et al., 2008), which is consistent with the observation that the inclusion of LF_N increases PA channel formation activity. Thus LF, BSA, and other protein components in blood may specifically or non-specifically block competing inactivation processes such as premature channel formation and aggregation, albeit these mechanisms of stabilization are modest relative to the gain in stability imparted by PA_8 formation.

LT stabilization during anthrax pathogenesis. Why would anthrax toxin preferentially assemble into the shorter-half-lived, heptameric form? We have proposed that PA_7 complexes may form on cell surfaces to expedite endocytosis of intact PA complexes, (Kintzer et al., 2009). Another rationale for the formation of the heptameric LT may be that it allows for spatial control of toxin levels. During the initial stages of anthrax infection, bacterial replication is localized to various organs,(Mabry et al., 2006) facilitating bacteremia (S. Welkos et al., 2001) and suppression of the immune system (Pezard et al., 1991; S. Welkos et al., 2001). LT components initially exist at low levels in the blood (Boyer et al., 2009). We postulate that Atx may act locally to compromise the host's immune system, while simultaneously limiting systemic damage to the host and premature death. Therefore, heptameric complexes may act nearest to its sites of secretion in regions of more intense bacterial infection. Active, heptameric complexes may only be able to travel limited distances from the sites of infection due to their attenuated half-lives in plasma (Figure 3.2c). Octameric complexes, on the other hand, persist for longer periods in plasma, allowing them to potentially impart cytotoxic effects further away from the sites of infection. Thus Atx may assemble into more stable and less stable forms of Atx to limit the highest intensities of cytotoxicity to regions immediately surrounding the sites of infection. Through this mechanism, zones of infection can be established and immune system function can be dampened without causing system-wide shock. The supply of the longer-half-lived octameric form will depend on the free concentrations of monomeric PA and LF. Indeed, at the terminal stages of an anthrax infection, high concentrations of LT, L-capsular γ-DPGA, and *B. anthracis* levels have been reported in the hours preceding death of the host. Thus as the infection intensifies, the stabilized form of the octameric toxin may then accumulate, inflicting more system-wide shock. Moreover, our results indicate that PA_7LF_3 complexes cannot persist under fever-like temperatures, but PA_8LF_4 complexes remain quite viable at elevated temperatures (Figure 3.2c). Thus PA_8LF_4 complexes may provide a means for Atx to endure the elevated temperatures associated with natural host-responses to *B. anthracis* infection ("Update: Investigation of bioterrorism-related anthrax and interim guidelines for clinical evaluation of persons with possible anthrax," 2001). Finally, while PA octamer formation may provide a molecular mechanism for Atx stabilization in plasma, our studies do not preclude other potential stabilization mechanisms, such as PA's interaction with albumins, other chaperones, and the

capsular material, γ-DPGA, which is also secreted by *B. anthracis* during infection (Ezzell et al., 2009).

3.5 Materials and Methods

Proteins. Recombinant WT PA_{83}, carboxy-terminally His_6-tagged PA_{83} (His_6-PA_{83}) (Sun et al., 2007), and all other PA mutants were over-expressed in the periplasm of the *E. coli* strain, BL21(DE3). The 83-kDa monomers were purified from the periplasm as previously described (Wigelsworth et al., 2004). Recombinant LF and LF_N (LF residues 1-263) were overexpressed from pET15b constructs (Lacy et al., 2002) and then purified from the cytosol as previously described (Wigelsworth et al., 2004) Soluble human anthrax receptor domain, sANTXR2, from the capillary morphogenesis protein 2, CMG2, was expressed, purified, and liberated of its affinity tag as previously described (Wigelsworth et al., 2004).

Isolation of PA_7 and PA_8 complexes. Heptameric PA-LF and PA-LF_N complexes were produced using Q-sepharose-purified PA oligomers (Kintzer et al., 2009) (which are >90% heptameric my EM) and then forming complexes with a two-fold stoichiometric excess of LF or LF_N (LF/LF_N:PA). The resulting complexes were purified by S400 gel filtration chromatography and judged >90% PA_7 by EM. PA_8LF_4 and $PA_8(LF_N)_4$ were prepared by assembling $_nPA$ in the presence of either LF or LF_N, respectively; the resulting complexes were incubated for 5 minutes at 37 ˚C in 0.1 M sodium cacodylate pH 7 at ~2 mg/mL PA concentration; and then the incubated mixture was purified on an S400 gel filtration column (Kintzer et al., 2009). The homogeneity of all samples were verified by EM and nanoESI-MS measurements as previously described (Kintzer et al., 2009). The PA-LF_N complexes were consistently ~90% PA_8 (Kintzer et al., 2009). The purified PA-LF complexes were ~70% PA_8 (Table 3.1). The overall yield of enriched PA_8-containing complexes was ~10% for PA-LF complexes and 20-30% for PA-LF_N complexes.

Purification of bovine-plasma-assembled PA complexes. Defibrinated bovine plasma (Rockland Immunochemicals, Inc.) was adjusted to pH 8.0 or pH 7.3 with 0.1 M Tris or 0.1 M Hepes, respectively. His_6-PA_{83} monomer and LF_N were mixed in a one-to-one molar ratio, at a final PA concentration of 100 μg/mL in defibrinated bovine plasma and incubated for 1 hour at 37 ˚C or 42 ˚C. After one hour, the assembled His_6-PA-LF_N complexes were mixed with 50 μL Ni^{2+}-NTA-sepharose affinity resin (GE Healthcare, Inc.) for one hour at room temperature. The resin was washed with fives volumes of Buffer M: 20 mM Tris, 0.15 M NaCl, 20 mM imidazole, pH 8, and eluted with one volume of Buffer M supplemented with 50 mM increments of imidazole to separate plasma proteins from PA-LF_N complexes, which eluted at ~150-200 mM imidazole. The purity of the eluted fractions was assessed by SDS-PAGE. The oligomeric composition was assessed by EM.

Electron microscopy. Aliquots of PA complexes were adjusted to 20-30 nM (with respect to the monomer concentration) by diluting in either Buffer E (20 mM Tris, 150 mM NaCl, pH 8) for PA-LF_N complexes or Buffer E + 0.01% dodecyl-β-D-maltopyranoside (Sigma-Aldrich, St. Louis, MO) for PA-LF complexes. The presence of the detergent allowed for imaging of predominantly axially-oriented LT complexes. 4 μl of sample was applied to a freshly glow-discharged 400 mesh formvar-carbon coated grid for 1 minute. The grid was then washed in 5 successive drops of water and stained for 1 minute with 2% uranyl acetate (Sigma-Aldrich, St. Louis, MO). Negative-stain EM images were recorded on a Tecnai 12 electron microscope (FEI Company, Hillsboro, OR) operated at 120 kV at a magnification of 49,000×

using a CCD camera. The micrograph resolution was 2.13 Å/pixel. Particle images were selected using automatic or manual particle picking using boxer in EMAN (Ludtke et al., 1999).
Reference images of 2D-projections of low resolution density maps generated from the crystal structures of the PA_7 (PDB 1TZO) (Lacy, Wigelsworth, Melnyk et al., 2004) and PA_8 (PDB 3HVD) (Kintzer et al., 2009) prechannel oligomers were produced using SPIDER (Frank et al., 1996). Boxed images of the PA oligomer particles were subjected to successive cycles of alignment, multivariate statistical analysis, and classification (Stark et al., 1995; van Heel et al., 1996). The last classification step was done using only the lowest order eigenvectors (White et al., 2004) to separate the data by size and the heptameric and octameric oligomerization states. Final class-average images, consisting of 20-30 classes, were manually inspected and tabulated to determine the oligomeric composition of each sample (Table 3.1). Ambiguous classes were omitted from the analysis.

Since a crystal structure reference is not available for the PA channel, we used reference-free alignment to initially generate 20-30 reference classes, of which 5-10 were used for subsequent rounds of alignment, classification, and averaging. This procedure was sufficient to separate prechannels from axial and sagittal views of the PA channel and allow the generation of class-averages.

LT macrophage cytotoxicity. LT cytotoxicity was monitored by an enzyme-coupled lactate dehydrogenase (LDH) release assay (Decker & Lohmann-Matthes, 1988a). Immortalized bone marrow macrophages from 129 mice (a gift from the Vance Lab at UC Berkeley) were grown to confluence in RPMI 1640 medium (Invitrogen, Inc.) supplemented with 10% fetal bovine serum (Invitrogen, Inc.), 100 units/mL penicillin (Sigma-Aldrich, St. Louis, MO), and 100 μg/mL streptomycin (Sigma-Aldrich, St. Louis, MO) in a humid, 5%-CO_2 atmosphere at 37 ˚C. One day prior to conducting assays, cells were trypsinized and re-plated at a density of 10^5 cells/well. Cells were treated with a constant amount of LF (1 μg/mL) and varying concentrations of either PA_{83} or oligomeric LT complexes (0.01-100 μg/mL) in ice-cold PBS. The toxin-treated cells were then incubated for 4 hours at 37 ˚C. Triplicate assays were performed for each condition. The cells were then centrifuged at 1400 RPM. The supernatant was removed and incubated with 20 μL of lactate solution (36 mg/mL in phosphate-buffered saline) and 20 μL of *p*-iodonitrotetrazolium chloride (2 mg/mL in phosphate-buffered saline with 10% dimethyl sulfoxide). The enzymatic reaction was started by the addition of 20 μL of nicotinamide adenine dinucleotide (NAD^+)/diaphorase solution (13.5 units/ml diaphorase and 3 mg/ml NAD^+). After a 15-minute incubation, the products were observed using an spectrophotometric microplate reader (Bio-Rad Laboratories, Richmond, CA) at a wavelength of 490 nm. The change in the absorbance signal is proportional to the number of lysed cells, where the amount of LDH released was normalized to the value obtained in wells treated with 1% Triton X-100 detergent. Effective-concentration-for-50%-lysis values (EC_{50}) were determined by fitting the normalized cell-lysis-versus-PA-concentration data in ORIGIN6.1 (OriginLab Corp., Northampton, MA). The stability of the LT complexes was assessed by measuring the EC_{50} values of the LT complexes after they were incubated at 37 ˚C or 42 ˚C for specified times in various buffer conditions.

Electrophysiology. Voltage-clamp electrophysiology experiments were performed using an Axoclamp 200B amplifier and AXOCLAMP acquisition software (Molecular Devices) as described (Kintzer et al., 2009). Data analyses were performed using CLAMPFIT (Molecular Devices) and ORIGIN6.1. Relative membrane insertion activities for PA were assayed as follows. A planar lipid bilayer (PLB) was painted using a 3% solution of the lipid [1,2-

diphytanoyl-*sn*-glycerol-3-phosphocholine (DPhPC; Avanti Polar Lipids, Alabaster, AL) dissolved in *n*-decane] inside either a 100-μm aperture of a 1-mL, white delrin cup bathed in universal bilayer buffer (UBB) (10 mM oxalic acid, 10 mM MES, 10 mM phosphoric acid, 1 mM EDTA, 100 mM KCl) at pH 5.5 or 6.6. PA oligomer complexes (0.1 nM) were added to the cis compartment, which was held at a membrane potential ($\Delta\psi$) of +20 mV and a proton gradient (ΔpH) of 1 unit. ($\Delta\psi \equiv \Delta\psi_{cis} - \psi_{trans}$, where $\psi_{trans} \equiv 0$ mV; $\Delta pH \equiv pH_{cis} - pH_{trans}$, where $pH_{cis} = 5.6$ and $pH_{trans} = 6.6$.) Channel insertion increased over a period of minutes and stabilized after 20 to 30 minutes, allowing the final current to be recorded.

The PLB-insertion activity of PA or PA-LF_N complexes was assessed before and after incubation at 37 ˚C in 0.1 M sodium cacodylate (Sigma-Aldrich, St. Louis, MO), pH 7.4. PA or PA-LF_N complexes were added to the cis compartment to a final concentration of 0.1 nM. Channel insertion activity was then reported by the current obtained per mole of PA complex. The activity for each sample was measured, and the fraction of inserted channels (*f*) was calculated. We define *f* as the ratio of the current obtained from a sample after 37-˚C incubation to the current obtained from the sample before the incubation. In a separate case, where the insertion efficiencies of PA_7 and $PA_7(LF_N)_3$ complexes were compared, the insertion efficiency was normalized relative to the insertion activity of unliganded PA_7 complexes.

Circular dichroism (CD) spectroscopy. CD measurements of the PA channel transition were obtained on a JASCO Model 810 spectropolarimeter (JASCO, Inc., Easton, MD). Triplicate-averaged scans were collected over the wavelength range from 260 to 190 nm at 1-nm increments. In time course experiments, the CD signal at 222 nm was recorded at a 1-Hz sampling rate. To determine the pH dependence of the prechannel-to-channel transition, samples were diluted to 50 nM in 2 mL of buffer (10 mM potassium phosphate, 10 mM potassium acetate, 0.1 M potassium chloride, pH 8), in a 1 cm quartz cuvette containing a Teflon stir bar, at 25 ˚C or 37 ˚C. The prechannel-to-channel transition of PA-LF_N complexes was observed as a nearly instantaneous change in CD at 222 nm (CD_{222}) upon changing the pH of the buffer by addition of aliquots of 0.4 M phosphoric acid.

Synchrotron radiation circular dichroism (SRCD) spectroscopy. Synchrotron radiation CD (SRCD) experiments were performed on beamline UV1 at the Institute for Storage (ISA) Ring Facilities, University of Aarhus, Denmark. SRCD spectra of WT PA_{83} monomer were obtained at a protein concentration of 1.4 mg/ml using a 0.005 cm pathlength, cylindrical Suprasil (Hellma) cuvette at 20 ˚C. Spectra were recorded using the following buffers: 20 mM sodium phosphate, 150 mM sodium chloride, pH 7.5; 20 mM sodium phosphate, 150 mM sodium chloride, pH 6.5; or 20 mM sodium phosphate, 150 mM sodium fluoride, pH 7.5. Data were collected over a wavelength range of 260 to 175 nm at intervals of 1 nm; 10 scans of the sample and the baseline (consisting of the buffer alone) were averaged, subtracted and smooth with a Savitsky-Golay filter using CDTOOLS (Lees, Smith, Wien, Miles, & Wallace, 2004). Secondary structure analyses used the CONTINLL (Provencher & Glockner, 1981; van Stokkum et al., 1990) and CDDSTR (Compton & Johnson, 1986) algorithms available on DICHROWEB server (Lobley, Whitmore, & Wallace, 2002) with reference dataset SP175 (Lees, Miles, Wien, & Wallace, 2006).

SRCD spectra of WT PA_7, ANTXR2, and WT PA_7-sANTXR2 complexes were obtained as above in buffer (20 mM sodium phosphate pH 7.5, 100 mM sodium fluoride, 1 mM magnesium sulfate) All reductions in pH were made just prior to measurement using small volumes of 1 M phosphoric acid (< 1% of the total volume). The protein concentrations were 0.19 mg/ml (monomer concentration) for the PA_7 oligomer, 0.095 mg/ml PA_7 oligomer plus

0.045mg/ml sANTXR2 (an 11-fold molar excess), and 0.08 mg/ml for sANTXR2 alone. All protein concentrations were determined using duplicate quantitative amino acid analyses. Spectra for PA_7 oligomer alone, PA_7 oligomer plus sANTXR2, and sANTXR2 alone were obtained using a 0.05-cm-, 0.1-cm-, and 0.1-cm-pathlength cells as above, respectively.

Mass spectrometry. Mass spectra were acquired using a quadrupole time-of-flight (Q-TOF) mass spectrometer equipped with a Z-spray ion source (Q-Tof Premier, Waters, Milford, MA). Ions were formed using nanoelectrospray (nano-ESI) emitters prepared by pulling borosilicate capillaries (1.0 mm O.D./0.78 mm I.D., Sutter Instruments, Novato CA) to a tip I.D. of ~1 μm with a Flaming/Brown micropipette puller (Model P-87, Sutter). The instrument was calibrated with CsI clusters formed by nano-ESI using a 20 mg/mL solution of CsI in 70:30 Milli-Q water:isopropanol prior to mass measurement. The protein solutions were prepared by mixing 10 mM ammonium bicarbonate solutions (pH 7.8) of purified $_nPA$ and LF_N, allowing the oligomers to assemble at room temperature for one hour. Immediately prior to mass analysis, an aliquot of the solution containing the complexes was diluted 1:4 into 200 mM ammonium acetate solutions at pH 6.2-8.0. A platinum wire (0.127 mm diameter, Sigma, St. Louis, MO) was inserted through the capillary into the solution and electrospray was initiated and maintained by applying 1-1.3 kV to the wire relative to instrument ground. The nano-ESI capillaries were resistively heated to 37 ˚C by a NiCr-wire-wrapped aluminum collar (Sterling & Williams, 2009). Raw data were smoothed three times using the Waters MassLynx software mean smoothing algorithm with a 40-unit window. Average charge states for ion populations were calculated as an intensity-weighted average of each charge state in a given distribution.

SDS-resistance PAGE analysis. SDS-resistance assays (Miller et al., 1999) were performed on purified $PA_7(LF_N)_3$ and $PA_8(LF_N)_4$ complexes. Complexes were diluted to 1 mg/ml final concentration (with respect to PA) in the following buffers, which vary depending upon the pH: 0.1 M Tris-Cl (pH 8.0), sodium cacodylate (pH 6.5 to 7.5), 0.1 M 2-(*N*-morpholino)ethanesulfonic acid (pH 6.0), and sodium acetate (pH 5.0 to 5.5). The complexes were incubated for 1 hour. 1.25% SDS then was added, and the samples were run on a 12% polyacrylamide gel, which was stained in coomassie brilliant blue G-250.

Chapter 4

Anthrax toxin receptor drives protective antigen oligomerization and stabilizes the heptameric and octameric oligomer by a similar mechanism

4.1 Abstract

Anthrax toxin is comprised of protective antigen (PA), lethal factor (LF), and edema factor (EF). These proteins are individually nontoxic; however, when PA assembles with LF and EF, it produces lethal toxin and edema toxin, respectively. Assembly occurs either on cell surfaces or in plasma. In each milieu, PA assembles into a mixture of heptameric and octameric complexes that bind LF and EF. While octameric PA is the predominant form identified in plasma under physiological conditions (pH 7.4, 37 °C), heptameric PA is more prevalent on cell surfaces. The difference between these two environments is that the anthrax toxin receptor (ANTXR) binds to PA on cell surfaces. It is known that the extracellular ANTXR domain serves to stabilize toxin complexes containing the PA heptamer by preventing premature PA channel formation—a process that inactivates the toxin. The role of ANTXR in PA oligomerization and in the stabilization of toxin complexes containing octameric PA are not understood. Using a fluorescence assembly assay, we show that the extracellular ANTXR domain drives PA oligomerization. Moreover, a dimeric ANTXR construct increases the extent of and accelerates the rate of PA assembly relative to a monomeric ANTXR construct. Mass spectrometry analysis shows that heptameric and octameric PA oligomers bind a full stoichiometric complement of ANTXR domains. Electron microscopy and circular dichroism studies reveal that the two different PA oligomers are equally stabilized by ANTXR interactions. We propose that PA oligomerization is driven by dimeric ANTXR complexes on cell surfaces. Through their interaction with the ANTXR, toxin complexes containing heptameric and octameric PA oligomers are similarly stabilized. Considering both the relative instability of the PA heptamer and extracellular assembly pathway identified in plasma, we propose a means to regulate the development of toxin gradients around sites of infection during anthrax pathogenesis.

4.2 Introduction

Anthrax toxin (Atx) (J. A. Young & Collier, 2007) is a key virulence factor produced by pathogenic strains of *Bacillus anthracis*. Atx consists of three nontoxic protein components: protective antigen (PA) is an 83-kDa, cell-binding component of Atx that ultimately forms an oligomeric translocase channel, which delivers the two enzyme components, lethal factor (LF) and edema factor (EF), into the cytosol of a host cell (Beall et al., 1962; H Smith & Keppie, 1954; Stanley & Smith, 1961). LF is a 90-kDa, zinc-dependent protease (Duesbery & Vande Woude, 1999a; Duesbery et al., 1998; Pannifer et al., 2001), which cleaves host-cell mitogen-activated protein kinase kinases (Duesbery & Vande Woude, 1999a; Duesbery et al., 1998). While PA and LF are individually nontoxic, the combination of LF and PA creates lethal toxin (LT), which can alter cellular physiology and cause death (Pezard et al., 1991). EF is a 89-kDa, Ca^{2+}/calmodulin-activated adenylyl cyclase (Drum et al., 2002; Leppla, 1982, 1984). Analogously, PA and EF combine to form edema toxin (ET), which induces tissue swelling and may also cause death (Fish & Lincoln, 1968b; Pezard et al., 1991).

To achieve cytotoxicity, PA, LF, and EF must first self-assemble into holotoxin complexes. There are two different types of assembly pathways: (i) a cell-surface pathway and (ii) a plasma-based/extracellular pathway. In the former mechanism, PA forms complexes on the surface of host cells in a receptor-dependent manner. PA first binds to one of two known Atx receptors (ANTXR): ANTXR1 (Bradley et al., 2001) and ANTXR2 (Scobie et al., 2003). The PA-ANTXR interaction (Santelli et al., 2004) is stable and dissociates with a half-life measured in days (Wigelsworth et al., 2004); the interaction involves domains 2 and 4 in PA, such that the latter domain coordinates the receptor's Ca^{2+} or Mg^{2+} metal ion adhesion site (Lacy, Wigelsworth, Melnyk et al., 2004; Lacy, Wigelsworth, Scobie, Young, & Collier, 2004; Santelli et al., 2004; Wigelsworth et al., 2004). Receptor-bound PA is then cleaved by a furin-type protease to make the proteolytically-activated form, called $_{n}$PA. After a 20-kDa portion of $_{n}$PA (PA_{20}) dissociates, the remaining 63-kDa (PA_{63}), receptor-bound portion assembles into a mixture of ring-shaped heptameric (PA_7) (Lacy, Wigelsworth, Melnyk et al., 2004; Milne et al., 1994; Petosa et al., 1997) and octameric (PA_8) (Kintzer, Sterling et al., 2010a; Kintzer et al., 2009) oligomers. The complexes are endocytosed (Abrami et al., 2003) and brought to an acidic compartment (Friedlander, 1986). Under acidic pH conditions, the PA oligomers form translocase channels (Katayama et al., 2008; Miller et al., 1999), allowing the passage of LF and EF into the cytosol.

In a second assembly mechanism, PA, LF, and EF form LT and ET complexes in the blood. *In vivo* studies of anthrax infection measured high concentrations of toxin components in the blood of infected animals (H Smith & Keppie, 1954; Stanley & Smith, 1961). At the later stages of anthrax, PA and LF concentrations reach up to 100 μg/mL and 20 μg/mL, respectively (Mabry et al., 2006). Analysis of the circulating toxin components revealed that the majority of detectable PA exists as the proteolytically-processed PA_{63} form, which is either assembled or capable of assembling with LF in a manner analogous to what is observed on cell surfaces (Ezzell & Abshire, 1992a; Ezzell et al., 2009; Mabry et al., 2006). *In vitro* bovine-plasma assembly experiments reveal that PA oligomers and LT complexes may form efficiently from full-length PA and LF, where the resulting oligomers contain mixtures of PA_7 and PA_8 complexes (Kintzer, Sterling et al., 2010a; Kintzer et al., 2009). PA_7 complexes have a strong propensity for aggregation under physiological conditions (due to their premature conversion to the channel state), suggesting that the toxin requires additional stabilization mechanisms to remain efficacious during infection (Kintzer, Sterling et al., 2010a; Kintzer et al., 2009; Vernier et al., 2009). Since PA_8 complexes are more stable in plasma under physiological conditions (pH 7.4, 37 °C), it has been proposed (Kintzer, Sterling et al., 2010a) that the soluble fraction of LT circulating in bloodstream of infected animals (Ezzell & Abshire, 1992a) may contain an enriched population of the PA_8 oligomer.

While it is clear that PA_8 functions as a stable complex in plasma, it is unknown whether PA_7 and PA_8 complexes are stabilized differentially on cell surfaces. When the PA heptamer binds to its cellular receptor, ANTXR, the interaction inhibits channel formation, significantly stabilizing PA complexes by ~2 pH units (Lacy, Wigelsworth, Melnyk et al., 2004; Santelli et al., 2004). Previous studies have also shown that ANTXR2 dimerization leads to an increase in the formation of PA_8 in vitro, presumably by populating dimeric intermediates along the assembly pathway (Kintzer et al., 2009). Here we explore the role of the ANTXR in the PA assembly pathway and determine the degree of stabilization the receptor imparts on the two different PA oligomers produced during assembly.

4.3 Results

PA oligomerization is accelerated in the presence of ANTXR2 dimers. While ANTXR2 dimerization enhances the formation of PA_8 (Kintzer et al., 2009), it is not known whether the rate and extent of PA oligomerization are influenced by a dimeric ANTXR complex. A previous study indicates that LF's PA binding domain (LF_N, the first 263 residues of LF) can increase the rate of PA oligomerization, while msANTXR2 did not appear to influence assembly greatly (Wigelsworth et al., 2004). To ask whether ANTXR2 dimerization affects the rate of PA oligomerization, we produced a dimeric ANTXR2 construct (dsANTXR2), which is an amino-terminal fusion of glutathione S-transferase (GST) and the extracellular domain of ANTXR2. The GST domain forms tight homodimers (Ji et al., 1993) with an equilibrium dissociation constant of less than 1 nM (Fabrini et al., 2009). We previously verified that this construct is fully homodimeric by mass spectrometry (Kintzer et al., 2009). Structurally, the amino-termini of adjacent monomeric soluble ANTXR2 extracellular domains (msANTXR2) in the crystal structure of the $PA_7(ANTXR2)_7$ structure (Lacy, Wigelsworth, Melnyk et al., 2004) are ~55 Å apart (Figure 4.1A). This distance is similar to the distance between the carboxy-termini (~44 Å) in the crystal structure of the GST dimer (Ji et al., 1993), and we infer that the 6-amino acid linkers positioned between the GST domains and the ANTXR2 domains can span this 11-Å differential. Finally, as our model in Figure 4.1A indicates, the amino-terminus of the ANTXR2 points away from the PA-ANTXR interface, and there are no steric constraints, which would prevent the ANTXR2 dimer from forming via the GST interaction either in a PA dimer or higher-order PA_7/PA_8 oligomer complex. Thus this dimeric fusion construct could in principle stabilize the formation of productive dimeric PA intermediates during assembly.

We measure the rate of PA oligomerization using Förster resonance energy transfer (FRET). AlexaFluor 555 and 647 reactive maleimides are conjugated to PA monomers via sulfhydryl modification of the unique Cys residue introduced by the K563C mutation, forming PA K563C*AF_{555} and PA K563C*AF_{647}, respectively. These residues are sufficiently close together in the PA oligomer to allow FRET between adjacent monomers (Wigelsworth et al., 2004). We monitor PA assembly using a 1:1 mixture of AF_{555}-donor-and AF_{647}-acceptor-labeled nicked-PA ($_n$PA) monomers (50 nM each) and the ratio of the fluorescence emission intensities at 668 and 566 nm (F_{668}/F_{566}). As shown in previous studies (Wigelsworth et al., 2004), we also find the extent of $_n$PA oligomerization in the absence of co-assembly factors is slight over the time course of one hour (Figure 4.1B). Consistent with previous studies (Wigelsworth et al., 2004), the presence of msANTXR2 does not stimulate PA assembly appreciably; rather it modestly increases the extent of assembly when compared to the $_n$PA control. We fit the resulting FRET, F, vs time (t) data with a second-order rate model (Wigelsworth et al., 2004)

$$F(t) = A / (1 + kt) + constant \qquad \text{(Eq. 1)}$$

For msANTXR stimulated assembly, we estimate that the observed rate constant, k, is 0.05 (±0.03) s^{-1} with an amplitude, A, of -0.15 (±0.02). Both LF_N and dsANTXR greatly stimulate the extent of PA assembly, A values of -1.12 (±0.02) and -1.29 (±0.04), respectively (Figure 4.1B). We find that, relative to msANTXR, dsANTXR2 with a k of 0.19 (±0.01) s^{-1} accelerates the rate of oligomerization ~6-fold (Figure 4.1B). Thus we conclude that ANTXR dimerization stimulates PA assembly.

Mass spectrometry analysis of $PA_7(LF_N)_3$ and $PA_8(LF_N)_4$ co-complexes with msANTXR2. Quantitative fluorescence (Wigelsworth et al., 2004) and X-ray crystallographic studies (Lacy, Wigelsworth, Melnyk et al., 2004) similarly report that PA_7 binds 7 msANTXR2 domains. Using mass spectrometry (MS), we can also determine the stoichiometry of anthrax

toxin complexes. Previous studies reported that $_{n}$PA and LF_N form PA-LF_N complexes containing PA_7 and PA_8 (Kintzer et al., 2009). Here we find that when this mixture of PA-LF_N complexes is liganded by an excess of msANTXR2, two high-molecular mass species of 677,125 (±70) Da and 791,823 (±128) are formed. These masses are consistent with the theoretical molecular masses of the $PA_7(LF_N)_3(msANTXR2)_7$ and $PA_8(LF_N)_4(msANTXR2)_8$ complexes, respectively (Figure 4.2, Table 4.1). (Note, for simplicity, we refer to these complexes as PA_7-msANTXR2 and PA_8-msANTXR2, respectively.) Also present at slightly lower relative abundances are the assembly intermediates, $PA_2LF_N(msANTXR2)_2$ and $PA_4(LF_N)_2(msANTXR2)_4$ (Figure 4.2). Finally, the free monomers, msANTXR, PA_{20} and LF_N, are observed in the range *m*/*z* 1000–3500 (Figure 4.2). Thus we conclude that the PA oligomer architecture does not preclude the binding of a complete stoichiometric complement of ANTXR domains.

EM analysis of the stability of PA_7 and PA_8 co-complexes with msANTXR2. Using electron microscopy (EM), we measure the relative pH-dependent stabilities of the two different PA oligomers. Here we equate complex stability with the ability of the complex to remain soluble. Prior studies show that insoluble toxin complexes are also inactive (Kintzer, Sterling et al., 2010a). To examine the stability of these complexes, we briefly incubate the oligomeric mixture of PA-msANTXR2 complexes (78% PA_7, 22% PA_8) for 5 min at 37 °C under a range of pH conditions, and then we analyze the composition of the resulting soluble complexes by EM (Figure 4.3). At pH 8.0, we observe mainly distinct axially-oriented oligomeric particles, but at pH 5.0, we largely observe indiscernible aggregates (Figure 4.3A). We find that the number of soluble PA-msANTXR2 prechannel co-complex particles per micrograph decreases as a function of pH with a pH midpoint of 5.8 (Figure 4.3B, Table 4.2). The sharp decrease in the average number of soluble prechannel co-complex particles per micrograph also coincides with the appearance of large aggregates (Figure 4.3A). The appearance of the latter is indicative of premature formation of the PA channel (Kintzer, Sterling et al., 2010a). Data from a similar study of ANTXR-free PA oligomer particles (Kintzer, Sterling et al., 2010a) show a different result, where the pH-dependent transition was biphasic with two different pH midpoints, corresponding to the PA_7 and PA_8 oligomers (Figure 4.3B) (Kintzer, Sterling et al., 2010a). We conclude that when PA_7 and PA_8 complexes bind to msANTXR2 they are stabilized similarly and their solubility as a function of pH reveals a coincident sigmoidal pH dependence.

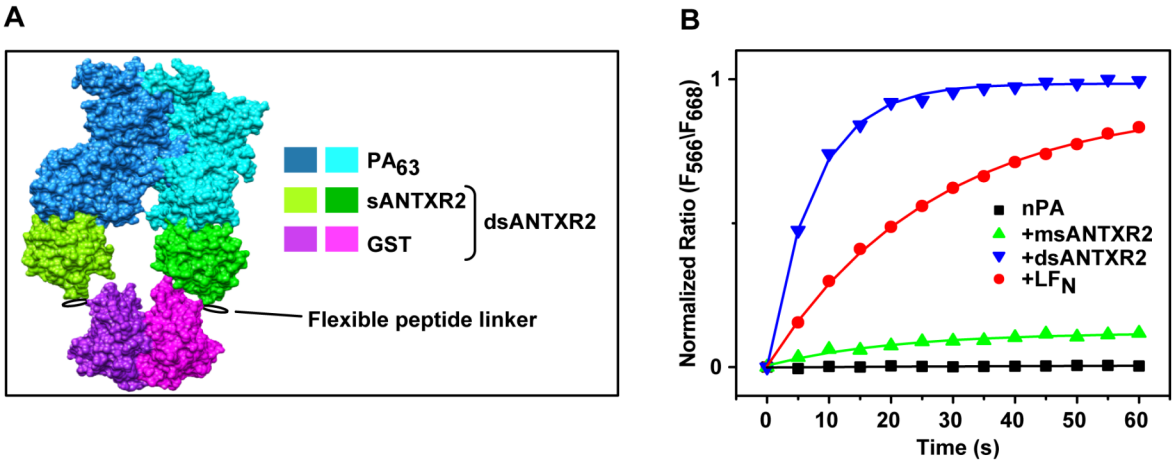

Figure 4.1. ANTXR2 dimerization stimulates PA assembly. (A) A manually constructed model of dsANTXR2 bound to two adjacent PA_{63} subunits in a PA_7 oligomer. The surface rendering is colored according to the legend on the right. The model is based upon the crystal structures of GST (PDB 5GST) (Ji, Armstrong, & Gilliland, 1993) and PA_7(msANTXR2)$_7$ (PDB 1TZN) (Lacy, Wigelsworth, Melnyk et al., 2004). A flexible linker is shown in black that links the carboxy-terminus of GST to the amino-terminus of msANTXR2. **(B)** FRET-probed PA-assembly kinetics at pH 7.4. A 1:1 mixture of $_n$PA K563C*AF_{555} and $_n$PA K563C*AF_{647} monomers (100 nM total monomer) was either allowed to assemble on its own (black ■) or mixed with 100 nM of the following assembly co-factors, dsANTXR2 (blue ▼), msANTXR2 (green ▲), or LF_N (red ●), and allowed to assemble. To track the time course of PA assembly, the ratio of acceptor to donor fluorescence (F_{668}/F_{566}) was measured every five minutes for one hour at room temperature. The resulting records are normalized to the largest signal obtained for the dsANTXR co-assembly reaction. Solid lines are best-fit lines obtained using a second-order rate model (Eq. 1). The rate constants, k, are 0.19 (±0.01) s^{-1} for dsANTXR2, 0.031 (±0.003) s^{-1} for LF_N, and 0.05 (±0.03) s^{-1} for msANTXR2, and the amplitudes, A, are -1.12 (±0.02) for dsANTXR2, -1.29 (±0.04) for LF_N, and -0.15 (±0.02) for msANTXR2. Note due to the lack of an observable change in FRET signal, no kinetic parameters were obtained for the assembly of $_n$PA alone, and the data were fit to a straight line.

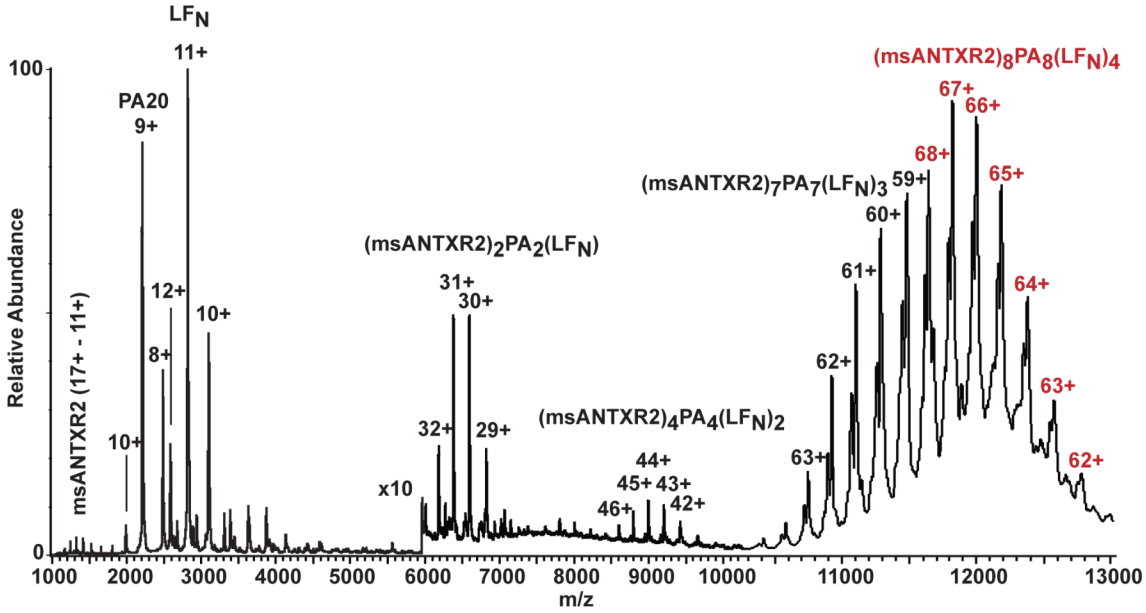

Figure 4.2. Nanoelectrospray mass spectrometry analysis of PA-LF$_N$-msANTXR2 oligomer complexes. Nanoelectrospray MS of sANTXR-PA-LF$_N$ complexes (~2 μM) in 200 mM ammonium acetate, 2 mM ammonium bicarbonate, 0.2 mM magnesium acetate, pH 7.8. The *y*-axis is scaled 10× in the range *m*/*z* 6000–13,000, and the *x*-axis is expanded in the range *m*/*z* 10,000–13,000 to aid viewing low relative abundance and closely spaced peaks in these regions. See also Table 4.1 for the respective molecular mass values for each complex.

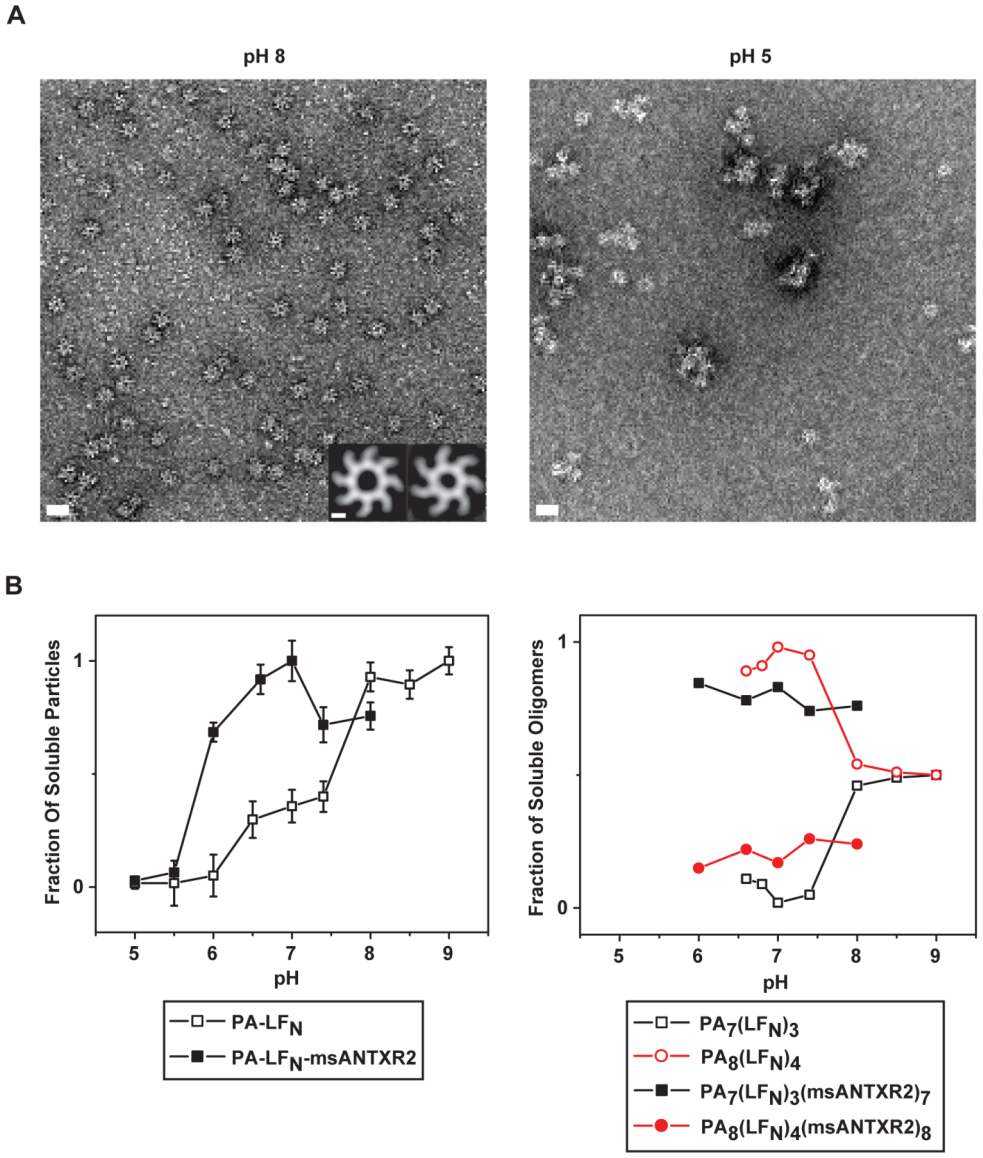

Figure 4.3. EM analysis of the stability of PA_7-msANTXR2 and PA_8-msANTXR2 complexes from pH 8.0 to 5.0. (A) Representative micrographs (49,000×) of PA-msANTXR2 complexes following a 5-minute exposure to 37 ºC at either pH 8.0 (left) or pH 5.0 (right). A 20-nm scale bar is shown in white for either micrograph. (inset on left) Class-average images of PA_7-msANTXR2 and PA_8-msANTXR2 complexes; a 5-nm scale bar is shown. **(B)** Quantitative analysis of the number of soluble PA oligomers and the relative proportions of PA_7 and PA_8, identified from electron micrographs at each pH. (left) A plot of the average number of soluble prechannels versus pH for both free PA complexes (□, data taken from (Kintzer, Sterling et al., 2010a)) and msANTXR2-bound PA complexes (■) complexes. Error bars are propagated from the standard deviations of the mean number of particles obtained from at least 10 micrographs for each pH. (right) A plot of the relative proportions of PA_7 (black ■) and PA_8 (red ●) complexes determined using class-average image analysis for both PA-LF_N (open symbols, data taken from (Kintzer, Sterling et al., 2010a)) and PA-LF_N-msANTXR2 (filled symbols) complexes.

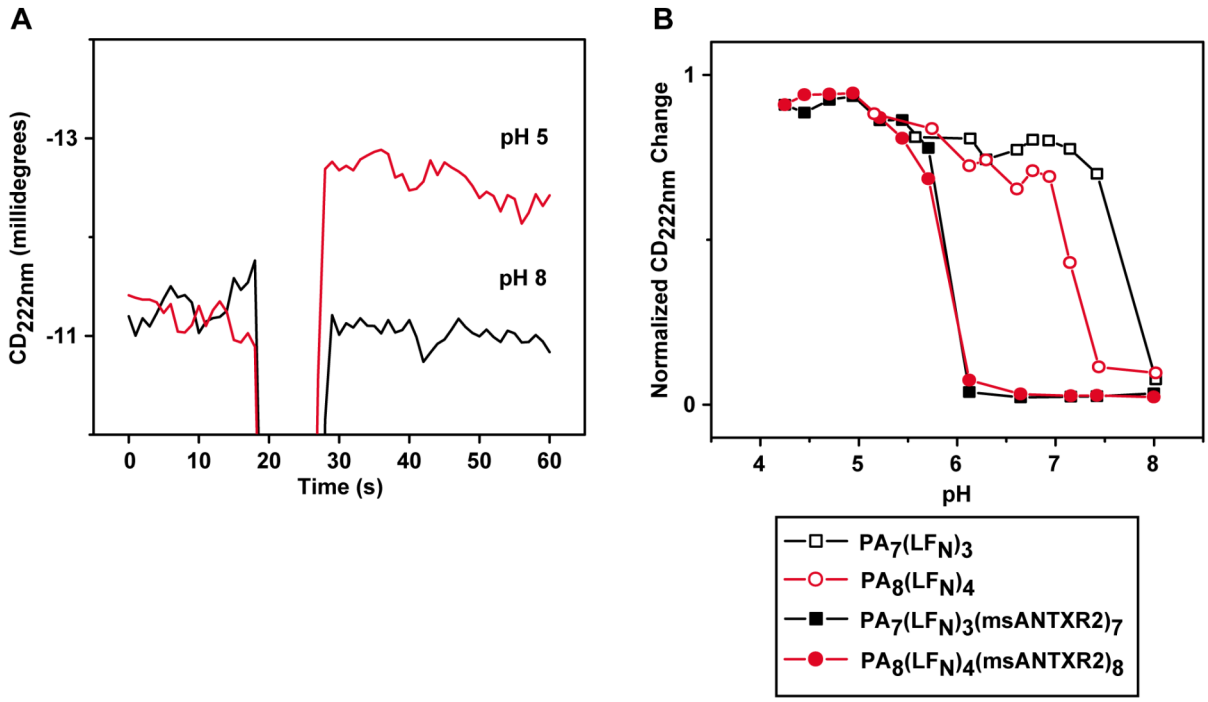

Figure 4.4. The pH dependence of CD-signal changes for PA_7- and PA_8-msANTXR2 complexes. (A) Time-course records of the CD signal at 222 nm (CD_{222}) for either an acid pulse (pH 5.0 final, red trace) or a control with no pH pulse (pH 8.0 final, black trace). **(B)** The pH-dependence of the CD_{222}-signal change for $PA_7(LF_N)_3$ (black □, data taken from (Kintzer, Sterling et al., 2010a)), $PA_8(LF_N)_4$ (red ○, data taken from (Kintzer, Sterling et al., 2010a)), $PA_7(LF_N)_3(msANTXR2)_7$ (black ■), $PA_8(LF_N)_3(msANTXR2)_8$ (red ●) complexes. Traces were normalized to the initial and final CD_{222} signals obtained.

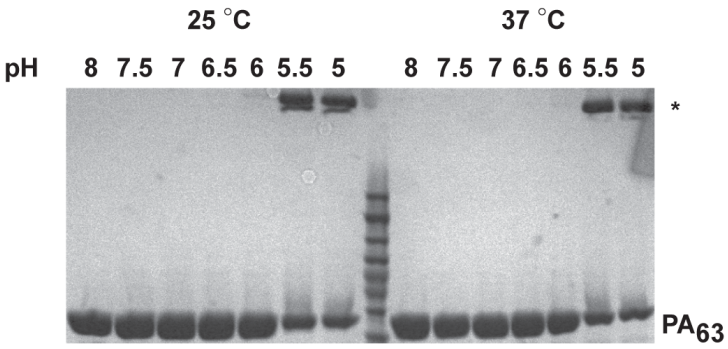

Figure 4.5. The formation of SDS-resistant $PA_7(LF_N)_3(msANTXR2)_7$ complexes is temperature-independent. SDS-resistance assays (Miller, Elliott, & Collier, 1999) were performed with $PA_7(LF_N)_3(msANTXR2)_7$ complexes, which were incubated at the indicated pH at either 25 ˚C or 37 ˚C. The two species of interest on the SDS-PAGE gels are indicated as either the high-molecular-weight, SDS-resistant PA oligomer band (*) or low-molecular-weight SDS-soluble, PA_{63} monomer band (PA_{63}).

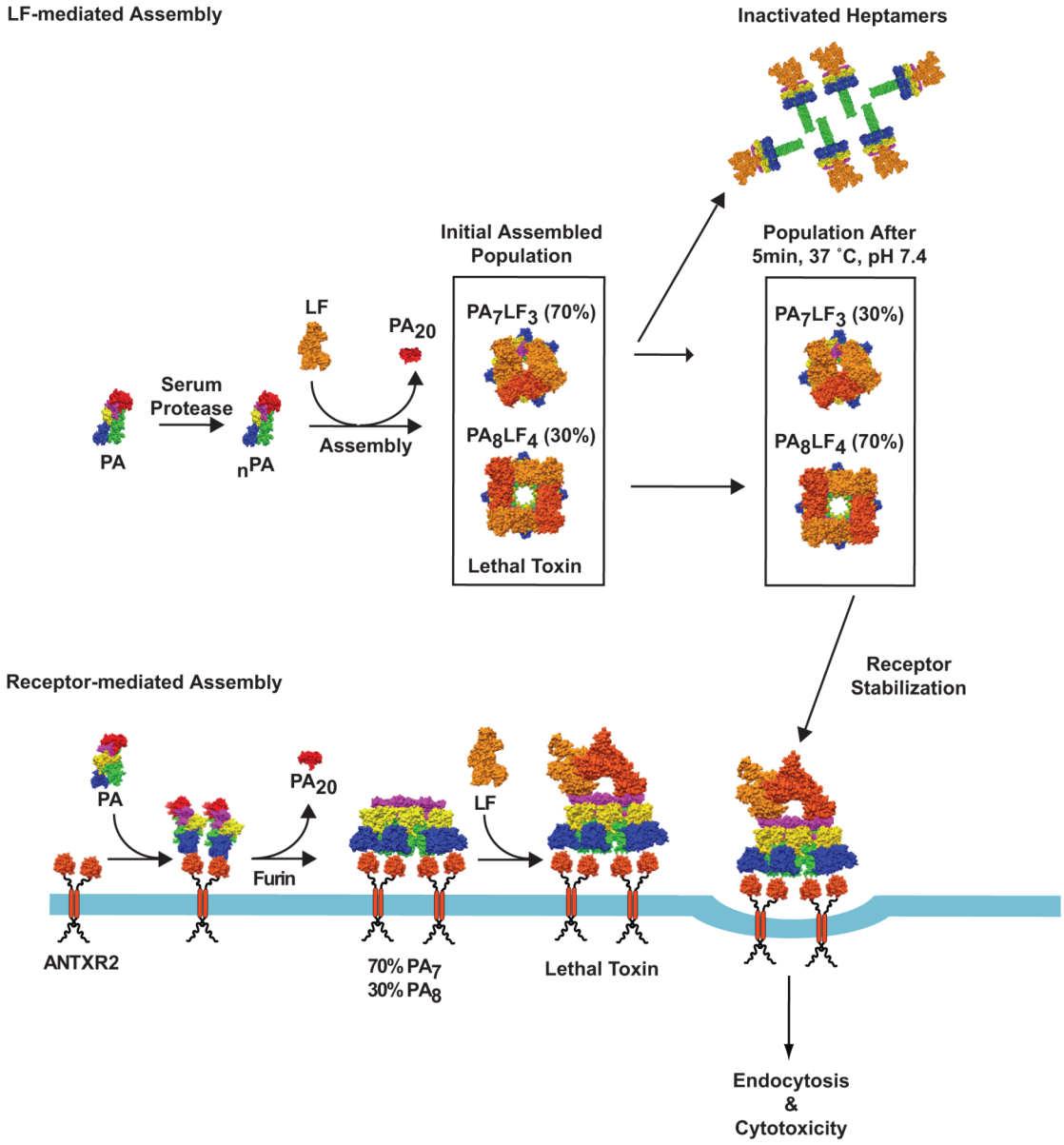

Figure 4.6. A model for anthrax toxin assembly. A model for anthrax toxin assembly in plasma and at cells surfaces. In principle, PA components may assemble into a 70:30 PA_7:PA_8 mixture of toxin complexes in plasma. However, PA_7 readily converts to the channel state and aggregates within 5 minutes under these conditions, leaving PA_8 as the predominant soluble toxin complex capable of infecting cells (Kintzer, Sterling et al., 2010a). By contrast, both oligomeric forms are equally stable at the cell surface, where binding to ANTXR2 serves to prevent premature channel formation until PA_7 or PA_8 complexes are properly internalized and the endosomal compartment is acidified to pH values < 6. On cell surfaces, PA may also oligomerize into a 70:30 PA_7:PA_8 mixture (Kintzer et al., 2009), where assembly is driven through interactions with dimeric ANTXR complexes. These complexes are then able to bind LF and become internalized into cells.

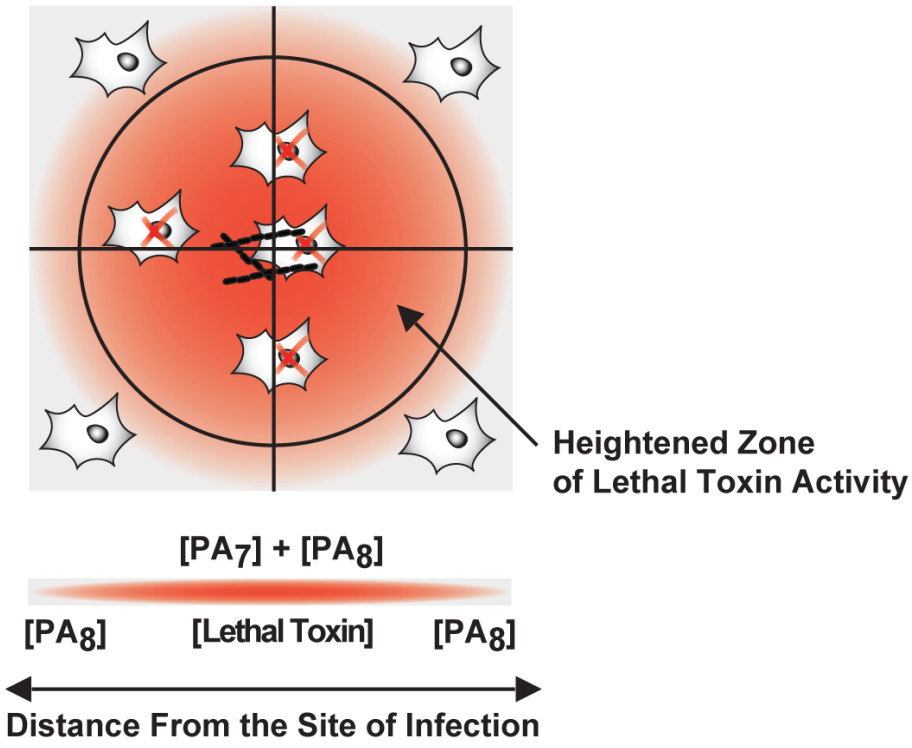

Figure 4.7. A model for the regulation of toxin activity in plasma. The assembly of LT complexes with different lifetimes may serve as a means to regulate toxin activity in plasma during infection. The reduced lifetime of PA_7 complexes in plasma may limit their cytotoxic effects to local areas in close proximity to the site of *B. anthracis* infection. By contrast, PA_8, which is produced at lower levels, has a longer lifetime, thereby allowing it to exert cytotoxic effects over longer distances.

Sample	Measured molecular mass[a] (Da)	Theoretical molecular mass[b] (Da)	Deviation (%)
$msANTXR_8(PA)_8(LF_N)_4$	791,823 (±128)	790,609	0.15
$msANTXR_7(PA)_7(LF_N)_3$	677,125 (±70)	676,327	0.12
$msANTXR_4(PA)_4(LF_N)_2$	395,722 (±33)	395,305	0.11
$msANTXR_2(PA)_2LF_N$	197,815 (±19)	197,652	0.08

Table 4.1. Measured[a] and theoretical[b] molecular masses for msANTXR-PA-LF_N complexes. [a]Molecular masses are measured using nanoelectrospray MS according to the method described in Kintzer et al. (Kintzer et al., 2009).[b] Theoretical molecular masses are derived using the amino acid sequences of msANTXR, PA_{63}, and LF_N.

pH	Mean number of particles per micrograph[c]	Oligomeric composition[d]		
		PA_8 (%)	PA_7 (%)	Total particles (*N*)
8.0	18 (±4)	23	77	364
7.4	20 (±7)	26	74	381
7.0	28 (±8)	17	83	494
6.5	26 (±6)	22	78	482
6.0	19 (±4)	16	84	857
5.5	2 (±1)	n.d.[e]	n.d.	n.d.
5.0	1 (±1)	n.d.	n.d.	n.d.

Table 4.2. Negative-stain[a] EM analysis PA-msANTXR2 co-complexes following an exposure at 37 °C[b]. [a]Negative-stain electron micrographs using uranyl acetate stain, 2%. [b]A pre-assembled population of PA-msANTXR2 complexes (containing 78% PA_7 and 22% PA_8) was incubated for 5 minutes at 37 °C at the specified pH. [c]The mean number of particles per micrograph (*n* of 10 micrographs) given as ±s.d. [d]Oligomeric composition is determined using crystal-structure-referenced alignment and classification analysis (Kintzer, Sterling et al., 2010a; Kintzer et al., 2009). The percentage reported is computed from the total number of particles, *N*, comprising all PA_7 and PA_8 classes, where oligomeric composition is equal to the total number of PA_7 or PA_8 particles divided by *N*. [e]n.d., not determined. Class-average image analyses of these pH conditions are not shown due to the low particle counts observed. The low particle counts are attributed to severe aggregation (as shown in Figure 4.3A).

We then asked if the monophasic sigmoidal transition in the number of soluble PA-msANTXR2 prechannel co-complex particles resulted from the two different PA oligomers having identical pH dependencies for channel formation (and aggregation). To address this question, we measured the relative proportions of the PA_7-msANTXR2 and PA_8-msANTXR2 complexes at each pH. From the negative-stain electron micrographs taken at each pH value, we apply a reference-based alignment, classification, and averaging analysis of all distinct soluble particles (Figure 4.3A, inset) (Kintzer et al., 2009). This analysis, which generates average images of the ring-shaped particles, shows that the percentages of PA_7 and PA_8 are constant over the range of pH 8 to 6 (Figure 4.3B, Table 4.2). The constant percentages observed for these msANTXR2-bound oligomer complexes are in stark contrast to what is observed with msANTXR-free PA oligomer complexes (Figure 4.3B). Thus, when in complex with the msANTXR2 domain, PA_7 and PA_8 have identical pH dependent stabilities and tend to aggregate with identical pH midpoints of 5.8.

Circular dichroism changes in PA_7-msANTXR2 and PA_8-msANTXR2 complexes. Circular dichroism (CD) spectroscopy studies provide a structural probe for PA's transition from the prechannel state to the channel state. This pH-dependent structural transition likely explains the decrease in complex stability and solubility observed, since PA channels tend to aggregate in solution (Kintzer, Sterling et al., 2010a). The secondary structure increases reported by CD signals have been associated with channel formation because the pH-dependent CD-signal change occurs at similar pH values as observed with other probes for channel formation, including EM, MS, and SDS-PAGE (Kintzer, Sterling et al., 2010a). Using the CD signal at 222 nm (CD_{222nm}), we can measure the pH-dependent conformational changes in purified PA_7-msANTXR2 and PA_8-msANTXR2 complexes (Figure 4.4A, B). These purified samples also contain full complements of LF_N, but they are highly enriched >90% in either the PA_7 or PA_8 oligomer (Kintzer et al., 2009). Records of the pH-dependent CD_{222nm} signal change of the PA oligomer-msANTXR2 complexes at 37 ºC (Figure 4.4A) show equivalent results for either PA oligomer from pH 4.0 to 8.0 (Figure 4.4B). The pH-dependent CD_{222nm} signal changes for the PA_7-msANTXR2 and PA_8-msANTXR2 complexes coincide, such that the prechannel-to-channel transition midpoint is pH 5.8 (Figure 4.4B). Relative to the PA oligomers assayed under similar conditions in the absence of msANTXR (Kintzer, Sterling et al., 2010a), this pH 5.8 midpoint is stabilized by ~1.8 and ~1.2 pH units for the PA_7 and PA_8 oligomers, respectively.

The pH-dependence of PA_7-msANTXR2 channel formation is temperature-independent. PA_7 channel formation is both temperature-dependent as well as pH-dependent (Kintzer, Sterling et al., 2010a; Miller et al., 1999). However, while PA_7 forms SDS-resistant aggregates upon channel formation, PA_8 apparently does not (Kintzer, Sterling et al., 2010a). We investigated the temperature-dependence of PA_7-msANTXR2 channel formation using the SDS-resistance assay (Figure 4.5). PA_7-msANTXR2 complexes were incubated at 25 ºC or 37 ºC for 1 hour at pH conditions from pH 8.0 to pH 5.0. Using SDS-PAGE, we can monitor the formation of a low-mobility SDS-resistant form, which is likely an aggregated form of the heptameric PA channel (Kintzer, Sterling et al., 2010a). In the absence of msANTXR2, PA_7 forms an SDS-resistant species at pH 7.4 and 7.0, at 25 ºC and 37 ºC, respectively (Kintzer, Sterling et al., 2010a). However, here we show, in the presence of msANTXR2, that the SDS-resistant species first appeared at pH 5.5 at 25 ºC and also at 37 ºC (Figure 4.5). Therefore, we conclude that the pH-dependence of PA_7-msANTXR2 channel formation is temperature-independent.

4.4 Discussion

PA assembles on cell surfaces once it is proteolytically nicked by a cell-surface furin-type protease (Beauregard, Collier, & Swanson, 2000) after the RKKR sequence within a solvent accessible loop in domain 1 (Petosa et al., 1997). This solvent accessible loop is also recognized by an unknown serum protease found in various types of mammalian plasma (Ezzell & Abshire, 1992a). The resulting products of the cleavage by either type of protease are the amino-terminal 20-kDa fragment, PA_{20}, and the carboxy-terminal, 63-kDa fragment, PA_{63} (Blaustein et al., 1989). The PA_{63} portion self-assembles into either a heptameric (Kintzer et al., 2009; Lacy, Wigelsworth, Melnyk et al., 2004; Milne et al., 1994; Petosa et al., 1997) or octameric (Kintzer et al., 2009) ring-shaped oligomer, which can maximally bind up to three or four LF or EF molecules, respectively. Since assembly is initially limited by this proteolytic activation step, then Atx assembly can occur in two distinct environments, i.e., either (i) on cell surfaces or (ii) free in solution in extracellular environments such as plasma.

The cell-surface pathway is proposed to begin once secreted PA monomers bind to cell-surface ANTXRs (Bradley et al., 2001; Scobie et al., 2003). Furin-type proteases then activate PA, allowing toxin assembly and internalization to ensue. A complementary model has also been proposed based on predominantly *in vivo* results; the model suggests that PA monomers are proteolyzed in the host bloodstream (Ezzell & Abshire, 1992a), assembling into toxin complexes prior to reaching cell-surfaces (Ezzell et al., 2009). We recently proposed that the octameric toxin stably circulates in plasma, while the heptameric toxin is unstable, forming aggregates of the prematurely formed channel state (Kintzer, Sterling et al., 2010a; Kintzer et al., 2009). Toxin aggregates have also been observed *in vivo*, although their oligomeric composition is unknown (Ezzell & Abshire, 1992a). While the cell-surface assembly model and plasma-based assembly model are not mutually exclusive (Kintzer, Sterling et al., 2010a; Kintzer et al., 2009), future *in vivo* studies are needed to distinguish the relative importance of the two assembly pathways during anthrax infection. Here we provide evidence that cell-surface assembly is likely driven by receptor dimerization; however, unique from plasma-based assembly, the two different oligomeric forms, PA_7 and PA_8, are similarly stabilized by ANTXR2 interactions on cell surfaces.

ANTXR2 dimers stimulate PA oligomerization. The assembly of Atx on cell surfaces is not well understood. On one hand, proteolysis, assembly, and internalization have been shown to be rapid under physiological conditions, occurring within minutes (Liu & Leppla, 2003). The mechanism of cell-surface assembly is not fully understood in part because the structure of the full-length ANTXR is unknown and in part because individual assembly intermediates have not been isolated from cells. It is known, however, that while the soluble extracellular domain of ANTXR2 is monomeric, as evidenced in crystallographic (Lacy, Wigelsworth, Melnyk et al., 2004; Santelli et al., 2004) and mass spectrometry studies (Figure 4.2), the full-length ANTXR2 is thought to dimerize via its transmembrane single-pass helix domain, as demonstrated in studies of the transmembrane domain in a liposomal system (Go et al., 2006). Since ANTXR2 dimerization enhances the formation of PA_8, it was proposed that it may also facilitate assembly at the cell-surface by populating dimeric intermediates, because PA_8 complexes are produced in that environment (Kintzer et al., 2009). In further support of this hypothesis, we also find evidence for even-numbered receptor-bound dimeric and tetrameric species, $PA_2(LF_N)(msANTXR2)_2$ and $PA_4(LF_N)_2(msANTXR2)_4$, in our mass spectra (Figure 4.2). We conclude that the cell-surface assembly mechanism likely occurs through dimeric PA intermediates, which are stabilized via dimeric ANTXR complexes; and this mechanism is akin

to a putative extracellular plasma-based assembly mechanism, whereby either EF or LF stabilizes dimeric PA intermediates that can serve to drive assembly (Kintzer et al., 2009).

Previous studies have shown that the rate PA assembly is accelerated in the presence of LF_N (Wigelsworth et al., 2004), which is believed to bridge a binding site spanning the surface of a PA dimer (Cunningham et al., 2002). In this report, we consider the role of a dimeric receptor (dsANTXR2) on the kinetics of PA assembly. Our kinetic FRET measurements show that ANTXR2 dimers stimulate PA assembly (Figure 4.1B). Furthermore, PA assembles ~6-fold faster with dsANTXR2 (relative to what is observed when assembling with LF_N.) This acceleration of the assembly kinetics may reflect that PA binds ANTXR2 with a higher affinity than LF_N (170 pM versus 1 nM, respectively) (Elliott, Mogridge, & Collier, 2000; Wigelsworth et al., 2004). Therefore, we propose that ANTXRs, LF, and EF can stimulate PA oligomerization by populating dimeric PA intermediates, which are precursor intermediates in the PA oligomerization mechanism.

Stabilization of PA complexes by ANTXR2. The ANTXR-dependent stabilization of PA oligomers has been demonstrated on cell-surfaces and in solution (Lacy, Wigelsworth, Melnyk et al., 2004; Miller et al., 1999; Milne et al., 1994). The mechanism of receptor-mediated stabilization of PA complexes occurs by reducing the pH threshold for PA channel formation by ~2 pH units. ANTXR2 prevents channel formation by forming a metal-ion dependent structural bridge that spans domains 2 and 4, restricting the conformational changes necessary for channel formation (Lacy, Wigelsworth, Melnyk et al., 2004; Santelli et al., 2004). While PA_7 complexes have been shown to be stabilized by ANTXR2 interactions (Lacy, Wigelsworth, Melnyk et al., 2004), the relative stabilities of $PA_7ANTXR2_7$ and $PA_8ANTXR2_8$ complexes has not been reported. In the absence of msANTXR2, it has been demonstrated that PA_7 and PA_8 form channels at different pH values (Kintzer, Sterling et al., 2010a). Our EM measurements of pH-dependent PA oligomer aggregation suggest that PA_7- and PA_8-msANTXR2 complexes instead form channels at equivalent pH values with a pH midpoint of 5.8 (Figure 4.3B). Our CD measurements also suggest that PA_7- and PA_8-msANTXR2 complexes form channels at a pH midpoint of 5.8 (Figure 4.4). Further evidence of this conclusion is provided by our analysis of the percentages of soluble PA_7 and PA_8 oligomer complexes over the tested pH range. From pH 8.0 to 6.0, we find the relative ratio of PA_7 and PA_8 complexes is unaltered, indicating that both PA_7 and PA_8 prechannels are stabilized by msANTXR2 (Figure 4.3B). These results are consistent with studies of PA oligomerization on cell surfaces, revealing that the inherently less stable PA_7 complex is favored 2:1 over the PA_8 complex (Kintzer et al., 2009). Therefore, we infer that PA_7 and PA_8 are likely to form similar structural interactions with ANTXR2, since both oligomers are equally stabilized. We conclude that PA_7- and PA_8-msANTXR2 complexes form channels with identical pH dependencies and possess equivalent stability when bound to ANTXR2 on cell surfaces.

Role of ANTXR2 stabilization during pathogenesis. In plasma, LT complexes containing PA_8 oligomers are inherently more stable than those containing PA_7 oligomers, thus allowing the LT containing PA_8 complexes to persist for longer periods of time in that environment (Kintzer, Sterling et al., 2010a). This stabilization mechanism defines an important role for PA_8 oligomers in anthrax pathogenesis. However, as we report here, toxin complexes containing either PA_7 or PA_8 oligomers are equally stabilized by interactions with ANTXR2 (Figure 4.6), and thus the 70:30 ratio of heptamers to octamers observed on cell surfaces (Kintzer et al., 2009) can be fully explained by the receptor-mediated stabilization data presented here (Figure 4.3B). Therefore, Atx assembly may be a means to regulate toxin activity and generate

toxin gradients in the host (Figure 4.7). We expect that, due to its relatively short half life, PA_7 activity may effectively localize near to sites of infection (Kintzer, Sterling et al., 2010a), whereas PA_8 may circulate systemically and provide a longer-range source of toxin activity. The stabilization imparted upon binding to the ANTXR allows for PA_7 containing toxin complexes to be more concentrated and efficacious at sites proximal to the site of infection. The levels of available free LF may control the levels of PA_8 complexes produced. This mechanism should provide a means to maintain higher levels of toxin activity near to the sites of infection while preventing premature system-wide shock until PA_8 complexes are produced on a larger scale. As the infection progresses and a fever in the host develops, PA_8 complexes may be required because they are more thermostable and remain active even after extended exposure to elevated temperatures (Kintzer, Sterling et al., 2010a). Future work should investigate the types of Atx complexes produced throughout the various stages of anthrax pathogenesis.

4.5 Materials and Methods

Proteins. Recombinant wild-type PA_{83} (Sun et al., 2007) was over-expressed in the periplasm of the *Escherichia coli* strain, BL21(DE3). The 83-kDa PA monomer was purified from the periplasm as described (Wigelsworth et al., 2004). Recombinant LF_N (LF residues 1-263) was overexpressed in BL21(DE3) via a pET15b construct (Lacy et al., 2002) and then purified from the cytosol as described (Wigelsworth et al., 2004). Soluble human anthrax receptor domain, msANTXR2, from the capillary morphogenesis protein 2 (residues 40-217) (Scobie et al., 2003) was expressed and purified as described (Santelli et al., 2004). The six-histidine affinity tags were removed from msANTXR2 and LF_N by treatment with bovine α-thrombin. A soluble, dimeric fusion of human anthrax receptor domain to glutathione S-transferase (GST), dsANTXR2, was also expressed and purified as described (Kintzer et al., 2009).

Preparation of purified PA_7-msANTXR2 and PA_8-msANTXR2 co-complexes. $PA_7(LF_N)_3$ was produced using Q-sepharose-purified PA oligomers (Kintzer et al., 2009) by forming complexes with a two-fold stoichiometric excess of LF_N (LF_N:PA) and purified as described (Kintzer, Sterling et al., 2010a). The resulting complexes contained >90% PA_7. $PA_8(LF_N)_4$ was prepared by assembling $_nPA$ in the presence of LF_N ($_nPA$-LF_N, a mixture that contains ~20-30% PA_8), following incubation and purification by gel filtration as described (Kintzer, Sterling et al., 2010a; Kintzer et al., 2009). PA-msANTXR2 complexes were formed by mixing 1 μM $PA_7(LF_N)_3$ or $PA_8(LF_N)_4$ with ten molar equivalents of purified msANTXR2 (10 μM) in Buffer E (20 mM Tris, 150 mM NaCl, pH 8) plus 1 mM $MgCl_2$. The complex was formed at room temperature over the course of 15 minutes.

PA_{83} labeling with fluorescent dyes. A PA_{83} mutant K563C was expressed and purified in the presence of 5 mM DTT. Prior to the reaction, the DTT was removed by buffer exchange on a G25 desalting column (GE Healthcare, USA), equilibrated in nitrogen-purged Buffer E. Labeling reactions were initiated by mixing DTT-free PA_{83} K563C with 10 molar equivalents of Alexa fluor 555 C_5 maleimide (AF_{555}) or Alexa fluor 647 C_5 maleimide (AF_{647}) (Invitrogen, USA) in the presence of 100 μM tris(2-carboxyethyl)phosphine (TCEP, Sigma Aldrich, USA) and incubated at room temperature for 3 hours. The reaction was quenched with 5 mM DTT and purified on a G25 desalting column to remove free, unreacted dye molecules. Labeling efficiency was determined by comparing dye and protein absorbance values. Labeling efficiencies of >90% were achieved for either dye.

FRET-based PA assembly assay. Dye-labeled, nicked PA ($_n$PA K563C*AF_{555} or $_n$PA K563C*AF_{647}) was prepared as described previously (Christensen et al., 2006). To initiate assembly, $_n$PA K563C*AF_{555} and $_n$PA K563C*AF_{647} were each diluted to 50 nM in 10 mM sodium cacodylate, 100 mM potassium chloride, 1 mM magnesium chloride, pH 7.4 either in the presence or absence of 100 nM LF_N, 100 nM msANTXR2, or 100 nM dsANTXR2. Assembly was observed as an increase in the emission intensity ratio at 668 and 566 (±2) nm (F_{668}/F_{566}) upon excitation at 555 (±5) nm, which reached a steady state in about one hour. Emission values were obtained every five minutes on a Horiba Jobin Yvon FluoroMax-3 spectrofluorometer, using quartz cuvettes with a 1-cm path length.

Mass Spectrometry. Mass spectra of the protein complexes were acquired using a quadrupole time-of-flight (Q-TOF) mass spectrometer equipped with a Z-spray ion source (Q-TOF Premier, Waters, Milford, MA). Ions were formed using a nanoelectrospray (nano-ESI) emitter prepared by pulling borosilicate capillaries (1.0 mm O.D./0.78 mm I.D., Sutter Instruments, Novato CA) to a tip I.D. of ~1 μm with a Flaming/Brown micropipette puller (Model P-87, Sutter). The instrument was calibrated with CsI clusters formed by nano-ESI using a 20 mg/mL solution of CsI in 70:30 Milli-Q water:2-propanol prior to mass measurement. The protein solution was concentrated to ~10 μm followed by dialysis into 10 mM ammonium bicarbonate, 1 mM magnesium acetate, pH 7.8. Immediately prior to mass analysis, the solution was diluted 1:4 with 200 mM ammonium acetate, pH 7.8. A platinum wire (0.127 mm diameter, Sigma, St. Louis, MO) was inserted through the capillary into the solution and electrospray was initiated and maintained by applying 1-1.3 kV to the wire (relative to instrument ground). Each raw dataset was smoothed three times using the Waters MassLyn software mean smoothing algorithm with a window of 25 *m*/*z* (mass-charge ratio).

Electron microscopy. PA-msANTXR2 complexes were prepared in Buffer E plus 1 mM $MgCl_2$ as described above, applied to a freshly glow-discharged 400 mesh formvar-carbon coated grids, and stained with 2% uranyl acetate (Sigma-Aldrich, St. Louis, MO) as described (Kintzer, Sterling et al., 2010a; Kintzer et al., 2009). Negative-stain EM images were recorded on a Tecnai 12 electron microscope (FEI Company, Hillsboro, OR) operated at 120 kV at a magnification of 49,000× using a CCD camera. The micrograph resolution was 2.13 Å/pixel. Particle images were selected using manual particle picking using boxer in EMAN (Ludtke et al., 1999). Boxed images of the PA oligomer particles were subjected to successive cycles of reference-free and reference-based alignment, multivariate statistical analysis, and classification using SPIDER (Frank et al., 1996; Stark et al., 1995; van Heel et al., 1996), as described (Kintzer, Sterling et al., 2010a; Kintzer et al., 2009). Final class-average images were manually inspected to determine their oligomeric state and tabulated to determine the oligomeric composition of each sample (Table 4.2).

Circular dichroism (CD) spectroscopy. CD measurements of the PA channel transition were obtained on a JASCO Model 810 spectropolarimeter (JASCO, Inc., Easton, MD). To determine the pH-dependence of the prechannel-to-channel transition, PA-msANTXR2 co-complexes were diluted to 50 nM in 2 mL of the buffer: 10 mM potassium phosphate, 10 mM potassium acetate, 0.1 M potassium chloride, 1 mM magnesium chloride, pH 8. The CD measurement was made using a 1×1-cm quartz cuvette containing a Teflon stir bar, at 25 ºC or 37 ºC. Recordings of the CD_{222nm} signal were conducted at a 1-Hz sampling rate. During the recording the pH of the sample was reduced by adding 0.4 M phosphoric acid to obtain the desired pH, as described (Kintzer, Sterling et al., 2010a). The CD_{222nm} transition was then

observed and recorded for an additional 60 s. The final pH of the sample in the cuvette was determined using a pH meter.

SDS-resistance PAGE analysis. SDS-resistance assays (Miller et al., 1999) were performed with purified PA_7-msANTXR2 complexes. The purified $PA_7(LF_N)_3$ samples were complexed with msANTXR2 as described above, forming PA_7-msANTXR2. PA_7-msANTXR2 complexes were diluted to 1 mg/ml final concentration (with respect to PA) in Buffer E plus 1 mM $MgCl_2$. The following buffers were added to preformed complexes, which vary depending upon the pH: 0.1 M Tris-Cl (pH 8.0), sodium cacodylate (pH 6.5 to 7.5), 0.1 M 2-(*N*-morpholino)ethanesulfonic acid (pH 6.0), and sodium acetate (pH 5.0 to 5.5). The complexes were incubated for 1 hour at 25 ºC or 37 ºC. 1.25% SDS then was added, and the samples were run on a 12% polyacrylamide gel, which was stained in Coomassie Brilliant Blue G-250. to regulate the development of toxin gradients around sites of infection during anthrax pathogenesis.

Chapter 5

Molecular basis for the pH-dependent trigger of anthrax toxin protective antigen channel formation

5.1 Abstract

Channel- and pore-forming toxins are secreted by pathogenic bacteria as soluble monomeric proteins, which oligomerize either in solution or upon the surface of targeted host cells. Changes in local chemical environment trigger conformational changes in the oligomer, allowing the formation of a transmembrane channel or pore. *Bacillus anthracis* secretes a tripartite toxin and a γ-poly-D-glutamic acid capsule. The channel-forming component, protective antigen (PA), assembles either in solution or at the host cell membrane. Once internalized, acidic endosomal pH conditions cause conformational changes in the oligomer, ultimately allowing it to form a membrane-spanning β-barrel. Here we describe the structural and molecular bases for the pH-dependent barrier to channel formation. Using structural, thermodynamic, and kinetic analyses, we suggest that molecular interactions at the interface of domains 2 and 4 (D2-D4), a hydrophobic constriction site called the ϕ-lamp, and a charged residue in the membrane insertion loop (MIL) work in concert to define the rate-limiting, pH-dependent step. A 1.9 Å crystal structure of a critical D2-D4 mutant, with heightened pH-sensitivity, provides a structural basis for the pH-trigger site. This suggests a scheme for the channel formation mechanism where protonation of the MIL triggers dissociation of D2-D4, allowing constriction of the PA lumen, which is held together by the ϕ clamp. Finally, we provide the first evidence that polyanionic compounds, such as the γ-poly-D-glutamic acid capsule can regulate channel formation by binding PA oligomers and stabilizing the D2-D4 interface.

5.2 Introduction

Pathogenic bacteria secrete channel- and pore-forming toxins, often as monomeric protein subunits that can then assemble at the host cell surface into non-membrane inserted pre-pores or pre-channel oligomeric structures (Bann, 2012; Choe et al., 1992; E. Gouaux, 1997; Rossjohn et al., 1997; Wiener et al., 1997). A series of conformational changes triggered by changes in local environment on or within the host cell then allow these pre-channel oligomers to obtain their final membrane-inserted channel state. Crystallographic and electrophysiological studies have suggested substructures within the individual monomer subunits unfold, for example, in response to ligand binding or changes in pH, and then refold to form the transmembrane domain (De & Olson; M. Mueller et al., 2009; Song et al., 1996b; Yamashita et al.). In some cases these conformational changes involve half of the total residues, resulting in large structural changes in the oligomeric architecture (M. Mueller et al., 2009). Local environmental sensing of pH conditions within the cell can provide critical signals to a toxin or virus complex (Choe et al., 1992; Rossjohn et al., 1997; Wiener et al., 1997). Nevertheless, the molecular basis for these conformational changes, allowing the prechannel oligomer to transform into the channel state, are not well understood.

Anthrax toxin (Atx) (J. A. Young & Collier, 2007) consists of three nontoxic protein components and is a key virulence factor produced by pathogenic strains of *B. anthracis*. The

protective antigen component (PA; 83 kDa) binds to cells and ultimately forms an oligomeric translocase channel. The translocase channel allows the toxin's other two other enzymatic components, lethal factor (LF; 90 kDa) and edema factor (EF; 89 kDa), to translocate into the cytosol of a host cell (Beall et al., 1962; H Smith & Keppie, 1954; Stanley & Smith, 1961). LF is a Zn^{2+}-dependent protease, which cleaves host-cell mitogen-activated protein kinase kinases (Duesbery et al., 1998). While PA and LF are individually nontoxic, the combination of LF and PA creates lethal toxin , which can alter cellular physiology and cause death. EF is a Ca^{2+}- and calmodulin-activated adenylyl cyclase (Drum et al., 2002). Likewise, PA and EF combine to form edema toxin, which induces tissue swelling and also death.

To achieve cytotoxicity, PA, LF, and EF must first self-assemble into holotoxin complexes. There are two different pathways: (i) a cell-surface assembly pathway and (ii) a plasma-based/extracellular assembly pathway. In the former, PA forms complexes on the surface of host cells in a receptor-dependent manner. PA first binds to one of two known Atx receptors (ANTXR) (Bradley et al., 2001; Scobie et al., 2003). The PA-ANTXR interaction involves PA domain 2 (D2) and domain 4 (D4), where the latter coordinates the receptor's Ca^{2+} or Mg^{2+} metal ion adhesion site (Lacy, Wigelsworth, Melnyk et al., 2004; Santelli et al., 2004). Receptor-bound PA is then cleaved by a furin-type protease to make the proteolytically-activated form, called $_n$PA. After a 20-kDa portion of $_n$PA dissociates, the remaining 63-kDa, receptor-bound portion assembles into a mixture of ring-shaped heptameric (PA_7) and octameric (PA_8) oligomers (Kintzer et al., 2009; Lacy, Wigelsworth, Melnyk et al., 2004). In the latter assembly pathway, extracellular proteases can similarly activate PA, allowing for co-assembly of LF/EF and PA in the blood serum (Kintzer, Sterling et al., 2010b). Similarly, PA forms PA_7 and PA_8 complexes in plasma (Kintzer, Sterling et al., 2010b).

Assembled toxin complexes are then endocytosed (Abrami et al., 2003) and brought to an acidic compartment (Friedlander, 1986). Under these acidic conditions, either PA oligomer can transform into the translocase-channel state (Katayama et al., 2008; Miller et al., 1999). Endosomal acidification also creates a transmembrane proton gradient, which drives LF and EF unfolding (Krantz et al., 2004; Thoren et al., 2009) and translocation (Brown, Thoren, & Krantz, 2011; Krantz et al., 2006) into the host cell's cytosol.

While the PA channel architecture is not yet known in atomic detail, the current model of the structure (based on electrophysiology (Benson et al., 1998; Nassi et al., 2002b) and electron microscopy studies (Katayama et al., 2008)) is consistent with that containing an ~100-Å-long β barrel. To transform into this channel state, a β hairpin is thought to be contributed by each monomer's D2 (specifically strands 2β1-2β3) (Benson et al., 1998; Nassi et al., 2002b; Petosa et al., 1997). Therefore, 2β1-2β3 must unfold and then subsequently refold to form the final β barrel structure (Petosa et al., 1997). Ultimately, it is believed that the hydrophobic tips of the β strands in the barrel can penetrate the lipid bilayer, thereby forming an aqueous passageway for LF/EF to translocate through into the host cell.

The PA prechannel-to-channel transition has become a subject of recent study (Bann, 2012). The transition itself is highly cooperative, occurring rapidly at pH 7 in solution; however, when PA prechannels are bound to ANTXR2, the required pH threshold for channel formation is shifted to pH 5 (Lacy, Wigelsworth, Melnyk et al., 2004; Miller et al., 1999). Recent studies suggest that PA-ANTXR2 interactions begin to dissociate at pH 6 (Pilpa, Bayrhuber, Marlett, Riek, & Young, 2011). Histidine protonation within PA (Miller et al., 1999) and H121 in the ANTXR domain (Lacy, Wigelsworth, Melnyk et al., 2004; Santelli et al., 2004) were hypothesized to be responsible for triggering the pH-dependent prechannel-to-channel transition.

Nonetheless, 2-fluorohistidine studies have suggested that histidine protonation may be important for dissociation from ANTXR2, but not for channel formation in solution (Wimalasena et al., 2007; Wimalasena et al., 2010). Other independent mutagenesis studies of the ANTXR2 interaction with PA revealed that H121 did not affect the pH-dependence of PA's prechannel-to-channel transition (Scobie et al., 2007). A recent EM structure of the PA channel described the basic architecture of the channel and supports the hypothesis that D2 and D4 separate once the channel state forms (Katayama et al., 2008). In fact, the interaction of the ANTXR2 with PA acts as a 'molecular clamp' and holds these domains together and can effectively shift the pH dependence of channel formation, depending on the stability of the interaction (Lacy, Wigelsworth, Melnyk et al., 2004; Rainey et al., 2005; Santelli et al., 2004; Scobie et al., 2007). However, the structural, thermodynamic, and kinetic basis for the pH-dependence of channel formation are unclear.

Pathogenic strains of *Bacillus anthracis* also secrete a poly-γ-D-glutamic acid capsule (γ-DPGA), which consists of long, linear polypeptides (50 to 200 kDa) that are polymerized via the γ-carboxylate side chain and the α-amino group of adjacent D-Glu monomers (Bruckner, Kovacs, & Denes, 1953). The genes responsible (Green, Battisti, Koehler, Thorne, & Ivins, 1985a; Makino et al., 1989; S. L. Welkos, 1991a) for producing γ-DPGA (Makino et al., 1989), anchoring it to the peptidoglycan cell wall (Candela & Fouet, 2005), and cleaving it into smaller (15 to 50 kDa), dissociable fragments (Candela & Fouet, 2005; Makino, Watarai, Cheun, Shirahata, & Uchida, 2002b; Scorpio, Chabot, Day, O'Brien et al., 2007; Uchida et al., 1993b), may augment its virulence by allowing the bacillus to evade the host innate immune system (Makino et al., 2002b; Maurer, 1965a; Scorpio, Chabot, Day, O'Brien et al., 2007). Several studies have suggested that γ-DPGA binds Atx *in vivo* (Ezzell et al., 2009; Jang et al., 2011). However, molecular basis and functional consequences for these interactions are not known.

Here we report that molecular contacts between D2 and D4, protonation of the MIL, and ϕ-clamp interactions are critical for the pH-dependent conformational changes required for PA's prechannel-to-channel transition. We also found that polyanionic compounds, like γ-DPGA, can stabilize PA and prevent channel formation. Together, these sites form the molecular basis of ANTXR-dependent and independent pH sensing by the PA oligomer complex during channel formation.

5.3 Results

Interactions between D2 and D4 modulate the pH-dependence of PA channel formation. Previous EM studies suggest that D2 and D4 separate in the channel state (Katayama et al., 2008), whereas in the prechannel state, they form extensive contacts. We hypothesize that molecular interactions between D2 and D4 could regulate the pH-dependence of PA channel formation; however, we also expected that D4 would be superfluous to the channel's principle function as a transporter for LF and EF. We first asked whether PA complexes lacking the entirety of D4 were functional. Nicked-$PA_{\Delta D4}$ monomers were assembled with LF_N and analyzed using EM (Figure 5.1A). Consistent with previous observations, the assembled complexes formed primarily elongated particles—indicative of channel formation (Katayama et al.; Kintzer, Sterling et al., 2010b). However, $(PA_{\Delta D4})_7$ and $(PA_{\Delta D4})_8$ prechannels were also observed (Figure 5.1A). EM analysis of 1000 single particles by reference-free alignment, classification, and averaging revealed three major classes, $(PA_{\Delta D4})_7$ prechannels, $(PA_{\Delta D4})_8$ prechannels, and channels, with relative proportions of 1.6% (n = 16), 32.1% (n = 321), and 66.3% (n = 663), respectively (Figure 5.1A). Our analysis could not identify the oligomeric state of the channel

structures we observed. The proportions we observed are consistent with the notion that most of the $(PA_{\Delta D4})_7$ prechannels prematurely form the channel. In fact, $(PA_{\Delta D4})_7$ forms channels at all pH conditions tested (from pH 7 to 10). We conclude that D4 makes interactions that stabilize the prechannel complex.

To address whether the $PA_{\Delta D4}$ complexes form functional translocases, WT PA_7, $(PA_{\Delta D4})_7$, or purified $(PA_{\Delta D4})_8$ complexes (see Experimental Procedures) were applied to planar lipid bilayers. Membrane-inserted channels were then complexed with LF_N, which blocks channel conductance. Excess LF_N was perfused with fresh buffer. Translocation was assayed by then raising the $\Delta\psi$ to 50 mV and observing the change in channel conductance as the LF_N moiety translocated through the PA channel. We found that WT PA_7, $(PA_{\Delta D4})_7$, or purified $(PA_{\Delta D4})_8$ translocate LF_N with $t_{1/2}$ values (mean (±s.d.)) of 14 (±1), 19 (±1), and 16 (±1) s, respectively (Figure 5.7A). Therefore, $PA_{\Delta D4}$ forms functional translocase channels and D4 is superfluous to the channel's translocase function.

The binding site for anthrax toxin receptor (ANTXR) on PA includes contacts in both D2 and D4; and this large contact area effectively clamps these two PA domains, preventing premature channel formation at near neutral pH conditions (Kintzer, Sterling, Tang, Williams, & Krantz, 2010; Lacy, Wigelsworth, Melnyk et al., 2004). We hypothesized that the contacts formed between D2 and ANTXR should be sufficient to mediate entry of $PA_{\Delta D4}$ into cells (Santelli et al., 2004). WT PA and $PA_{\Delta D4}$ monomers were applied to J774 macrophage cells in the presence of constant 1 μg/mL LF and their effective-concentration-for-50%-lysis values (EC_{50}) were measured by lethal toxin cytotoxicity assay using a mouse macrophage cell line. We found that $PA_{\Delta D4}$ was in fact cytotoxic, albeit its activity was 100-fold less than WT (Figure 5.7B).

D2 and D4 must separate to form the channel state. Since $PA_{\Delta D4}$ forms channels even at high pH, we hypothesized that interactions at the D2-D4 interface could represent a pH-dependent barrier to channel formation. We thought that crosslinking the D2-D4 interface would actually prevent conversion to the channel. PA residues K446 and I708 were identified as candidates for crosslinking studies. These positions were mutated independently or simultaneously to cysteine residues and tested for channel formation using CD and planar bilayer electrophysiology (Figure 5.1B, 5.1C, 5.8). We found that the cross-linked mutant K446C/I708C, but not the corresponding single mutants, prevented channel formation by CD (Figure 5.1B) and electrophysiology (Figure 5.1C, 5.8). Furthermore, only when the reductant, TCEP, was added to the cross-linked mutant was channel formation observed. Therefore, PA channel formation can be reversibly inhibited by crosslinking the D2 and D4, and these domains must separate by a distance greater than a typical disulfide bond to allow the oligomer to form the channel state (Figure 5.1D).

The γ-DPGA capsule inhibits PA channel formation. Previous studies indicated that ethylenediaminetetraacetic acid (EDTA) inhibited PA channel insertion into planar lipid bilayers (PLBs) at neutral pH (Blaustein et al., 1989). Given the structural similarity between this molecule and the basic unit of the *B. anthracis* γ-DPGA capsule, we hypothesized that EDTA could actually mimic γ-DPGA and bind PA (Ezzell et al., 2009). We extracted γ-DPGA capsule from the cell surface of *Bacillus lichenformis*, which have similar purity, size, linkage, and stereochemistry as the *B. anthracis* capsule (Bruckner et al., 1953; Troy, 1973). This material was shown previously to be free of contaminants, such as proteins or deoxyribonucleic acid (Scorpio, Chabot, Day, O'Brien et al., 2007).

We hypothesized that binding of γ-DPGA and EDTA to PA could affect its channel insertion activity. Since, PA_7 complexes readily form channels at physiological pH and

temperature (Kintzer, Sterling et al., 2010b) we hypothesized that γ-DPGA could bind stabilize PA prechannels through putative interactions in solution (Ezzell et al., 2009). We found that both γ-DPGA and EDTA inhibited PA_7 insertion in to planar lipid bilayers (PLBs, Figure 5.2A, 5.9). The inhibitory effects on channel formation by γ-DPGA and EDTA were reversed with the PA K446M mutant (Figure 5.2B). Lowering the pH to 6.5 or using pre-formed PA channels also prevented inhibition by γ-DPGA and EDTA (Figure 5.3C). These data suggest that, rather than chelating a trace metal or simply inhibiting PA insertion into PLBs, these molecules restrict the necessary pH-dependent conformational changes required for channel formation.

To estimate the affinity of γ-DPGA and EDTA for PA, we determined inhibition constants ($K_{inhibit}$) by titrating these compounds in electrophysiology insertion experiments. The initial and final steady-state current values were recorded for each addition of 10-100ng of PA_7 in the absence and presence of increasing concentrations of γ-DPGA and EDTA (Figure 5.2A, 5.9). The resulting data fit to a single-site binding model (Equation 4), enabling the determination of $K_{inhibit}$ values. γ-DPGA and EDTA were determined to have a $K_{inhibit}$ values of 34 (±8 nM) and 0.31 (±0.1 mM), suggesting that γ-DPGA has much higher affinity for PA. We hypothesized that the affinity of general polyanionic compounds for PA could scale with the amount of negative charge present. Therefore, a series of polyanionic compounds were screened for inhibition activity (Table 5.1, Figure 5.9). We found that ethyleneglycoltetraacetic acid (EGTA), γ-DPGA 10mer, γ-DPGA 2mer, inositol hexakisphosphate (IP6), and heparin sulfate inhibited PA_7 insertion into PLBs with $K_{inhibit}$ values of 0.56 (±0.3 mM), 0.1 (±0.1 mM), 2 (±0.5 mM), 97 (±30 μM), respectively (Table 5.1). Smaller γ-DPGA peptides had the added complication of blocking the PA channel with equilibrium constants (K_{block}) within an order of magnitude of $K_{inhibit}$ (Table 5.1). Nevertheless, the $K_{inhibit}$ values scale approximately with the estimated amount of negative charge on each tested compound. Neutral and positively-charged compounds had no effect on PA insertion (data not shown).

We also used CD experiments to measure the pH-dependence of channel formation in the presence and absence of γ-DPGA or EDTA at 37 ˚C, where PA forms channels at pH 7.4 (Figure 5.3D) (Kintzer, Sterling et al., 2010b). We found from phosphoric acid titrations that PA_7 forms channels at lower pH (~0.25) in the presence of both 1 μM γ-DPGA or 10 mM EDTA, suggesting that binding of these compounds to PA restrict the prechannel to channel transition (Figure 5.3D). Similar effects were observed for other polyanionic compounds (data not shown). We conclude that PA has a generic polyanionic, small-molecule binding site, that modulates the pH-dependent conformational changes required for channel formation.

Structure of PA K446M reveals disruption of the D2-D4 interface. An examination of the D2-D4 interface (Figure 5.3A) reveals a solvated pocket flanked by residues H336, E443, K446, Y660, I708, and N709, which form clear interactions in the high resolution PA monomer structure (3TEW). In particular, K446 forms hydrogen bonds with a water molecule (water 982) and the backbone carbonyls of E443 and I708 (Figure 5.3B). In addition to making contacts with K446 and H336, respectively, Y660 and N709 form hydrogen bonds with waters 912 and 982. H336 also connects K446 to Y660 via hydrogen bonds to water 1015 and I334 (Figure 5.3C). We hypothesized that these interactions clamp D2 and D4, thereby stabilizing the prechannel against pH-dependent conformational changes. As a corollary, disrupting these interactions could promote the dissociation of D2 and D4, which is required for channel formation.

We next sought the structural changes associated with disrupting interactions with K446. In efforts, to conserve the overall hydrophobicity and steric bulk, while eliminating the hydrogen-bonding capability, a methionine mutation was introduced at residue 446. Large

orthorhombic crystals of PA K446M in the space group $P2_12_12_1$ were obtained at 19 ˚C, diffracting X-rays to 1.91 Å. The structure was solved by molecular replacement, placing a single PA (1ACC) (Petosa et al., 1997) monomer in the asymmetric unit (Table 5.2). The $2F_o$-F_c electron density map is of sufficient quality to place unresolved loops in 1ACC structure (residues 98-101, 162-174, 276-287, 343-350, and 512-515). The placement of manually built residues was supported by the presence of strong electron density (>1σ) in simulated-annealing (SA) omit maps (Figure 5.10). These include the furin-type-proteolysis site RKKR (residues 162-174), which has been modeled in a recent high-resolution crystal structure of PA (3TEW) (Feld et al., 2011), and some of the putative β-barrel lining residues, 276-287 and 343-350, of the PA channel (Nassi, Collier, & Finkelstein, 2002a). Bann and colleagues also describe the structure of a PA fluorohistidine analogue (3MHZ) (Wimalasena et al., 2010), which differs only slightly from the native PA structure. However, the K446M structure (4EE2) shows significant conformational changes at the interface of D2-D4. The structural rearrangements were modeled into strong, continuous SA omit electron density (>1σ) and F_o-F_c difference electron density maps (>2σ, Figure 5.10).

The structure at the D2-D4 interface reveals that hydrogen-bonding interactions with K446 are disrupted (Figure 5.3B, 5.3D), leading to an unanticipated rearrangement of the WT PA D2-D4 interface (Figure 5.3C). The M446 residue changes conformation, breaking hydrogen bonds with E443, I708, and water 982, moving 3.7 Å to form van der Waals interactions with the adjacent I334 and nearby W346. Furthermore, water 1015 is not present. This water is critical to making bridging contacts that connect K446 to H336 and Y660 (Figure 5.3B, 5.3D). We conclude that the K446M mutation disrupts interactions that stabilize the D2-D4 interface.

To assess whether the observed conformational changes in the PA K446M structure effect the flexibility of D2 and D4, we estimated the per-residue deviations of this K446M crystal structure relative to the high-resolution PA structure (3TEW) (Feld et al., 2011) using LSQKAB in the CCP4 suite (Figure 5.10A). We found that the K446M mutant had large regions of deviations >1 Å in D2 and D4, including regions of D1. Analysis of *B* factors in the K446M structure agrees with the structural deviations calculation, where higher values (>30 $Å^2$) were observed at the interface of D2 and D4 as well as D1 relative to the high-resolution structure of PA (3TEW) (Figure 5.10A). We conclude that K446 stabilizes the D2-D4 interface through a network of interactions, which include key water molecules.

The D2-D4 interface controls the pH-threshold of channel formation. Our structure suggests that the K446M mutation disrupts the D2-D4 by promoting significant flexibility in the prechannel complex. We next asked whether the other specific residue contacts in the D2-D4 interface were responsible for controlling the pH-dependent conformational changes responsible for channel formation. Residues, H336, E443, K446, Y660, I708, and N709, were mutagenized and their equilibrium pH-thresholds for channel formation were measured in the presence and absence of soluble ANTXR2 (sANTXR2) using an SDS-resistance assay (Figure 5.4A, Table 5.3) (Kintzer, Sterling et al., 2010b; Miller et al., 1999). Shifts in the pH-threshold were observed at each position using Ala-substituded variants. These mutants were purified as prechannel complexes at pH 9 to prevent premature channel formation. The mutant Y660A was not isolable because it formed channels even at pH > 9 (Figure 5.4B). Mutations in the positions K446, I708, and H336 increased the pH midpoint for channel formation by ~0.5 pH units.

The chemical specificity of the D2-D4 interface was then tested by introducing a series of hydrophobic (F, M, L) charged (D, E, K, R), and neutral residues (Q, N, C). The mutations H336L and K446Q increased the equilibrium pH-threshold by 1 pH unit, while most other

substitutions only shifted the pH-threshold by 0.5 pH units (Figure 5.4B, Table 5.3). The fact that most mutations tested exhibit 0.5 pH unit shifts suggests that the D2-D4 interface has high molecular specificity and is largely intolerant to structural perturbation. Therefore, small changes in the structure can translate to large changes in the pH-threshold. For example, an attempt at swapping residues K446 and N709 to restore WT pH-threshold by introducing the mutation K446N/N709K causes a 1-pH unit increase in the pH-threshold (Table 5.3).

Our results suggest that H336 and K446 modulate the pH-dependence of channel formation in solution. However, previous studies found ANTXR2 to also stabilize PA against channel formation. Therefore, we tested whether mutations in the D2-D4 interface regulate the pH-dependence of ANTXR2-bound complexes. Representative PA mutants were screened in the presence of sANTXR2 and we found that the mutations H336L and K446Q shift the pH-threshold by 0.25 pH units (Figure 5.4C). These mutants did not possess anthrax receptor binding defects in agreement with other prior studies (Lacy, Wigelsworth, Melnyk et al., 2004; Santelli et al., 2004; Wigelsworth et al., 2004). However, using the well-characterized ANTXR2-binding deficient mutant D683A (Lacy, Wigelsworth, Melnyk et al., 2004; Santelli et al., 2004; Wimalasena et al., 2010), the pH-threshold was shifted by similar amounts as H366 and K446 in the presence (Figure 5.4C), but not the absence of ANTXR2 (Figure 5.4B). Therefore, H336 and K446 modulate the pH-dependence of channel formation when PA is complexed with its host-cell receptor.

D2-D4 separation defines the rate-limiting barrier to channel formation. We hypothesize that breaking D2-D4 interactions may be a rate-limiting step in the mechanism of channel formation. Also we expect that because the formation of the channel state is essentially "irreversible" that the kinetic rate constant defining the prechannel-to-channel transition is the most critical parameter defining the conformational change. To test our model directly, we used CD signal changes at 222 nm (CD_{222}) to measure the rate of channel formation. CD was previously employed to measure the equilibrium pH-thresholds for PA complexes (Kintzer, Sterling et al., 2010b); however, these measurements suffered from slow-mixing dead times that tended to obscure the rate of channel formation. Therefore, we employed a motor-driven titrator to deliver small aliquots of phosphoric acid directly to an efficiently stirred cuvette containing 50 nM PA_7 or PA_8 complexes. This technique delivers a pH pulse with sub-second mixing times, allowing for the acquisition of kinetic data for channel formation (Figure 5.5A). The data obtained were reasonable as we observed comparable 20-30% changes in CD_{222} upon lowering the pH to 7 consistent with previous results (Kintzer, Sterling et al., 2010b); and moreover, we could determine the kinetic rate constant for channel formation by fitting to a single-exponential model (Equation 1).

To test whether the interactions identified at the D2-D4 interface (Figure 5.3) form a rate-limiting barrier to channel formation, we measured channel formation rates for WT and mutant PA_7 complexes (Figure 5.5B). WT PA_7 complexes formed the channel state with a rate constant of 0.14 (±0.01) s^{-1} (Figure 5.5A, Table 5.3). PA K446A formed channels with a rate constant of 0.63 (±0.01) s^{-1}, which is five-fold faster than WT (Table 5.3). We then measured the kinetics of channel formation for various PA mutants at the D2-D4 interface (Figure 5.5B). Alanine substitutions for PA residues H336, E443, K446, Y660, and I708, formed channels with three- to six-fold fold faster rate constants as compared to WT, suggesting that they participate in the rate-limiting step of channel formation mechanism (Table 5.3).

To estimate the energetic contributions of each mutant to channel formation, we used the rate constants to obtain activation Gibbs free energies, $\Delta G^{\ddagger}$ (Equation 2), which describe the

difference in energy between the prechannel state and the transition state at pH 7 (Figure 5.5B). For WT PA_7 at pH 7, the $\Delta G^{\ddagger}$ was determined to be 0.51 (±0.02) kcal mol^{-1} (Table 5.3). Measurements at pH 5 suggest that the rate-limiting step is pH-dependent, as the barrier drops to 0.24 (±0.01) kcal mol^{-1}. We then estimated the relative energetic contributions of each mutant to the transition state by determining the change in activation energy relative to WT ($\Delta\Delta G^{\ddagger}$). Interestingly, H336A, E443A, K446A, Y660K, and I708A had $\Delta\Delta G^{\ddagger}$ values of -0.32 (±0.03), -0.23 (±0.04), -0.40 (±0.03), -0.40 (±0.03), and -0.45 (±0.03) kcal mol^{-1}, respectively. Values of $\Delta\Delta G^{\ddagger}$ less than zero suggest that the mutants destabilize the D2-D4 interface. However, N709A was similar to WT, with a $\Delta\Delta G^{\ddagger}$ value of 0.08 (±0.03) kcal mol^{-1} (Figure 5.5B, Table 5.3).

We next investigated whether the residues at the D2-D4 interfaces form a rate-limiting barrier to channel formation when bound to ANTXR2. This effectively shifts the pH-threshold for channel formation to pH 5.25 (Table 5.3). We again estimated the $\Delta\Delta G^{\ddagger}$ in the presence of sANTXR2 (Kintzer, Sterling, Tang, Williams et al., 2010). In this case, only the most destabilized mutants shifted the kinetic rate constants relative to WT. We found H336L, K446Q, and the sANTXR2 non-binding mutant, D683A, to have $\Delta\Delta G^{\ddagger}$ values of -0.13 (±0.01), -0.15 (±0.01), and -0.09 (±0.01) kcal mol^{-1}, respectively. However, E443K, Y660K, I708D, and N709A are more similar to WT, with $\Delta\Delta G^{\ddagger}$ values of -0.005 (±0.001), -0.006 (±0.001), -0.01 (±0.01), and -0.003 (±0.001) kcal mol^{-1}, respectively (Figure 5.5B, Table 5.3). The D683A mutant does not have an effect on channel formation in the absence of sANTXR2, with a value of -0.003 (±0.001) kcal mol^{-1} (Table 5.3). These results correlate identically with the ~0.25 pH shift in pH-threshold exhibited by H336L, K446Q, and D683A in SDS-resistance assays (Figure 5.4C, Table 5.3). Therefore, the D2-D4 interface is also the rate-limiting barrier to channel formation when bound to ANTXR2.

To correlate the changes in channel formation rate constants with changes in the pH-dependence of PA mutants, we plotted the $\Delta\Delta G^{\ddagger}$ values (Figure 5.5B) versus the pH-threshold for each PA mutant (Figure 5.5C, 5.4B, 5.4C). We observe a linear correlation (R^2=0.96) between $\Delta\Delta G^{\ddagger}$ values versus the pH-threshold in the presence (Figure 5.11C) and absence of sANTXR2 (Figure 5.5C), suggesting that they are mechanistically related.

PA_7 complexes were mainly used in these studies, owing to their ease of preparation. However, previous studies showed that subtle changes in the orientation of D4 (Figure 5.11A) could have significant effects on the discrimination between PA_7 and PA_8 oligomers during assembly (Feld et al., 2011; Kintzer et al., 2009). Indeed, we found that PA_8 forms channels 2-fold slower than PA_7 at pH 7 (Figure 5.11B). Using the linear fit parameters from a logarithmic plot of rate versus pH-threshold, we determined the equilibrium pH-thresholds for PA_7 or PA_8 complexes to be 7.1 (±0.1) and 6.9 (±0.1), respectively (Figure 5.5C). These values are consistent with previous studies, which suggested that PA_7 or PA_8 complexes have different pH-thresholds (Kintzer, Sterling et al., 2010b). Therefore, we conclude that subtle changes in structure at the D2-D4 (Figure 5.11A) interface have significant effects on the pH-threshold of channel formation.

Localization of the pH-sensing region in PA to the MIL. The molecular mechanism of pH-sensing by PA remains elusive. We hypothesized that the contacts between D4 and the membrane insertion loop (MIL, residues 302-324) of PA (Miller et al., 1999) could govern the observed pH-dependence. Contrary to previous studies, we found that the $PA_{\Delta MIL}$ mutant (in which the MIL was deleted) forms channels at lower pH than wild-type PA, suggesting that residues within the MIL regulate pH-dependent conformational changes (Figure 5.4A). To assess whether the MIL could be a pH-sensor we measured the kinetics of channel formation as a

function of pH by CD (Figure 5.5D). Mutation of a bona fide pH-sensor would perturb the pH-dependent kinetics when mutated or deleted. For WT PA_7, the pH titrations best fit a two-barrier model (Equation 3), one with a steep pH-dependence (barrier 1) and a second with little dependence on pH (barrier 2). In general for WT PA_7, the kinetic data is best described by the fit parameters, n_1 and n_2, the number of protons involved in barriers 1 and 2, respectively. (See Experimental Procedures) For WT PA_7, barrier 1 is highly proton dependent, with n_1 equalling 3.1 (±0.3), while barrier 2 has n_2 of 0.0046 (±0.003) (Figure 5.5D). $PA_{\Delta MIL}$ heptamers, by contrast, exhibit relatively little pH-dependence, with proton dependences n_1 and n_2 of 0.069 (±0.01) and 0.011 (±0.01), respectively (Figure 5.5D). To localize the pH-sensor, we next mutated all five protonatable residues in the MIL (E302, H304, E308, H310, D315) to alanine. A single mutant, E302A, yielded flat pH-dependence, with n_1 and n_2 of 0.62 (±0.1) and 0.024 (±0.01), respectively (Figure 5.5D). The other mutants tested did not affect the pH-dependent kinetics (Figure 5.12). Importantly, K446M and F427A mutants, which shift the overall pH-dependence to higher and lower pH, respectively, but are not titratable residues, do not affect n_1 appreciably (Figure 5.5D). Therefore, E302 likely serves as a pH-sensor for channel formation, while K446 and F427 cooperatively modulate the rate-limiting conformational changes required for channel formation (Figure 5.5D).

To further confirm the effect perturbing the pH-sensor on PA_7 insertion into bilayers, we compared the channel forming activity of PA mutants at pH 7 (Figure 5.6A) and pH 5.5 (Figure 5.6B). We found at pH 7 that E302A and K446M had a higher rate of insertion, while F427A slows the rate of insertion, as compared with WT complexes. The initial rates of insertion at pH 7 were determined to be 0.99 (±0.2), 2.3 (±0.4), 0.031 (±0.01), and 6.1 (±2) s^{-1}, for PA_7, E302A, F427A, and K446M respectively (Figure 5.6A). However, at pH 5.5, the initial rates of insertion were determined to be 4.0 (±0.05), 3.3 (±0.2), 3.4 (±0.2), and 3.5 (±0.1) s^{-1} (Figure 5.6B). The determined $\Delta\Delta G^{\ddagger}$ values for these mutants in bilayers at the respective pH values of 7 and 5.5 (Figure 5.6C) are consistent with the maximal rates observed at pH 7 and 5.5 by CD (Figure 5.5D). These data suggest that E302A acts as a pH-sensor, lowering the pH-dependent barrier to channel formation, similar to K446M (Figure 5.6C). Interestingly, F427 provides nearly 3 kcal mol^{-1} of free energy to the channel formation mechanism.

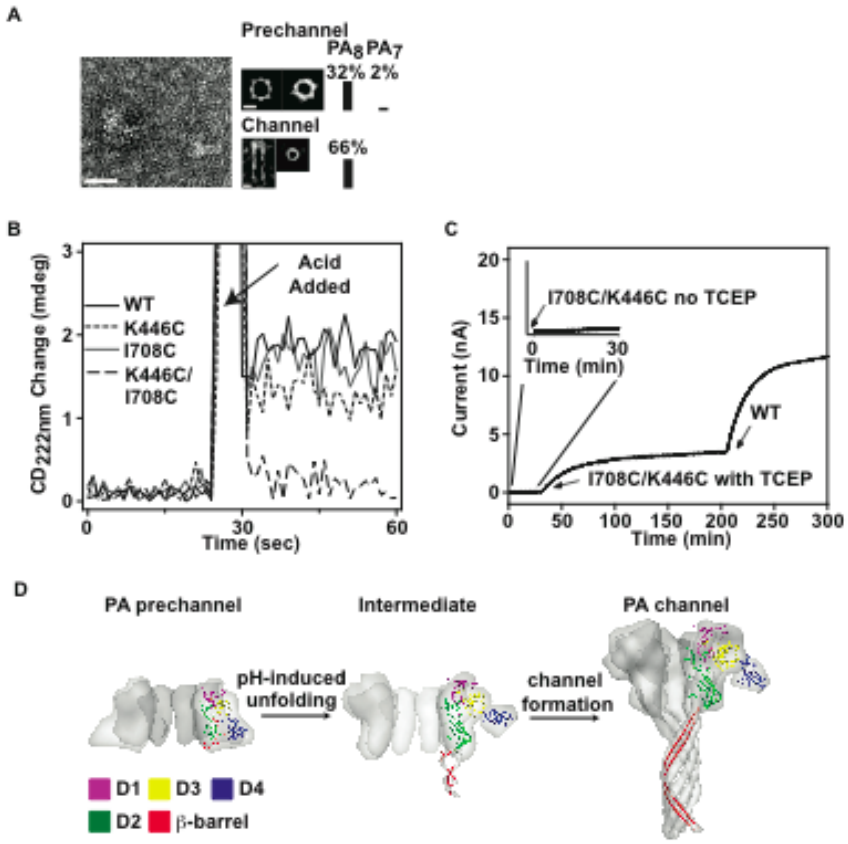

Figure 5.1. D2-D4 unfolding and refolding during channel formation. (A) (left) Electron micrographs of nicked $PA_{\Delta D4}$ assembled in the presence of LF_N at 49000× magnification. A 25-nm scale bar is shown. (right) Analysis of particles (n = 1000) by reference-free alignment, classification, and averaging reveals three classes of PA oligomers: (top, right) PA_7 prechannels (2%; n = 16), PA_8 prechannels (32%; n = 321), (bottom, right) and channels (66%; n = 661). Two different vantages of the channel were evident, a narrow-pore axial view and sagittal view. Percentages of the total oligomer distribution are shown next to representative class averages for each oligomer. A 5-nm scale bar is shown. (B) Time-course measurements of the CD signal change at 222 nm after addition of phosphoric acid (pH 5.5 final) to WT (black), K446C (short dash), I708C (grey), and I708C K446C disulfide-bonded (long dash) PA_7 mutants. The plotted CD signal change is the absolute value of the difference between final and initial CD values. (C) Electrophysiology measurements of PA_7 I708C K446C channel insertion at pH 6.6 in the presence or absence (inset) of TCEP. WT PA_7 was added on the same membrane as the mutants to control for membrane variability. Representative traces are shown from at least three replicates. (D) The prechannel-to-channel transition and the domain structure of PA. A hypothetical model for PA's prechannel-to-channel transition, where D4 separates from D2 as a result of pH changes, allowing the β-strands required for forming the transmembrane β-barrel to unfurl and properly fold into the channel state. Low resolution structures are shown overlayed with the respective PA octamer crystal structure (3HVD) (Kintzer et al., 2009) and a computational model of the PA channel (1V36) (Nguyen, 2004). The relevant functional domains are individually colored. The putative β-barrel forming residues (red) (Nassi, Collier, & Finkelstein, 2002b), which make contacts with domain 4 (blue) are shown.

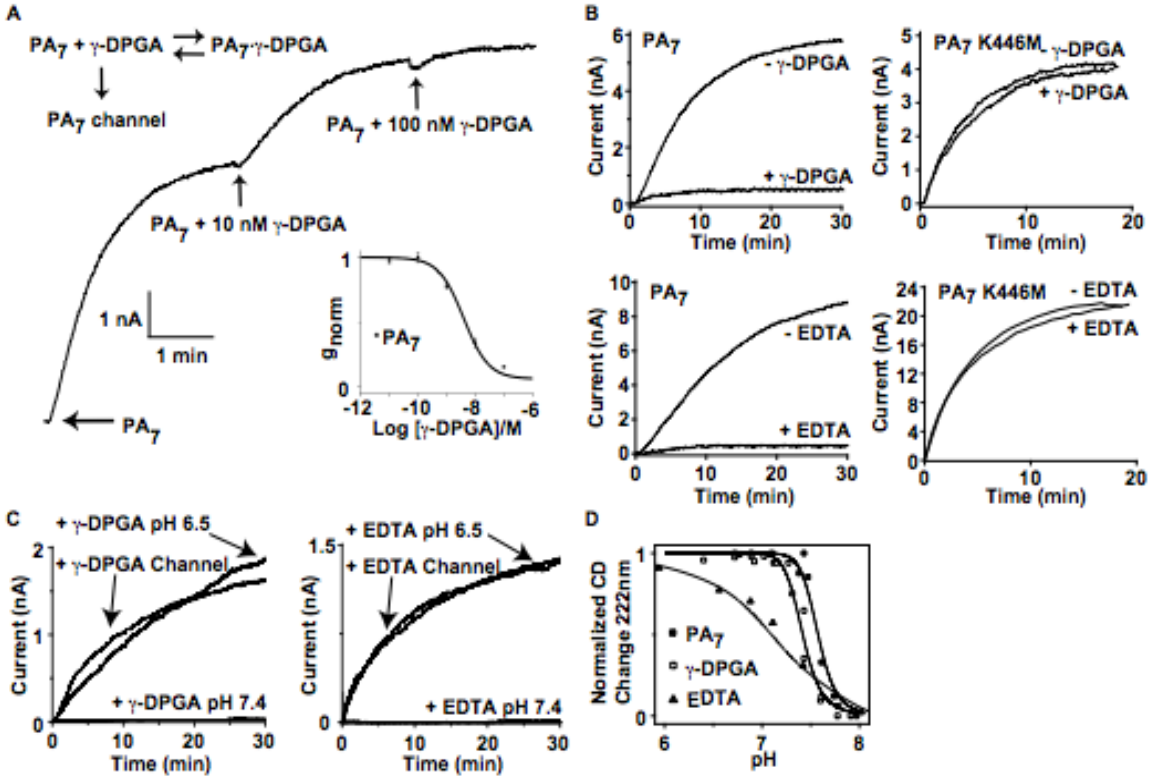

Figure 5.2. γ-DPGA inhibits PA channel formation. (A) An example electrophysiology recording of WT PA_7 channel formation in the presence and absence of γ-DPGA. The upper inset shows a basic kinetic scheme for the inhibition by γ-DPGA or other polymers. The lower inset shows the single-binding site fit (Equation 1) to the inhibition data. (B) Electrophysiology measurements of PA_7 and K446M mutant channel formation at pH 7.4 in the presence or absence of (B, top) 100 nM γ-DPGA or (B, bottom) 1 mM EDTA. (C) PA_7 channel insertion in the presence of (left) γ-DPGA or (right) EDTA, at pH 7.4, 6.5, or using preformed PA channels. Representative traces are shown from at least three replicates. (D) CD measurements of the pH-dependence, from pH 8 to 5, of PA_7 channel formation in the absence (closed square) or presence of 1 μM γ-DPGA (open square) or 10 mM EDTA (closed triangle), at 37˚C. Solid-lines are meant to guide the eye.

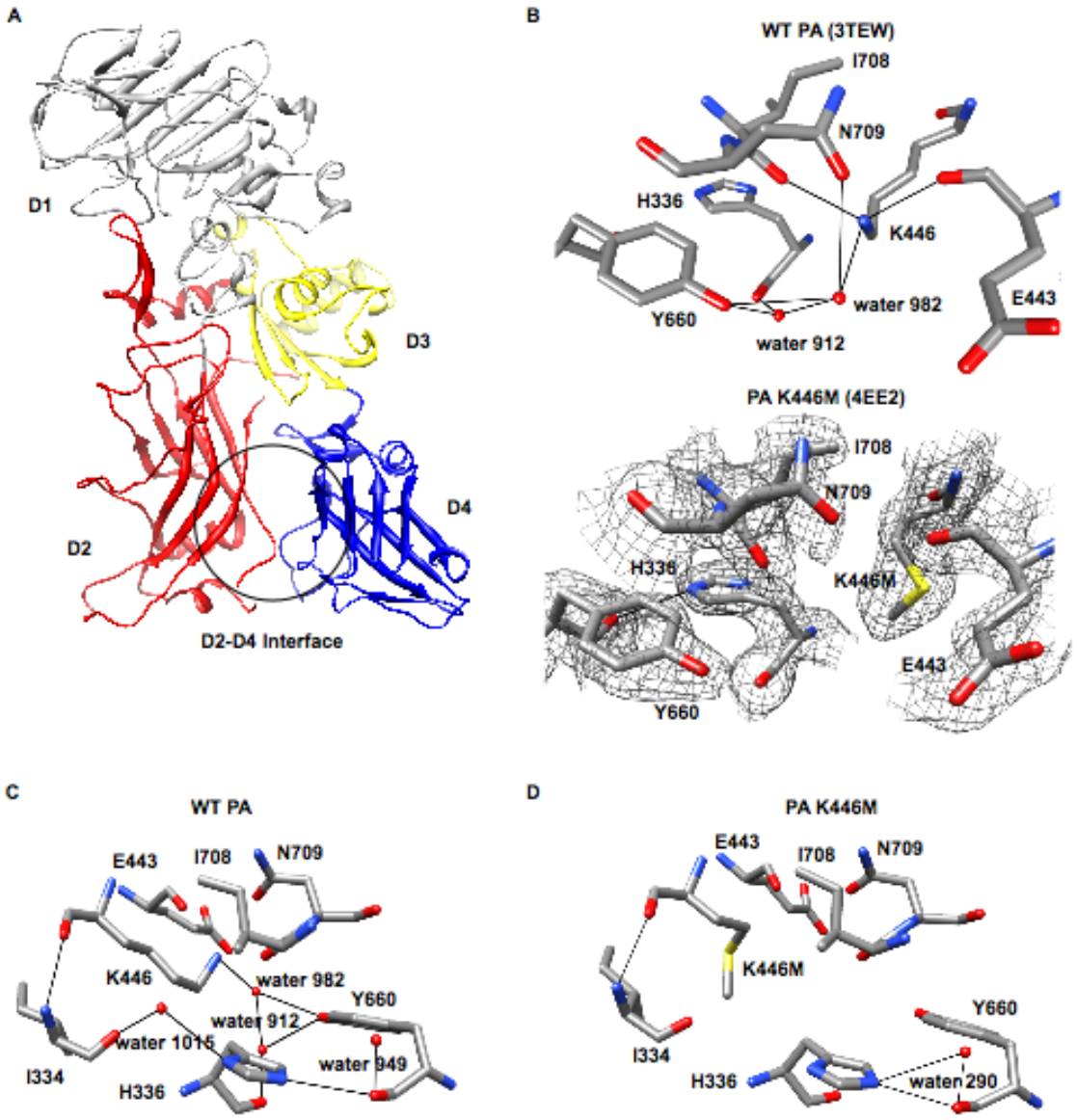

Figure 5.3. Crystal structure of PA K446M reveals disruption of the D2-D4 interface. (A) Structure of the PA_{83} K446M monomer to 1.91Å (4EE2) with domains 2, 3, and 4 highlighted in red, yellow, and blue, respectively. (B) Molecular interactions at the D2-D4 interface of (top) PA_{83} (3TEW) and (bottom) the structure of the K446M mutant are shown. Hydrogen-bonds between water molecules and H336, K446, I708, N709, and Y660 are illustrated in black. $2F_o$-F_c electron density for PA K446M is shown in gray, contoured at 2σ). Depictions of H336 for (C) PA_{83} and (D) K446M are shown to illustrate additional hydrogen-bonding rearrangements.

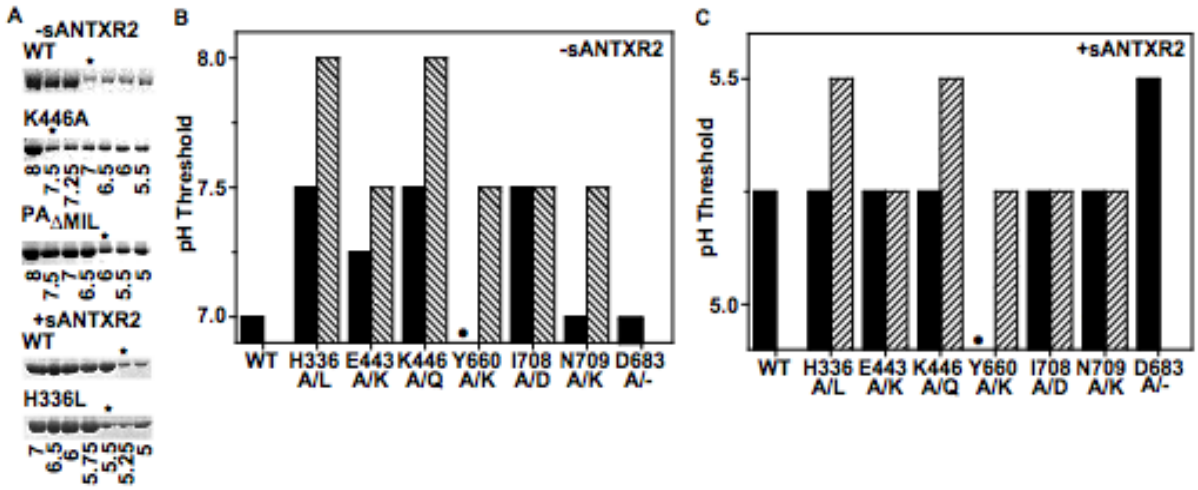

Figure 5.4. Molecular interactions at the D2-D4 interface regulate the pH-dependence of channel formation. (A) SDS-resistance assays performed with mutant PA_7 complexes at 25 ˚C. The pH-threshold for channel formation was estimated on SDS-PAGE gels as a disappearance of the low-molecular-weight SDS-soluble, PA_{63} monomer band (PA_{63}). The estimated pH-thresholds are indicated by (*). Representative gels for WT, ΔMIL, and K446A complexes in the (A, top) absence and (A, bottom) presence of sANTXR2 are shown. Several mutants were measured at each position to determine the sidechain specificity. Representative alanine mutants (black) and the most destabilized mutant (striped) at each position are shown in the (B) absence and (C) presence of sANTRX2 receptor. (●) The threshold for PA_7 Y660A could not be measured because it formed channels at every pH tested. The D683A mutant is shown as a negative control for ANTXR2-binding.

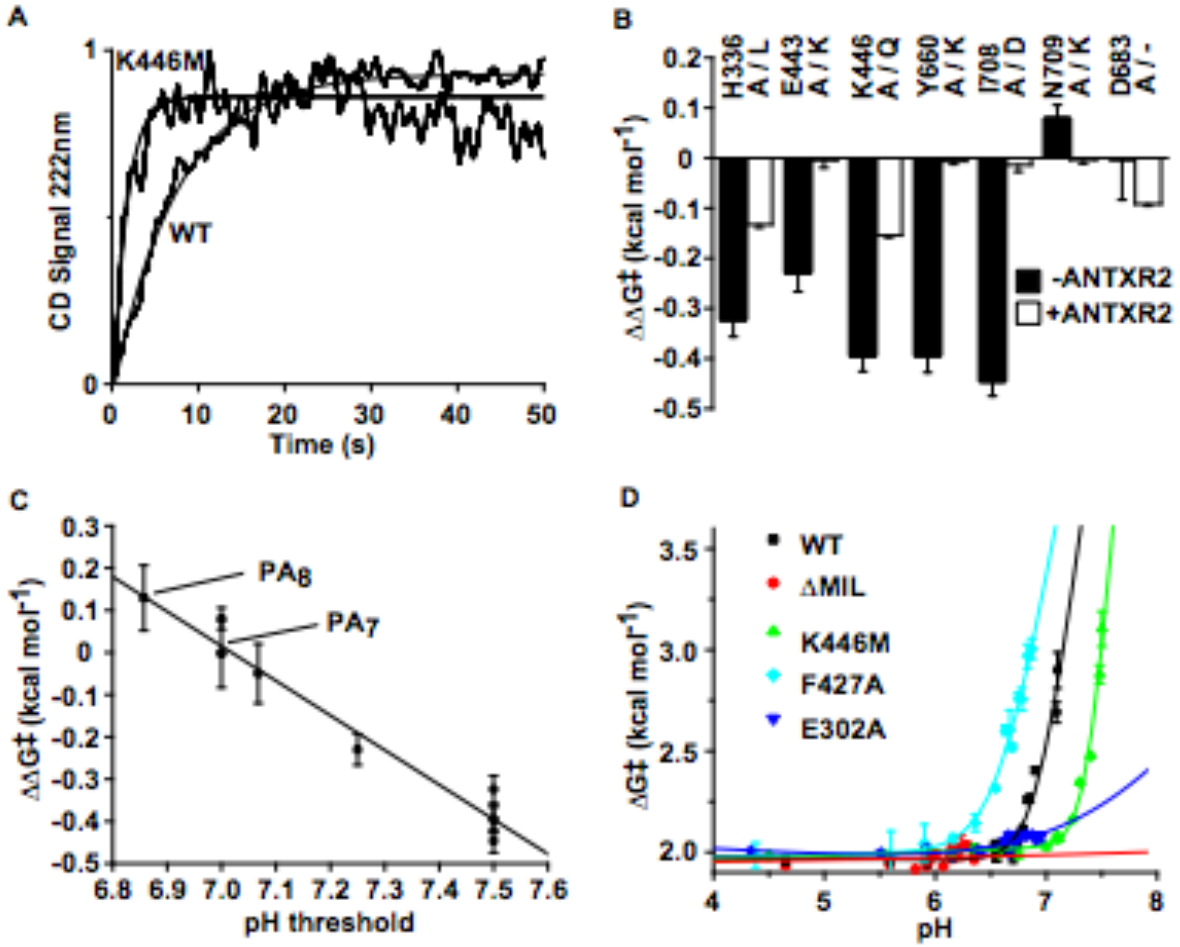

Figure 5.5. Dissociation of domains 2 and 4 is the rate-limiting step for channel formation. Circular dichroism measurements of channel formation rates. (A) Kinetic traces of the CD_{222} signal in response to a pH-jump from 7.5 to 6.6 for WT PA_7 and K446A mutant. Rate constants were determined from fits to a single-exponential function (Equation 1) and are shown in black. (B) Thermodynamic contribution of residues at the interface of D2-D4 to the rate of channel formation in the (black bars) absence and (white bars) presence of sANTXR2. Transition-state free energies differences between mutant and PA_7 complexes ($\Delta\Delta G^{\ddagger} = \Delta G^{\ddagger}_{MUT} - \Delta G^{\ddagger}_{WT}$) were calculated from kinetic rate constants using Equation 2. Each data point is the average of five independent experiments. Error bars represent propagated errors from the standard deviation in the mean of at least three measurements. (C) Correlation of kinetic rates with equilibrium pH-threshold measurements. A plot of the $\Delta\Delta G^{\ddagger}$ value for each PA mutant versus pH-threshold. The linear fit line is shown in black ($R^2 = 0.98$) and was used to calculate pH-thresholds for PA_7 and PA_8, indicated by arrows. Errors for the calculated pH-thresholds were propagated from the errors on the linear fit parameters. (D) Analysis of the pH-dependent kinetic barriers to channel formation. A plot of $\Delta G^{\ddagger}$ values versus pH. $\Delta G^{\ddagger}$ values were calculated from rate constants, measured from pH 7.5 to 5, for PA_7 (black) complexes and ΔMIL (red), E302A (blue), F427A (cyan), and K446M (green) mutants. Solid lines represent fits to a function with two pH-dependent barriers (Equation 3).

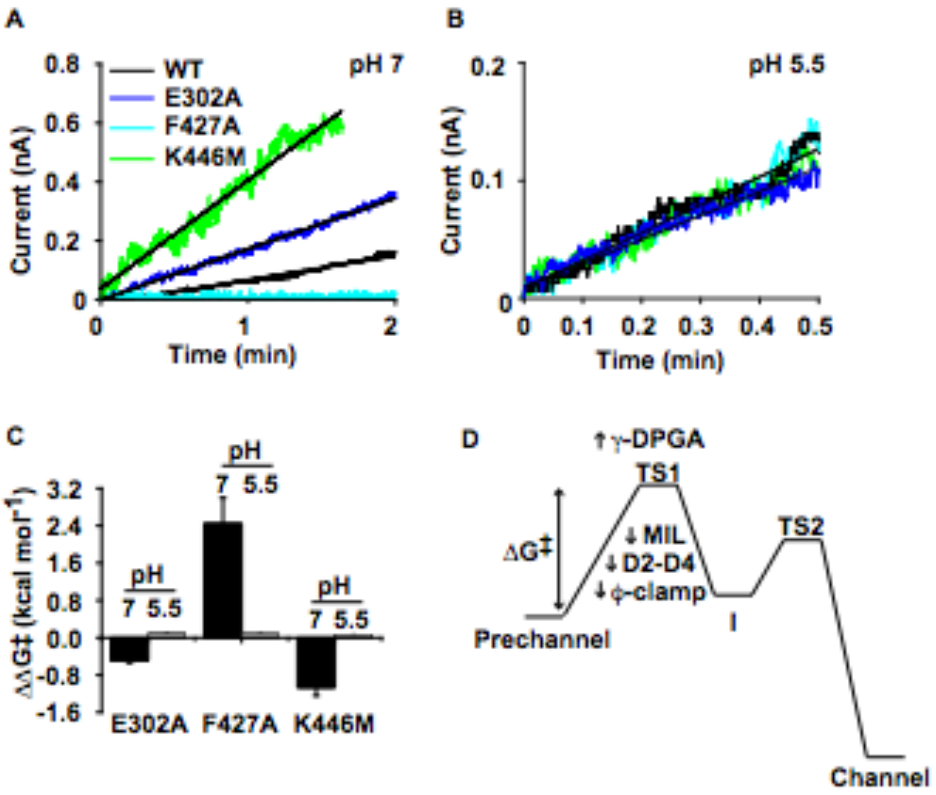

Figure 5.6. Molecular basis for the pH-dependence of PA channel formation. Electrophysiology measurements of PA_7 (black), E302A (blue), F427A (cyan), and K446M (green) mutant channel insertion rates at (A) 7 and (B) 5.5. Initial rates are shown with linear fit lines colored in black. (C) Transition-state free energy differences, $\Delta\Delta G^{\ddagger}$, between mutant and WT complex channel formation using initial rate measurements at pH 7 and 5.5. Initial rates (channels/min) were corrected for the relative single-channel conductance of mutant complexes. Error bars represent the standard deviation in the mean of three independent measurements. (D) A schematic barrier diagram for PA channel formation. The effects of pH, D2-D4 destabilization, ϕ clamp, and γ-DPGA on the pH-dependent free-energy barrier, $\Delta G^{\ddagger}$, are shown. Arrows indicate the respective contribution of these factors in lowering or raising the pH-dependent barrier's transition-state (TS1) free energy. A pH-independent barrier also exists, following a putative intermediate (I) species, passing through a second transition-state (TS2), which presumably involves β-barrel formation.

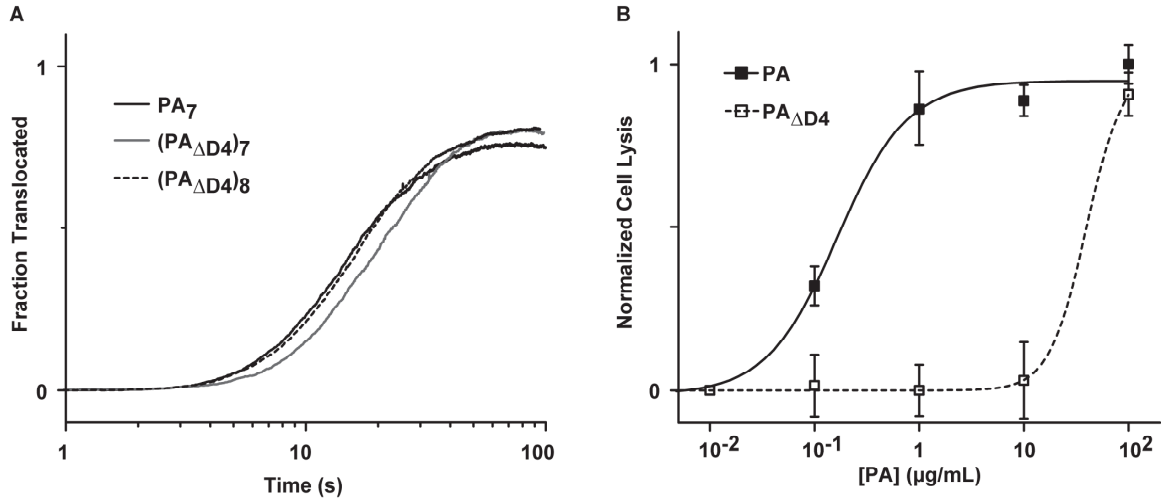

Figure 5.7. $PA_{\Delta D4}$ forms functional complexes. (A) Electrophysiology measurements of PA translocase activity. WT PA_7 (black), $(PA_{\Delta D4})_7$ (grey), and $(PA_{\Delta D4})_8$ (dashed) were compared for their ability to translocate LF_N in planar lipid bilayers at pH 5.6 under a 50 mV $\Delta\psi$. All three constructs translocate LF_N with similar rates, as judged by the time it takes to translocate half the protein in seconds ($t_{1/2}$). The $t_{1/2}$ values are given as mean values ±s.d.; WT PA_7 $t_{1/2}$ = 14 (±1), $(PA_{\Delta D4})_7$ $t_{1/2}$ = 19 (±1), $(PA_{\Delta D4})_8$ $t_{1/2}$ = 16 (±1) s. Averaged translocation recordings are shown (n = 3). (B) Cytotoxicity measurements with PA lacking domain 4 ($PA_{\Delta D4}$). WT PA and $PA_{\Delta D4}$ monomers were serially diluted into PBS and applied to macrophages at a constant 1 μg/mL LF concentration. Cell-death was measured after four hours and EC_{50} values were determined to be 0.16 (±0.04) μg/mL and 40 (±2) μg/mL, for WT PA (closed square) and $PA_{\Delta D4}$ (open square), respectively. Error bars are the mean ±s.d. (n = 3).

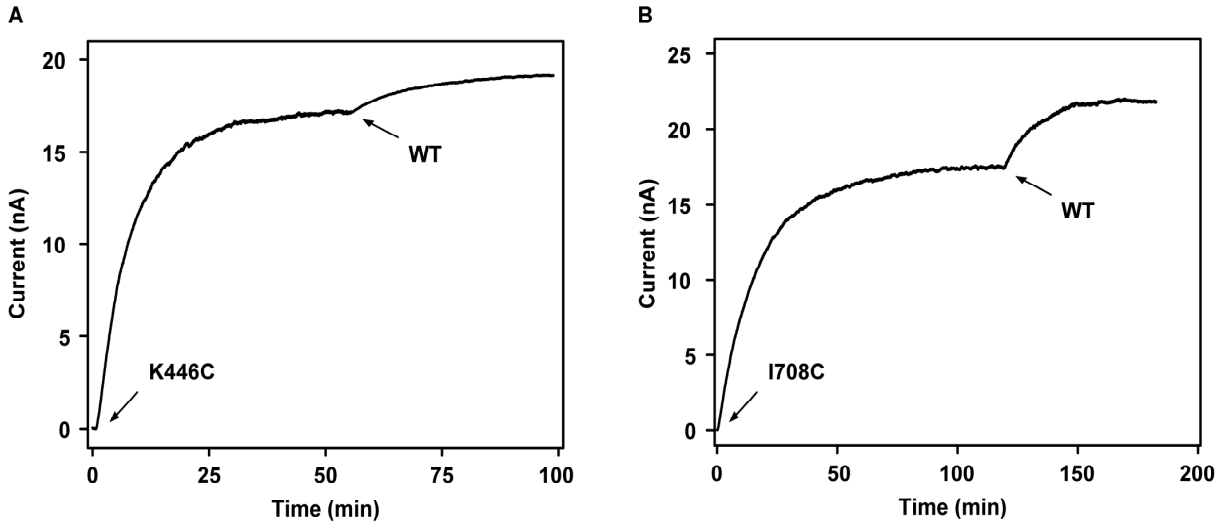

Figure 5.8. Single-Cys control experiments for PA D2-D4 crosslinks. Planar lipid bilayer electrophysiology measurements of PA channel insertion at pH 6.6 for single Cys mutants (A) PA_7 K446C and (B) PA_7 I708C. WT PA was added on the same membrane as the mutants to control for membrane variability. Representative traces are given based on multiple replicates ($n \geq 3$).

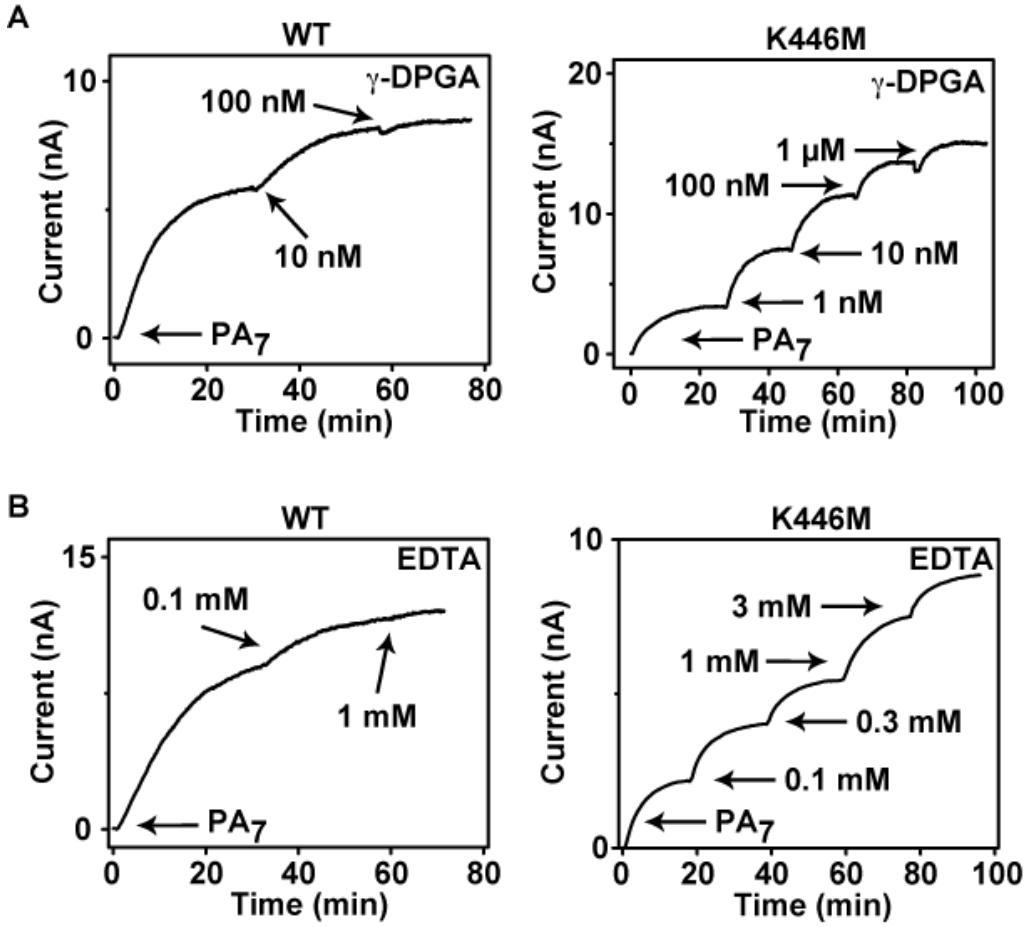

Figure 5.9. Raw electrophysiology traces of PA_7 insertion inhibition. Titrations of (A) γ-DPGA and (B) EDTA using (top) PA_7 WT and (bottom) K446M mutant complexes are shown. 10-100ng PA_7 complexes were added to PLBs bathed in pH 7.4 buffer containing 0-1 μM γ-DPGA or 0-10 mM EDTA. Steady state currents were recorded for estimation of $K_{inhibit}$ values. Representative traces for several successive additions of PA_7 are shown.

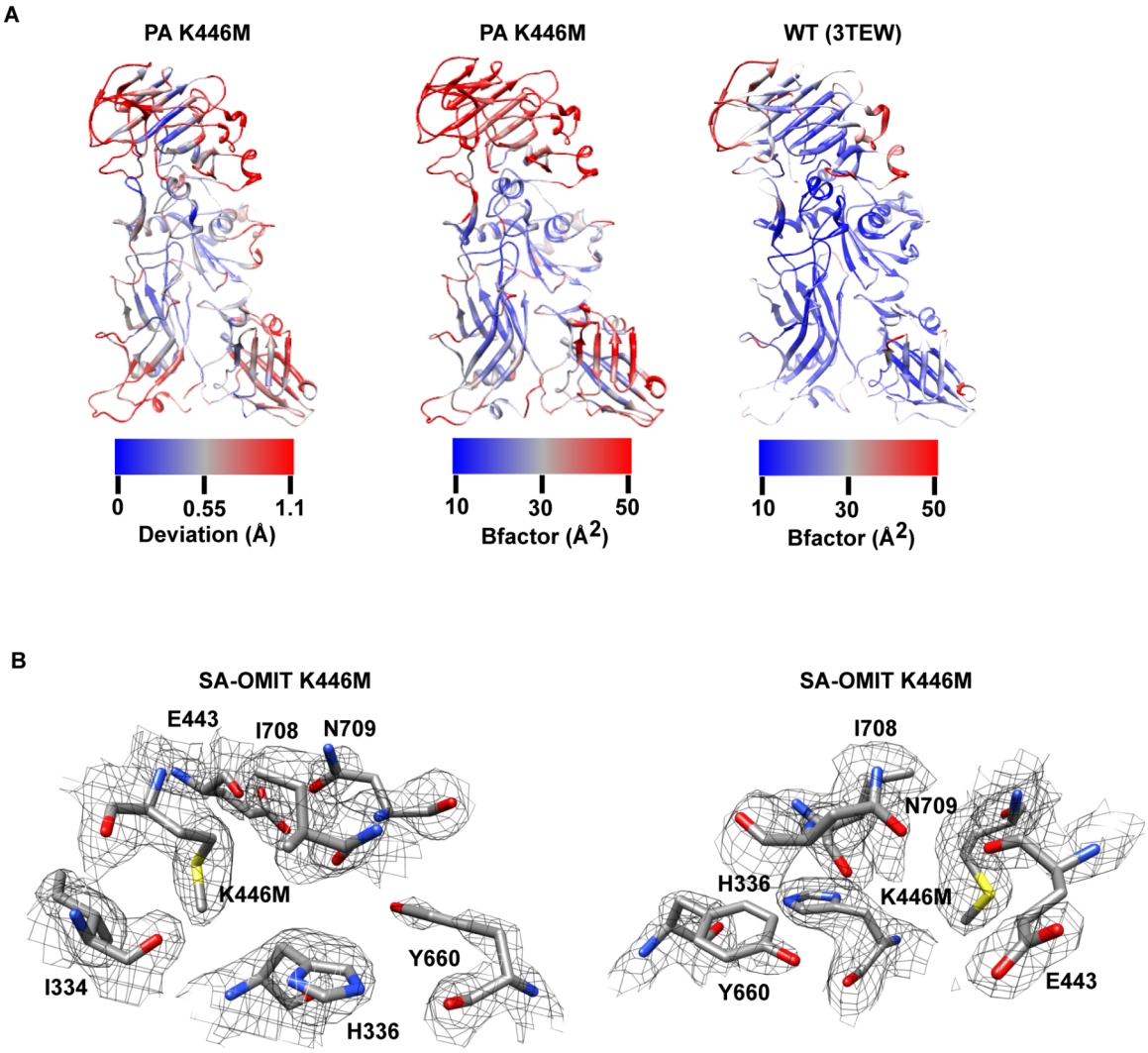

Figure 5.10. PA K446M structure analysis. (A) Structural comparison of PA_{83} (3TEW) (Feld, Kintzer, Tang, Thoren, & Krantz, 2011) and K446M (4EE2). (left) The per-residue deviations between K446M and PA_{83} structures were calculated using LSQKAB (MacDowell et al., 2004) and plotted onto the structure of K446M as a color gradient. Deviations of 0.07 to 1.1 Å are represented by blue-to-red color gradient. The median deviation value of 0.55 Å is set to gray. (middle) Average *B*-factor values per residue are shown for PA K446M and (right) PA_{83} (3TEW), plotted as a blue-to-red color gradient ranging from 10 to 50 $Å^2$. The midpoint *B*-factor value of 30 $Å^2$ is set to gray. Color gradients were created and rendered as attributes in CHIMERA (Pettersen et al., 2004a). (B) Simulated-annealing (SA) omit electron density maps contoured at 1σ are shown. The $2F_o$-F_c maps were generated by a standard SA refinement procedure in PHENIX (Adams et al., 2004b).

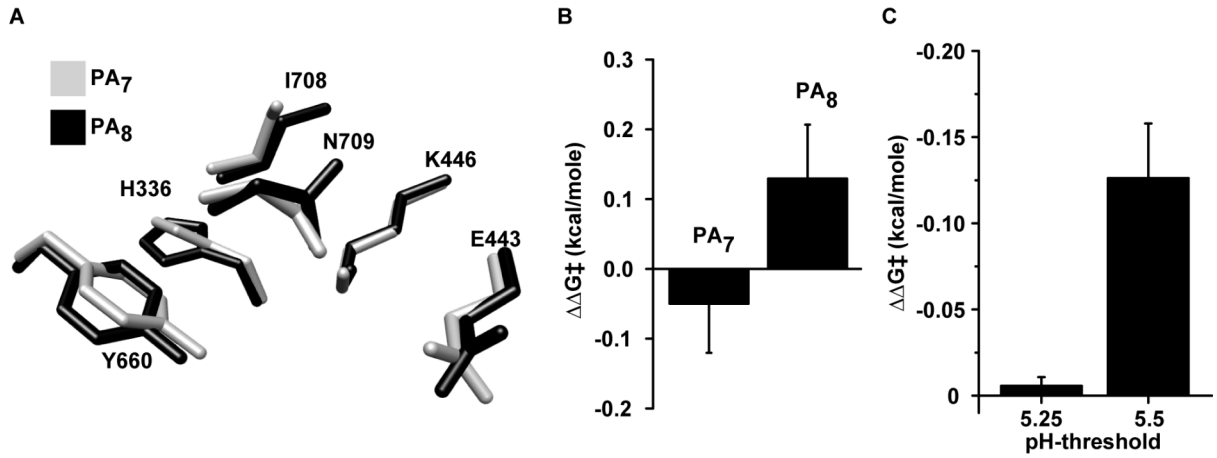

Figure 5.11. Structural basis for thermostability differences between PA_7 and PA_8 oligomers. (A) Structural alignment of the D2-D4 interface of PA_7 (1TZO, gray) (Lacy, Wigelsworth, Melnyk et al., 2004) and PA_8 (3HVD, black) (Kintzer et al., 2009) shown in sticks. (B) The activation free energy ($\Delta G^{\ddagger}$) for the prechannel-to-channel transition of PA_7 and PA_8 is shown. $\Delta\Delta G^{\ddagger}$ values were calculated from rate constants determined by CD kinetic measurements. (C) Activation free energy changes ($\Delta\Delta G^{\ddagger}$) correlate with equilibrium pH-threshold measurements for PA_7-ANTXR2 complexes. A plot of average $\Delta\Delta G^{\ddagger}$ values for all mutants versus their pH-thresholds, as determined by SDS-resistance (Table 5.1). Error bars represent the mean (±s.d.) for all mutants tested, where $n = 5$ for each mutant.

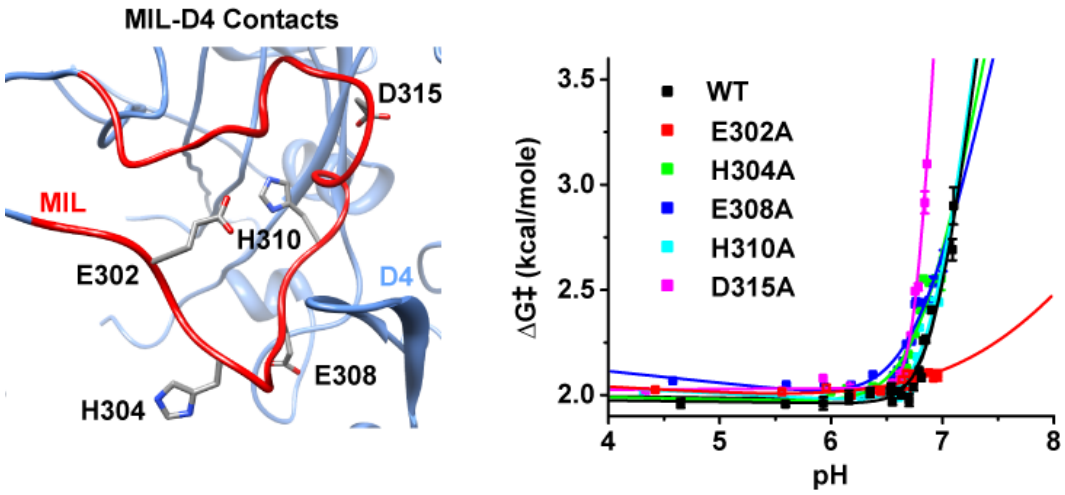

Figure 5.12. Charged residues in the MIL regulate pH-dependent channel formation kinetics. (left) A model for MIL-D4 contacts based on the PA_7 structure (1TZO) (Lacy, Wigelsworth, Melnyk et al., 2004). The charged residues in the MIL are shown (red). D4 is shown in blue. (right) CD channel formation kinetics for each charged MIL mutant are shown. Channel formation rate constants were measured for each MIL mutant at 50 nM PA_7 after lowering the pH from 7.5 to 4.5 with 1 M phosphoric acid. Rate constants were converted to transition state free energies (ΔG‡) for analysis of thermodynamic parameters. Fits to a pH-dependent two-barrier model are shown as solid lines. Error bars represent the standard deviation in the mean of at least three measurements.

Table 5.1. PA Channel Insertion Inhibition and Blocking by Polyanionic Compounds.

Ligand	K_{block}[a]	$K_{inhibit}$[b]
EDTA	78 (±2 mM)	0.31(±0.1 mM)
EGTA	25 (±6 mM)	0.56 (±0.3 mM)
γ-DPGA[c]	5.5 (±2 μM)	34 (±8 nM)
γ-DPGA 10mer	0.6 (±0.1mM)	0.1 (±0.1 mM)
γ-DPGA 2mer	20 (±2 mM)	2 (±0.5 mM)
Heparin sulfate[d]	1.1 (±0.1 mM)	20 (±6 μM)
IP6	4.8 (±1 mM)	0.87 (±0.2 μM)

[a] K_{block} is the concentration required to block one half of the open PA channels.
[b] $K_{inhibit}$ is the concentration required to inhibit insertion of one half of the maximum possible PA channels.
[c] K_{block} and $K_{inhibit}$ values for γ-DPGA were calculated based on their average molecular weights of 100,000 g/mol

Table 5.2. PA_{83} K446M (4EE2) Crystal Statistics.

Resolution Range (Å)	40.71-1.91 (1.94-1.91)
<I/σ(I)>	31.4 (2.5)
R_{sym}	0.111 (0.506)
Unique Reflections	61138
Redundancy	4.0 (3.7)
Completeness (%)	98.9 (96.1)
Space Group	$P2_12_12_1$
a, *b*, *c* (Å)	71.216, 93.512, 116.918
α, β, γ (°)	90, 90, 90
R_{free} (%)	26.67
R_{work} (%)	23.05
Solvent content (%)	47.55
Matthews Coefficient (Å^3/Da)	2.35
Wilson B (Å^2)	28.41
Water molecules	157
Bonds rmsd (Å)	0.0069
Angles rmsd (°)	1.075
Average *B Factor*	44.80
Ramachadran	(%)
Favored	97.4
Allowed	2.6
Disallowed	0
Molprobity Clashscore	8.13

Last resolution shell statistics are shown in parentheses. $R_{sym} = \Sigma|I - \langle I \rangle| / \Sigma I$, where I is intensity. $R_{work} = \Sigma||Fo| - |Fc|| / \Sigma|Fo|$. R_{free}, the free R-value. Statistics were calculated using PHENIX.

Table 5.3. Channel formation data for PA mutants

PA Residue!	PA Mutant	pH[3]	pH with ANTXR2[4]	Rate constant[5] (s^{-1})	$\Delta G^{\ddagger 5}$ (kcal/mole)	Rate with ANTXR2	$\Delta G^{\ddagger}$ with ANTXR2
WT[1]	--	7	5.25	0.14 (± 0.01)	0.51 (± 0.02)	0.22 (± 0.03)	0.39 (± 0.01)
E443	A	7.25	5.25	0.33 (± 0.01)	0.28 (± 0.03)	0.22 (± 0.06)	0.39 (± 0.01)
	K	7.5	5.25	N.D.[2]	N.D.	N.D.[2]	N.D.
H336	A	7.5	5.25	0.48 (± 0.01)	0.19 (± 0.02)	N.D.	N.D.
	L	8	5.5	N.D.	N.D.	0.37 (± 0.06)	0.25 (± 0.01)
	F	7.5	N.D.	N.D.	N.D.	N.D.	N.D.
	D	7.5	N.D.	N.D.	N.D.	N.D.	N.D.
	R	7.5	N.D.	N.D.	N.D.	N.D.	N.D.
I708	A	7.5	5.25	0.77 (± 0.01)	0.07 (± 0.01)	0.23 (± 0.06)	0.37 (± 0.1)
	C	7.5	N.D.	N.D.	N.D.	N.D.	N.D.
	D	7.5	5.25	N.D.	N.D.	N.D.	N.D.
	N	7.5	N.D.	N.D.	N.D.	N.D.	N.D.
K446	A	7.5	5.25	0.63 (± 0.01)	0.12 (± 0.02)	N.D.	N.D.
	C	7.5	N.D.	N.D.	N.D.	N.D.	N.D.
	E	7.5	N.D.	N.D.	N.D.	N.D.	N.D.
	M	7.5	N.D.	N.D.	N.D.	N.D.	N.D.
	N	8	5.5	N.D.	N.D.	0.41 (± 0.05)	0.23 (± 0.01)
	Q	8	N.D.	N.D.	N.D.	N.D.	N.D.
	R	7.5	N.D.	N.D.	N.D.	N.D.	N.D.
N709	A	7	5.25	0.1 (± 0.01)	0.59 (± 0.01)	0.22 (± 0.03)	0.39 (± 0.01)
	C	7.5	N.D.	N.D.	N.D.	N.D.	N.D.
	D	7.5	5.25	N.D.	N.D.	N.D.	N.D.
	K	7.5	N.D.	N.D.	N.D.	N.D.	N.D.
	M	7	N.D.	N.D.	N.D.	N.D.	N.D.
Y660	F	7.5	N.D.	N.D.	N.D.	N.D.	N.D.
	K	7.5	5.25	0.63 (± 0.01)	0.12 (± 0.02)	0.23 (± 0.03)	0.38 (± 0.01)
N709/K446	K/N	8.5	5.5	N.D.	N.D.	N.D.	N.D.
D683	A	7	5.5	0.14 (± 0.04)	0.51 (± 0.08)	0.32 (± 0.03)	0.29 (± 0.01)

[1] Wild-type PA.

[2] N.D., Not determined.

[3] The pH threshold for channel formation as measured by SDS-resistance.

[4] The pH threshold measured in the presence of soluble ANTXR2.

[5] The first-order rate constant for channel formation as measured by circular dichroism.

[6] A transition-state free energy calculated from the measured rates of channel formation.

5.5 Discussion

Microenvironment sensing of virulence factors. Many opportunistic pathogens utilize proton gradients as chemical cues to efficiently target their effectors to host cells. Changes in pH can trigger conformational changes in a broad class of toxins, causing the formation of transmembrane channels (Donovan, Simon, Draper, & Montal, 1981; Kagan, Finkelstein, & Colombini, 1981; Rozengurt, Higgins, Chanter, Lax, & Staddon, 1990; Schuerch et al., 2005). However, the molecular mechanism of pH-sensing, in many cases, remains unknown.

The protective antigen component of anthrax toxin utilizes endosomal proton gradients as a chemical trigger for channel formation in the endosomal membrane of host cells (Friedlander, 1986). LF and EF are translocated through the PA channel via the proton motive force maintained across the membrane (Krantz et al., 2006). This is an elegant example of how a toxin uses proton gradients to target molecules to the host cytosol. Our studies provide structural (Figure 5.3) and functional (Figure 5.1, 5.2, 5.4, 5.5, 5.6) evidence for the pH-dependent conformational changes involved in PA channel formation.

The PA prechannel-to-channel transition. The PA channel architecture is thought to contain an ~100-Å-long β barrel. To transform into this structure, a β hairpin is contributed by each monomer's D2 (residues 275-350 or 2β1-2β3) (Figure 5.1D). Thus this 2β1-2β3 structure from domain 2 must unfold and then subsequently refold to form the final β-barrel structure in the channel state (Petosa et al., 1997). Ultimately, the hydrophobic tips of the β strands in the barrel plunge into the lipid bilayer, creating an aqueous conduit for the LF and EF components to translocate through to enter the cytosol of the host cell.

A recent EM structure of the channel suggests that the lumen of PA contracts and D2-D4 separate upon channel (Katayama et al.). Previous studies also found residue F427 in an active-site loop critical for its protein translocation function, called the ϕ clamp, converges significantly, collapsing to create a narrow, central channel (Krantz et al., 2005). Moreover, the ϕ-clamp site also affects the efficiency or extent of channel formation (Sun et al., 2008). These reports suggest that contraction of the PA lumen occurs during channel formation. Prior to our studies, it was unclear whether collapse of the central lumen or other pH-dependent conformational changes were rate-limiting. In principle, there are likely several barriers that may define the kinetic mechanism of channel formation (Figure 5.6D). We identified two major barriers: a pH-dependent (pH-sensing) barrier and a pH-independent barrier (Figure 5.5, 6).

The pH-sensing barrier. We suggest that a single charged residue, E302, in the MIL is responsible for the pH-sensing capability of PA (Figure 5.5, 5.6). In the PA_7 prechannel structure, the MIL makes contacts with D4 of the neighboring subunit (Figure 5.12), including several hydrophobic and hydrogen-bonding interactions. This likely defines the deprotonated, resting state, of the MIL. Protonation of E302 may cause a conformational change in the MIL, allowing it to undock from D4, promoting destabilization of the D2-D4 interface and channel formation. We estimate that protonation of E302 lowers the pH-dependent barrier by nearly 1 kcal mol^{-1} from kinetic studies (Figure 5.5, 6). However, further structural studies are required to understand the conformational changes in the MIL that trigger channel formation. The MIL, in addition to forming part of the transmembrane channel structure, may serve as a chemostat, reversibly undergoing conformational changes depending on the protonation state of E302.

The D2-D4 interface controls PA oligomer pH sensing. Here we reveal the importance of the D2-D4 interface in the mechanism of channel formation (Figure 5.1-5.6). The separation of these domains is crucial, rate-limiting, and modulates the pH-dependence. We have shown that D4 is dispensable to the mechanism of channel formation and translocation in vitro and in cellular

assays (Figure 5.7); however, $PA_{\Delta D4}$ prechannels are unable to regulate pH-dependent conformational changes and can form the channel state even at pH 8 (Figure 5.1A).

The molecular contacts between D2 and D4 may serve to stabilize the prechannel and restrict pH-dependent conformational changes required to form the channel. Prior to this study, D4 was thought to be superfluous to PA channel function. We suggest that Interactions involving PA residues H336, E443, K446, Y660, I708, N709, and several water molecules participate in hydrogen bonds that stabilize the D2-D4 interface by nearly 2 kcal mol^{-1} (Figure 5.3, 5.5, 5.6). Our crystal structure of PA K446M suggests a mechanism for channel formation where breaking interactions with K446 disrupts the interface of D2-D4, promoting their separation and channel formation. This is consistent with mutagenesis studies, which suggest that the interactions formed with K446 raise the pH-dependent barrier to channel formation by about 1 kcal mol^{-1} (Figure 5.5, 5.6). In our structure, the K446M substitution severs three hydrogen bonds, propagating flexibility throughout the D2-D4 interface, likely causing it to dissociate (Figure 5.3, 5.10A).

γ-poly-D-Glutamic acid. We additionally suggest a role for the γ-poly-D-glutamic acid capsule in stabilizing PA prechannels (Figure 5.2). Our studies suggest the existence of a molecular binding site on PA, likely involving residues that regulate the pH-dependence of channel formation (Figure 5.2B, Table 5.1). We can crudely place at least part of the γ-DPGA binding site in PA's D2-D4 interface. The stabilization by γ-DPGA may be important for maintaining the thermostability of PA complexes *in vivo*. Further studies will define the binding site of γ-DPGA and determine its functional role in regulating the activity of PA complexes.

Overall mechanism of channel formation. We propose a mechanistic model for PA channel formation that involves the regulation of pH-dependent conformational changes by D2-D4, MIL, ϕ clamp, and γ-DPGA (Figure 5.6D). A possible mechanism begins with protonation of E302 in the MIL, which may undergo conformational changes that destabilize the D2-D4 interface of PA, causing D2 and D4 to dissociate. This leads to contraction of the PA lumen, which is stabilized by interactions between F427 residues at the ϕ-clamp. This defines the rate-limiting, pH-dependent barrier to channel formation (Figure 5.6D). Formation of the putative β barrel has not been studied. However, this likely represents the second, pH-independent barrier that we have identified. Further biophysical studies are necessary to fully define this barrier.

5.4 Materials and methods

Reagents. All chemicals were obtained from Sigma-Aldrich unless otherwise specified.

Proteins. Recombinant wild-type (WT) PA and mutants thereof, were over-expressed in the periplasm of the *Escherichia coli* strain, BL21(DE3) (Kintzer et al., 2009). PA monomers lacking D4 ($PA_{\Delta D4}$) were prepared by the insertion of a stop codon following residue D596. PA monomers were purified from the periplasm (Wigelsworth et al., 2004). Recombinant LF_N (LF's amino-terminal, PA-binding domain, residues 1-263) was overexpressed in BL21(DE3) using a pET15b construct (Lacy et al., 2002) and then purified from the cytosol (Kintzer et al., 2009; Thoren et al., 2009). Site-directed mutagenesis was performed using the commercial Quikchange procedure (Agilent Technologies). The six-histidine affinity tags were removed from LF_N by treatment with bovine α-thrombin (Thoren et al., 2009). The soluble human ANTXR domain from the capillary morphogenesis protein 2 (sANTXR2) was overexpressed in BL21(DE3) as a C175A mutant, using a pET15b construct and purified from the cytosol (Kintzer, Sterling, Tang, Williams et al., 2010).

Isolation of PA oligomer complexes. WT PA_7 and PA_8 complexes were produced as described (Kintzer, Sterling et al., 2010b; Kintzer et al., 2009). Briefly, PA monomer was nicked with bovine trypsin (BT) at a 1:1000 wt/wt (BT:PA) ratio at room temperature for 10 minutes. Soybean trypsin inhibitor (STI) was added at a 1:100 wt/wt (STI:PA) ratio to inhibit the protease. The resulting nicked PA was purified over Q sepharose anion exchange, allowing PA to assemble into highly-enriched PA_7 prechannel complexes (Kintzer et al., 2009). $PA_{\Delta D4}$ complexes were prepared by an alterative method, where the trypsin-nicked $PA_{\Delta D4}$ was co-assembled with LF_N and further purified by S200 gel filtration chromatography in Buffer A (20 mM Tris, 150 mM NaCl, pH 8) (Kintzer et al., 2009). This produces 70-80% $(PA_{\Delta D4})_7$ complexes and was used for electrophysiology and electron microscopy (EM) studies. $(PA_{\Delta D4})_8$ complexes were purified from this mixture by first dialyzing against 10 mM Tris pH 8 and then purifying over S400 gel filtration in Buffer A. Sample homogeneity was verified by EM and nanoelectrospray ionization mass spectrometry (Kintzer et al., 2009). $(PA_{\Delta D4})_7$ complexes under these solution conditions already formed channels in solution, which precluded their analysis by mass spectrometry. $(PA_{\Delta D4})_8$ complexes remained in the prechannel state under these conditions, however. SDS-resistance assays using PAGE were performed as required to identify prechannel-to-channel transitions for PA_7 complexes (Kintzer, Sterling et al., 2010b; Kintzer, Sterling, Tang, Williams et al., 2010; Miller et al., 1999).

Isolation of the γ-poly-D-glutamic acid capsule. Bacillus licheniformis (ATCC 9945A, Manassas, VA) was cultivated to produce γ-DPGA. Employing sterile techniques, cultures were grown in the presence of Mn^{2+}, which has been shown to regulate the resulting polymeric chirality, as described (Cromwick & Gross, 1995). Liquid cultures were grown in flasks shaking at ~200 rpm until OD_{600} exceeded 4, or for roughly 90 hours. The culture was spun down and pellets discarded. The supernatant was boiled for 10 minutes to denature any depolymerases and then cooled to 4 °C. The cooled supernatant was added to four volumes cold ethanol and slowly stirred for ~6 hours at 4 °C. γ-DPGA was collected by centrifugation, resuspended and dialyzed against H_2O to remove contaminating salts. The resulting γ-DPGA was filtered, lyophilized, dissolved in water, brought to pH 7.4 with KOH, and stored at -80 °C. The γ-DPGA produced by *B. licheniformis* ranged from 50 to 200 kDa (Cromwick & Gross, 1995). γ-DPGA is not stained by Coomassie like α-linked proteins but is stained by methylene blue (Candela & Fouet, 2005). Samples were run on SDS-PAGE gels and stained with Coomassie Blue R250 to test for the presence of contaminating proteins. Gels were then stained with 0.002 % (w/v) methylene blue in 0.1 × TAE (4 mM Tris - Acetate, 0.1 mM EDTA) buffer to visualize γ-DPGA.

Synthetic γ-DPGA oligomers. Synthetic 90 % pure γ-DPGA 10mers and 20mers were obtained from Biopeptide Co., Inc. (San Diego, CA) and used without further analysis or purification. A synthetic, pure γ-DPGA dipeptide was obtained from Bachem Americas, Inc. (Torrance, CA).

Electron microscopy. PA complexes applied to a freshly glow-discharged 400 mesh formvar-carbon coated grids and stained with 2% uranyl acetate (Sigma-Aldrich, St. Louis, MO) as previously described (Kintzer, Sterling et al., 2010b; Kintzer, Sterling, Tang, Williams et al., 2010; Kintzer et al., 2009). Negative-stain EM images were recorded on a Tecnai 12 electron microscope (FEI Company, Hillsboro, OR) operated at 120 kV at a magnification of 49,000× using a CCD camera. The micrograph resolution was 2.13 Å/pixel. Particle images were selected using boxer in EMAN (Ludtke et al., 1999). Boxed images of the PA oligomer particles were subjected to successive cycles of reference-free and reference-based alignment, multivariate statistical analysis, and classification using SPIDER, (Frank et al., 1996; Stark et al., 1995; van Heel et al., 1996) as described (Kintzer, Sterling et al., 2010b; Kintzer, Sterling, Tang, Williams

et al., 2010; Kintzer et al., 2009). Final class-average images were manually inspected to determine their oligomeric state and tabulated to determine the oligomeric composition of each sample. Less than 5% of the classified particles were not able to be recognized and were rejected as "junk" images.

Circular dichroism spectroscopy. Circular dichroism (CD) measurements of the PA channel transition were obtained on a JASCO Model 810 spectropolarimeter (JASCO, Inc., Easton, MD) (Kintzer, Sterling et al., 2010b; Kintzer, Sterling, Tang, Williams et al., 2010). The pH-dependence of PA channel formation was measured as described previously (Kintzer, Sterling et al., 2010b). Briefly, PA_7 complexes were diluted to 50 nM 10 mM potassium phosphate, 10 mM potassium acetate, 0.1 M potassium chloride, pH 8 in the presence or absence of 1 μM γ-DPGA or 10 mM EDTA at 37˚C. Recordings of the CD_{222nm} signal were conducted at a 1-Hz sampling rate. During the recording, the pH of the sample was reduced by adding 1 M phosphoric acid to obtain the desired pH. The final pH of the sample in the cuvette was determined using a pH meter.

For kinetic, pH-jump measurements, sub-second mixing times were achieved using a Hamilton Microlab 500 titrator (Hamilton, Reno, NV), which rapidly delivered 10-20 μL aliquots of 1 M phosphoric acid into the cuvette under vigorous stirring by a small Teflon stir bar. The final pH was recorded following each measurement. Five kinetic transients were collected and averaged for each rate measurement. Amplitude (A) versus time (t) data were then fit to a single exponential,

$$A(t) = A_o \exp(-kt) + c \quad \text{(Equation 1)}$$

where A_o is the signal amplitude at time zero, c is an offset, and k is the observed first-order rate constant. Rate constants were converted to Gibbs free energies,

$$\Delta G^{\ddagger} = -RT\ln k \quad \text{(Equation 2)}$$

where R is the universal gas constant and T is temperature. $\Delta G^{\ddagger}$ values were compared among PA mutants that could perturb the barrier to channel formation. To estimate the pH-dependent barriers, plots of $\Delta G^{\ddagger}$ were fit to an equation describing two pH-dependent barriers,

$$\Delta G^{\ddagger} = -RT\ln((\exp(\Delta G^{\ddagger}_1 - n_1(\text{pH-pH}_0))/RT) + (\exp(\Delta G^{\ddagger}_2 - n_2(\text{pH-pH}_0))/RT)) \quad \text{(Equation 3)}$$

where $\Delta G^{\ddagger}_1$ and $\Delta G^{\ddagger}_2$ are the free energy barriers, referenced at pH_0, and n_1, n_2 are the number of protons involved in the transition. Table 5.3 summarizes all fit parameters for all the tested PA complexes.

Crystallization, X-ray diffraction, and refinement. PA K446M monomers were purified over S200 gel filtration in 20 mM Tris, 150 mM NaCl, pH 8. Initial crystals were obtained from sparse mANTXRix screening via a Mosquito nanoliter robot (TTP Labtech, Cambridge, MA) in 100 nL hanging drops at 19 ˚C using the vapor-diffusion method. Diffraction quality crystals were obtained in 2 μL hanging drops by mixing protein at 29 mg/mL PA K446M monomer 1:1 with the well solution (100 mM Tris pH 8-8.8, 15-25% (w/v) polyethylene glycol monomethyl ether 2000 Da average molecular weight, 200 mM trimethylamine *N*-oxide). Large, rectangular rods grew over two to three days to dimensions of 0.5-1 mm. Crystals were harvested in a one-to-one mixture of well solution and cryoprotectant (50% (w/v) polyethylene glycol 400 Da average molecular weight) and plunged into liquid N_2. X-ray diffraction data were collected at a wavelength of 1.1159 Å (11,111 eV) at 100 K at the Advanced Light Source at the Lawrence Berkeley National Laboratory (beamline 8.3.1) on a Quantum 315r CCD detector (MacDowell et al., 2004). A single crystal, belonging to the $P2_12_12_1$ space group, diffracted X-rays to 1.9 Å with unit-cell dimensions, a = 71.216, b = 93.512, and c = 116.918 Å (Table 5.2). The diffraction data were indexed and scaled in HKL2000 (Otwinowski & Minor, 1997). The PA K446M structure

was solved by molecular replacement (MR) using PHASER (Storoni, McCoy, & Read, 2004b) in CCP4 (Dodson, Winn, & Ralph, 1997). The MR search model was a single loop-stripped PA monomer from the protein databank (PDB) accession code 1ACC (Petosa et al., 1997). A single PA monomer was found in the asymmetric unit. Initial rigid-body refinement was performed in PHENIX (Adams et al., 2004a), followed by multiple rounds of main chain, residue, and solvent modeling in COOT (Emsley & Cowtan, 2004b). Residues with appreciable $2F_o$-F_c electron density (>1σ) were modeled manually, using composite simulated-annealing omit electron density computed in PHENIX to confirm residue placement. Refinement of individual coordinates and individual atomic displacement parameters (or *B* factors) allowed the convergence of R_{free} and R_{work} values. The final model's overall geometry was assessed using MOLPROBITY (Davis et al., 2007). The coordinates and structure factors for PA K446M have been deposited in the Protein Data Bank (PDB) with accession code 4EE2.

Planar lipid bilayer electrophysiology. Voltage-clamp planar-lipid bilayer electrophysiology experiments were performed using an Axoclamp 200B amplifier and CLAMPEX10.2 software (Molecular Devices, Sunnyvale, CA) (Kintzer, Sterling et al., 2010b; Kintzer et al., 2009). Data were acquired at 400 Hz and low-pass filtered at 200 Hz. Data analysis was carried out with CLAMPFIT (Molecular Devices) and ORIGIN6.1 (OriginLab Corp., Northampton, MA). A planar lipid bilayer was painted using a 3% solution of the lipid 1,2-diphytanoyl-*sn*-glycerol-3-phosphocholine (Avanti Polar Lipids, Alabaster, AL) dissolved in neat *n*-decane inside a 100 μm aperture of a 1 ml, white delrin cup bathed in universal bilayer buffer (UBB, 10 mM oxalic acid, 10 mM MES, 10 mM phosphoric acid, 1 mM EDTA, 100 mM KCl) (Kintzer et al., 2009). The membrane potential (Δψ) was held at +20 mV unless specified otherwise.

For disulfide cross-linked PA insertion experiments, 10 μL of PA was diluted to 100 nM into buffer with or without 1 mM of Tris(2-carboxyethyl) phosphine HCl (TCEP) prior to adding to the cis chamber, which was bathed in UBB at pH 6.6. Control aliquots of WT PA were added to the same membrane in these experiments to confirm membrane quality and integrity in situ.

To measure the effect of polyanionic compounds on PA channel formation and insertion at physiological pH, PA_7 was added to the *cis* chamber, bathed in 30 mM buffer (10 mM pipes, oxalic acid, and phosphoric acid), 0.1 M KCl, pH 7.4, to 10 ng/mL in the presence or absence of pH 7.4 solutions of γ-DPGA, γ-DPGA oligopeptides, IP6 (phytic acid), and heparin sulfate (sodium salt from porcine intestinal mucosa). Insertion was allowed to proceed for 30-60 minutues, until the current reached a steady-state. Steady-state current values were determined for PA_7 in the absence and presence of additives to determine the relative insertion efficiency. For determining channel blocking (K_{block}) and inhibition (K_{inhbit}) constant, additive solutions were titrated in the cis compartment. K_{block} was determined fraction of steady-state current blocked in response to the titration of polyanionic compounds, from a constant population of inserted channels. K_{inhbit} was determined from repeated measurements of PA_7 steady-state insertion activity at increasing concentrations of polyanionic compounds. The fractions of blocked or inhibited channels were fit to the single-site binding model,

$$f = 1/(1+K/[L]) \quad \text{(Equation 4)}$$

where *f* is the fraction of inhibited or blocked channels, *K*, the equilibrium constant and, [L], the ligand concentration. Results are summarized in Table 5.1.

Lethal toxin macrophage cytotoxicity assays. LT cytotoxicity was monitored by an enzyme-coupled lactate dehydrogenase release assay (Decker & Lohmann-Matthes, 1988b). Immortalized bone marrow macrophages from 129 mice were grown to confluence in RPMI 1640 medium (Invitrogen, Inc.) supplemented with 10% fetal bovine serum (Invitrogen), 100

units/mL penicillin (Sigma-Aldrich), and 100 μg/mL streptomycin (Sigma-Aldrich) in a humid, 5%-CO_2 atmosphere at 37 ˚C. One day prior to conducting assays, cells were trypsinized and replated at a density of 10^5 cells/well. Cells were treated with a constant amount of LF (1 μg/mL) and varying concentrations of PA (0.01-100 μg/mL) in ice-cold PBS. The toxin-treated cells were then incubated for 4 hours at 37 ˚C. Triplicate assays were performed for each condition. Cells were then centrifuged at 1400 RPM. The supernatant was removed and assayed colorimetrically according to a prior method (Kintzer, Sterling et al., 2010b) using an spectrophotometric microplate reader (Bio-Rad Laboratories, Richmond, CA) at a wavelength of 490 nm. The change in the absorbance signal is proportional to the number of lysed cells, where the amount of LDH released was normalized to the value obtained in wells treated with 1% Triton X-100 detergent. Effective-concentration-for-50%-lysis values (EC_{50}) were determined by fitting the normalized cell-lysis-versus-PA-concentration data in ORIGIN6.1.

Planar lipid bilayer electrophysiology translocation experiments. LF_N translocation experiments were carried out as described (Kintzer et al., 2009). Briefly, PA complexes were diluted to 100 nM in 20 mM Tris pH 8, 150 mM NaCl and added to the cis chamber at a final concentration of 100 pM at a $\Delta\psi$ of 20 mV in UBB, pH 5.6. Excess PA was removed by perfusion with 10 volumes of UBB and LF_N was then added at 20 nM to achieve >99 % channel blockage. Free LF_N was removed by perfusion with 10 volumes of UBB and translocation was initiated by stepping the $\Delta\psi$ to +50 mV. The translocation kinetics were quantified by determining the time for half of the protein to translocate ($t_{1/2}$) (Kintzer et al., 2009).

References

Abrami, L., Kunz, B., & van der Goot, F. G. (2010). Anthrax toxin triggers the activation of src-like kinases to mediate its own uptake. *Proc Natl Acad Sci U S A, 107*(4), 1420-1424.

Abrami, L., Liu, S., Cosson, P., Leppla, S. H., & van der Goot, F. G. (2003). Anthrax toxin triggers endocytosis of its receptor via a lipid raft-mediated clathrin-dependent process. *J. Cell Biol., 160*(3), 321-328.

Adams, P. D., Gopal, K., Grosse-Kunstleve, R. W., Hung, L. W., Ioerger, T. R., McCoy, A. J., et al. (2004a). Recent developments in the PHENIX software for automated crystallographic structure determination. *J. Synchrotron Rad., 11*(Pt 1), 53-55.

Arbuthnott, J. P., Freer, J. H., & Bernheimer, A. W. (1967). Physical states of staphylococcal alpha-toxin. *J Bacteriol, 94*(4), 1170-1177.

Ashiuchi, M., Shimanouchi, K., Nakamura, H., Kamei, T., Soda, K., Park, C., et al. (2004). Enzymatic synthesis of high-molecular-mass poly-gamma-glutamate and regulation of its stereochemistry. *Appl Environ Microbiol, 70*(7), 4249-4255.

Bann, J. G. (2012). Anthrax toxin protective antigen-Insights into molecular switching from prepore to pore. *Protein Sci, 21*(1), 1-12.

Baucheron, S., Tyler, S., Boyd, D., Mulvey, M. R., Chaslus-Dancla, E., & Cloeckaert, A. (2004). AcrAB-TolC directs efflux-mediated multidrug resistance in Salmonella enterica serovar typhimurium DT104. *Antimicrob Agents Chemother, 48*(10), 3729-3735.

Beall, F. A., Taylor, M. J., & Thorne, C. B. (1962). Rapid lethal effects of a third factor of anthrax toxin. *J. Bacteriol., 83*, 1274-1280.

Beauregard, K. E., Collier, R. J., & Swanson, J. A. (2000). Proteolytic activation of receptor-bound anthrax protective antigen on macrophages promotes its internalization. *Cell Microbiol, 2*(3), 251-258.

Benson, E. L., Huynh, P. D., Finkelstein, A., & Collier, R. J. (1998). Identification of residues lining the anthrax protective antigen channel. *Biochemistry, 37*(11), 3941-3948.

Bhakdi, S., Bayley, H., Valeva, A., Walev, I., Walker, B., Kehoe, M., et al. (1996). Staphylococcal alpha-toxin, streptolysin-O, and Escherichia coli hemolysin: prototypes of pore-forming bacterial cytolysins. *Arch Microbiol, 165*(2), 73-79.

Blaustein, R. O., Koehler, T. M., Collier, R. J., & Finkelstein, A. (1989). Anthrax toxin: channel-forming activity of protective antigen in planar phospholipid bilayers. *Proc. Natl Acad. Sci. U.S.A., 86*(7), 2209-2213.

Blaustein, R. O., Lea, E. J., & Finkelstein, A. (1990). Voltage-dependent block of anthrax toxin channels in planar phospholipid bilayer membranes by symmetric tetraalkylammonium ions. Single-channel analysis. *J. Gen. Physiol., 96*(5), 921-942.

Bourgogne, A., Drysdale, M., Hilsenbeck, S. G., Peterson, S. N., & Koehler, T. M. (2003). Global effects of virulence gene regulators in a Bacillus anthracis strain with both virulence plasmids. *Infect Immun, 71*(5), 2736-2743.

Boyer, A. E., Quinn, C. P., Hoffmaster, A. R., Kozel, T. R., Saile, E., Marston, C. K., et al. (2009). Kinetics of lethal factor and poly-D-glutamic acid antigenemia during inhalation anthrax in rhesus macaques. *Infect. Immun., 77*(8), 3432-3441.

Bradley, K. A., Mogridge, J., Mourez, M., Collier, R. J., & Young, J. A. (2001). Identification of the cellular receptor for anthrax toxin. *Nature, 414*(6860), 225-229.

Brown, M. J., Thoren, K. L., & Krantz, B. A. (2011). Charge requirements for proton gradient-driven translocation of anthrax toxin. *J. Biol. Chem., 286*(26), 23189-23199.

Bruckner, V., Kovacs, J., & Denes, G. (1953). Structure of poly-D-glutamic acid isolated from capsulated strains of *B. anthracis*. *Nature, 172*(4376), 508-508.

Candela, T., & Fouet, A. (2005). *Bacillus anthracis* CapD, belonging to the gamma-glutamyltranspeptidase family, is required for the covalent anchoring of capsule to peptidoglycan. *Mol. Microbiol., 57*(3), 717-726.

Chabot, D. J., Scorpio, A., Tobery, S. A., Little, S. F., Norris, S. L., & Friedlander, A. M. (2004). Anthrax capsule vaccine protects against experimental infection. *Vaccine, 23*(1), 43-47.

Choe, S., Bennett, M. J., Fujii, G., Curmi, P. M., Kantardjieff, K. A., Collier, R. J., et al. (1992). The crystal structure of diphtheria toxin. *Nature, 357*(6375), 216-222.

Chowdhury, S. K., Katta, V., & Chait, B. T. (1990). Probing conformational-changes in proteins by mass-spectrometry. *J. Am. Chem. Soc., 112*(24), 9012-9013.

Christensen, K. A., Krantz, B. A., & Collier, R. J. (2006). Assembly and disassembly kinetics of anthrax toxin complexes. *Biochemistry, 45*(7), 2380-2386.

Collaborative Computational Project, N. (1994). The CCP4 suite: programs for protein crystallography. *Acta Crystallogr. D Biol. Crystallogr., 50*(Pt 5), 760-763.

Compton, L. A., & Johnson, W. C., Jr. (1986). Analysis of protein circular dichroism spectra for secondary structure using a simple mANTXRix multiplication. *Anal. Biochem., 155*(1), 155-167.

Cromwick, A. M., & Gross, R. A. (1995). Effects of manganese (II) on Bacillus licheniformis ATCC 9945A physiology and gamma-poly(glutamic acid) formation. *Int J Biol Macromol, 17*(5), 259-267.

Cunningham, K., Lacy, D. B., Mogridge, J., & Collier, R. J. (2002). Mapping the lethal factor and edema factor binding sites on oligomeric anthrax protective antigen. *Proc. Natl Acad. Sci. U.S.A., 99*(10), 7049-7053.

Czajkowsky, D. M., Sheng, S., & Shao, Z. (1998). Staphylococcal alpha-hemolysin can form hexamers in phospholipid bilayers. *J Mol Biol, 276*(2), 325-330.

Das, S. K., Darshi, M., Cheley, S., Wallace, M. I., & Bayley, H. (2007). Membrane protein stoichiometry determined from the step-wise photobleaching of dye-labelled subunits. *Chembiochem, 8*(9), 994-999.

Davis, I. W., Leaver-Fay, A., Chen, V. B., Block, J. N., Kapral, G. J., Wang, X., et al. (2007). MolProbity: all-atom contacts and structure validation for proteins and nucleic acids. *Nucleic Acids Res., 35*(Web Server issue), W375-383.

De, S., & Olson, R. Crystal structure of the Vibrio cholerae cytolysin heptamer reveals common features among disparate pore-forming toxins. *Proc Natl Acad Sci U S A, 108*(18), 7385-7390.

Decker, T., & Lohmann-Matthes, M. L. (1988a). A quick and simple method for the quantitation of lactate dehydrogenase release in measurements of cellular cytotoxicity and tumor necrosis factor (TNF) activity. *J. Immunol. Methods, 115*(1), 61-69.

Dobo, A., & Kaltashov, I. A. (2001). Detection of multiple protein conformational ensembles in solution via deconvolution of charge-state distributions in ESI MS. *Anal. Chem., 73*(20), 4763-4773.

Dodd, D., Reese, J. G., Louer, C. R., Ballard, J. D., Spies, M. A., & Blanke, S. R. (2007). Functional comparison of the two Bacillus anthracis glutamate racemases. *J Bacteriol, 189*(14), 5265-5275.

Dodson, E. J., Winn, M., & Ralph, A. (1997). Collaborative Computational Project, number 4: providing programs for protein crystallography. *Methods Enzymol, 277*, 620-633.

Donovan, J. J., Simon, M. I., Draper, R. K., & Montal, M. (1981). Diphtheria toxin forms transmembrane channels in planar lipid bilayers. *Proc Natl Acad Sci U S A, 78*(1), 172-176.

Drum, C. L., Yan, S. Z., Bard, J., Shen, Y. Q., Lu, D., Soelaiman, S., et al. (2002). Structural basis for the activation of anthrax adenylyl cyclase exotoxin by calmodulin. *Nature, 415*(6870), 396-402.

Duesbery, N. S., & Vande Woude, G. F. (1999a). Anthrax lethal factor causes proteolytic inactivation of mitogen- activated protein kinase kinase. *J. Appl. Microbiol., 87*(2), 289-293.

Duesbery, N. S., Webb, C. P., Leppla, S. H., Gordon, V. M., Klimpel, K. R., Copeland, T. D., et al. (1998). Proteolytic inactivation of MAP-kinase-kinase by anthrax lethal factor. *Science, 280*(5364), 734-737.

Elliott, J. L., Mogridge, J., & Collier, R. J. (2000). A quantitative study of the interactions of Bacillus anthracis edema factor and lethal factor with activated protective antigen. *Biochemistry, 39*(22), 6706-6713.

Emsley, P., & Cowtan, K. (2004a). Coot: model-building tools for molecular graphics. *Acta Crystallogr. D Biol. Crystallogr., 60*(Pt 12 Pt 1), 2126-2132.

Ezzell, J. W., & Abshire, T. G. (1992b). Serum protease cleavage of *Bacillus anthracis* protective antigen. *J. Gen. Microbiol., 138*, 543-549.

Ezzell, J. W., Abshire, T. G., Panchal, R., Chabot, D., Bavari, S., Leffel, E. K., et al. (2009). Association of *Bacillus anthracis* capsule with lethal toxin during experimental infection. *Infect. Immun., 77*(2), 749-755.

Fabrini, R., De Luca, A., Stella, L., Mei, G., Orioni, B., Ciccone, S., et al. (2009). Monomer-dimer equilibrium in glutathione transferases: a critical re-examination. *Biochemistry, 48*(43), 10473-10482.

Feld, G. K., Kintzer, A. F., Tang, II, Thoren, K. L., & Krantz, B. A. (2011). Domain Flexibility Modulates the Heterogeneous Assembly Mechanism of Anthrax Toxin Protective Antigen. *J Mol Biol*.

Feld, G. K., Thoren, K. L., Kintzer, A. F., Sterling, H. J., Tang, II, Greenberg, S. G., et al. (2010). Structural basis for the unfolding of anthrax lethal factor by protective antigen oligomers. *Nat Struct Mol Biol, 17*(11), 1383-1390.

Firoved, A. M., Miller, G. F., Moayeri, M., Kakkar, R., Shen, Y., Wiggins, J. F., et al. (2005). *Bacillus anthracis* edema toxin causes extensive tissue lesions and rapid lethality in mice. *Am. J. Pathol., 167*(5), 1309-1320.

Fish, D. C., & Lincoln, R. E. (1968a). In vivo-produced anthrax toxin. *J. Bacteriol., 95*(3), 919-924.

Fish, D. C., Mahlandt, B. G., Dobbs, J. P., & Lincoln, R. E. (1968). Purification and properties of in vitro-produced anthrax toxin components. *J Bacteriol, 95*(3), 907-918.

Fraczkiewicz, R., & Braun, W. (1998). Exact and efficient analytical calculation of the accessible surface areas and their gradients for macromolecules. *J. Comp. Chem., 19*, 319-333.

Frank, J., Radermacher, M., Penczek, P., Zhu, J., Li, Y., Ladjadj, M., et al. (1996). SPIDER and WEB: processing and visualization of images in 3D electron microscopy and related fields. *J. Struct. Biol., 116*(1), 190-199.

Friedlander, A. M. (1986). Macrophages are sensitive to anthrax lethal toxin through an acid-dependent process. *J. Biol. Chem., 261*(16), 7123-7126.

Furini, S., Domene, C., Rossi, M., Tartagni, M., & Cavalcanti, S. (2008). Model-based prediction of the alpha-hemolysin structure in the hexameric state. *Biophys J, 95*(5), 2265-2274.

Gadsby, D. C., Vergani, P., & Csanady, L. (2006). The ABC protein turned chloride channel whose failure causes cystic fibrosis. *Nature, 440*(7083), 477-483.

Go, M. Y., Chow, E. M., & Mogridge, J. (2009). The cytoplasmic domain of anthrax toxin receptor 1 affects binding of the protective antigen. *Infect. Immun., 77*(1), 52-59.

Go, M. Y., Kim, S., Partridge, A. W., Melnyk, R. A., Rath, A., Deber, C. M., et al. (2006). Self-association of the transmembrane domain of an anthrax toxin receptor. *J. Mol. Biol., 360*(1), 145-156.

Gouaux, E. (1997). Channel-forming toxins: tales of transformation. *Curr Opin Struct Biol, 7*(4), 566-573.

Gouaux, J. E., Braha, O., Hobaugh, M. R., Song, L., Cheley, S., Shustak, C., et al. (1994). Subunit stoichiometry of staphylococcal alpha-hemolysin in crystals and on membranes: a heptameric transmembrane pore. *Proc Natl Acad Sci U S A, 91*(26), 12828-12831.

Green, B. D., Battisti, L., Koehler, T. M., Thorne, C. B., & Ivins, B. E. (1985b). Demonstration of a capsule plasmid in *Bacillus anthracis*. *Infect. Immun., 49*(2), 291-297.

Guichard, A., McGillivray, S. M., Cruz-Moreno, B., van Sorge, N. M., Nizet, V., & Bier, E. (2010). Anthrax toxins cooperatively inhibit endocytic recycling by the Rab11/Sec15 exocyst. *Nature, 467*(7317), 854-858.

Hanby, W. E., & Rydon, H. N. (1946). The capsular substance of *Bacillus anthracis*: With an appendix by P. Bruce White. *Biochem. J., 40*(2), 297-309.

Hille, B. (1968). Pharmacological modifications of the sodium channels of frog nerve. *J. Gen. Physiol., 51*(2), 199-219.

Ivanovics, G., & Erdos, L. (1937). The nature of the capsule substance of *B. anthracis*. *Zeitschrift fur Immunitatsforschung, 90*, 5-19.

Jancarik, J., & Kim, S. H. (1991). Sparse mANTXRix sampling: A screening method for crystallization of proteins. *J. Appl. Cryst., 24*, 409-411.

Jang, J., Cho, M., Chun, J. H., Cho, M. H., Park, J., Oh, H. B., et al. (2011). The Poly-{gamma}-D-Glutamic Acid Capsule of Bacillus anthracis Enhances Lethal Toxin Activity. *Infect Immun, 79*(9), 3846-3854.

Ji, X., Armstrong, R. N., & Gilliland, G. L. (1993). Snapshots along the reaction coordinate of an SNAr reaction catalyzed by glutathione transferase. *Biochemistry, 32*(48), 12949-12954.

Jurchen, J. C., Garcia, D. E., & Williams, E. R. (2004). Further studies on the origins of asymmetric charge partitioning in protein homodimers. *J. Am. Soc. Mass Spectrom., 15*(10), 1408-1415.

Jurchen, J. C., & Williams, E. R. (2003). Origin of asymmetric charge partitioning in the dissociation of gas-phase protein homodimers. *J. Am. Chem. Soc., 125*(9), 2817-2826.

Kagan, B. L., Finkelstein, A., & Colombini, M. (1981). Diphtheria toxin fragment forms large pores in phospholipid bilayer membranes. *Proc Natl Acad Sci U S A, 78*(8), 4950-4954.

Katayama, H., Janowiak, B. E., Brzozowski, M., Juryck, J., Falke, S., Gogol, E. P., et al. (2008). GroEL as a molecular scaffold for structural analysis of the anthrax toxin pore. *Nature Struct. Mol. Biol., 15*(7), 754-760.

Kintzer, A. F., Sterling, H. J., Tang, I. I., Abdul-Gader, A., Miles, A. J., Wallace, B. A., et al. (2010b). Role of the protective antigen octamer in the molecular mechanism of anthrax lethal toxin stabilization in plasma. *J. Mol. Biol., 399*(5), 741-758.

Kintzer, A. F., Sterling, H. J., Tang, I. I., Williams, E. R., & Krantz, B. A. (2010). Anthrax toxin receptor drives protective antigen oligomerization and stabilizes the heptameric and octameric oligomer by a similar mechanism. *PLoS ONE, 5*(11), e13888.

Kintzer, A. F., Thoren, K. L., Sterling, H. J., Dong, K. C., Feld, G. K., Tang, I. I., et al. (2009). The protective antigen component of anthrax toxin forms functional octameric complexes. *J. Mol. Biol., 392*, 614-629.

Konermann, L., & Douglas, D. J. (1998). Equilibrium unfolding of proteins monitored by electrospray ionization mass spectrometry: Distinguishing two-state from multi-state transitions. *Rap. Comm. Mass Spectrom., 12*(8), 435-442.

Krantz, B. A., Finkelstein, A., & Collier, R. J. (2006). Protein translocation through the anthrax toxin transmembrane pore is driven by a proton gradient. *J. Mol. Biol., 355*(5), 968-979.

Krantz, B. A., Melnyk, R. A., Zhang, S., Juris, S. J., Lacy, D. B., Wu, Z., et al. (2005). A phenylalanine clamp catalyzes protein translocation through the anthrax toxin pore. *Science, 309*(5735), 777-781.

Krantz, B. A., Trivedi, A. D., Cunningham, K., Christensen, K. A., & Collier, R. J. (2004). Acid-induced unfolding of the amino-terminal domains of the lethal and edema factors of anthrax toxin. *J. Mol. Biol., 344*(3), 739-756.

Lacy, D. B., Lin, H. C., Melnyk, R. A., Schueler-Furman, O., Reither, L., Cunningham, K., et al. (2005). A model of anthrax toxin lethal factor bound to protective antigen. *Proc. Natl Acad. Sci. U.S.A., 102*(45), 16409-16414.

Lacy, D. B., Mourez, M., Fouassier, A., & Collier, R. J. (2002). Mapping the anthrax protective antigen binding site on the lethal and edema factors. *J. Biol. Chem., 277*(4), 3006-3010.

Lacy, D. B., Wigelsworth, D. J., Melnyk, R. A., Harrison, S. C., & Collier, R. J. (2004). Structure of heptameric protective antigen bound to an anthrax toxin receptor: a

role for receptor in pH-dependent pore formation. *Proc. Natl. Acad. Sci. U.S.A., 101*(36), 13147-13151.

Lacy, D. B., Wigelsworth, D. J., Scobie, H. M., Young, J. A., & Collier, R. J. (2004). Crystal structure of the von Willebrand factor A domain of human capillary morphogenesis protein 2: an anthrax toxin receptor. *Proc. Natl Acad. Sci. U.S.A., 101*(17), 6367-6372.

Laskowski, R. A., MacArthur, M. W., Moss, D. S., & Thornton, J. M. (1993). PROCHECK: a program to check the stereochemical quality of protein structures. *J. Appl. Cryst., 26*, 283-291.

Lees, J. G., Miles, A. J., Wien, F., & Wallace, B. A. (2006). A reference database for circular dichroism spectroscopy covering fold and secondary structure space. *Bioinformatics, 22*(16), 1955-1962.

Lees, J. G., Smith, B. R., Wien, F., Miles, A. J., & Wallace, B. A. (2004). CDtool-an integrated software package for circular dichroism spectroscopic data processing, analysis, and archiving. *Anal Biochem, 332*(2), 285-289.

Leppla, S. H. (1982). Anthrax toxin edema factor: a bacterial adenylate cyclase that increases cyclic AMP concentrations of eukaryotic cells. *Proc. Natl Acad. Sci. U.S.A., 79*(10), 3162-3166.

Leppla, S. H. (1984). *Bacillus anthracis* calmodulin-dependent adenylate cyclase: chemical and enzymatic properties and interactions with eucaryotic cells. *Adv. Cyclic Nucleotide Protein Phosphorylation Res., 17*, 189-198.

Leppla, S. H. (1991). The anthrax toxin complex. In J. E. Alouf & J. H. Freer (Eds.), *Sourcebook of bacterial protein toxins* (pp. 277–302). London: Academic Press.

Liu, S., & Leppla, S. H. (2003). Cell surface tumor endothelium marker 8 cytoplasmic tail-independent anthrax toxin binding, proteolytic processing, oligomer formation, and internalization. *J. Biol. Chem., 278*(7), 5227-5234.

Lobley, A., Whitmore, L., & Wallace, B. A. (2002). DICHROWEB: an interactive website for the analysis of protein secondary structure from circular dichroism spectra. *Bioinformatics, 18*(1), 211-212.

Locher, K. P., Lee, A. T., & Rees, D. C. (2002). The E. coli BtuCD structure: a framework for ABC transporter architecture and mechanism. *Science, 296*(5570), 1091-1098.

Ludtke, S. J., Baldwin, P. R., & Chiu, W. (1999). EMAN: semiautomated software for high-resolution single-particle reconstructions. *J. Struct. Biol., 128*(1), 82-97.

Mabry, R., Brasky, K., Geiger, R., Carrion, R., Jr., Hubbard, G. B., Leppla, S., et al. (2006). Detection of anthrax toxin in the serum of animals infected with Bacillus anthracis by using engineered immunoassays. *Clin. Vaccine Immunol., 13*(6), 671-677.

MacDowell, A. A., Celestre, R. S., Howells, M., McKinney, W., Krupnick, J., Cambie, D., et al. (2004). Suite of three protein crystallography beamlines with single superconducting bend magnet as the source. *J. Synchrotron Rad., 11*(Pt 6), 447-455.

Makino, S., Uchida, I., Terakado, N., Sasakawa, C., & Yoshikawa, M. (1989). Molecular characterization and protein analysis of the cap region, which is essential for encapsulation in *Bacillus anthracis*. *J. Bacter., 171*(2), 722-730.

Makino, S., Watarai, M., Cheun, H. I., Shirahata, T., & Uchida, I. (2002a). Effect of the lower molecular capsule released from the cell surface of *Bacillus anthracis* on the pathogenesis of anthrax. *J. Infect. Dis., 186*(2), 227-233.

Maurer, P. H. (1965b). Antigenicity of polypeptides (poly alpha amino acids). 13. Immunological studies with synthetic polymers containing only D- or D- and L-alpha-amino acids. *J. Exp. Med., 121*(3), 339-&.

McKay, A. R., Ruotolo, B. T., Ilag, L. L., & Robinson, C. V. (2006). Mass measurements of increased accuracy resolve heterogeneous populations of intact ribosomes. *J. Am. Chem. Soc., 128*(35), 11433-11442.

McPherson, A., Jr. (1976). The growth and preliminary investigation of protein and nucleic acid crystals for X-ray diffraction analysis. *Methods Biochem. Anal., 23*(0), 249-345.

Miller, C. J., Elliott, J. L., & Collier, R. J. (1999). Anthrax protective antigen: prepore-to-pore conversion. *Biochemistry, 38*(32), 10432-10441.

Milne, J. C., Furlong, D., Hanna, P. C., Wall, J. S., & Collier, R. J. (1994). Anthrax protective antigen forms oligomers during intoxication of mammalian cells. *J. Biol. Chem., 269*(32), 20607-20612.

Minton, A. P. (2000). Implications of macromolecular crowding for protein assembly. *Curr Opin Struct Biol, 10*(1), 34-39.

Mitra, K., Schaffitzel, C., Shaikh, T., Tama, F., Jenni, S., Brooks, C. L., 3rd, et al. (2005). Structure of the E. coli protein-conducting channel bound to a translating ribosome. *Nature, 438*(7066), 318-324.

Moayeri, M., Wiggins, J. F., & Leppla, S. H. (2007). Anthrax protective antigen cleavage and clearance from the blood of mice and rats. *Infect. Immun., 75*(11), 5175-5184.

Mogridge, J., Cunningham, K., & Collier, R. J. (2002). Stoichiometry of anthrax toxin complexes. *Biochemistry, 41*(3), 1079-1082.

Mogridge, J., Mourez, M., & Collier, R. J. (2001). Involvement of domain 3 in oligomerization by the protective antigen moiety of anthrax toxin. *J. Bacteriol., 183*(6), 2111-2116.

Mueller, M., Grauschopf, U., Maier, T., Glockshuber, R., & Ban, N. (2009). The structure of a cytolytic alpha-helical toxin pore reveals its assembly mechanism. *Nature, 459*(7247), 726-730.

Mueller, P., Rudin, D. O., Tien, H. T., & Westcott, W. C. (1963). Methods for the formation of single bimolecular lipid membranes in aqueous solution. *J. Phys. Chem., 67*, 534-535.

Murakami, S., Nakashima, R., Yamashita, E., & Yamaguchi, A. (2002). Crystal structure of bacterial multidrug efflux transporter AcrB. *Nature, 419*(6907), 587-593.

Nassi, S., Collier, R. J., & Finkelstein, A. (2002a). PA63 channel of anthrax toxin: an extended beta-barrel. *Biochemistry, 41*(5), 1445-1450.

Nguyen, T. L. (2004). Three-dimensional model of the pore form of anthrax protective antigen. Structure and biological implications. *J Biomol Struct Dyn, 22*(3), 253-265.

Novak, J. M., Stein, M. P., Little, S. F., Leppla, S. H., & Friedlander, A. M. (1992). Functional characterization of protease-treated *Bacillus anthracis* protective antigen. *J. Biol. Chem., 267*(24), 17186-17193.

Okinaka, R. T., Cloud, K., Hampton, O., Hoffmaster, A. R., Hill, K. K., Keim, P., et al. (1999). Sequence and organization of pXO1, the large *Bacillus anthracis* plasmid harboring the anthrax toxin genes. *J. Bacteriol., 181*(20), 6509-6515.

Oldham, M. L., Khare, D., Quiocho, F. A., Davidson, A. L., & Chen, J. (2007). Crystal structure of a catalytic intermediate of the maltose transporter. *Nature, 450*(7169), 515-521.

Olofsson, A., Kaveus, U., Thelestam, M., & Hebert, H. (1988). The projection structure of alpha-toxin from Staphylococcus aureus in human platelet membranes as analyzed by electron microscopy and image processing. *J Ultrastruct Mol Struct Res, 100*(2), 194-200.

Otwinowski, Z., & Minor, W. (1997). Processing of X-ray diffraction data collected in oscillation mode. In C. W. Carter Jr. & R. M. Sweet (Eds.), *Methods in Enzymology* (Vol. 276: Macromolecular Crystallography, part A, pp. 307-326). New York: Academic Press, Inc.

Pannifer, A. D., Wong, T. Y., Schwarzenbacher, R., Renatus, M., Petosa, C., Bienkowska, J., et al. (2001). Crystal structure of the anthrax lethal factor. *Nature, 414*(6860), 229-233.

Pastan, I., & FitzGerald, D. (1991). Recombinant toxins for cancer treatment. *Science, 254*(5035), 1173-1177.

Petosa, C., Collier, R. J., Klimpel, K. R., Leppla, S. H., & Liddington, R. C. (1997). Crystal structure of the anthrax toxin protective antigen. *Nature, 385*(6619), 833-838.

Pettersen, E. F., Goddard, T. D., Huang, C. C., Couch, G. S., Greenblatt, D. M., Meng, E. C., et al. (2004a). UCSF Chimera--a visualization system for exploratory research and analysis. *J Comput Chem, 25*(13), 1605-1612.

Pezard, C., Berche, P., & Mock, M. (1991). Contribution of individual toxin components to virulence of *Bacillus anthracis*. *Infect. Immun., 59*(10), 3472-3477.

Pilpa, R. M., Bayrhuber, M., Marlett, J. M., Riek, R., & Young, J. A. (2011). A receptor-based switch that regulates anthrax toxin pore formation. *PLoS Pathog, 7*(12), e1002354.

Provencher, S. W., & Glockner, J. (1981). Estimation of globular protein secondary structure from circular dichroism. *Biochemistry, 20*(1), 33-37.

Rainey, G. J., Wigelsworth, D. J., Ryan, P. L., Scobie, H. M., Collier, R. J., & Young, J. A. (2005). Receptor-specific requirements for anthrax toxin delivery into cells. *Proc. Natl Acad. Sci. U.S.A., 102*(37), 13278-13283.

Ross, J. M. (1957). The pathogenesis of anthrax following the administration of spores by the respiratory route. *J. Pathol. Bacteriol., 73*, 485-494.

Rossjohn, J., Feil, S. C., McKinstry, W. J., Tweten, R. K., & Parker, M. W. (1997). Structure of a cholesterol-binding, thiol-activated cytolysin and a model of its membrane form. *Cell, 89*(5), 685-692.

Rozengurt, E., Higgins, T., Chanter, N., Lax, A. J., & Staddon, J. M. (1990). Pasteurella multocida toxin: potent mitogen for cultured fibroblasts. *Proc Natl Acad Sci U S A, 87*(1), 123-127.

Santelli, E., Bankston, L. A., Leppla, S. H., & Liddington, R. C. (2004). Crystal structure of a complex between anthrax toxin and its host cell receptor. *Nature, 430*(7002), 905-908.

Schatz, G., & Dobberstein, B. (1996). Common principles of protein translocation across membranes. *Science, 271*(5255), 1519-1526.

Schuerch, D. W., Wilson-Kubalek, E. M., & Tweten, R. K. (2005). Molecular basis of listeriolysin O pH dependence. *Proc Natl Acad Sci U S A, 102*(35), 12537-12542.

Scobie, H. M., Marlett, J. M., Rainey, G. J., Lacy, D. B., Collier, R. J., & Young, J. A. (2007). Anthrax toxin receptor 2 determinants that dictate the pH threshold of toxin pore formation. *PLoS ONE, 2*(3), e329.

Scobie, H. M., Rainey, G. J. A., Bradley, K. A., & Young, J. A. (2003). Human capillary morphogenesis protein 2 functions as an anthrax toxin receptor. *Proc. Natl Acad. Sci. U.S.A., 100*(9), 5170-5174.

Scorpio, A., Chabot, D. J., Day, W. A., O'Brien D, K., Vietri, N. J., Itoh, Y., et al. (2007). Poly-gamma-glutamate capsule-degrading enzyme treatment enhances phagocytosis and killing of encapsulated *Bacillus anthracis*. *Antimicrob. Agents Chemother., 51*(1), 215-222.

Sirard, J. C., Mock, M., & Fouet, A. (1994). The three *Bacillus anthracis* toxin genes are coordinately regulated by bicarbonate and temperature. *J. Bacteriol., 176*(16), 5188-5192.

Siuzdak, G., Bothner, B., Yeager, M., Brugidou, C., Fauquet, C. M., Hoey, K., et al. (1996). Mass spectrometry and viral analysis. *Chemistry & Biology, 3*(1), 45-48.

Skaper, S. D. (2011). Ion channels on microglia: therapeutic targets for neuroprotection. *CNS Neurol Disord Drug Targets, 10*(1), 44-56.

Smith, H., & Keppie, J. (1954). Observations on experimental anthrax: demonstration of a specific lethal factor produced in vivo by *Bacillus anthracis*. *Nature, 173*, 689.

Smith, H., Keppie, J., & Stanley, J. L. (1954). Observations on the cause of death in experimental anthrax. *Lancet, 267*(6836), 474-476.

Song, L., Hobaugh, M. R., Shustak, C., Cheley, S., Bayley, H., & Gouaux, J. E. (1996a). Structure of staphylococcal alpha-hemolysin, a heptameric transmembrane pore. *Science, 274*(5294), 1859-1866.

Souba, W. W. (1993). Glutamine and cancer. *Ann Surg, 218*(6), 715-728.

Stanley, J. L., & Smith, H. (1961). Purification of factor I and recognition of a third factor of the anthrax toxin. *J. Gen. Microbiol., 26*, 49-66.

Stark, H., Mueller, F., Orlova, E. V., Schatz, M., Dube, P., Erdemir, T., et al. (1995). The 70S *Escherichia coli* ribosome at 23 A resolution: fitting the ribosomal RNA. *Structure, 3*(8), 815-821.

Sterling, H. J., & Williams, E. R. (2009). Origin of supercharging in electrospray ionization of noncovalent complexes from aqueous solution. *J. Am. Soc. Mass Spectrom.*

Storoni, L. C., McCoy, A. J., & Read, R. J. (2004a). Likelihood-enhanced fast rotation functions. *Acta Crystallogr. D Biol. Crystallogr., 60*(Pt 3), 432-438.

Sun, J., Lang, A. E., Aktories, K., & Collier, R. J. (2008). Phenylalanine-427 of anthrax protective antigen functions in both pore formation and protein translocation. *Proc Natl Acad Sci U S A, 105*(11), 4346-4351.

Sun, J., Vernier, G., Wigelsworth, D. J., & Collier, R. J. (2007). Insertion of anthrax protective antigen into liposomal membranes: effects of a receptor. *J. Biol. Chem., 282*(2), 1059-1065.

Thoren, K. L., Worden, E. J., Yassif, J. M., & Krantz, B. A. (2009). Lethal factor unfolding is the most force-dependent step of anthrax toxin translocation. *Proc. Natl Acad. Sci. U.S.A., 106*(51), 21555-21560.

Troy, F. A. (1973). CHEMISTRY AND BIOSYNTHESIS OF POLY(GAMMA-D-GLUTAMYL) CAPSULE IN BACILLUS-LICHENIFORMIS .1. PROPERTIES OF MEMBRANE-MEDIATED BIOSYNTHETIC REACTION. *Journal of Biological Chemistry, 248*(1), 305-315.

Uchida, I., Makino, S., Sasakawa, C., Yoshikawa, M., Sugimoto, C., & Terakado, N. (1993a). Identification of a novel gene, dep, associated with depolymerization of the capsular polymer in *Bacillus anthracis*. *Mol. Microbiol., 9*(3), 487-496.

Update: Investigation of bioterrorism-related anthrax and interim guidelines for clinical evaluation of persons with possible anthrax. (2001). *Morb. Mortal. Wkly. Rep., 50*(43), 941-948.

Van den Berg, B., Clemons, W. M., Jr., Collinson, I., Modis, Y., Hartmann, E., Harrison, S. C., et al. (2004). X-ray structure of a protein-conducting channel. *Nature, 427*(6969), 36-44.

van Heel, M., Harauz, G., Orlova, E. V., Schmidt, R., & Schatz, M. (1996). A new generation of the IMAGIC image processing system. *J. Struct. Biol., 116*(1), 17-24.

van Stokkum, I. H., Spoelder, H. J., Bloemendal, M., van Grondelle, R., & Groen, F. C. (1990). Estimation of protein secondary structure and error analysis from circular dichroism spectra. *Anal. Biochem., 191*(1), 110-118.

Vernier, G., Wang, J., Jennings, L. D., Sun, J., Fischer, A., Song, L., et al. (2009). Solubilization and characterization of the anthrax toxin pore in detergent micelles. *Protein Sci., 18*(9), 1882-1895.

Ward, R. J., & Leonard, K. (1992). The Staphylococcus aureus alpha-toxin channel complex and the effect of Ca2+ ions on its interaction with lipid layers. *J Struct Biol, 109*(2), 129-141.

Watson, P., & Spooner, R. A. (2006). Toxin entry and trafficking in mammalian cells. *Adv Drug Deliv Rev, 58*(15), 1581-1596.

Weis, W., Brown, J. H., Cusack, S., Paulson, J. C., Skehel, J. J., & Wiley, D. C. (1988). Structure of the influenza virus haemagglutinin complexed with its receptor, sialic acid. *Nature, 333*(6172), 426-431.

Welkos, S., Little, S., Friedlander, A., Fritz, D., & Fellows, P. (2001). The role of antibodies to *Bacillus anthracis* and anthrax toxin components in inhibiting the early stages of infection by anthrax spores. *Microbiology, 147*(Pt 6), 1677-1685.

Welkos, S. L. (1991a). Plasmid-associated virulence factors of non-toxigenic (pX01-) Bacillus anthracis. *Microb Pathog, 10*(3), 183-198.

Wesche, J., Elliott, J. L., Falnes, P. O., Olsnes, S., & Collier, R. J. (1998). Characterization of membrane translocation by anthrax protective antigen. *Biochemistry, 37*(45), 15737-15746.

White, H. E., Saibil, H. R., Ignatiou, A., & Orlova, E. V. (2004). Recognition and separation of single particles with size variation by statistical analysis of their images. *J. Mol. Biol., 336*(2), 453-460.

Wiener, M., Freymann, D., Ghosh, P., & Stroud, R. M. (1997). Crystal structure of colicin Ia. *Nature, 385*(6615), 461-464.

Wigelsworth, D. J., Krantz, B. A., Christensen, K. A., Lacy, D. B., Juris, S. J., & Collier, R. J. (2004). Binding stoichiometry and kinetics of the interaction of a human anthrax toxin receptor, CMG2, with protective antigen. *J. Biol. Chem., 279*(22), 23349-23356.

Wimalasena, D. S., Cramer, J. C., Janowiak, B. E., Juris, S. J., Melnyk, R. A., Anderson, D. E., et al. (2007). Effect of 2-fluorohistidine labeling of the anthrax protective antigen on stability, pore formation, and translocation. *Biochemistry, 46*(51), 14928-14936.

Wimalasena, D. S., Janowiak, B. E., Lovell, S., Miyagi, M., Sun, J., Zhou, H., et al. (2010). Evidence that histidine protonation of receptor-bound anthrax protective antigen is a trigger for pore formation. *Biochemistry, 49*(33), 6973-6983.

Yamashita, K., Kawai, Y., Tanaka, Y., Hirano, N., Kaneko, J., Tomita, N., et al. Crystal structure of the octameric pore of staphylococcal {gamma}-hemolysin reveals the {beta}-barrel pore formation mechanism by two components. *Proc Natl Acad Sci U S A, 108*(42), 17314-17319.

Young, J. A., & Collier, R. J. (2007). Anthrax toxin: receptor binding, internalization, pore formation, and translocation. *Annu. Rev. Biochem., 76*, 243-265.

Young, J. J., Bromberg-White, J. L., Zylstra, C., Church, J. T., Boguslawski, E., Resau, J. H., et al. (2007). LRP5 and LRP6 are not required for protective antigen-mediated internalization or lethality of anthrax lethal toxin. *PLoS Pathogen, 3*(3), e27.

Zhang, S., Udho, E., Wu, Z., Collier, R. J., & Finkelstein, A. (2004). Protein translocation through anthrax toxin channels formed in planar lipid bilayers. *Biophys. J., 87*(6), 3842-3849.

Zhao, Y., Yang, J., Shi, J., Gong, Y. N., Lu, Q., Xu, H., et al. (2012). The NLRC4 inflammasome receptors for bacterial flagellin and type III secretion apparatus. *Nature, 477*(7366), 596-600.

Zheng, L., Baumann, U., & Reymond, J. L. (2004). An efficient one-step site-directed and site-saturation mutagenesis protocol. *Nucleic Acids Res., 32*(14), e115.

Zwartouw, H. T., & Smith, H. (1956a). Polyglutamic acid from Bacillus anthracis grown in vivo; structure and aggressin activity. *Biochem J, 63*(3), 437-442.